Influence of water on the short-term and long-term mechanical properties of swelling clays : experiments on self-supporting films and molecular simulations

Benoît Carrier

UNIVERSITÉ PARIS-EST

ÉCOLE DOCTORALE SCIENCE INGÉNIERIE ET ENVIRONNEMENT

THÈSE

présentée pour l'obtention du diplôme de

DOCTEUR

DE

L'UNIVERSITÉ PARIS-EST

Spécialité: *Science des Matériaux*

par

Benoît CARRIER

Sujet de la thèse :

Effet de l'eau sur les propriétés mécaniques à court et long termes des argiles gonflantes : expériences sur films autoporteurs et simulations moléculaires.

Thèse soutenue le 6 décembre 2013 devant le jury composé de :

Rapporteurs :	**Dr. Laurent MICHOT**
	Dr. François-Xavier COUDERT
Examinateurs :	**Pr. Pierre DELAGE**
	Dr. Roland PELLENQ
	Dr. Matthieu VANDAMME
Directeur de thèse :	**Dr. Henri VAN DAMME**

Remerciements

Je souhaite exprimer toute ma reconnaissance à mes encadrants de thèse auprès de qui j'ai passé trois années extrêmement enrichissantes. Je remercie en particulier Henri Van Damme d'avoir accepté de diriger ce travail et d'avoir prodigué de précieux conseils scientifiques tout au long de ces 3 ans. Je ne ressortais jamais d'une rencontre avec Henri sans une liste de dizaines de référence qu'il était capable de citer de tête. Je remercie également Roland Pellenq d'avoir collaboré activement à ce projet. Roland m'a accueilli à Boston à de nombreuses reprises toujours très chaleureusement poure des échanges scientifiques fructueux. Last but not least, je remercie Matthieu Vandamme d'avoir tout d'abord initié le projet, puis pour son encadrement régulier et enthousiaste tout au long de ces trois ans.

J'ai passé trois années extrêmement stimulantes et formatrices auprès d'Henri, Roland et Matthieu et j'en garderai un excellent souvenir. Et, partant vers des horizons éloignés du monde académique, je suis certain de repenser à ces années avec nostalgie.

Je remercie les membres de mon jury pour leurs suggestions et questions constructives. Je remercie Pierre Delage d'avoir accepté de présider le jury et Laurent Michot et François-Xavier Coudert pour leur lecture détaillée de mon manuscrit.

Ma thèse a été financée par le Ministère de l'Écologie, de Développement durable et de l'énergie et suivie par la Commission de Formation Doctorale des IPEF. Je remercie l'ensemble des acteurs de la Commission pour avoir permis la réalisation de ce projet et en particulier Serge Piperno pour son suivi.

J'ai réalisé ma thèse au Laboratoire Navier à l'École des Ponts ParisTech, dans l'équipe multi-échelle. Je remercie Karam Sab, Directeur du laboratoire, d'avoir hébergé ce travail. Je remercie également Michel Bornert, animateur de l'équipe multi-échelle d'avoir soutenu ce travail et pour son apport scientifique essentiel à la majeure partie des expériences présentées dans ce manuscrit. Je souhaite également exprimer toute ma gratitude à tous

les membres du laboratoire qui ont rendu ce travail possible. J'ai bénéficié du soutien constant des équipes techniques - Nicolas, Alain, Daniel, Gilles, Christophe - et administratives - Marie-Francoise et Rachida notamment. Je remercie tout particulièrement Géraldine pour son aide précieuse et sa réactivité lors de la mise en place de toutes mes expériences.

Je remercie également tous mes collègues de travail pour toutes les discussions scientifiques ou les déjeuners ou cafés que nous avons partagés. Je remercie en particulier Laurent pour son aide lors de la mise en place de mes simulations moléculaires et Linlin pour son aide lors des expériences au MEB environnemental. Je remercie Francois Chevoir de m'avoir donné l'occasion d'enseigner la physique statistique à l'École des Ponts.

Je remercie toute ma famille pour son soutien inestimable tout au long de mon parcours académique. Je lui suis reconnaissant de m'avoir transmis le goût des défis scientifiques et de la recherche de l'excellence et de m'avoir toujours extrêmement bien entouré. Enfin, je remercie Noëlle pour m'avoir soutenu pendant ces 3 ans.

Abstract

The study of clay-based materials has many applications in civil and environmental engineering. These applications include underground nuclear waste disposal, the natural risks associated to the swelling and shrinkage of soils, and the extraction of hydrocarbons. They pose significant technological challenges that require to understand and to predict the mechanical behavior of clays, in particular on the long term. Swelling clays are complex porous multiscale materials and their properties are very sensitive to water. In this thesis, we aim at understanding the impact of water on the short-term and long-term mechanical properties of clays. Our strategy was to combine numerical simulations at the scale of the nanometer and experiments at the scale of the micrometer to have a better insight of the interplay between these scales. We performed molecular simulations to estimate the effect of water and of the interlayer cation on the swelling, elastic and creep properties of clay layers, which are inaccessible to experiments at this scale. We also carried out a comparative study of various numerical models of increasing complexity in order to better understand the interactions that governs the cohesion between the clay layers. We measured experimentally the properties of well-ordered self-supporting clay films. We investigated the impact of relative humidity and of the nature of the interlayer cation on the mechanical properties of these clay films. In particular, we quantified the humidity-induced swelling of these films by using a combination of environmental scanning electron microscopy and digital image correlation. We also performed tensile tests and creep tests on these films at controlled relative humidity. We compared the data obtained by our experiments to the results of the molecular simulations. This comparison makes it possible to discuss the elementary deformation mechanisms and the scales relevant to the understanding of the hydromechanical behavior of clays.

Keywords: smectite clay, hydromechanical coupling, self-standing film, viscoelasticity, creep, swelling, ESEM, molecular simulation.

Résumé

L'étude des matériaux argileux a de nombreuses applications en génie civil et environnemental. Ces applications, telles que l'enfouissement des déchets nucléaires, les risques naturels liés au gonflement et au retrait des sols, et l'extraction d'hydrocarbures, posent des défis technologiques qui nécessitent de comprendre et de prédire le comportement mécanique des argiles, en particulier sur le long terme. Les argiles gonflantes sont des matériaux complexes, poreux et multi-échelles dont les propriétés sont très sensibles à l'eau. Dans cette thèse, nous cherchons à comprendre l'effet de l'eau sur les propriétés mécaniques à court et long terme des argiles. Notre stratégie est de combiner des simulations numériques à l'échelle du nanomètre et des expériences à l'échelle du micromètre afin de mieux comprendre l'interaction entre ces échelles. Nous avons effectué des simulations moléculaires pour quantifier l'effet de l'eau et du cation interfoliaire sur les propriétés de gonflement, élastiques et de fluage des feuillets d'argile, qui à cette échelle sont inaccessibles à l'expérience. Nous avons également effectué une étude comparative de différents modèles de feuillets d'argile de complexité croissante afin de mieux comprendre les interactions qui régissent la cohésion entre les feuillets d'argile. Nous avons mesuré expérimentalement les propriétés de films d'argile autoporteurs bien ordonnés. Nous avons montré l'effet de l'humidité relative et de la nature du cation interfoliaire sur les déformations de ces films d'argile. En particulier, nous avons quantifié le gonflement de ces films induit par l'humidité en combinant microscopie électronique à balayage environnementale et corrélation d'images numériques. Nous avons également effectué des essais de traction et de fluage sur ces films à humidité contrôlée. Nous avons comparé les données obtenues par nos expériences aux résultats des simulations moléculaires. Cette comparaison permet de discuter les mécanismes élémentaires de déformation et les échelles pertinentes pour la compréhension du comportement hydromécanique des argiles.

Mots clés : smectite, couplage hydro-mécanique, film autoporteur, viscoélasticité, gonflement, MEB environnemental, simulation moléculaire.

Résumé long

Comprendre le comportement hydromécanique des matériaux argileux répond à des défis environnementaux, technologiques et économiques importants. En France, par exemple, une roche argileuse, l'argilite, a été choisie comme roche hôte potentielle pour le stockage géologique de déchets radioactifs. En génie civil, le retrait et le gonflement des argiles a des répercussions considérables sur la stabilité des sols et des fondations des bâtiments. Dans l'industrie pétrolière, les propriétés des matériaux argileux ont un impact important sur les opérations de forage et de production puisque les shales, une autre roche argileuse, sont rencontrés aussi bien comme roches de couverture de réservoirs d'hydrocarbures que comme roches mères de pétrole et de gaz. La prédiction de la réponse de ces matériaux tout au long de la phase d'exploitation de ces infrastructures géotechniques requiert de quantifier leurs propriétés hydromécaniques non seulement à court terme mais aussi à long terme.

Les matériaux argileux ont une structure et un réseau poreux multi-échelles et complexes. C'est pourquoi les liens entre le comportement à l'échelle du feuillet et le comportement macroscopique ne sont pas totalement compris. L'objectif de cette thèse est de mieux comprendre les mécanismes fondamentaux de l'hydratation et de la déformation des matériaux argileux et de fournir aux modèles aux échelles supérieures une base physique forte afin de construire des lois de comportement macroscopiques prédictives et robustes. Nous étudions en particulier l'impact de l'eau sur les propriétés mécaniques suivantes des argiles : gonflement, résistance, élasticité et fluage. Nous avons utilisé deux approches parallèles pour explorer ces propriétés : des simulations moléculaires et des expériences sur des films d'argile. Les simulations moléculaires ont permis d'étudier le comportement à l'échelle du feuillet d'argile, tandis que réaliser des expériences sur des films d'argile fins et bien organisés avait pour objectif de combler la lacune entre l'échelle du feuillet et de l'échelle de l'ingénieur.

Nous avons tout d'abord mesuré le gonflement induit par l'humidité de

films minces autoportants de montmorillonite, une argile gonflante très répandue, en combinant microscopie électronique à balayage environnementale (ESEM) et corrélation d'images numériques (DIC). Les films mesuraient de 30 à 60 microns d'épaisseur. Ils ont été préparés par dépôt et évaporation d'une suspension d'argile et par décollement des dépôts fortement orientés ainsi préparés. Le but de la fabrication de ces échantillons originaux était d'obtenir des échantillons mésoscopiques qui puissent être utilisés pour combler expérimentalement la lacune entre l'échelle du feuillet d'argile et l'échelle d'un échantillon d'argile macroscopique. Plusieurs échantillons de montmorillonite ont été utilisés : l'argile de référence Swy-2, la même argile homoionisée avec des ions sodium ou calcium, et une cloisite sodique. La tranche des films d'argile a été observée par ESEM à différentes valeurs d'humidité relative entre 14 % et 95 %. Les images ESEM ont ensuite été analysées par DIC pour mesurer le gonflement ou le retrait des films. Nous avons également mesuré les isothermes d'adsorption/désorption en pesant les échantillons dans un environnement à humidité contrôlée. Nous avons ensuite comparé nos données d'adsorption/désorption et de gonflement/retrait à celles déjà publiées sur l'espace interfoliaire, obtenues par diffraction des rayons X, et à des estimations numériques de la quantité d'eau interfoliaire que nous avons obtenues par dynamique moléculaire. Le gonflement ainsi que l'hystérésis de ce gonflement se sont avérés comparables pour les films mésoscopiques et pour l'espace interfoliaire. La même correspondance entre le film et l'espace interfoliaire a été observée pour la quantité d'eau adsorbée. Cela suggère que, dans l'intervalle des valeurs humidités relatives explorées, les films se comportent comme un empilement ordonné de feuillets gonflant librement, sans aucune contribution significative de la mésoporosité.

Nous avons ensuite étudié les interactions responsables de la cohésion des feuillets d'argile. Il n'y a en effet aucune liaison covalente qui lie les feuillets d'argile entre eux. Quelles sont donc les interactions qui confèrent au matériau sa cohésion ? Les propriétés de gonflement des argiles dépendent à la fois de la nature du cation interfoliaire et de la charge de surface des feuillets. Notre objectif est de mieux comprendre comment ces paramètres influent sur les interactions et la cohésion entre les feuillets d'argile. L'in-

térêt de cette question dépasse les seuls matériaux argileux et ce travail peut être appliqué à d'autres matériaux lamellaires chargés séparés par des cations et un solvant. Nous avons cherché à déterminer le niveau de complexité nécessaire à la modélisation de la cohésion des matériaux lamellaires chargés, en fonction de la charge de la surface, de la valence des cations et de la distance entre les surfaces chargées. Pour répondre à cette question, nous avons réalisé des simulations numériques d'électrolytes confinés entre des feuillets d'argile chargés. En plus de la théorie analytique champ-moyen Derjaguin-Landau-Verwey-Overbeek (DLVO), nous utilisons différents modèles numériques de complexité croissante, du Modèle Primitif au modèle tout atomistique. Dans le Modèle Primitif, les feuillets sont décrits par des surfaces planes infinies uniformément chargées, les ions hydratés par des sphères chargées et le solvant par un continuum diélectrique, tandis que dans le modèle tout atomistique toute la structure moléculaire des feuillets et du solvant est décrite. En particulier, nous avons développé un modèle de complexité intermédiaire entre le Modèle Primitif et le modèle tout atomistique : le Modèle Primitif à Solvant Explicite, dans lequel les cations sont modélisées par des charges ponctuelles et les molécules de solvant sont modélisés par des dipôles ponctuels. Ce Modèle Primitif à Solvant Explicite a donné des résultats proches du modèle tout atomistique pour un coût de calcul bien inférieur. Par ailleurs, en comparant les résultats du Modèle Primitif à Solvant Explicite à ceux du Modèle Primitif, nous avons montré que la prise en compte du solvant explicite à un effet significatif sur la cohésion du modèle. Les forces de corrélation ioniques, dues à la polarisation instantanée du nuage d'ions dans l'espace interfoliaire et toujours attractives, sont toujours présentes entre les feuillets et jouent toujours un rôle important, même dans le cas de feuillets portant une faible charge de surface à faible équilibrée par des contre-ions monovalents.

Nous avons également calculé les propriétés élastiques des particules de la montmorillonite par des simulations de dynamique moléculaire en utilisant un modèle tout atomistique. En raison de la souplesse du matériau dans la direction orthogonale aux feuillets d'argiles lorsque ces derniers sont hydratés, le calcul de l'ensemble du tenseur de rigidité était complexe: afin d'obtenir

des résultats convergés et stables, nous avons dû mettre en œuvre la méthode du bain élastique. Cette méthode permet d'atténuer les déformations thermiques et de calculer la rigidité via les fluctuations de déformation lors de simulations isothermes-isobares. Nous avons étudié l'effet de la teneur en eau, de la température, de la pression hydrostatique et du cation interfoliaire sur les propriétés élastiques des feuillets de montmorillonite. En particulier, nous avons montré que les coefficients de rigidité hors plan calculés à 300 K différaient sensiblement des mêmes coefficients calculés à 0 K par minimisation. Les coefficients hors plan étaient très sensibles à la température et à la teneur en eau. En revanche, la dépendance des coefficients dans le plan à la température était faible. Par ailleurs, la diminution des coefficients dans le plan avec la teneur en eau peut être entièrement expliquée par la variation de la géométrie du système en raison du gonflement de l'espace interfoliaire. Cette différence entre les coefficients hors plan et les coefficients dans le plan s'explique par la nature très différentes des interactions agissant dans le plan des feuillets et orthogonalement à ce plan. Le comportement élastique dans le plan des feuillets est gouverné par une élasticité cristalline alors qu'orthogonalement au plan il est gouverné par une élasticité entropique. En outre, le cation interfoliaire a un effet sur les propriétés élastiques de la montmorillonite seulement dans les états les plus secs.

Afin de compléter les calculs de modules élastiques par simulation moléculaire à l'échelle du feuillet, nous avons mesuré expérimentalement les propriétés élastiques des films fins d'argile. Nous avons conçu un dispositif expérimental original qui permet de solliciter en traction des films d'argile à humidité contrôlée. Les échantillons étaient sollicités en traction dans le plan des films d'argile afin d'isoler les mécanismes de déformation parallèles aux feuillets d'argile. Afin de pouvoir mesurer la déformation de ces échantillons très fragiles, nous avons du utiliser une méthode sans contact : nous avons employé les techniques de corrélation d'image afin de mesurer la déformation globale des échantillons. Nous avons montré que ce montage expérimental permettait de mesurer la déformation globale avec une bonne précision. Nous avons étudiés l'effet du cation interfoliaire et de la teneur en eau sur les propriétés élastiques des films. En particulier, nous avons mis en évidence la

diminution du module d'Young avec la teneur en eau. De plus, les films de montmorillonite calcique étaient plus raides que les films de montmorillonite sodique et leur module d'Young était plus sensible à la teneur en eau. Enfin, nous avons comparé les résultats obtenus expérimentalement à l'échelle des films avec les résultats obtenus par simulations moléculaires à l'échelle du feuillet d'argile. Les modules d'Young mesurés expérimentalement avaient le même ordre de grandeur que les modules de cisaillement hors plan mesurés par dynamique moléculaire, ce qui suggère l'importance du cisaillement des feuillets dans les mécanismes de déformation. Cependant, les résultats de dynamique moléculaire ne montrent pas de dépendance marquée des propriétés élastiques au cation interfoliaire, au contraire des expériences de traction. Cette différence indique que la structure à l'échelle mésoscopique, qui dépend du cation, joue un rôle important dans la réponse élastique des matériaux argileux.

Enfin, nous avons étudié les propriétés de fluage des argiles, et en particulier l'effet de l'eau sur ces propriétés. Nous avons réalisé des tests de fluages à humidité relative contrôlée sur les films d'argile autoporteurs. Le résultat principal de ces expériences fut que, après un période transitoire de quelques centaines de secondes, la déformation est une fonction linéaire du logarithme du temps. La pente de cette fonction linéaire était une fonction croissante de la teneur en reau et de la charge. De plus, l'amplitude du fluage était beaucoup plus importante pour les échantillons de montmorillonite sodique que pour les échantillons de montmorillonite calcique. Nous avons également réalisé des simulations moléculaires du comportement mécanique des feuillets d'argile au cours du temps. La relation entre la contrainte de cisaillement appliquée et le taux de cisaillement était donné par la loi de Bingham : le taux de cisaillement était égal à zéro jusqu'à une contrainte d'écoulement au-delà de laquelle le taux de cisaillement était une fonction affine de la contrainte de cisaillement. La contrainte d'écoulement et la viscosité décroissaient avec la teneur en eau et étaient plus élevées dans le cas de la montmorillonite calcique que dans les cas de la montmorillonite sodique. Le fluage logarithmique des films ne peut donc être expliqué par ce fluage linéaire obtenu numériquement à l'échelle du feuillet. Afin de vérifier que l'effet de la taille finie des

feuillets joue ou pas un rôle dans l'explication du fluage logarithmique, nous avons étudié un modèle analytique simple de joint collé que nous avons appliqué à l'échelle du feuillet d'argile. Cependant ce modèle a fait apparaître un fluage qui dépendait linéairement de la racine carrée du temps et non pas de son logarithme. Nos résultats indiquent donc que le fluage logarithmique des matériaux argileux ne trouve pas son origine à l'échelle du feuillet mais à l'échelle mésoscopique d'un ensemble de feuillets ou de particules d'argile.

Contents

List of Figures

List of Tables

Chapter 1

Introduction

THIS CHAPTER *presents the industrial and the scientific contexts of this thesis. Understanding the hydromechanical behavior of clay-based materials responds to significant environmental, technological and economical challenges. In France, for instance, a clayey rock, argillite, is considered as a potential host for nuclear waste underground disposal. In civil engineering, the shrinkage and swelling of clays has huge repercussions on the stability of soils and building foundations. In the petroleum industry, the properties of clay materials have important implications for drilling and production operations since shales, a clay-based rock, is encountered both as sealing formations of hydrocarbon reservoirs and source rocks for oil and gas. The prediction of the response of these materials during the whole exploitation phase of these geotechnical infrastructures requires the estimation of their hydromechanical properties not only on the short term, but also on the long term. Clay materials exhibit complex multiscale structure and pore network. Therefore, the links between the behavior at the scale of the layers and the macroscopic behavior are not yet fully understood. The objective of this work is to understand the fundamental mechanisms of hydration and deformation of clay materials, in order to supply models at a larger scale with a solid physical basis and to build robust predictive macroscopic constitutive laws. We focus on the impact of water on the following mechanical properties of clays: swelling, strength,*

elasticity, and creep. We used two parallel approaches to investigate these properties: molecular simulations and experiments on clay films. Molecular simulations made it possible to study the behavior at the scale of the layer. Performing experiments on well-ordered thin clay films aimed at filling the gap between the scale of the layer and the engineering scale.

CE CHAPITRE *présente le contexte industriel et scientifique de cette thèse. Comprendre le comportement hydromécanique des matériaux argileux répond à des défis environnementaux, technologiques et économiques importants. En France, par exemple, une roche argileuse, l'argilite, a été choisie comme roche hôte potentielle pour le stockage géologique de déchets radioactifs. En génie civil, le retrait et le gonflement des argiles a des répercussions considérables sur la stabilité des sols et des fondations des bâtiments. Dans l'industrie pétrolière, les propriétés des matériaux argileux ont un impact important sur les opérations de forage et de production puisque les shales, une autre roche argileuse, sont rencontrés aussi bien comme roches de couverture de réservoirs d'hydrocarbures que comme roches mères de pétrole et de gaz. La prédiction de la réponse de ces matériaux tout au long de la phase d'exploitation de ces infrastructures géotechniques nécessite de quantifier leurs propriétés hydromécaniques non seulement à court terme mais aussi à long terme. Les matériaux argileux ont une structure et un réseau poreux multiéchelles et complexes. C'est pourquoi les liens entre le comportement à l'échelle du feuillet et le comportement macroscopique ne sont pas totalement compris. L'objectif de ce travail est de comprendre les mécanismes fondamentaux de l'hydratation et de la déformation des matériaux argileux, dans le but de fournir aux modèles aux échelles supérieures une base physique solide et de construire des lois de comportement macroscopiques prédictives. Nous étudions en particulier l'impact de l'eau sur les propriétés mécaniques suivantes des argiles : gonflement, résistance, élasticité et fluage. Nous avons utilisé deux approches parallèles pour explorer ces propriétés : des simulations*

moléculaires et des expériences sur des films d'argile. Les simulations moléculaires ont permis d'étudier le comportement à l'échelle du feuillet d'argile. Réaliser des expériences sur des films d'argile fins et bien organisés avait pour objectif de combler la lacune entre l'échelle du feuillet et l'échelle de l'ingénieur.

Contents

1.1 Industrial context

1.1.1 Underground storage of nuclear waste

Nuclear energy is the main source of electric power in France. In 2011, 78 % of the total electricity supply was produced by nuclear power plants (OECD, 2012). The management of radioactive waste, produced by power plants or other applications of nuclear physics, such as medical uses or research, is a major challenge for the nuclear industry. In France, in 2012, about 2 kg of radioactive waste were produced per year per capita (ANDRA, 2012). 59 % of this waste is produced by the nuclear energy industry. This waste poses significant risks to the environment and to people. These radiological risks are assessed on the basis of two parameters: the half-life and the level of radioactivity of the radionuclides (ANDRA, 2012). Depending on their amount of emitted radiation, wastes are classified into four categories: Very-Low-Level Waste (VLLW), Low-Level Waste (LLW), Intermediate-Level Waste (ILW) and High-Level Waste (HLW). In addition,

the wastes are divided between Very-Short-Lived waste (VSL), Short-Lived waste (SL) and Long-Lived waste (LL). Their radioactive half-life ranges from below 100 days (VSL) to above 31 years (LL).

In France, the general principles of the management of radioactive waste were established by the 1991 Waste Act (République française, 1991), known as the "Loi Bataille", and detailed by the 2006 Planning Act on the sustainable management of radioactive materials and waste (République française, 2006). The National Radioactive Waste Management Agency (ANDRA) is responsible for the long-term management of all radioactive waste produced in France. For the repository of Long-Lived and High-Level waste (ILW-LL and HLW), deep geological disposal has been selected as the reference solution. ANDRA is in charge of the design and the implementation of the underground repository.

The Long-Live and High-Level waste represents a small volume (about 3 % of the total volume of radioactive waste), but concentrates 99 % of the total radioactivity of radioactive waste (ANDRA, 2012). Some of this waste presents a significant radiological risk for very long periods, up to 100,000 years. Therefore, to ensure appropriate containment on such a time scale, a deep disposal facility called CIGÉO (for Industrial Center for Geological Disposal) is being developed by ANDRA. Figure 1.1 displays a general overview of CIGÉO. The site is located in eastern France in both the departments of Meuse and Haute-Marne. An underground laboratory already exists in this location to study the geological layer and test the implementation of the repository. The commissioning of the disposal site is planned for 2025. The total cost, including the initial investment costs and the costs for monitoring and for closure, was estimated in 2012 between 16.5 and 36 billion euros (Cour des Comptes, 2012).

The concept of the geological disposal relies on two successive barriers: the waste packages and the geological barrier (ANDRA, 2005b). The waste packages consist of vitrified waste embedded in steel or concrete. These packages will be placed in underground disposable cells. In addition, the disposal cells will be closed by a plug of bentonite. When hydrated, the bentonite swells strongly, closing the gaps between the plug and the rock and therefore min-

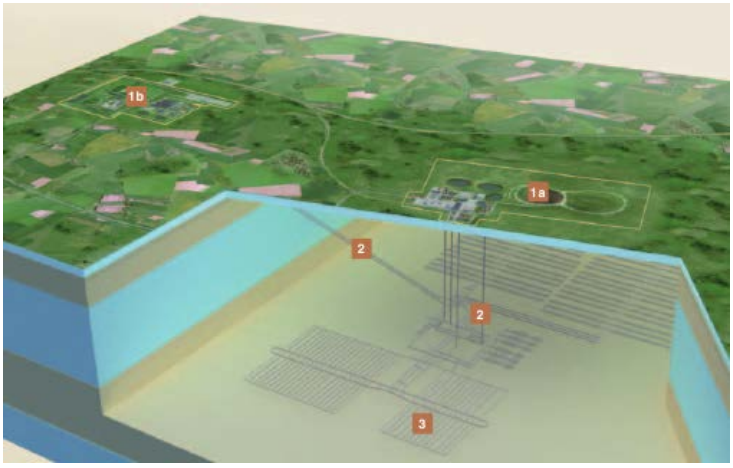

Figure 1.1 – Overview of the Industrial Center for Geological Disposal (CIGÉO project) for underground disposal of nuclear waste. (1) Surface installations. (2) Connecting infrastructures. (3) Underground installations. Credit: *The deep geological disposal concept as developed by ANDRA*, ADS Geological.

imizing the risk of leaks at the rock-plug interface. Moreover, upon confined hydration, the permeability of the plug itself decreases because of significant changes in the microstructure (Cui et al., 2007a; Delage et al., 2010). Figure 1.2 shows a disposal cell of HLW waste, closed by a bentonite plug and a concrete plug. When the package will be degraded after hundreds of years, the geological barrier and the plug are expected to confine the radionuclides on longer time scales.

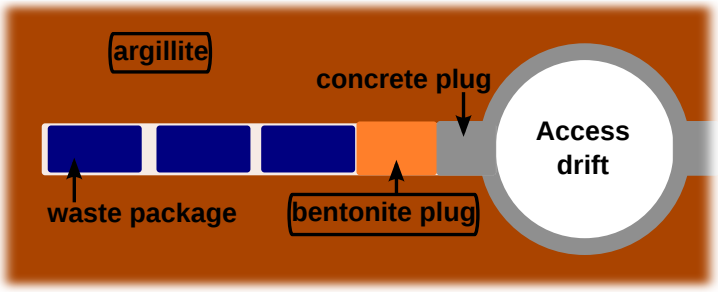

Figure 1.2 – Disposal cell of HLW radioactive waste. Waste packages are installed in a cavity excavated in the argillite host rock. The cell is closed by a bentonite plug and a concrete plug.

The storage center will be implemented in a Callovo-Oxfordian argillite layer (ANDRA, 2005b). The layer is about 500 m deep and 130 m thick and provides a stable geological environment. The argillite is a clayey sedimentary rock that exhibits a very low permeability, on the order of 10^{-4} to 10^{-8} mD, and can thus limit the diffusion of radionuclides on long time scales to prevent any pollution of the biosphere.

Clays are the main component of both the argillite geological barrier and the bentonite engineered barrier. Indeed, the main components of argillite are clay minerals (with a mass fraction w of 40-45 % on average), carbonates ($w \sim$ 22-37 %) and quartz ($w \sim$ 25-30 %) (Gaucher et al., 2004). The bentonite selected by ANDRA for the plug is the MX-80 (ANDRA, 2005a), which is a natural clay found in Wyoming in the United States. The main components of the MX-80 are smectite clay ($w \sim 80$ %) and secondary minerals ($w \sim$ 20 %).

The presence of smectite clays confers to argillite an ability to creep, i.e. to deform over time under constant mechanical load. This creep could relax the stress and close the fractures in the excavated damaged zone (ANDRA, 2005b). However, the low speed of the phenomenon makes it difficult to assess its effect over the whole lifetime of the repository.

Other countries are considering radioactive waste disposal concepts in which clay materials also play an important role. For instance, Belgium is considering a Boom clay layer as a candidate host for its long-lived waste disposal. In contrast, Switzerland and Finland are considering repositories in granite layers for their waste. However, in this latter case, bentonite is to be used in large quantities for embedding the waste packages and for closing the disposal cells.

Therefore, the design and the evaluation of the effectiveness of geological storage requires a thorough study of the short-term and long-term behaviors of clay materials. The time scales involved in this project are far greater than those accessible by experimental works. In addition, the host rock will be subjected to a wide range of environmental conditions in terms of moisture, temperature, and mechanical stress. Therefore, going beyond empirical model is necessary: one should aim at building models able to predict the long-term

behavior of the bentonite plug and the host rock over a large range of thermo-hygro-mechanical solicitations.

1.1.2 Stability of soils

In civil engineering, the swelling of clays has a great impact on the stability of the building foundations. Figure 1.3 shows the effect of the shrinkage and swelling of a clay-rich soil on a house.

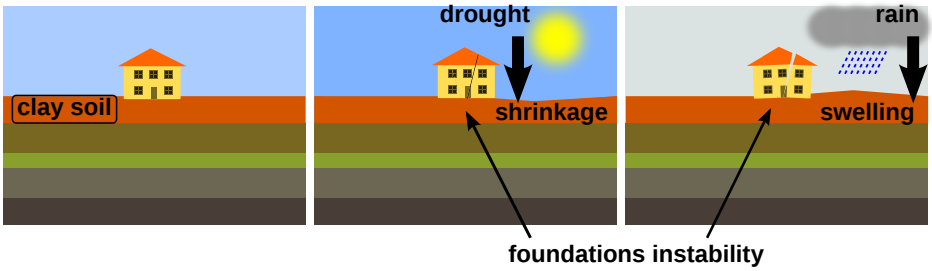

Figure 1.3 – Impact of a clay-rich soil on the stability of a building. Drying or resaturation of the upper layer of a clay soil causes significant changes of its volume, which can lead to unacceptable differential settlements.

The economic consequences of the shrinkage-swelling phenomenon of expansive clays on buildings are considerable and represent the second item of insurance compensation for natural disaster in France, after floods. The Commissariat Général au Développement Durable estimated the total cost of shrinking and swelling to 3.5 billion euros between 1995 and 2006 (CGDD, 2010). In the United States, the cost of damage to buildings caused by shrinkage and swelling was estimated at 2.3 billion dollars per year (Jones and Holtz, 1973). Because of these high economic stakes, better characterizing the ability of clay soils to shrink and swell is necessary to reduce the vulnerability of existing and future buildings to this phenomenon and establish reliable criteria for the settlement of claims.

In addition, clay-rich soils also exhibit delayed deformations under stress. Such creep is also a major challenge for the evaluation of the stability of soils and the assessment of natural risks. Indeed, such time-dependent deformations are known to play a significant role in the stability of slopes and can

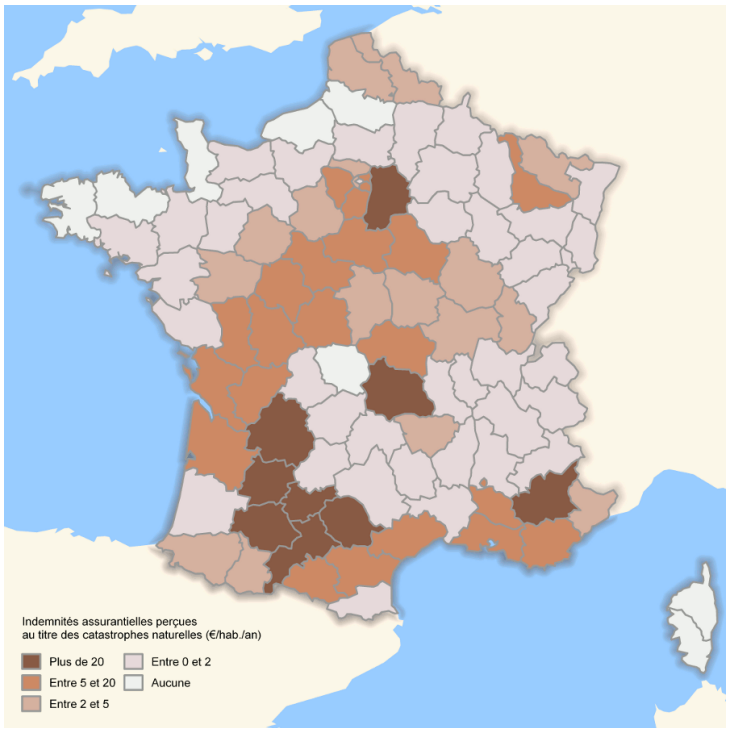

Figure 1.4 – Map of the insurance benefits received for shrinkage-swelling natural disasters (in euros per year per capita). Credit: (CGDD, 2010)

eventually lead to landslides (USGS, 2004). Shear stress can cause a deformation over time of a slope-forming soil. Even though this shear stress is not sufficient to produce instantaneous failure, it leads to delayed deformations, which can make the slope reach its point of failure.

1.1.3 Shales in petroleum engineering

In the oil and gas industry, the hydration and mechanical properties of clay materials are also of importance (van Oort, 2003; Anderson et al., 2010). Shale is a sedimentary rock very commonly encountered during exploration and exploitation of reservoirs of hydrocarbons. Indeed, as one of the most common rock formations on Earth and because of their low permeability, shales constitute often the sealing formations which cover oil or natural gas reservoirs. Shales can also be a source rock for natural gas. Shale is a multi-scale heterogeneous rock made of clay minerals and of silt-size mineral grains

(mostly quartz), which is very similar to argillite but, unlike argillite, exhibits a strong layering at the macroscopic scale, due to compaction of the rock and diagenetic processes.

The evaluation of the mechanical properties of shales in reservoir conditions is important to characterize the reservoir by interpreting seismic data and model the response of the reservoir to production and depletion. In addition, understanding how those properties evolve with time is critical, since the whole exploitation phase of a single well lasts for about 20 to 30 years for conventional hydrocarbons and for about 10 years for unconventional hydrocarbons.

During drilling operations, when the well goes through a layer of shale, in contact with the aqueous drilling fluid the clay swells, which can lead to well-bore instabilities. In the worst case, the shale may collapse on the drilling head and block it in the well. The cost of well-bore instabilities due to the swelling of clays has been estimated from 500 million to 1 billion US dollars per year worldwide (Bloys et al., 1994; Aadnoy and Ong, 2003). To prevent these instabilities, swelling inhibitors such as KCl or organic polymers can be added to the drilling fluid. However, developing inhibitors which are efficient, cost effective, environmentally friendly, and which do not affect the rheological properties of the drilling fluid remains a challenge (Anderson et al., 2010).

One critical aspect of shale reservoirs is their permeability, which must be as high as possible to guarantee the economic viability of the exploitation. The permeability of those reservoirs being low (i.e. on the order of 10^{-6} mD), hydraulic fracturing is used in order to improve the access to the hydrocarbons in the shale formations (Economides and Nolte, 2000). However, when in contact with the aqueous fracturing fluid, the clay can swell, which decreases the permeability of the formation and is detrimental to the production (Striolo et al., 2012). In addition, time-dependent deformations of shale can mitigate the impact of hydraulic fracturing on the permeability of the fractured reservoirs (Cuisiat et al., 2002). Therefore, being able to predict both the elastic and delayed deformations of shale is critical to designing efficient hydraulic fracture schemes.

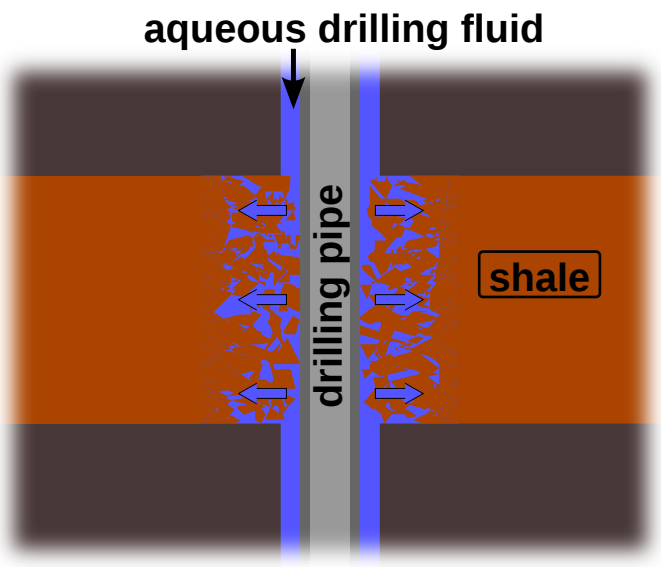

Figure 1.5 – Wellbore instability during drilling through a clay-rich shale. Water (blue arrows) diffuses through the shale layer. Upon hydration the clay swells and the shale formation collapses on the drilling pipe.

A better understanding of the behavior of clay materials therefore responds to significant economic and technological challenges. The coupling between hydration and mechanical response is especially critical to this effort since the swelling of the clays present in argillite, bentonite, soils, and shales is caused by hydration. Moreover, the prediction of the response of clayey materials during the whole exploitation phase of a geotechnical infrastructure requires the estimation of the mechanical properties of the materials not only on the short term, but also on the long term.

1.2 Scientific context

1.2.1 Multiscale structure of clay materials

According to Guggenheim and Martin (1995), "The term "clay" refers to a naturally occurring material composed primarily of fine-grained minerals, which is generally plastic at appropriate water contents and will harden when

Group	Structure	Charge per unit formula $-X$	Structural formula
Pyrophyllite	TOT	0.	$Si_4O_{10}Al_2(OH)_2$
Talc	TOT	0.	$Si_4O_{10}Mg_3(OH)_2$
Smectite	TOT	-0.2 to -0.6	$M^+_X(Si_{4-x}Al_xO_{10})(Al_{2-y}R_y)(OH)_2$
Vermiculite	TOT	-0.6 to -0.9	$M^+_X(Si_{4-x}Al_xO_{10})(Mg_{3-y}R_y)(OH)_2$
Kaolinite	TO	0.	$Si_4O_{10}Al_4(OH)_8$
Lizardite	TO	0.	$Si_4O_{10}Mg_6(OH)_8$

Table 1.1 – Examples of structures of various clay groups. In the Structure column, T refers to tetrahedral sheet and O to octahedral sheet. X refers to the number of interlayer monovalent cations per unit cell, and x and y to the quantity of substitutions in the tetrahedral and octahedral sheets, respectively. Therefore, to ensure charge neutrality, $X = x + y$. In the Structural formula column, M refers to an interlayer monovalent cation and R to a metallic atom.

dried or fired." The plasticity of clays, i.e. their ability to deform under shear stress when hydrated, is imparted by the "clay minerals", which are phyllosilicates. Minerals that do not impart plasticity to clays are called "associated minerals". Phyllosilicates are a family of silicate minerals with a layered structure made of two basic structures: silicate tetahedra and aluminum octahedra. These tetrahedra and octahedra are linked together to form two types of layers: 1:1 layers made of one tetrahedral sheet (T) and one octahedral sheet (O), and 2:1 layers made of one octahedral sheet between two tetrahedral sheets. The octahedral sheet can be either dioctahedral or trioctahedral, if two thirds of the octahedral sites or all sites are occupied by metallic atoms, respectively. Figure 1.6 displays the tetrahedral and octahedral structural units and the structures of a 2:1 layer and of a 1:1 layer. Clay minerals can be classified according to the structure of the phyllosicilate layers (Meunier, 2005). Table 1.1 gives some examples of clay groups and their structures.

In addition, because of atomic substitutions in the crystalline structure, the 2:1 layers can bear a negative charge. This negative charge is counterbalanced by cations in the interlayer space. 2:1 phyllosilicates can be classified in function of this layer charge. Talc and pyrophyllite are tri- and diocta-

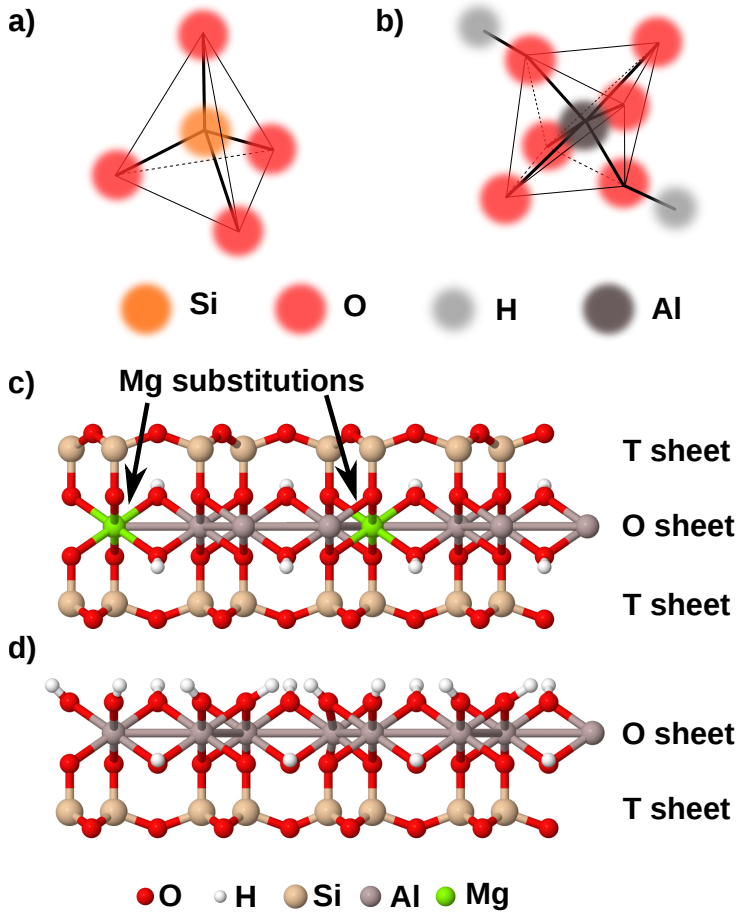

Figure 1.6 – Structure of a clay layer. a) Tetrahedral unit. b) Octahedral unit. c) Structure of montmorillonite. Montmorillonite is a TOT dioctahedral clay, which bears a negative surface charge because of metallic atomic substitutions (here magnesium) in the octahedral sheet. d) Structure of kaolinite. Kaolinite is a TO dioctahedral clay.

hedral zero charge 2:1 phyllosilicates, respectively. Smectites are low-charge 2:1 phyllosicilates. According to the nomenclature of the Association Internationale pour l'Étude des Argiles (AIPEA) (Bailey, 1980), the charge per formula unit $-X = -(x + y)$ of smectites lies between -0.2 and -0.6 where x and y are the numbers of substitutions per formula unit, in the tetrahedral sheet and the octahedral sheet, respectively (see Table 1.1). For smectites, this charge per unit cell corresponds to a surface charge between -0.07 C.m^{-2}

and -0.21 C.m^{-2}. Vermiculites (with a charge per formula unit $-X$ between -0.6 and -0.9) and micas (with a charge per formula unit $-X$ below -1) are 2:1 phyllosilicates with a higher charge.

Smectites can then be further subdivided in function of the location of the substitutions, which occur either in the tetrahedral sheet or in the octahedral sheet, and of the structure of the octahedral sheet. For instance, saponite is a trioctahedral smectite with tetrahedral substitutions, hectorite and stevensite are trioctahedral smectites with octahedral substitutions, and beidellite is a dioctahedral smectite with tetrahedral substitutions. Figure 1.7 displays the classification of clay minerals and the place of smectite in this classification.

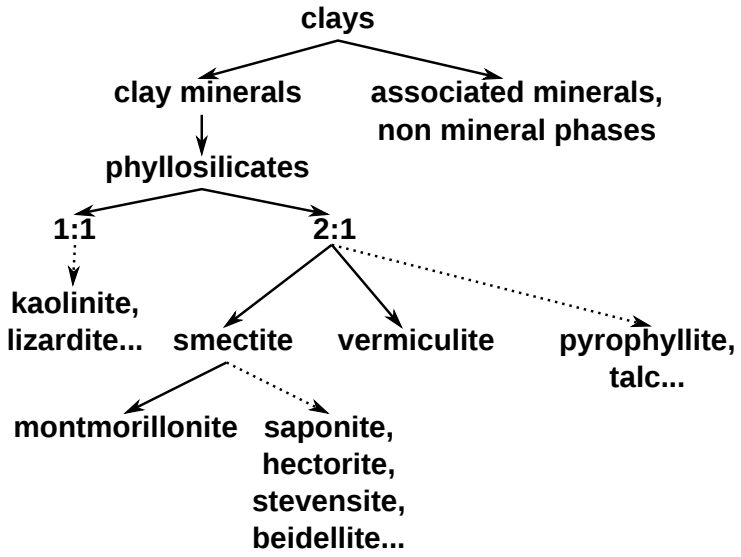

Figure 1.7 – Classification of clay minerals.

This thesis focuses on montmorillonite clay, which is the most common clay of the smectite group. Montmorillonite is a dioctahedral smectite, in which most substitutions are located in the octahedral layer, as shown on Figure 1.6-c. Its typical surface charge is approximatively -0.12 C.m^{-2}. This negative charge is balanced by interlayer cations, Na^+ and Ca^{2+} being the most common. The interlayer space also contains water molecules in various amounts.

While at the scale of the layer, clays have an imperfect crystalline structure, at the larger scales clay materials exhibit complex multiscale structure

and pore network. Figure 1.8 displays the multiscale structure of argillite. At the macroscopic scale, argillite is made of mineral inclusions (quartz and carbonates) embedded in a clay matrix. This clay matrix plays a great role in the mechanical behavior of argillite because of its softness with respect to the inclusions and of the sensitivity of its properties to water. At the nanometer scale, the matrix is made up of phyllosilicate layers. The clay layers are stacked to form ordered structures called "particles" separated by mesopores. The thickness of the particles depends on the charge and size of the cation and on the charge of the layer (Shomer and Mingelgrin, 1978; Schramm and Kwak, 1982; Laird, 2006). The clustering of these particles forms "aggregates", the size of which ranges from 1 to 10 μm, typically. Moreover, the size of the mesopores also depends on the nature of the counterions. For a given interlayer cation, Salles et al. (2010) highlighted a strong correlation between the surface energy of montmorillonite and the size of the mesopores.

1.2.2 Hydric behavior of clay materials: swelling and adsorption

Swelling clays, such as montmorillonite, have the property to expand significantly in presence of water. At the scale of the engineer, the swelling of clays can be measured by macroscopic geotechnical tests (e.g. oedometer test, macroscopic free swelling test...) (Delage et al., 1998, 2010; Push and Yong, 2006). The very significant swelling exhibited by clay materials upon hydration is due to the clay minerals present in the material, which are able to adsorb a high quantity of water.

At the scale of the clay layer, the interlayer spacing can be measured by X-ray diffraction (XRD) experiments (Mooney et al., 1952; Bérend et al., 1995; Cases et al., 1997; Ferrage et al., 2005). XRD makes it possible to monitor the interlayer spacing in function of relative humidity. Relative humidity h_r is the ratio of the vapor pressure p_V in the air to the saturated vapor pressure $p_S(T)$ at the considered temperature T: $h_r = p_V/p_S(T)$. XRD patterns show that the basal spacing increases with relative humidity in a discrete fashion with the intercalation of 0, 1, 2, and 3 layers of water molecules. This dis-

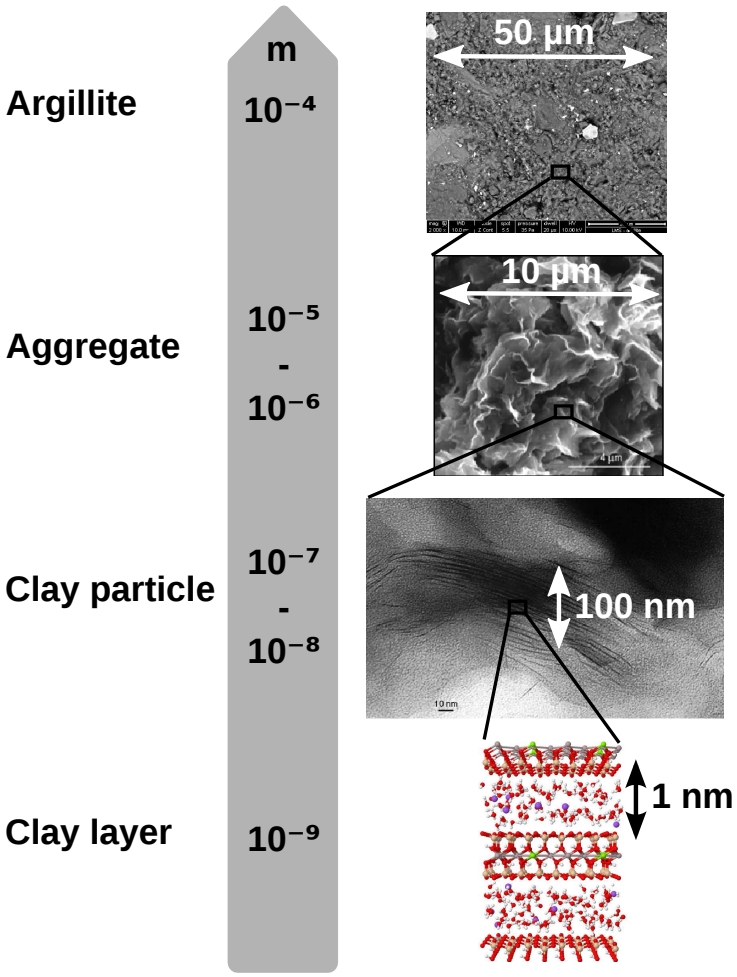

Figure 1.8 – Multiscale structure of an argillite clay rock. From bottom to top: atomic structure of hydrated montmorillonite layers; Smectite clay observed by Transmission Electron Microscopy (Laird, 2006); Smectite clay observed by Scanning Electron Microscopy (Push and Yong, 2006); Scanning Electron Microscopy picture of Argillite (Wang, 2012).

crete swelling regime is called the "crystalline swelling" regime and occurs for basal spacings between 9 and 18 Å, typically. Molecular dynamics confirmed that water is adsorbed in successive layers in the interlayer space (Karaborni et al., 1996; Hensen and Smit, 2002; Tambach et al., 2004b). Bérend et al. (1995) and Cases et al. (1997) investigated the influence of the interlayer cation on the crystalline swelling and on the adsorption isotherms, i.e. on the quantity of adsorbed water in function of relative humidity at a given tem-

perature. They observed a great impact of the size and charge of the cation on the quantity of adsorbed water and the magnitude of the swelling. Ferrage et al. (2005) measured the basal spacing of monoionic montmorillonite samples with various counterions for relative humidities ranging from 0 to 80 %. Consistently with previous works, they observed structures with 0, 1, and 2 layers of interlayer water. However, they showed that the swelling of the interlayer space is not homogeneous in the sample. Moreover, the number of layers per particle decreases with the water content (Laird, 2006). Upon hydration, the particles are broken up in smaller particles. Some interlayer spaces grow and become interparticle spaces. Therefore, the number of layers per particle is lower at high relative humidities than at low relative humidities.

As the relative humidity is increased, the interlayer space is filled with more than 3 or 4 water layers and reaches the so-called "osmotic swelling" regime. The swelling is then governed by the difference of cation concentration between the interlayer space and the surrounding water. This osmotic swelling regime is highly dependent on the interlayer cation. When the counterion is monovalent, montmorillonite can be easily exfoliated, while in presence of a divalent cation, montmorillonite exhibits no or little extralamellar osmotic swelling (Segad et al., 2010). Between the crystalline and the osmotic swelling regimes, a gap has been reported for montmorillonite neutralized by monovalent counterions (Anderson et al., 2010; Delville, 2012). Indeed, basal spacings between 20 and 40 Å are never observed. The origin of this gap remains unclear. At relative humidities close to 100 %, pores of larger size begin to be filled with water. Therefore capillary pressure begins to have an effect on the swelling and this swelling can be modelled with poromechanics (Coussy, 2011).

However, determining the sequence of mechanisms that lead to hydration and swelling upon imbibition remains a challenge (Salles et al., 2010). The porosities at the different scales do not evolve independently from each other upon hydration. Therefore, there exist couplings between various physical phenomena occurring at various scales. Salles et al. (2010) used thermoporometry to investigate the swelling of mesopores (i.e. pores between 2 and

50 nm according to IUPAC nomenclature) in montmorillonite and suggested a sequence of hydration for montmorillonite. This hydration sequence is highly dependent on the interlayer cation. For Na-montmorillonite, the hydration sequence is the following (Salles et al., 2008): the first step is the hydration of the external surfaces of the particles by one layer of water for relative humidities below 10 %; Then, for relative humidities between 10 and 20 %, water fills the interlayer space with one water layer; For relative humidities higher than 20 %, water fills the mesopores, which start swelling in the osmotic regime for a relative humidity of 60 %; The second water layer in the interlayer space is formed for a relative humidity of 80 %; At higher humidities, a third or fourth water layer fills the interlayer space and eventually both the interlayer space and the mesopores are subjected to osmotic swelling. For Ca-montmorillonite (Salles et al., 2010), for relative humidities below 20 %, the external surfaces of the particles and the interlayer spaces are hydrated by one water layer. For relative humidities between 20 and 60 %, the interlayer spaces are fully hydrated by a second water layer. The filling of the mesopores starts only after the full hydration of the interlayer spaces and the swelling of the mesopores begins only at very high humidities, above 90 %.

1.2.3 Mechanical behavior of clay-based materials

The macroscopic mechanical behavior of clay-based materials is usually described by elasto-plastic constitutive laws. The modified Cam-Clay model (Roscoe and Burland, 1968) and the Barcelona model (Alonso et al., 1990) are examples of such laws for clay-based materials in saturated and unsaturated conditions, respectively. These constitutive laws are phenomenological models which exhibit both softening and hardening depending on the applied stress. These models require numerous parameters which need to be identified by macroscopic geotechnical experiments for each material. Indeed, clay-based materials are heterogeneous multiscale and multiphase materials, the behavior of which depends strongly on their microstructure.

In argillite, the elastic moduli of the mineral inclusions, such as quartz and carbonates, are an order of magnitude higher than the elastic modulus of

the clay matrix. Therefore, the mechanical behavior of clay-based materials depends strongly on the clay phase. The plate-like structure at the scale of the clay particles makes their mechanical response anisotropic, which is usually described by a transverse isotropic tensor (Ortega et al., 2007). Bobko and Ulm (2008) highlighted the nanogranular nature of the clay matrix by a self consistent approach. They performed nanoindentation tests on shales, assumed the material to be nanogranular and showed the existence of a threshold of packing density of those particles close to 0.5, below which the stiffness of the clay matrix vanishes. Above this threshold, the indentation modulus of the clay matrix is a linear function of the packing density.

In addition, clay-based materials are known to undergo significant delayed deformations. Creep can be measured by the oedometer test, which is an unidimensional consolidation test. Figure 1.9 displays the displacement of the load in function of time during an oedometer test on bentonite (Ichikawa et al., 2004). After the primary consolidation, i.e. the dissipation of the pore pressure, the displacement reaches the secondary consolidation regime and is a linear function of the logarithm of the time.

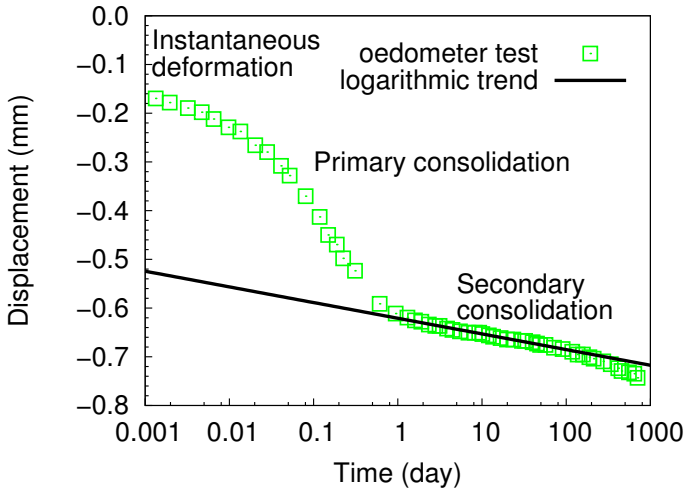

Figure 1.9 – Result of an oedometer test on bentonite. Data from Ichikawa et al. (2004).

In geotechnical engineering, creep is called secondary consolidation (or secondary compression) (Feda, 1992) and is characterized by the coefficient

of secondary consolidation C_α defined as:

$$C_\alpha = \frac{d\varepsilon}{d\log t} \tag{1.1}$$

where ε is the strain and t the time.

After a transient period, shales upon triaxial testing creep logarithmically with respect to time also. The amplitude of this creep increases with the clay content (Sone and Zoback, 2010).

Though ubiquitous in geomaterials, creep remains inadequately addressed. Indeed, its microscopic origin remains poorly understood. Its study is challenging because of the time scales involved and of the simultaneous occurrence of coupled deformation mechanisms (e.g. shrinkage, swelling, primary consolidation).

1.2.4 Hydro-mechanical behavior of clay-based materials

The mechanical properties of clay rocks and soils depend strongly on the amount of water present in the porosity. Uniaxial compression experiments on argillite (Bornert et al., 2010; Cariou et al., 2012; Pham et al., 2007) show that their Young's modulus and their strength depend highly on the water content. Figure 1.10 displays the stress-strain curves of uniaxial compression experiments performed by Bornert et al. (2010) on argillite at various relative humidities and shows that relative humidity impacts both the elasticity and the strength of the material. The analysis of those experiments by Digital Image Correlation techniques shows that the heterogeneity of the strain field is greater at high relative humidity than at low relative humidity because of micro-cracking due to the swelling of the clay matrix (Bornert et al., 2010). However, the spatial resolution of the observation was not fine enough to analyze in detail the behavior of the microstructure of the clay matrix. Indentation tests on argillite (Magnenet et al., 2011) showed a linear decrease of its Young's modulus with relative humidity. Nanoindentation tests on argillite in a humidity-controlled environment (Auvray et al., 2013)

have also highlighted the decrease of the Young's modulus of the clay matrix.

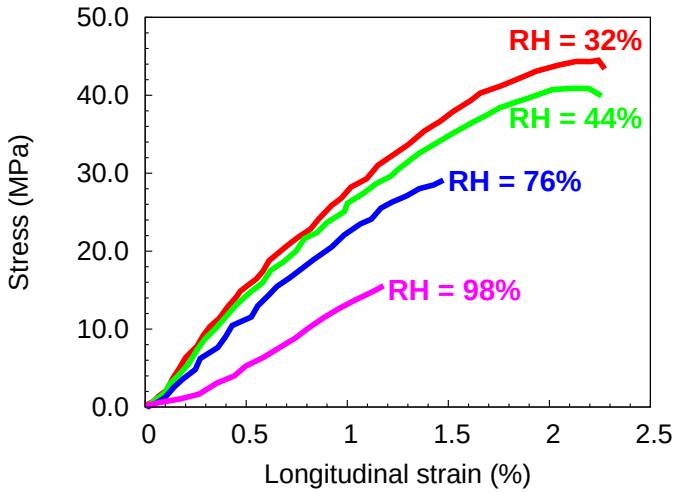

Figure 1.10 – Results of uniaxial compression tests on argillite for various relative humidities (RH). Data from Bornert et al. (2010).

The sensitivity of the mechanical properties of clay materials to water stems from the sensitivity of the clay layer itself. Many recent studies aimed at better characterizing and modeling the response of clay-based materials under hydromechanical loading in a bottom-up approach, i.e. by starting from the microscopic level of the clay layer in order to predict the macroscopic behavior (Ortega et al., 2007; Cariou et al., 2012). Micro-mechanical models have been developed to predict the behavior of the clay rock and its poromechanical parameters starting from the behavior of the clay layer (Cariou et al., 2012). However, the hydromechanical behavior at the scale of the clay layer and the relationship between the behavior of the layer and that of the upper scales need to be better characterized.

Creep properties of clay materials are also sensitive to water. The coefficient of secondary consolidation has been shown to depend on the water content (Mesri, 1973). Yang et al. (2011) measured the delayed deformations of argillite under uniaxial compression by Digital Image Correlation and showed that the creep response depends strongly on both the relative humidity and the applied stress.

1.3 Motivations and objectives

Hydration and its effects on the deformations and the mechanical properties of smectite have been traditionally studied at the macroscopic scale by geotechnical engineers. The hydration of smectite has also been characterized at the scale of the clay layer, experimentally by XRD (Mooney et al., 1952; Bérend et al., 1995; Cases et al., 1997; Ferrage et al., 2005) or numerically by molecular simulations (Karaborni et al., 1996; Hensen and Smit, 2002; Tambach et al., 2004b). However, because of the complex multiscale structure of clay materials and of the complexity of the complete sequence of hydration of clays (Salles et al., 2010), the impact of the interlayer swelling on the larger scales needs to be further investigated. The hydro-mechanical couplings of clays at the scales of the layer or of the particle has not yet been studied experimentally. Moreover, the time-dependent hydro-mechanical behavior at these scales remains unclear. Therefore, we aim at highlighting the mechanisms of short-term and long-term deformations at the scales of the layer and of the particle.

To build predictive constitutive laws useful to the engineer, the behavior at the scale of the clay layer needs to be upscaled at the macroscopic scale. However, the gap between the scale of the clay layer and the macroscopic scale is huge. Therefore, we aim at filling this gap experimentally by proposing an intermediate step. We use a bottom-up approach: starting from the study of the material at the scale of the layer, we intend to explain the behavior at the scale of a mesoscopic sample.

The objective of this work is to understand the fundamental mechanisms of hydration and deformation of clay materials. We focus on the multiscale aspects in space and time. This work aims at supplying models at a larger scale, such as micromechanical models, with a solid physical basis in order to build robust predictive macroscopic constitutive laws.

We consider especially the role of water in clays and its impact on the mechanical properties in unsaturated conditions. In addition, we focus on the deformations of clay materials over time. Thus, we aim at understanding the microscopic physical origin of the following mechanical properties: strength,

swelling, elasticity, and creep.

1.4 General strategy and thesis outline

The main questions under consideration in this work are:

- Swelling: What is the hydration sequence of swelling clays? Although the behavior of the clay layer upon hydration is known, the interplay between the different scales is not fully understood.
- Strength: Clay layers are not bonded covalently which each other. Therefore, what are the interactions responsible for the cohesion of the clay layers? We aim at understanding better these interactions and their consequences on the swelling properties of clays.
- Elasticity: What is the impact of water adsorption on the elastic properties of clay materials at the scale of the clay layer and at the mesoscale? Though the macroscopic response of clay materials is known to be dependent on the water content, the origin of this dependency has to be studied in more details.
- Creep: What are the physical mechanisms that play a role in the creep of clay materials? What is the impact of the water content on the delayed deformations?

To answer these questions, we use two parallel approaches. The first is based on molecular simulation, which allows us to understand the behavior of the material at the scale of the clay layer. Figure 1.11-b shows a typical simulation cell which contains sodium montmorillonite layers. The second approach is based on experiments on self-standing clay films. Figure 1.11-a shows a 50-microns-thick film of montmorillonite prepared by drying a clay suspension. The clay particles deposited almost parallel to each other and a well-ordered system was obtained. The rationale for creating such original samples was to obtain mesoscopic samples, i.e. samples that could be used to bridge the gap between the scale of the clay layer (reachable by molecular simulations or XRD experiments) and the engineering scale of a macroscopic clay sample. The combination of these two approaches aims at establishing the fundamental mechanisms of deformation at the scales of the clay layer

and of the clay particle.

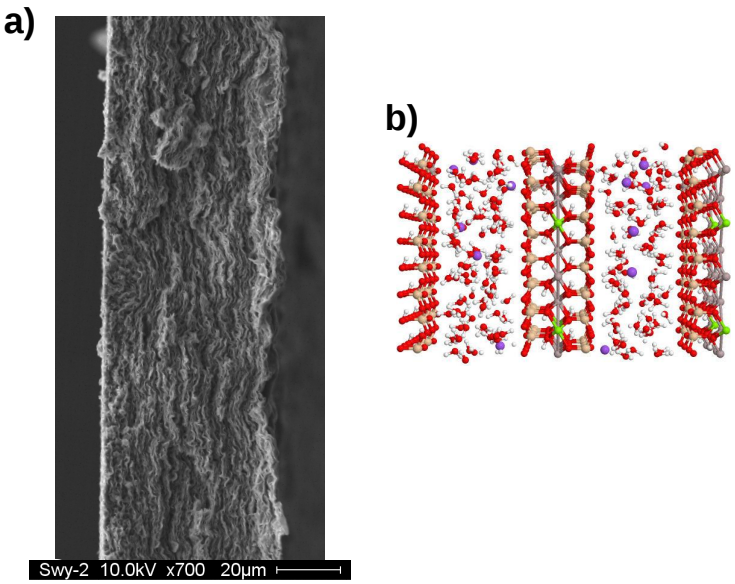

Figure 1.11 – a) Self-standing smectite clay film observed by Scanning Electron Microscopy. b) Simulation cell for molecular simulation of smectite layer.

Chapter 2 is devoted to the observation of the swelling of clay films. We present how we prepared the self-standing montmorillonite films and how we observed the edges of the films and measured their swelling with Environmental Scanning Electron Microscopy. We show that the films behave like an ordered stacking of clay layers.

Chapter 3 deals with the physical origin of the cohesion of charged lamellar materials, in particular clays. In this chapter, several analytical and numerical models of increasing complexity are introduced. We present a new model, the Explicit Solvent Primitive Model, the complexity of which is intermediate between the so-called Primitive Model and the all-atomistic model, this latter being considered as the reference model. The objective of introducing complexity in a discrete fashion is to discuss the impact of each ingredient of the models on the cohesion of lamellar materials.

Chapter 4 is devoted to the molecular simulations of swelling clays. We present the numerical tools we developed and used. We calculate how the water content impacts the mechanical properties at the scale of the clay

layer.

Chapter 5 presents the results of tensile experiments on self-standing clay films. The tests were run in a humidity-controlled environment. Therefore, we were able to vary the water content in the samples and to measure the elastic properties of the films in function of this water content. We analyze these results with respect to the results obtained by molecular simulation of swelling clays. We present the numerical tools we developed and used. And we measure how the water content impacts the mechanical properties at the scale of the clay layer.

Chapter 6 deals with the creep of clay materials. We present the results of creep tests performed on clay films. We show the role of the water amount adsorbed in the material and of the stress on the long-term behavior of the films. We finally suggest which fundamental mechanisms could explain the creep of clay materials.

Chapter 7 sums up the results presented in this thesis and presents perspectives for future research.

Chapter 2

Humidity-induced swelling of clay films

THIS CHAPTER *presents measurements of the humidity-induced swelling of thin self-standing films of montmorillonite clay by a combination of Environmental Scanning Electron Microscopy (ESEM) and Digital Image Correlation (DIC). The films were about 40-microns-thick. They were prepared by depositing and evaporating a suspension of clay and peeling off the highly oriented deposits. The rationale for creating such original samples was to obtain mesoscopic samples that could be used to bridge experimentally the gap between the scale of the clay layer and the engineering scale of a macroscopic clay sample. Several montmorillonite samples were used: the reference clay Swy-2, the same clay homoionised with sodium or calcium ions, and a sodium-exchanged Cloisite. The edges of the clay films were observed by ESEM at various relative humidity values between 14 % and 95 %. The ESEM images were then analyzed by DIC to measure the swelling or the shrinkage of the films. We also measured the adsorption/desorption isotherms by weighing the samples in a humidity-controlled environment. In order to analyze our results, we compared our swelling/shrinkage and adsorption/desorption data with previously published data on the interlayer spacing obtained by X-ray diffraction and with numerical estimates of the interlayer water content*

obtained by molecular dynamics simulations. The swelling as well as the hysteresis of this swelling were found to be comparable for the overall mesoscopic films and for the interlayer space. The same correspondence between film and interlayer space was observed for the amount of adsorbed water. This suggests that, in the range of relative humidities values explored, the films behave like freely swelling oriented stacks of clay layers, with no significant contribution from the mesoporosity. The relevance of this result for the behavior of clayey sedimentary rocks and the differences with the behavior of non-oriented samples are briefly discussed.

Ce Chapitre *présente des mesures de gonflement induit par l'humidité de films minces autoportants de montmorillonite par une combinaison de microscopie électronique à balayage environnementale (ESEM) et de corrélation d'images numériques (DIC). Les films mesuraient environ 40 microns d'épaisseur. Ils ont été préparés par dépôt et évaporation d'une suspension d'argile et par décollement des dépôts fortement orientés ainsi préparés. La raison de la fabrication de ces échantillons originaux était d'obtenir des échantillons mésoscopiques qui puissent être utilisés pour combler expérimentalement l'écart entre l'échelle du feuillet d'argile et l'échelle d'un échantillon d'argile macroscopique. Plusieurs échantillons de montmorillonite ont été utilisés : l'argile de référence Swy-2, la même argile homoionisée avec des ions de sodium ou de calcium, et une Cloisite sodique. La tranche des films d'argile a été observée par ESEM à différentes valeurs d'humidité relative entre 14 % et 95 %. Les images ESEM ont ensuite été analysés par DIC pour mesurer le gonflement ou le retrait des films. Nous avons également mesuré les isothermes d'adsorption/désorption en pesant les échantillons dans un environnement à humidité contrôlée. Afin d'analyser nos résultats, nous avons comparé nos données d'adsorption/désorption et de gonflement/retrait à celles déjà publiées sur l'espace interfoliaire, obtenues par diffraction des rayons X, et à des estimations numériques de la quantité d'eau interfoliaire obtenues par des simulations de dynamique moléculaire.*

Le gonflement ainsi que l'hystérésis de ce gonflement se sont révélés comparables pour les films mesoscopiques et pour l'espace interfoliaire. La même correspondance entre le film et l'espace interfoliaire a été observée pour la quantité d'eau adsorbée. Cela suggère que, dans l'intervalle de valeurs humidités relatives explorées, les films se comportent comme un empilement ordonné de feuillets gonflant librement, sans aucune contribution significative de la mésoporosité. La pertinence de ce résultat pour le comportement des roches sédimentaires argileuses et les différences avec le comportement d'échantillons non orientés sont brièvement discutées.

Contents

2.1 Introduction

As highlighted in Section 1.2, clay materials exhibit a complex multi-scale structure and porosity. Upon imbibition, various mechanisms at various scales are involved in the swelling process (Salles et al., 2010). This Chapter is dedicated to the observation of the swelling of montmorillonite self-standing films[1]. We aim at quantifying the swelling of smectite clays both at the scale of the clay layer and at larger scales. Specific attention is dedicated to the impact of the interlayer cation on the swelling.

Recently, Environmental Scanning Electron Microscopy (ESEM) made it possible to observe clay materials at the microscale under controlled environmental conditions (Romero and Simms, 2008). Montes-H (2005) and

1. Reproduced in part with permission from Carrier et al. (2013). Copyright 2013 American Chemical Society.

Montes-H et al. (2003, 2005) used ESEM and digital image analysis to investigate the swelling/shrinkage of bentonite, which is a montmorillonite-rich clay. They measured the swelling of about 50-μm-wide aggregates at relative humidities ranging from 10 % to 80 %. They investigated the influence of the interlayer cation and of the level of compaction. Adsorption isotherms and swelling depend strongly on the interlayer cation (Montes-H et al., 2003). For instance, Na-bentonite swells more than Ca-bentonite when the relative humidity is increased from 5 % to 80 %. Although raw bentonite contains more sodium cations than calcium cations, it behaves like a Ca-bentonite. (Maison, 2011) developed a micro-weighing device to weigh clay aggregates in an ESEM chamber. The swellings of clays from various natural clay deposits were observed and directly related to the clay water content. Wang (2012) and Wang et al. (2013a,b) observed the swelling behavior of an argillite in an ESEM chamber. They used Digital Image Correlation (DIC) (Sutton et al., 2009) to measure the strain field upon hydration. The deformations in the argillite were very heterogeneous and irreversible deformations were observed. The argillite exhibited significant swelling for relative humidities above 80 %. Moreover, the strain was anisotropic and was predominant in the direction normal to the bedding plane of the argillite.

In this work, we used ESEM to observe the swelling/shrinkage of thin films of montmorillonite clay upon variations of humidity. The objectives of this work are to investigate the effect of the nature of the interlayer cation on the swelling of a well-ordered clay-based structure and to better understand the swelling mechanisms of smectite clays. Such films were already studied by Zabat (1996). However, he did not consider the influence of humidity or water content on the properties of the films.

We prepared thin self-standing films of montmorillonite and we observed the edges of these films with an ESEM at various controlled relative humidities. We then applied DIC techniques on the high-resolution ESEM images to measure the swelling/shrinkage of the films. In another setup, we also measured the adsorption isotherms of the films, i.e. the quantity of water in the films at a given relative humidity.

The interest of this work lies in the fact that the swelling was measured on

a well-ordered system made of nearly parallel clay particles. In particular, we investigated the influence of the nature of the interlayer cation on the swelling behavior. Working on thin clay films provides a deeper insight into the swelling mechanisms at the mesoscale and into the interplay between mechanisms at micro- and mesoscales.

2.2 Materials and methods

We used four types of materials: the reference Wyoming montmorillonite Swy-2 (coined Swy-2-raw), the Swy-2 homoionised with sodium (coined Swy-2-Na), the Swy-2 homoionised with calcium (coined Swy-2-Ca) and the Wyoming montmorillonite Cloisite homoionised with sodium (coined Cloisite-Na). With those materials, we prepared self-standing clay films. On all films, we measured the water adsorption isotherms (see Section 2.2.4). On the films made with Swy-2-raw, Swy-2-Ca, and Cloisite-Na, we measured the humidity-induced swelling by using a combination of ESEM characterization (see Section 2.2.2) and DIC (see Section 2.2.3).

2.2.1 Sample preparation

The first smectite clay used in this work is the reference Wyoming montmorillonite Swy-2 purchased from the Source Clay Repository of the Clay Minerals Society (Costanzo and Guggenheim, 2001). The structural formula of the clay Swy-2 is $(Al_{3.23}Mg_{0.56}Fe_{0.42})(Si_{7.89}Al_{0.11})O_{20}(OH)_4(Ca_{0.16}Na_{0.36}K_{0.03})$ (Mermut and Faz Cano, 2001). Thus, the initial relative proportions of the sodium cations and of the calcium cations were about 2/3 and 1/3, respectively. First, the clay fraction with particles smaller than 2 μm was isolated by following the process described by (Arroyo et al., 2005). Then the clay was homoionised and deposited in thin films, as described next.

In order to isolate the particles smaller than 2 μm, the clay Swy-2 was first suspended in 300 mL of water. The suspension was then stirred using a magnetic stir-bar for 48 hours and centrifuged for 5 minutes at 2000 g (where g is the acceleration of gravity). The supernatant solution was collected,

while the deposit was dispersed in 300 mL of water and centrifuged for 3 minutes at 2000 g. The supernatant solution was collected and added to the supernatant already collected. The clay suspension was centrifuged for 15 minutes at 3000 g and the supernatant discarded. One third of the clay fraction was suspended again in water to prepare the natural clay samples Swy-2-raw. The other two thirds were saturated with sodium or calcium cations to prepare the Swy-2-Na and Swy-2-Ca samples, respectively.

To obtain homoionic samples, the clay was treated with concentrated solutions of sodium or calcium chloride. The clay fraction was dispersed into 250 mL of 1 N salt solution. The solution was stirred for 24 hours and centrifuged at 4000 g for 10 minutes. The supernatant was discarded. This process was repeated four times. The cation-saturated clay was then washed with water to remove chloride anions. The clay was suspended in 300 mL of water. The solution was put in a porous membrane tubing and dialyzed in 2 L of water. The water was stirred and changed every 24 hours until the silver nitrate test for chloride ions became negative. A clay suspension of concentration around 7 g/L was then obtained.

The clay suspension was deposited on a flat polyethylene surface to prepare thin films of oriented clay particles. After a 72-hours-long drying at room temperature and relative humidity, a solid thin film could be peeled off from the polyethylene surface. Depending on the quantity of clay in the system and on the water content, the thicknesses of the films were between 30 and 60 μm and the surface density of the dry films lay between 3 and 6 mg/cm^2.

We also used a Na-saturated Cloisite purchased from Southern Clay Products to prepare thin films. Cloisite is another purified natural low-charge Wyoming montmorillonite with an extremely limited number of tetrahedral substitutions. The layer charges of Cloisite and Swy-2 are the same, equal to about 0.7 per unit cell. The structural formula of Cloisite-Na (Pospísil et al., 2004) $(Al_{2.90}Mg_{0.59}Fe_{0.49}Ti_{0.01})(Si_{7.92}Al_{0.08})O_{20}(OH)_4Na_{0.70}$ is very close to the structural formula of the clay Swy-2.

To check the validity of the cation exchange protocol, the chemical compositions of the samples were analyzed by X-ray Energy Dispersive Spec-

troscopy (EDS) after carbon-coating. Figure 2.1 displays the EDS spectra of all clay samples. In the natural Swy-2 sample, both sodium and calcium cations were detected. In the Swy-2-Na and Swy-2-Ca samples, only sodium cations or calcium cations, respectively, were detected, while chloride anions were undetectable. In the Cloisite-Na sample, only sodium cations were detected.

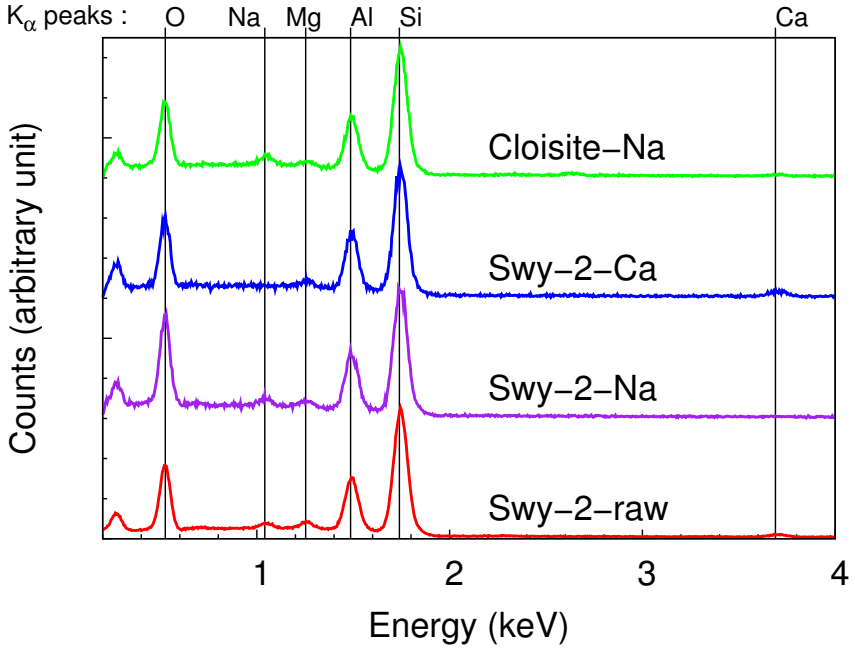

Figure 2.1: EDS spectra of Swy-2-raw, Swy-2-Na, Swy-2-Ca and Cloisite-Na. The positions of the K_α peaks of all elements present are reported at the top of the plot. The K_α peak for Ca at 3.690 keV is present only for the samples Swy-2-raw and Swy-2-Ca. The K_α peak for Na at 1.041 keV is present only for the samples Swy-2-raw, Swy-2-Na, and Cloisite-Na.

2.2.2 ESEM observation

The edges of the clay films were observed by Environmental Scanning Electron Microscopy (ESEM). We used a FEI Quanta 600 microscope. Acquisition was performed perpendicular to the edge of the sample. We broke the films to expose their edge. We did not use a blade to cut the films because they would have been crushed. One side of a few-millimeters-wide sample

Chamber pressure (Torr)	Chamber pressure (Pa)	Relative humidity (%)
0.80	107	14.1
2.00	267	35.1
3.13	417	55.0
4.30	573	75.5
5.40	720	94.8

Table 2.1: Vapor pressure in the ESEM chamber and corresponding relative humidity. The temperature of the sample was kept constant (3 °C) during all tests.

was then glued vertically on a small copper piece with a heat conducting adhesive. The upper half millimeter of the film jutted out the adhesive and the copper, so that the deformations were free in the zone observed with the ESEM. Figure 2.2 displays examples of an acquisition on each type of sample. For the Swy-2-raw, Swy-2-Ca, and Cloisite-Na samples, the particles were deposited almost in very good parallel arrangement and formed well-ordered structures. In contrast, we did not succeed in obtaining Swy-2-Na films with an ordered enough structure, therefore the Swy-2-Na samples were not used for humidity-induced swelling characterization.

During observation, the temperature of the samples was controlled with a Peltier cooling system. All observations were carried out at a constant sample temperature of 3 °C. The relative humidity was controlled by changing the water vapor pressure in the chamber, as shown in Table 2.1.

The clay sample was dried or hydrated step by step. Since the samples were very thin, their equilibration at each relative humidity required around 30 minutes only. To ensure that equilibrium was reached, two images of the samples were taken at five minute intervals and we checked that no deformation could be detected between the two states. At each step, after equilibration, high resolution images of several regions of the sample were acquired. The images were obtained by using a back-scattered electron detector. In this work, we acquired 4096×3775-pixel ESEM images at a magnification of 1500 or 2500. Therefore, the physical size of a pixel was 20 nm and 12.5 nm, respectively.

For each material (i.e. Swy-2-raw, Swy-2-Ca, Cloisite-Na), two different

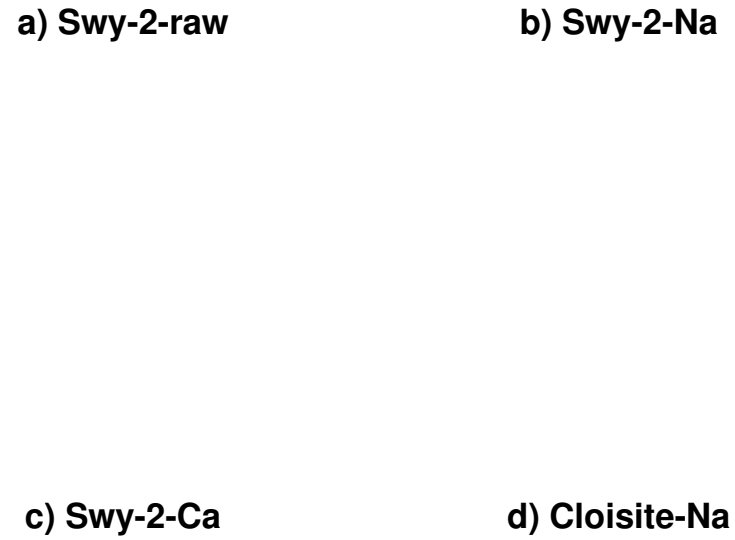

Figure 2.2: ESEM observation at a relative humidity of 35 % of the edges of (a) a Swy-2-raw film, (b) a Swy-2-Na film, (c) a Swy-2-Ca film, and (d) a Cloisite-Na film.

samples were observed at one or two different locations along the edge of the film. For the first sample of each material, the following sequence of increasing relative humidities was applied: 35.1 %, 55.0 %, 75.5 %, 94.8 %. For the second sample, the following sequence of relative humidities was applied: 35.1 %, 75.5 %, 35.1 %, 75.5 %, 94.8 %, 75.5 %, 35.1 %, 14.1 %, 94.8 %, 35.1 %. Before each sequence, a partial vacuum was applied to the chamber of the ESEM to replace the air with water vapor. Therefore, the initial state at a relative humidity of 35.1 % was reached by adsorption.

At each relative humidity, the swelling of the film with respect to the state of reference was inferred by using Digital Image Correlation techniques, as explained in the next section.

2.2.3 Digital Image Correlation technique

Digital Image Correlation (DIC) is a contact-free technique used to measure the deformation of samples between a reference image and an image of the deformed state (Bornert et al., 2008; Sutton et al., 2009).

First, a grid of points was chosen on the reference image, as shown in Figure 2.3. To compute the displacement of each point of the grid from the reference state to the deformed state, DIC searches matching points between the reference image and the image of the deformed state. Around each point of the reference grid, a correlation window is defined.

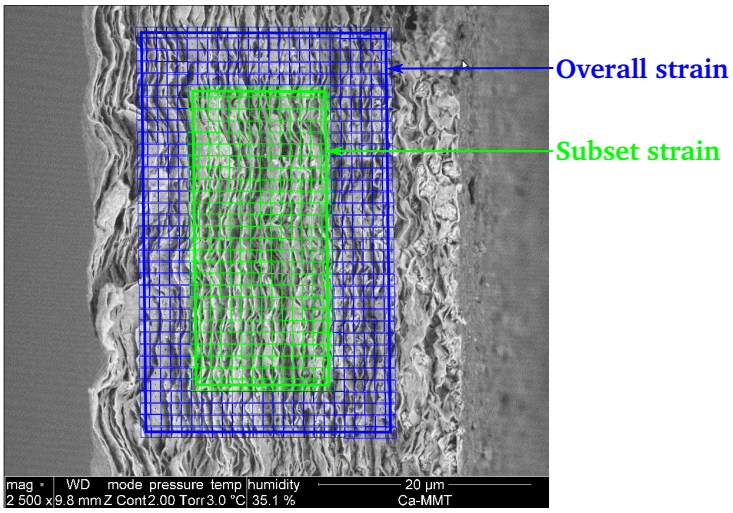

Figure 2.3: Grids of points used to measure the swelling strain of a Swy-2-Ca sample on two zones of various sizes. The deformations measured on the blue zone and on the green zone are referred as to the overall strain and to the subset strain, respectively.

To match points between the reference and the deformed states, we search the transformation Φ defined by:

$$\mathbf{x}_i = \Phi(\mathbf{X}_i), \tag{2.1}$$

where $\mathbf{X}_i$ is the pixel coordinates of a point in the reference state and $\mathbf{x}_i$ the pixel coordinates of the homologous point in the deformed state. The images provide the gray level of each pixel in the reference and the deformed state, noted $f(\mathbf{X}_i)$ and $g(\mathbf{x}_i)$, respectively. Assuming gray level conservation, the relationship between the gray levels is given by:

$$g(\mathbf{x}_i) = a.f(\mathbf{X}_i) + b + g', \tag{2.2}$$

where a and b capture the evolutions of contrast and brightness and g' is the image noise.

DIC consists in searching in the deformed image the subset which is most alike to the correlation window on the reference image. The level of similarity between a correlation window in the reference image and a subset of the deformed image is quantified by a correlation coefficient, for which we used the following expression (Doumalin, 2000):

$$C(\Phi) = 1 - \frac{\sum_{i\in D_i}\left(f(\mathbf{X}_i) - \overline{f}\right)\left(g(\mathbf{x}_i) - \overline{g}\right)}{\sqrt{\sum_{i\in D_i}\left(f(\mathbf{X}_i)^2 - \overline{f}\right)}\sqrt{\sum_{i\in D_i}\left(g(\mathbf{x}_i)\right) - \overline{g}\right)^2}}, \tag{2.3}$$

where D_i is the correlation window around point i, and $\overline{f}$ and $\overline{g}$ are the average of the gray level on D_i in the reference and the deformed states, respectively. With this definition, the correlation coefficient C lies between 0 and 2, is equal to 0 in the case of a perfect similitude and equal to 2 in the case of a perfect inversion of the gray levels. This expression of the correlation coefficient is insensitive to evolutions of brightness and contrast, which is a required property for the analysis of ESEM images. Such evolutions are indeed unavoidable when the humidity in the chamber is modified. The transformation Φ is obtained by minimizing the correlation coefficient. In practice, Φ is assumed to be a translation or the combination of a translation and a homogeneous transformation. The displacement field is then given by:

$$\mathbf{u}_i = \mathbf{x}_i - \mathbf{X}_i = \Phi(\mathbf{X}_i) - \mathbf{X}_i. \tag{2.4}$$

In a digital image, the pixel is the smallest unit of information. However,

DIC makes it possible to measure displacements with a resolution below the pixel. By interpolating gray levels, $C(\Phi)$ can be minimized with a transformation Φ with non-integer values. With an optimal set-up, displacements can be measured with a resolution of $1/100^{\text{th}}$ of a pixel.

The obtained displacements are then differentiated in space to yield deformations. The local transformation $\mathbf{F}_{ij}$ at point $\mathbf{X}$ is defined as the average of the transformation on a subset $D(\mathbf{X})$:

$$\mathbf{F}_{ij}(\mathbf{X}) \approx \langle \mathbf{F}_{ij} \rangle_{D(\mathbf{X})} = \frac{1}{D(\mathbf{X})} \int_{D(\mathbf{X})} \frac{\partial x_i}{\partial X_j} dV. \tag{2.5}$$

By using Green's theorem (Allais et al., 1994), the local transformation can be computed by an integration on a contour with a linear interpolation of the displacements between neighboring points:

$$\langle \mathbf{F}_{ij} \rangle_{D(\mathbf{X})} = \frac{1}{D(\mathbf{X})} \int_{\partial D(\mathbf{X})} x_i n_j dS, \tag{2.6}$$

where $\partial D(\mathbf{X})$ is the boundary of $D(\mathbf{X})$ and $\mathbf{n}$ is the local normal to $\partial D(\mathbf{X})$. The linear strain can then be obtained by taking the symmetric part of the displacement gradient:

$$\boldsymbol{\epsilon} = \frac{1}{2} \left(\mathbf{F}^t + \mathbf{F} \right) - \mathbf{1}, \tag{2.7}$$

where $\mathbf{F}^T$ is the transpose of the transformation $\mathbf{F}$. The axes of the strain tensor were chosen as the axes of the image. In the following Sections, the transversal strain is the component of the strain tensor orthogonal to the clay film, i.e. the out-of-plane component with regard to the plane of the film, and the longitudinal strain is the component of the strain tensor parallel to the film, i.e. the in-plane component. In a given direction, the strain we computed is the engineering strain ϵ, which is defined by:

$$\epsilon = \frac{l}{L} - 1, \tag{2.8}$$

where L and l are the lengths of an object in the reference state and in the deformed state, respectively.

By choosing contours of various sizes to compute the displacement gradient with the method of Allais et al. (1994), the strain can be measured at various scales. Equation (2.6) can also be used to compute the global deformation of a whole region by integrating on the boundary of this region. Although DIC makes it possible to characterize deformations locally, in this study we only used this technique to characterize the global deformation of the area of interest. Indeed, we could obtain no significant information from the analysis of the local strain field. The particles which jut out the sample can bend because of their flexibility and induce an apparent deformation which is independent from the homogeneous deformation

In this work, we used ESEM images of the edge of the clay films, acquired at a magnification of 1500 or 2500 depending on the amplitude of the swelling. The gray levels were encoded on 8 bits. The images were processed with the software CMV developed by M. Bornert (Bornert et al., 2010). The size of the correlation window was 50×50 pixels for a magnification of 1500 and 80×80 pixels for a magnification of 2500. In both cases, the physical size of the correlation window was 1 μm^2. Indeed, the contrast was sufficient at this scale for DIC, since each correlation window contained about two separate clay particles.

On each ESEM image, the average strain was measured by DIC on two zones of various sizes (Figure 2.3): a larger zone (in blue in Figure 2.3) and a smaller zone (in green in Figure 2.3). Performing DIC on two zones with various sizes aimed at verifying whether the size of the zone of interest had an influence on the measured strain. The error of the strain measurement by DIC originates in several phenomena: image noise, evolution of the contrast, image-processing parameters (Bornert et al., 2008). In this work, we considered only the average strain on large zones for which these measurement errors are negligible.

2.2.4 Water sorption isotherms

The water sorption isotherms were obtained on the 4 types of samples prepared (i.e. Swy-2-raw, Swy-2-Na, Swy-2-Ca, Cloisite-Na), by weighing

the samples in a desiccation chamber. The relative humidity was controlled in the chamber with saturated salt solutions. Air was first blown into a saturated salt solution to bring it to the desired moisture and then into the chamber. The relative humidity was recorded with a capacitive hygrometer with an accuracy of 1 %. The chamber was kept at room temperature (20 °C). After each change of the imposed relative humidity, the sample was weighed after equilibration, considered to be reached when the relative mass of the sample varied by less than 0.1 % over 10 min. The mass of the dry clay was measured after a 4-hours-long drying at 110 °C.

2.3 Results

2.3.1 Swelling and shrinkage

Figure 2.4 displays the edge of a film of Swy-2-Ca observed by ESEM at some of the various relative humidities considered. At each increase of humidity, a significant swelling orthogonal to the film can be observed with the naked eye.

The transversal strain (i.e. the strain orthogonal to the plane of the film) and the longitudinal strain (i.e. the strain in the plane of the film) of all samples are displayed in Figure 2.5 upon hydration only. First, one observes that the amplitude of the swelling was strongly dependent on the interlayer cation. Second, as expected, the strain response to hydration was very anisotropic. The longitudinal strain was more than one order of magnitude smaller than the transversal strain. However, the longitudinal strain was not equal to zero and increased slightly with relative humidity, all the more so as the transversal strain was large. This correlation between the longitudinal and the transversal strains suggests that the small longitudinal swelling was due to the spatial oscillations and misalignment of the clay particles which are not perfectly parallel to the mean plane of the film.

In order to validate the reproducibility of our measurements and to estimate the uncertainty of the method, we performed swelling measurements for each material on two different samples. On each film, one or two locations

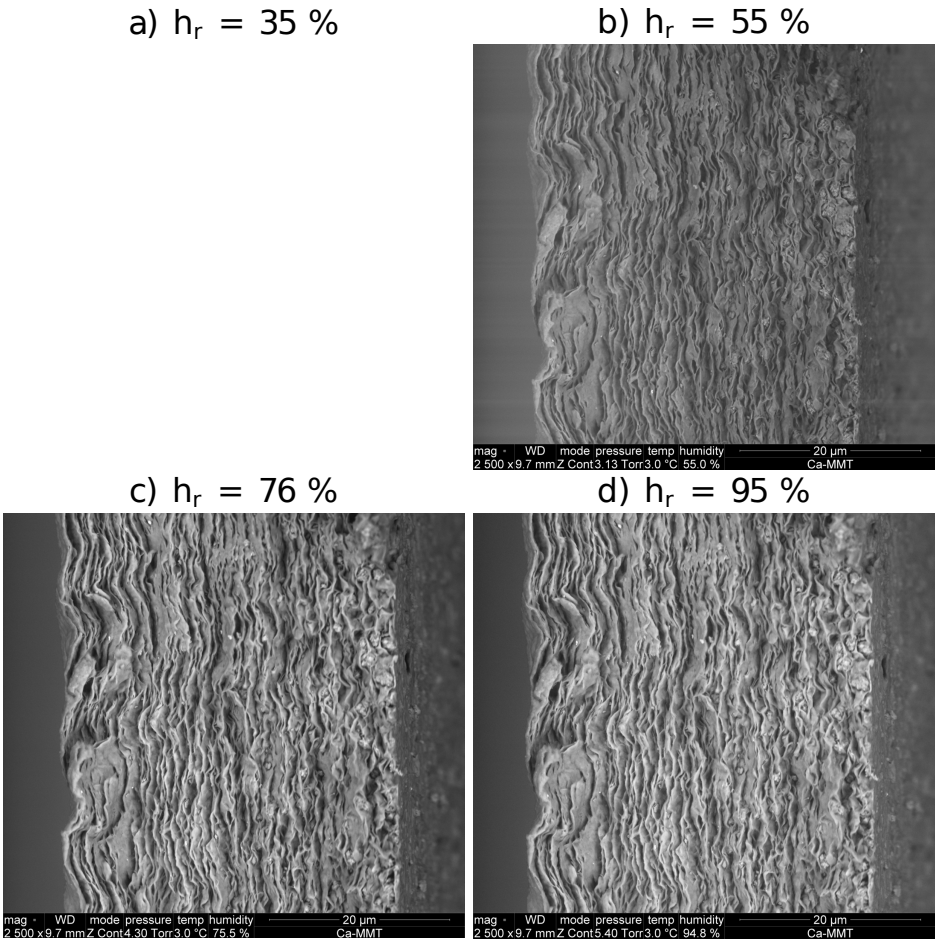

Figure 2.4: ESEM observation of the edge of a Swy-2-Ca film at various relative humidities h_r.

far from each other were analyzed. Moreover, at each location, the strain was measured on both a larger and a smaller zone (see Figure 2.3). When increasing the relative humidity from 35 % to 95 % the average transversal swelling was 27.5 % ± 2.5 % for Swy-2-raw, was 13.7 % ± 2.3 % for Swy-2-Ca and was 40.3 % ± 3.3 % for Cloisite-Na. At all relative humidities the coefficient of variation for the transversal swelling was around 8 % for Swy-2-raw and Cloisite-Na. For Swy-2-Ca the coefficient of variation was around 13 %, as a consequence of its smaller swelling. From those low relative errors, we concluded that our measurements were reproducible and meaningful. The observed uncertainty did not originate in the error in the DIC method,

which is negligible at this scale. A potential source of error stemmed from the fact that the sample was not perfectly vertical. For instance, in Figure 2.2-a, the top of the film is visible on the left, while in Figure 2.2-c, the bottom of the film is visible on the right. In both cases, the films exhibited a small angle α with the vertical axis. The relative error that this tilt induces on the transversal strain measurement is equal to $\alpha^2/2$. For $\alpha = 10\,^\circ$ and $20\,^\circ$, the relative errors are equal to 1.5 % and 6.1 %, respectively, which are smaller than the measured relative errors. Therefore, the observed uncertainties must have originated partly in the natural fluctuations of the structures and properties of the samples. Moreover, the strain did not depend on the size of the measurement zone. The deformation was homogeneous at this scale. Therefore, the green zone in Figure 2.3, which was about 10-μm-wide, is a representative elementary volume of the material. However, at a finer scale this homogeneity disappeared.

For samples Swy-2-raw, Swy-2-Ca, and Cloisite-Na, Figure 2.6 shows the transversal swelling (i.e. the swelling perpendicular to the film) when relative humidity was increased from 35 % to 95 % and then decreased from 95 % to 14 % (i.e. on a hydration-dehydration cycle). The displayed data are the strain measured on the larger zone at one location on one sample. These data correspond to the empty triangles pointing down in Figure 2.5.

The sample Swy-2-Ca swelled less than the other two samples for relative humidities above 35 %. However, this same sample deformed more than the other two at relative humidities below 35 %. A shrinkage of more than 8 % was observed for Swy-2-Ca between relative humidities of 35 % and 14 %, while Swy-2-raw and Cloisite-Na shrinked by 4 % only. For relative humidities below 75 %, Swy-2-raw and Cloisite-Na exhibited similar swellings or shrinkages. For relative humidities above 75 %, Cloisite-Na swelled significantly more than Swy-2-raw. For all samples, an hysteresis could be observed upon hydration and dehydration.

Figure 2.7-a, Figure 2.7-b, and Figure 2.7-c display the swellings of all films during two successive hydration/dehydration cycles. Except for the very first hydration step for the sample Swy-2-raw, no irreversible deformation was observed. Figure 2.7-d, Figure 2.7-e, and Figure 2.7-f show the humidity-

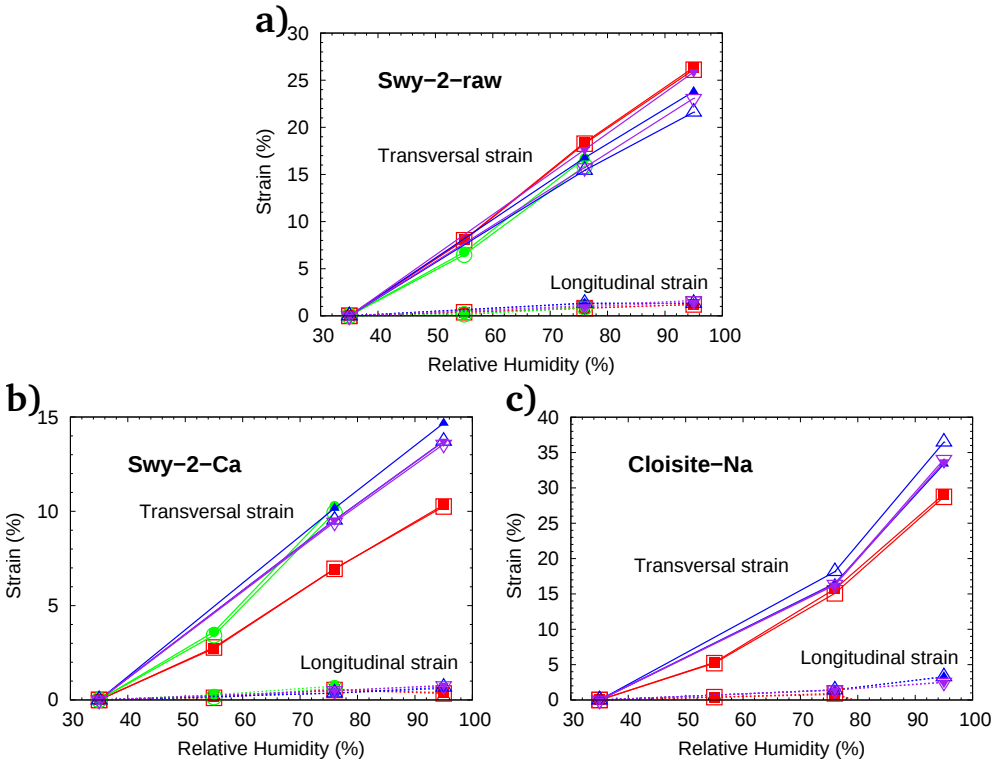

Figure 2.5: Transversal (solid lines) and longitudinal (dashed lines) strains of clay films: a) Swy-2-raw, b) Swy-2-Ca, c) Cloisite-Na. Each color or symbol shape corresponds to a different measurement. For each material, two different films were observed and on each film one or two independent locations were analyzed. The transversal strain is the component of the strain tensor orthogonal to the film, while the longitudinal strain is the component parallel to the film. The strains were measured for each sample on two zones (see Figure 2.3): a large zone (open symbols) and a smaller subset of this zone (plain symbols).

induced strains in function of the quantity of adsorbed water. These data were obtained from the combination of the swelling measurements displayed in Figure 2.7-a, -b, and -c with the adsorption isotherms displayed in Figure 2.8. The swellings in function of the amounts of water adsorbed in the films were well approximated by a linear relationship. Moreover, the hysteresis observed on the curves of the swelling versus relative humidity disappears when the swelling is plotted in function of the amount of adsorbed water. Therefore, the amount of water adsorbed in the film is the parameter which

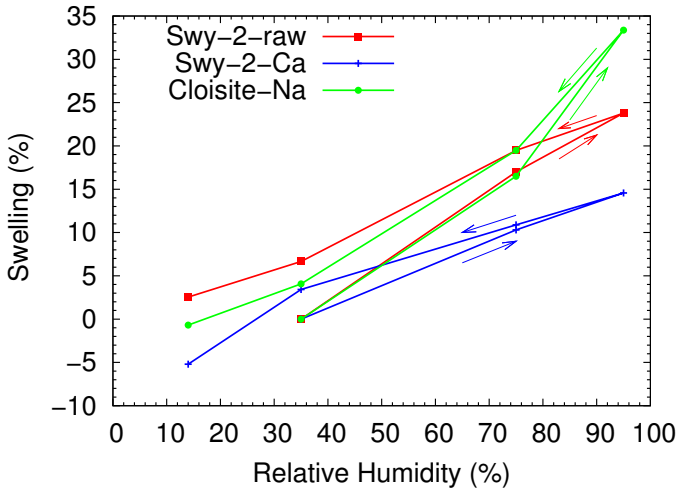

Figure 2.6: Transversal swelling (i.e. swelling perpendicular to the plane of the film) measured by ESEM and digital image correlation for three montmorillonite samples. The initial state at a relative humidity of 35 % was chosen as the reference state for the measurement of strains.

controls the swelling.

2.3.2 Water sorption-desorption isotherms

Figure 2.8 displays the water sorption-desorption isotherms of all montmorillonite samples at 20 °C. The displayed data are total adsorbed mounts, not excess adsorbed amounts. The experimental sorption isotherms were fitted with the D'Arcy-Watt equation (D'Arcy and Watt, 1970):

$$w = \frac{abh_r}{1 + bh_r} + ch_r + \frac{\alpha\beta h_r}{1 - \beta h_r} \tag{2.9}$$

where w is the water content, h_r the relative humidity, and a, b, c, α, and β are the fitted parameters. No quantitative analysis of the parameters was possible. The fitting was performed only to capture the trend of the isotherms and to provide a guide for the eye.

The amount of water adsorbed at a relative humidity of 90 % was roughly the same for all samples and was comprised between 0.24 and 0.25 g/g of dry clay. However, the shape of the isotherms varied significantly with the

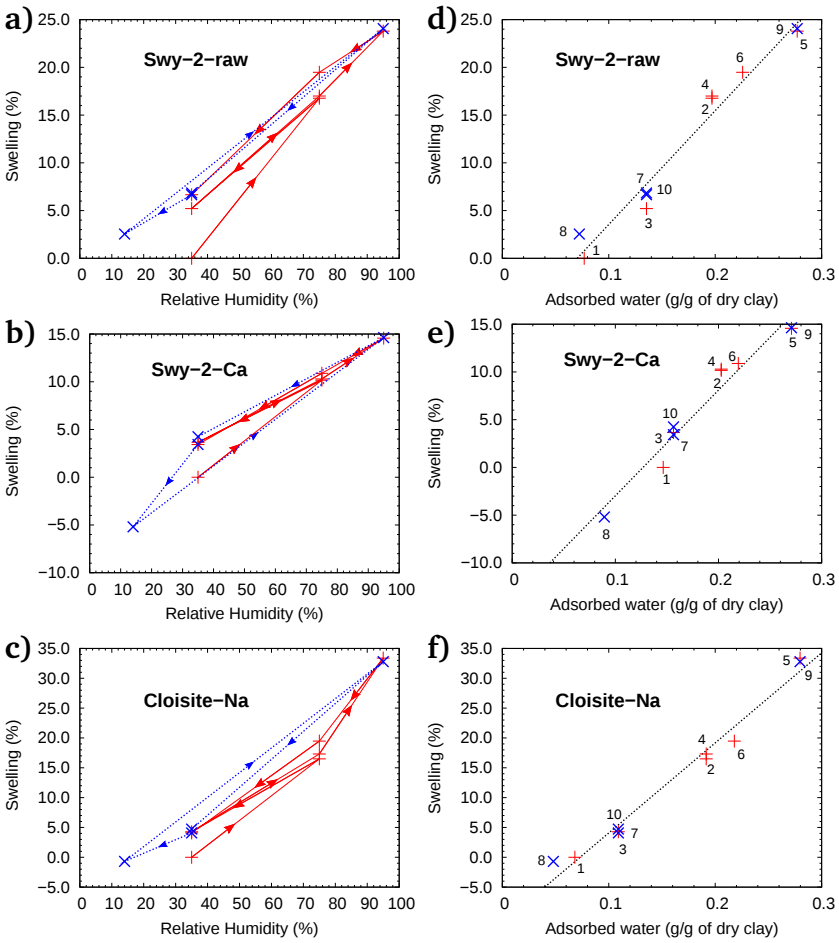

Figure 2.7: Swelling and shrinkage measured by ESEM and digital image correlation in function of the relative humidity (left). The first hydration/dehydration cycle is displayed in red (solid line) while the second hydration/dehydration cycle is displayed in blue (dashed line). a) Swy-2-raw, b) Swy-2-Ca, and c) Cloisite-Na. Swelling and shrinkage in function of the amount of water adsorbed: d) Swy-2-raw, e) Swy-2-Ca, and f) Cloisite-Na. Straight crosses correspond to the first hydration/dehydration cycle, while tilted crosses correspond to the second hydration/dehydration cycle. The black dashed line is a linear fit of the displayed data. The numbers on the plots of the right column are the orders of the experiments.

samples. The isotherm of the Ca-saturated sample Swy-2-Ca showed a high water adsorption between $h_r = 0$ % and 40 % and a low water adsorption between $h_r = 40$ % and 90 % (see Figure 2.8-c). In contrast, the adsorption

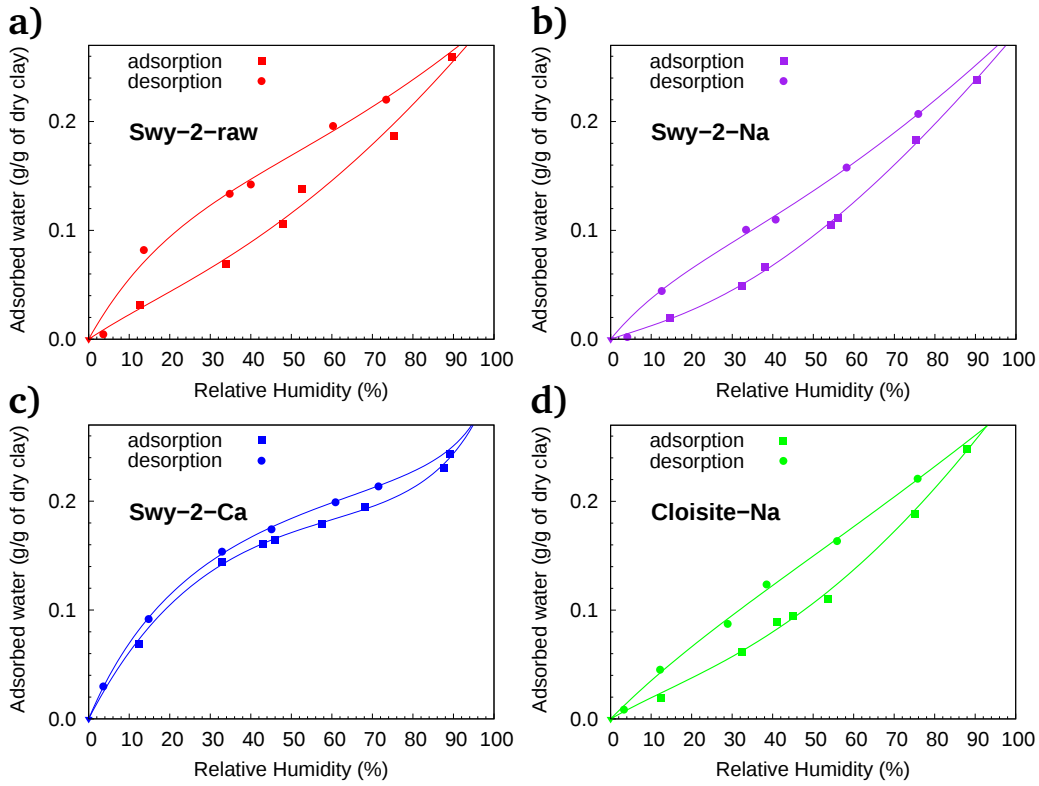

Figure 2.8: Water sorption-desorption isotherms at 20 °C. The solid lines are the curves fitted with the D'Arcy-Watt equation. a) Natural montmorillonite Swy-2-raw. b) Na-saturated montmorillonite Swy-2-Na. c) Ca-saturated montmorillonite Swy-2-Ca. d) Na-saturated montmorillonite Cloisite-Na. The mass of the dry clay was measured after a 4-hours-long drying at 110 °C.

isotherms of the Na-saturated samples Swy-2-Na and Cloisite-Na exhibited opposite convexity and a high potential for water adsorption at high relative humidities (see Figures 2.8-b and -d). The amplitude of the hysteresis differed depending on the interlayer cation. Indeed, while the amplitude of the hysteresis was very limited for the Ca-saturated sample Swy-2-Ca ($\sim$ 12 mg/g at $h_r = 45$ %), this hysteresis was much higher for the Na-saturated samples Swy-2-Na and Cloisite-Na ($\sim$ 44 mg/g at $h_r = 45$ %). The natural montmorillonite Swy-2-raw, which contains both Na and Ca cations, exhibited the same adsorption behavior as the Na-saturated samples, both in terms of convexity of the adsorption isotherm and of the amplitude of the hysteresis.

2.4 Discussion

Clay swelling is governed by two mechanisms: a crystalline interlayer swelling and an interparticle osmotic swelling. In order to determine the origin of the swelling of the clay films, we compared our data on the swelling and the quantity of adsorbed water in the films with available data on the hydration of the interlayer space. We will thus show that the clay films exhibit no osmotic swelling.

2.4.1 Comparison with available data on swelling

Figure 2.9 displays the results of the XRD experiments on montmorillonite of Bérend et al. (1995) and Cases et al. (1997). Their data are the only ones which we are aware of that cover a complete cycle of adsorption/desorption. The structural formula of the Wyoming montmorillonite used by Bérend et al. (1995) and Cases et al. (1997) is very similar to that of the Swy-2 montmorillonite used in our study: $(Al_{3.06}Mg_{0.51}Fe_{0.43})$-$(Si_{7.77}Al_{0.23})O_{20}(OH)_4(Na_{0.76})$ for the Na-saturated montmorillonite. Figure 2.9 also displays the data of Sato et al. (1992) on the montmorillonite Swy-1 for comparison and shows that the montmorillonites of Bérend et al. (1995) and Cases et al. (1997) and of Sato et al. (1992) exhibited the same interlayer swelling. The structural formula of Swy-1 is also very similar to that of Swy-2: $(Al_{3.01}Mg_{0.54}Fe_{0.41})(Si_{7.98}Al_{0.02})O_{20}(OH)_4(Ca_{0.12}Na_{0.32}KC_{0.05})$ (Van Olphen and Fripiat, 1979).

The interlayer spaces of the Na-saturated montmorillonite (Figure 2.9-a) swelled very differently from those of the Ca-saturated montmorillonite (Figure 2.9-b). The Na-saturated montmorillonite started forming the first layer of water at $h_r = 20$ % and the second at $h_r = 60$ %, while the Ca-saturated montmorillonite formed two layers of water at relative humidities below 40 %. Figure 2.9 also displays the typical values of the interlayer spacing for the dehydrated, mono-hydrated, and bi-hydrated montmorillonite: many data points lay outside these well delimited discrete hydration states, which correspond to heterogeneous states in which several discrete hydrates coexist (Ferrage et al., 2005).

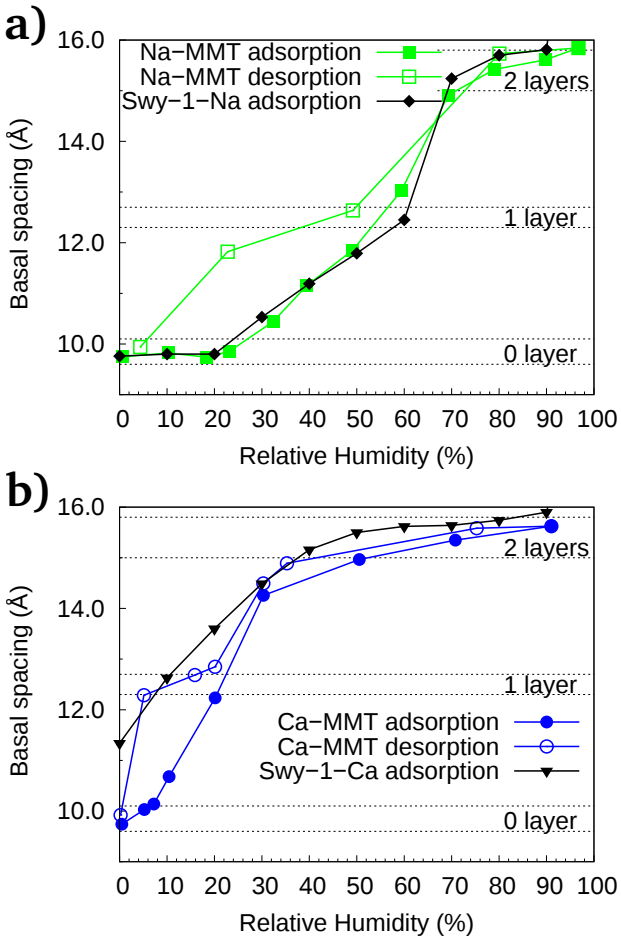

Figure 2.9: Evolution of the basal spacing d(001) measured by X-ray diffraction as a function of relative humidity: a) Na-saturated montmorillonites and b) Ca-saturated montmorillonites. The Na-MMT and Ca-MMT curves are the results of XRD experiments of Bérend et al. (1995) and Cases et al. (1997), respectively, on monoionic montmorillonite samples during adsorption and desorption. The Swy-1-Na and Swy-1-Ca curves are the results of Sato et al. (1992) on the Swy-1 reference clay during adsorption.

Figure 2.10 shows the comparison between the swelling of the interlayer space measured by XRD (Bérend et al., 1995; Cases et al., 1997) and our measurement of the swelling of thin films with Na or Ca interlayer cations by ESEM (already displayed in Figure 2.6). The swellings of the interlayer space were computed from the data displayed in Figure 2.9 with the engineering definition of strain $\epsilon = (d/d_{ref}) - 1$, where ϵ is the swelling, d the interlayer

spacing, and d_{ref} the reference interlayer spacing, chosen as the interlayer spacing at maximum relative humidity for each experiment. This choice is consistent with the definition of strain used in our own DIC measurements using the state at a relative humidity equal to 94.8 % as the reference state.

For each cation, the amplitudes of the swelling between h_r = 14 % and 95 % were identical for the interlayer space and for the film. The convexities of the swelling curves were also identical: convex for the Na-saturated samples and concave for the Ca-saturated samples, except at high relative humidities. However the match between the swellings of the interlayer space and of the film was not perfect. Indeed, the XRD experiments measured only the swelling of the clay layers, while our ESEM experiment measured the swelling of an ensemble of clay layers not perfectly aligned with each other.

2.4.2 Comparison with available data on amount of adsorbed water

Figure 2.11 shows the comparison between the amount of water adsorbed in the interlayer spaces and the amount adsorbed in the thin films for Na-saturated montmorillonite (Figure 2.11-a) and for Ca-saturated montmorillonite (Figure 2.11-b).

The quantity of water adsorbed in the interlayer space was computed from the XRD data presented in Figure 2.9 (Bérend et al., 1995; Cases et al., 1997) combined with molecular simulations results. The XRD data provided the interlayer spacing in function of relative humidity. We performed the molecular simulations that provided the interlayer spacing in function of the amount of water adsorbed (more details on how simulations were performed with be given in the next Chapter). To do so, we used the atomic structure of a montmorillonite clay layer, the CLAYFF force-field and performed molecular dynamics by using the same methodology as Cygan et al. (2004) used for a Na-montmorillonite. We thus computed the swelling of both Na-montmorillonite and Ca-montmorillonite. Figure 2.12 displays the results of an isobaric-isothermal (NPT ensemble) molecular dynamics simulation for

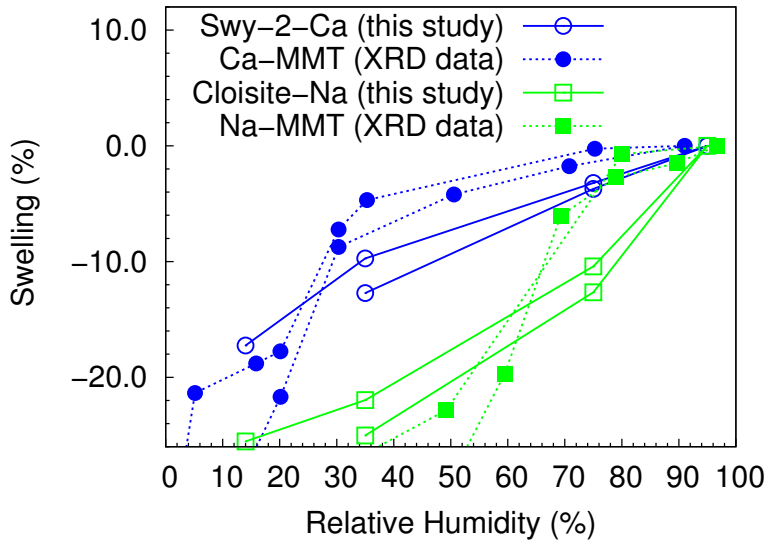

Figure 2.10: Comparison of the swelling/shrinkage of the interlayer space (dashed lines) and of the clay films (solid lines) in function of relative humidity. The interlayer swelling (Ca-MMT and Na-MMT curves) was computed from the measurement of the basal spacing by XRD (Bérend et al., 1995; Cases et al., 1997). The clay film swelling (Swy-2-Ca and Cloisite-Na curves) was our measurement obtained by combining ESEM with DIC. The reference state (0 % swelling) was chosen at the maximum relative humidity of each experiment (between 92 % and 95 %). Round symbols correspond to a Ca-saturated montmorillonite, while squared symbols correspond to a Na-saturated montmorillonite.

the two interlayer cations at 300 K and 1 bar. The two curves differ at low water content because of the different hydration properties of the cations. In contrast, the basal spacings are identical at larger amounts of water and are linear functions of the water content at high relative humidities. With these two sets of data (i.e. XRD and molecular simulations), we could compute the amount of water adsorbed in the interlayer space in function of relative humidity. The adsorption isotherms of the thin films are our experimental measurement of the quantity of water (already displayed in Figure 2.8).

One observes in Figure 2.11 that, for each cation, the quantity adsorbed in the film at $h_r = 90$ % was close to the quantity adsorbed in the interlayer space. Like for the swelling curves, the adsorption isotherms of the film and

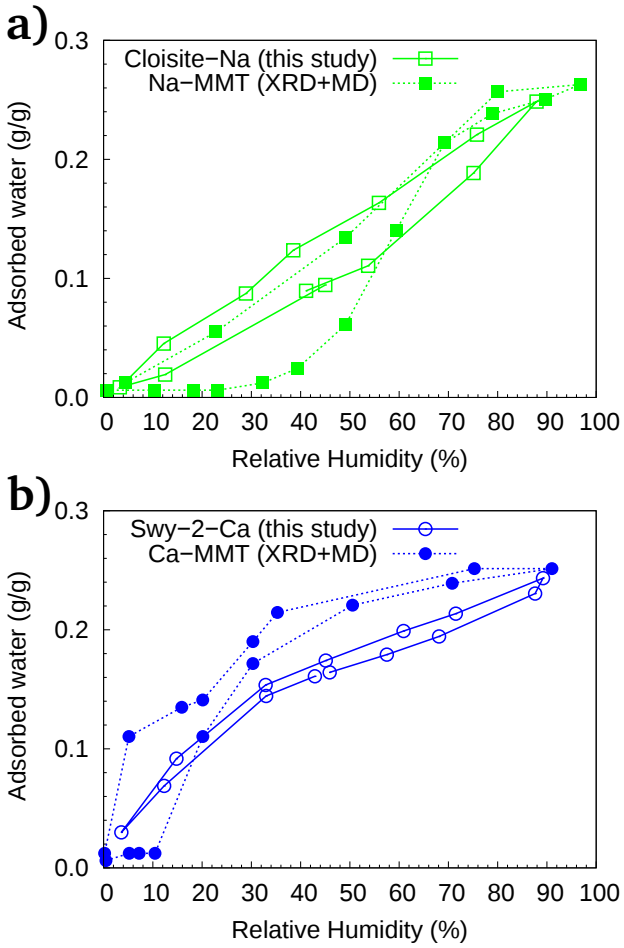

Figure 2.11: Comparison of the quantity of water adsorbed in the interlayer space (dashed lines) and in clay films (solid lines) in function of relative humidity. The quantity of water in the interlayer space (Na-MMT and Ca-MMT curves) was computed from the basal spacing measured by XRD (Bérend et al., 1995; Cases et al., 1997) combined with results obtained by molecular dynamics simulations. The quantity of water in the clay films (Cloisite-Na and Swy-2-Ca curves) was our experimental measurement of the adsorption/desorption isotherms (already displayed in Figure 2.8). (a) Na-saturated montmorillonite. (b) Ca-saturated montmorillonite.

of the interlayer space exhibited identical convexity. For the Ca-saturated montmorillonite, both the film and the interlayer space adsorbed most water at relative humidities smaller than 45 %. In contrast, for the Na-saturated montmorillonite, both the film and interlayer space adsorbed most water at

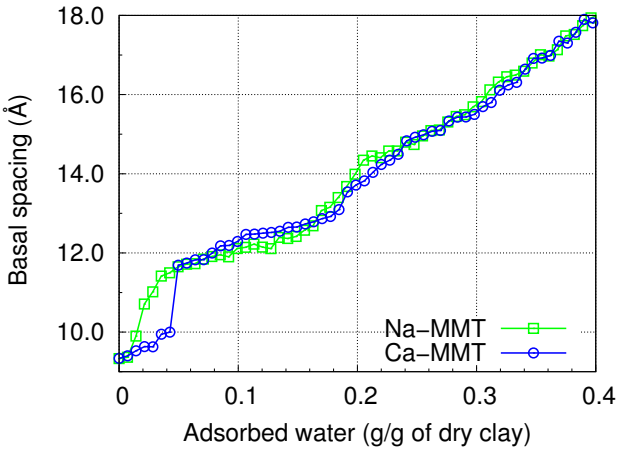

Figure 2.12: Basal spacing of a Na-montmorillonite (Na-MMT) and a Ca-montmorillonite (Ca-MMT) in function of the interlayer water content. The results were obtained by molecular dynamics simulation, according to a methodology that will be described in detail in Section 4.2 of Chapter 4.

relative humidities above 45 %. Moreover, for both Na- and Ca- saturated samples, the amplitude of the hysteresis for the interlayer space was the same as for the film: this hysteresis was much smaller for Ca-montmorillonite than for Na-montmorillonite.

The comparison of the swelling and the adsorption isotherms of the films with available data on the behavior of the interlayer space upon hydration and dehydration showed that the swelling of the clay films was driven by the interlayer crystalline swelling. This result was somewhat surprising, in the sense that the swelling of mesopores usually contributes significantly to the overall swelling of clay-based materials (Salles et al., 2010). A tentative explanation for such surprising result is developed in the next Section.

2.4.3 Pore structure and order in clay films

At a relative humidity of 35 %, the Swy-2-Ca film displayed in Figure 2.2-c was about 35-μm-thick upon dehydration. The measured surface density of dry clay of the sample was about 5.6 mg/cm^2 while the surface density of a dry clay layer computed from its structural formula was about 0.27 μg/cm^2:

therefore, about 21000 layers lay in the thickness of the film. At a relative humidity of 35 %, upon dehydration, the basal spacing of Ca-montmorillonite was 14.8 Å, as shown in Figure 2.9. The total thickness of a stacking of 21000 Ca-montmorillonite layers under these conditions was 31.1 μm. The mesoporosity of this sample, i.e. the fraction of the volume of the sample which was not occupied by the layers and the interlayer spaces, was therefore equal to about 11 %. For the Na-Cloisite displayed in Figure 2.2-d, at a relative humidity of 35 %, upon dehydration, the thickness of the film was about 50 μm. The data of Figure 2.9 show that the basal spacing was about 12.5 Å upon dehydration. The measured density of dry clay of the film was 9.6 mg/cm^2. Hence, about 35000 layers lay in the thickness of the film and the total thickness of the stacking of all these layers was about 43.8 μm upon dehydration at a relative humidity of 35 %. Therefore the mesoporosity was equal to about 12 %. Thus, both the Na-saturated sample and the Ca-saturated sample exhibited the same mesoporosity, slightly larger than 10 %. Sammartino et al. (2003) estimated that the mesoporosity of argillite occupies 86 % of the total porosity. The porosity of a typical argillite is equal to 18 % and the clay matrix fraction is smaller than 50 % (Wang, 2012). Therefore, the mesoporosity of the clay matrix of argillite is larger than 31 %. Thus, the mesoporosity of our clay films was at least three times as small as the mesoporosity of a natural isotropic clay matrix.

No or little mesopore swelling took place in contrast to what is observed in disordered macroscopic samples (Salles et al., 2010). Therefore, the presence of a small amount of mesoporosity did not contribute to the swelling of the specimen. The clay films did not undergo the very high swellings observed by ESEM on aggregates at relative humidities above 75 % (Montes-H et al., 2003), which has also been observed recently at the local scale in clay rocks (Wang, 2012). In contrast, like for individual clay layers, the clay films displayed significant swelling even at relative humidities below 50 %, while such a swelling at low relative humidity is not observed in regular macroscopic clay-based samples (Montes-H et al., 2003; Wang, 2012). A reason why the swelling of our films was similar to that of individual layers, while that of macroscopic samples is not, can be found in the order of the systems consid-

ered. Figure 2.13 shows schematically the difference of structure between a well-ordered clay film and an isotropic natural clay sample: in a disordered clay sample, the swelling of the layers, which occurs mostly orthogonally to the clay particles, is constrained by other particles and the material undergoes significant residual stresses. When mineral inclusions are present in the clay matrix, the constraints on the swelling are even larger and generate strong local strain heterogeneities, as observed by Wang (2012). In contrast, in an ordered clay film, the swelling of a clay particle is much closer to a free swelling. The swelling of each layer is not affected by the neighboring layer.

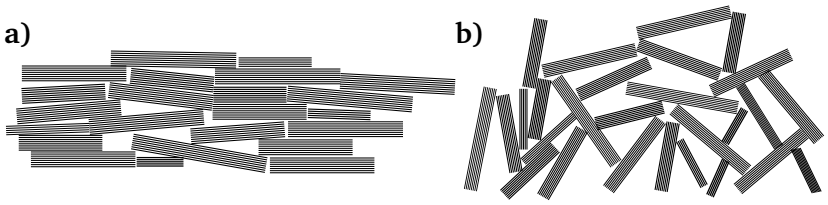

Figure 2.13: Schematic structure of (a) an ordered clay film, in which the particle orientation is strongly anisotropic, and of (b) a disordered clay sample, in which the particle orientation is less anisotropic.

2.5 Conclusion

The combined use of Environmental Scanning Electron Microscopy and Digital Image Correlation allowed us to observe and quantitatively measure the swelling of clay films at the micrometer scale. Successive tests on several samples showed that the method was reproducible. The swelling curves and isotherms adsorption depended significantly on the interlayer cation. The Ca-saturated montmorillonite swelled more and adsorbed more water in the 0 % to 45 % relative humidities range than the Na-saturated montmorillonite. But it swells less and adsorbs less water in the 45 % to 95 % RH range than the Na-saturated montmorillonite. The amplitude of the swelling of the natural montmorillonite Swy-2-raw, which contains about 1/3 of calcium and 2/3 of sodium, was close to the one of the Ca-montmorillonite and much smaller than the one of the Na-montmorillonite. However, the shape of the swelling

and adsorption isotherm curves of the natural montmorillonite was the same as for the Na-montmorillonite. Therefore the natural montmorillonite Swy-2-raw behaved mostly like the Na-saturated montmorillonite. This feature needs to be explained in more detail and requires further scrutiny.

The comparison between the swelling behavior of the interlayer space and of the thin films shows that the swelling of the thin films was entirely governed by the interlayer crystalline swelling. Thanks to how the films were prepared, their structure was highly ordered and their mesoporosity was very low. Therefore, the thin films can be described as a regular stacking of montmorillonite layers and interlayer spaces which can swell freely.

However, this conclusion should be restricted to the domain of relative humidities in which the study was performed (relative humidities between 14 % and 95 %) and in which the swelling mechanism is the so-called crystalline swelling, driven by the hydration of the cations and the surface oxygen atoms. It will most probably break down at larger water activity, in conditions where the osmotic swelling mechanism takes over. In those conditions, the homogeneous interlayer swelling of the Na-exchanged film would still go on, whereas the interlayer swelling of the Ca-exchanged film would be severely restricted by ion–ion correlation forces (Kjellander et al., 1988b,a).

Chapter 3

The cohesion of charged colloids

In this Chapter, *we investigated the interactions responsible for the cohesion of clay layers. The swelling properties of clays depend both on the nature of the interlayer cation and on the surface charge of the layers. We aimed at understanding better how these parameters impact the interactions and the cohesion between the clay layers. This question is of interest for a broader class of materials than clays only: this work can be applied to other charged lamellar materials separated by interlayer cations. This Chapter is dedicated to determine what level of complexity is required in the modeling of the system in order to capture the cohesive behavior of charged lamellar materials, depending on the charge of the surfaces, on the valency of the cations, and on the separation between the charged surfaces. To address this question we present computer simulations of confined electrolytes between charged clay layers. In addition to the analytical mean-field Derjaguin-Landau-Verwey-Overbeek (DLVO) theory, we used various numerical models of increasing complexity from the so-called Primitive Model to the full-atomistic model. In particular, we introduced the Explicit Solvent Primitive Model, in which the cations are modeled with point charges and the molecules of the solvent are modeled with soft spheres with embedded point dipoles. We showed that taking explicitly into account the solvent impacts significantly the cohesion of the model. Ionic correlation forces are always present between the lamellae*

and always play an important role, even in the case of lamellae carrying a low surface charge balanced by monovalent counterions.

DANS CE CHAPITRE, *nous avons étudié les interactions responsables de la cohésion des feuillets d'argile. Les propriétés de gonflement des argiles dépendent à la fois de la nature du cation interfoliaire et de la charge de surface des feuillets. Notre objectif est de mieux comprendre comment ces paramètres influent sur les interactions et la cohésion entre les feuillets d'argile. L'intérêt de cette question dépasse les seuls matériaux argileux et ce travail peut être appliqué à d'autres matériaux lamellaires chargés séparés par des cations et un solvant. Ce chapitre est consacré à la détermination du niveau de complexité nécessaire à la modélisation de la cohésion des matériaux lamellaires chargés, en fonction de la charge de la surface, de la valence des cations et de la distance entre les surfaces chargées. Pour répondre à cette question, nous présentons des simulations numériques d'électrolytes confinés entre des feuillets d'argile chargés. En plus de la théorie analytique champ-moyen Derjaguin-Landau-Verwey-Overbeek (DLVO), nous utilisons différents modèles numériques de complexité croissante, du Modèle Primitif au modèle tout atomistique. En particulier, nous avons développé un Modèle Primitif à Solvant Explicite, dans lequel les cations sont modélisés par des charges ponctuelles et les molécules de solvant sont modélisées par des dipôles ponctuels. Nous avons montré que la prise en compte du solvant explicite a un effet significatif sur la cohésion du modèle. Les forces de corrélation ioniques sont toujours présentes entre les feuillets et jouent toujours un rôle important, même dans le cas de feuillets portant une faible charge de surface équilibrée par des contre-ions monovalents.*

Contents

3.1 Introduction

This Chapter is devoted to understanding the interactions between charged layers separated by counterions in a solvent. The swelling of smectite clays (Anderson et al., 2010; Delville, 2012) results from the interactions of charged clay layers with ions and water. The swelling properties of clays are known to depend both on the nature of the counterions (Segad et al., 2010) and on the surface charge (Laird, 2006; Sato et al., 1992). However, the scope of the questions of the interactions between charged lamellae is of interest for a much broader class of materials than clay materials only. These interactions govern the behavior of many natural and engineered systems. For instance, in biology, Deoxyribose Nucleic Acid (DNA) condensation is the process by which a DNA macromolecule is compacted to form chromosomes. Such process involves the interaction between negatively charged DNA macromolecules and trivalent and tetravalent polyamines (Allahyarov et al., 2005; Teif and Bohinc, 2011). DNA condensation is essential to the processing of genetic information. Also, the cohesion between calcium silicate hydrates (C-S-H)

lamellae plays a key role in the setting (Pellenq and Van Damme, 2004) and the mechanical properties of cementitious materials (Pellenq et al., 2008). C-S-H is the main product of hydration of Portland cement and, like smectite clays, exhibits a plate-like structure with counterions and water molecules between charged silica chains (Pellenq et al., 2009).

3.1.1 From the mean-field theory to the Primitive Model

The cohesion and stability of such charged layers separated by a solvent containing counterions has long been discussed in the framework of the Derjaguin-Landau-Verwey-Overbeek (DLVO) theory (Derjaguin, 1941; Verwey et al., 1999; Israelachvili, 1991). The DLVO theory is the combination of the repulsive electrical double layer interaction with the attractive van der Waals interactions. The repulsive electrostatic interaction is obtained by solving analytically the Poisson-Boltzmann equation of a system made of positive point charges between negatively charged surfaces.

Making use of the Poisson-Boltzmann equation, the electrostatic pressure P between two charged surfaces in function of their surface separation D is given by:

$$P(D) = k_B T \left(\rho_0(D) - \rho_0(\infty)\right), \tag{3.1}$$

where k_B is the Boltzmann constant, T the temperature and $\rho_0(x)$ is the cation concentration at the mid-plane for a surface separation x (Israelachvili, 1991). This pressure depends only on the increase on the ionic concentration at the center of the pore and therefore its origin is entropic.

However, it is now known that a system of charged plates and counterions can generate strong attractive electrostatic interactions (Israelachvili, 1991). To study such systems numerically, Jönsson et al. (1980) introduced the so-called Primitive Model. In the Primitive Model, the charged lamellae and the hydrated cations are represented by uniformly charged infinite planar surfaces and by charged hard spheres, respectively, while the solvent is represented by a dielectric continuum. Monte Carlo simulations in the framework of the Primitive Model showed that fluctuations of the ionic concentration in

the interlayer space result in an instantaneous polarization and give rise to an attractive ionic fluctuation interaction (Valleau et al., 1991; Guldbrand et al., 1984). Thus, the behavior of the system is governed by a competition between repulsive entropic forces and attractive energetic forces (Jönsson and Wennerström, 2004). For divalent or trivalent cations, the attractive energetic contribution can exceed the repulsive entropic component of the pressure and results in one or several attractive wells of the pressure between the lamellae (Pellenq et al., 1997; Delville and Pellenq, 2000). Figure 3.1 shows the pressure between two montmorillonite layers in function of the distance between the layers, as predicted by the Primitive Model. Two cases are considered: a montmorillonite with sodium counterions and a montmorillonite with calcium counterions. As predicted by the Poisson-Boltzmann equation, in the case of sodium counterions, the pressure is always repulsive. In contrast, in the case of calcium counterions, attractive pressures are observed for pore sizes larger than 10 Å and could explain the experimental observation that exfoliating completely calcium montmorillonite layers is difficult.

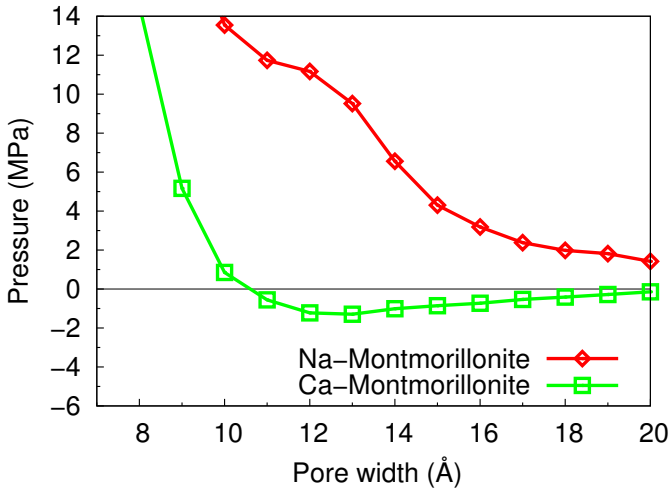

Figure 3.1: Interlayer pressure computed with the Primitive Model versus pore width for montmorillonite with sodium (red diamond symbols) or calcium (green square symbols) interlayer cations.

Figure 3.2 displays the pressure between the charged surfaces computed

with the Primitive Model in function of the surface charge (x-axis) and of the surface separation (y-axis) (Pellenq et al., 1997) in the case of divalent counterions. Figure 3.2 also reports the surface charge of smectite clays (about 0.015 e/Å^2) and of C-S-H (about 0.034 e/Å^2). For calcium smectite clays, the pressure well is about 2 MPa deep while for C-S-H, the pressure well is about 10 MPa deep. Therefore the ionic fluctuation interactions were reported as the reason for the reduced swelling of calcium smectite clays when compared to sodium smectite clays, for the setting of cement, and for the strong cohesion of C-S-H (Pellenq and Van Damme, 2004; Pellenq et al., 2008).

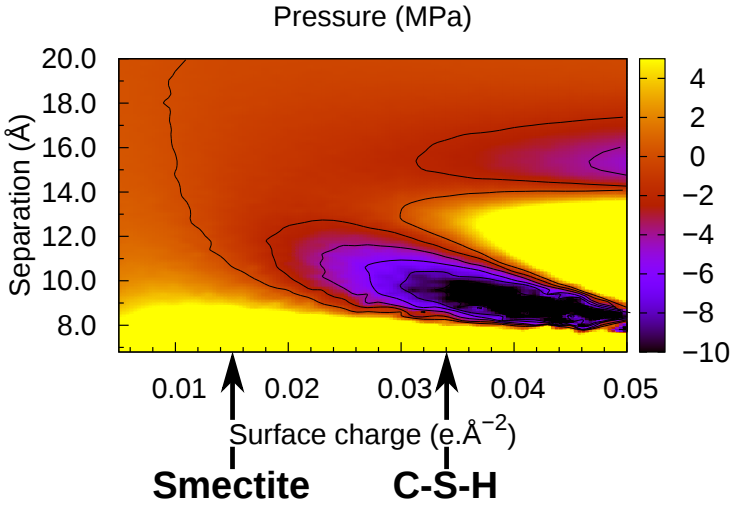

Figure 3.2: Interlayer pressure computed with the Primitive Model versus pore width and surface charge. The black lines are the 0, -2, -4, -6, -8 and -10 MPa isobars.

In addition to not considering these ionic fluctuations interactions, another limitation of the DLVO theory is the negligence of the effect of the finite size of the ions. This effect is taken into account by the Primitive Model or by more complex analytical models.

3.1.2 Beyond the Primitive Model

Nevertheless, the Primitive Model also has its own limitations. The surfaces of the slit pore are assumed to be flat and uniformly charged, the ions

are supposed to be fully hydrated and mobile and the solvent is considered to be a dielectric continuum the dielectric constant of which is the one of bulk water. These hypotheses make the Primitive Model questionable, in particular at low surface separation. In this case, the molecular structures of the solvent and the surfaces have to be taken into account. Therefore, numerous works adopted a full-atomistic description of the system to study for instance the intralamellar swelling of smectite clays (Hensen and Smit, 2002; Zheng et al., 2011; Tambach et al., 2004a,b) or the mechanical properties of calcium silicate hydrates (Shahsavari et al., 2009, 2011; Pellenq et al., 2009). However, the computational cost of these atomistic simulations is very significant and, for large interlayer spaces, coarse-grained simulations are needed. Accordingly, it is necessary to determine more precisely the complexity which needs to be introduced into the models of lamellar systems and the key physical ingredients responsible for the cohesion of such materials. Moreover, the link between the Primitive Model and the full-atomistic model has never been made clear.

This Chapter is dedicated to determine what level of complexity is required in the modeling of the system in order to get meaningful results, depending on the charge of the surfaces, on the valency of the cations, and on the separation between the charged surfaces. In particular, we answer the following questions: is the Primitive Model sufficient to study the effect of confined electrolytes on the cohesion of the system, especially when the pore width is small? At which critical value of the so-called electrostatic coupling do the fluctuations of the ionic concentrations have to be considered? The electrostatic coupling is defined as the ratio between the interaction energy between a counterion and a charged surface and the thermal energy (Delville and Pellenq, 2000), and is therefore proportional to the product of the counterion valency and the surface charge.

To address these questions, we present computer simulations of confined electrolytes between charged clay layers. In addition to the DLVO theory, we used various models of increasing complexity (see Figure 3.3): the Primitive Model (PM), the Explicit Solvent Primitive Model (ESPM) and the full-atomistic model. The Explicit Solvent Primitive Model is a model we

proposed to take into account explicitly the solvent while keeping the simplicity of the Primitive Model. As in the Primitive Model, in the ESPM model the charged lamellae are represented by infinite uniformly charged planes. The counterions and the solvent particles are represented by point charges and point dipoles, respectively, embedded in soft spheres. The ESPM model is described in details in Section 3.2.2.

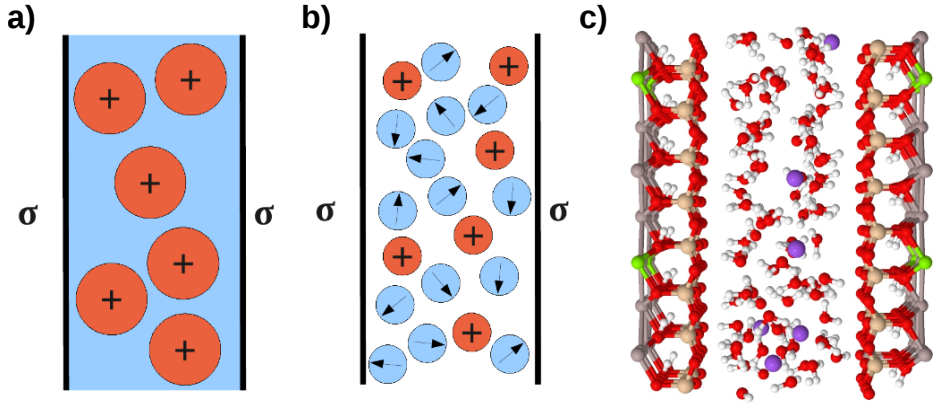

Figure 3.3: Models of increasing complexity of a montmorillonite clay: (a) Primitive Model, (b) Explicit Solvent Primitive Model, (c) Full-atomistic model.

We considered two realistic lamellar materials: a typical montmorillonite (labeled Mmt) and a typical vermiculite (labeled Vmt). Montmorillonite is a low-charge swelling clay while vermiculite is a clay mineral with a higher layer charge. In this work, the vermiculite layers were twice as charged as the montmorillonite layers. These two clay minerals were saturated with either sodium, calcium, or aluminum counterions. To investigate both the effect of surface charge and cation valency, six systems were therefore considered: Na-Mmt, Ca-Mmt, Al-Mmt, Na-Vmt, Ca-Vmt, and Al-Vmt. Using the full-atomistic model as a reference, we analyzed the six systems with all models. For each system, we generated a family of slit pores of various widths and we ran Monte-Carlo and Molecular Dynamics simulations.

3.2 Computational methods

In this Section, we present the computational details of the full-atomistic model and of the Explicit Solvent Primitive Model. The full-atomistic model describes the whole molecular structure of the clay layers and of the solvent and was used as a reference. In contrast, in the Explicit Solvent Primitive Model, the clay layers are considered as uniformly charged infinite planes and the solvent particles as point dipoles.

3.2.1 Full-atomistic model

First, we built realistic atomistic structures of layers of montmorillonite and vermiculite. We ran Grand Canonical Monte Carlo simulations to compute the water density in the interlayer space of montmorillonite and vermiculite at various pore widths. We then ran isothermal molecular dynamics simulations on these systems to compute the interaction pressure between the clay layers and the dielectric constant of the confined water. The number of water molecules in the pores during the isothermal simulations (NVT ensemble) was given by the densities previously computed by Grand Canonical Monte Carlo simulations.

Atomistic structure and force field

The two systems under consideration were atomistic models of montmorillonite and vermiculite. The atomic coordinates of both clays were taken from the atomic structure of pyrophyllite determined by X-ray diffraction (Lee and Guggenheim, 1981). The unit cell of pyrophyllite was duplicated in the x and y directions so that each clay layer contained 8 unit cells. The lateral dimensions of the layer were $L_x = 21.18$ Å and $L_y = 18.28$ Å and the thickness of the layer was $L_z = 6.56$ Å.

For the montmorillonite layers, every 8^{th} octahedral aluminum atom was substituted by a magnesium atom and every 32^{nd} tetrahedral silicon atom was substituted by an aluminum atom (Chavez-Paez et al., 2001). For the vermiculite layers, 3 of 16 tetrahedral silicon atoms were substituted by an

aluminum atom. All octahedral aluminum atoms and octahedral vacancies were substituted by magnesium atoms. The hydroxyl groups were oriented orthogonally to the basal plane. The substitutions were distributed randomly obeying the Lowenstein's rule (Loewenstein, 1954). The net surface charge $\sigma_{Vmt} = -0.248$ C.m^2 of the vermiculite layers was exactly twice as high as the net surface charge $\sigma_{Mmt} = -0.124$ C.m^2 of the montmorillonite layers. These surface charges correspond to half of the total charge density of the layers, each layer being in contact with two slit pores and therefore having two surfaces.

The simulation cells contained one or two clay layers in order for the aspect ratio of the cell to be larger than 1/2, as shown in Figure 3.4. The interlayer space was filled with the appropriate number of cations to ensure electric neutrality.

We used the CLAYFF force field (Cygan et al., 2004) to compute energies and forces between atoms. CLAYFF provides parameters for Na^+ and Ca^{2+} but not for Al^{3+}. For the Al^{3+} cation, we used the Lennard-Jones parameters proposed by Faro et al. (2010): $\sigma = 1.4472$ Å and $\epsilon = 0.2166$ kcal/mol. CLAYFF does not provide partial charges for neighbor oxygens associated with triple substitutions, which are present in the octahedral sheet of vermiculite. In order to determine the partial charges of these oxygen atoms, we first built the atomic structure of talc from the structure of pyrophyllite by filling all octahedral sites with magnesium atoms. The atomic structure of talc is the same as that of vermiculite, except that it contains no tetrahedral substitution. To ensure the electroneutrality of the atomic structure of talc, we used a partial charge $q = -1.2171$e for the bridging oxygens of the octahedral sheet neighboring 3 octahedral substitutions. We checked that only the partial charges of the neighboring atoms were affected by the substitutions by carrying a partial charge computation with the "charge equilibration method" (Rappé and Goddard, 1991). To ensure that each substitution in the tetrahedral sheet of talc brought an additional charge of -1e, we used a partial charge $q = -1.3357$e for the bridging oxygens neighboring tetrahedral and octahedral substitutions. Table 3.1 reports all partial charges used in this work for the oxygen atoms contained in the clay layers or in water.

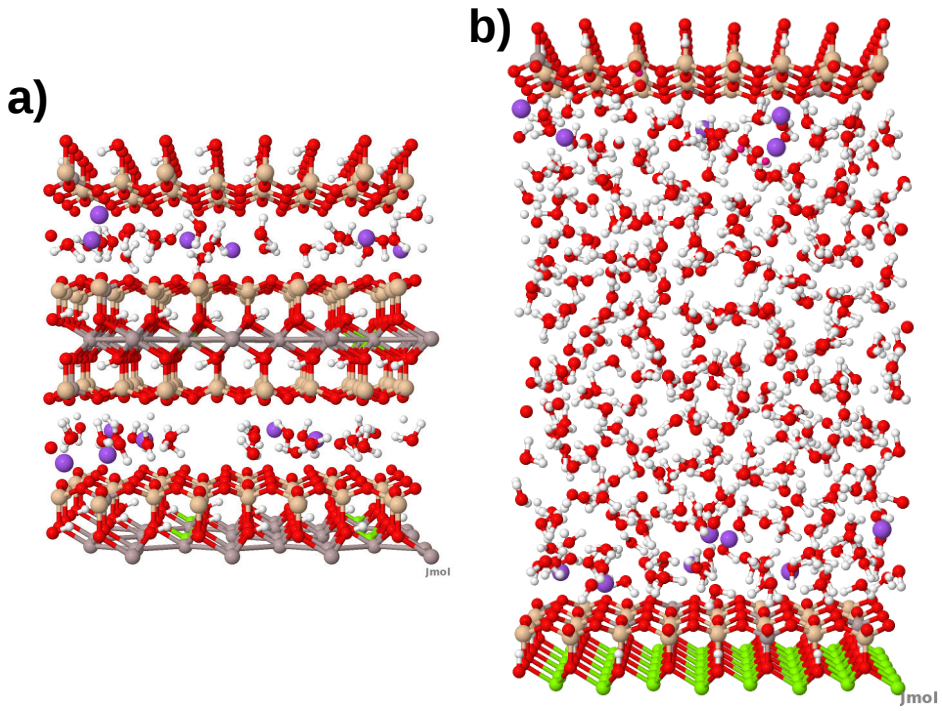

Figure 3.4: (a) Atomic configuration of Na-Montmorillonite. The pore width is 5 Å. (b) Atomic configuration of Na-Vermiculite. The pore width is 30 Å. Purple spheres are sodium ions, red spheres are oxygen atoms, white spheres are hydrogen atoms, green spheres are magnesium atoms, gray spheres are aluminum atoms and the beige spheres are silicon atoms.

The water model used by the CLAYFF force field is the flexible SPC model. The SPC model is a three-site water model. The water molecules interact via oxygen-oxygen Lennard-Jones interactions and via coulombic interactions. The Lennard-Jones parameters of the oxygen atom were: $\sigma =$ 3.1655 Å and $\epsilon = 0.1554$ kcal/mol. The partial charges of the oxygen atom and of the hydrogen atoms were -0.82e and 0.41e, respectively. In order to take into account the flexibility of the molecule, intramolecular harmonic bond stretch and angle bend terms are added to the energy and forces. For the bond stretch term, the equilibrium length is 1.0 Å and the force constant is equal to 554.1349 kcal/mol.Å^2. For the angle bend term, the equilibrium angle is 109.47^o and the force constant is equal to 45.7696 kcal/mol.rad^2. During the Monte Carlo simulations presented in the next Section, the angle

Position of the oxygen atom	Charge (e)	Source
water oxygen	-0.8200	CLAYFF
hydroxyl oxygen	-0.9500	CLAYFF
bridging oxygen	-1.0500	CLAYFF
bridging oxygen with octahedral substitution	-1.1808	CLAYFF
bridging oxygen with tetrahedral substitution	-1.1688	CLAYFF
hydroxyl oxygen with substitution	-1.0808	CLAYFF
bridging oxygens with 3 octahedral substitutions	-1.2171	this work
bridging oxygen with tetrahedral and octahedral substitutions	-1.3357	this work

Table 3.1: Partial charges used in this work for the oxygen atoms in function of the position and the environment of the oxygen atoms. The partial charges given by CLAYFF were reported by Cygan et al. (2004). e is the elementary positive charge.

and the bonds were kept rigid.

Grand Canonical Monte Carlo

To compute the water density in clay pores in equilibrium with bulk water, we ran Grand Canonical Monte Carlo (GCMC) simulations. We first computed the chemical potential of bulk water. In all simulations, we used the rigid SPC model (Berendsen et al., 1981).

The probability of insertion or deletion of a molecule in dense systems is very low. Therefore GCMC simulations of bulk water require the use of Configurational-Bias Monte Carlo (CBMC) technique (Frenkel and Smit, 2002). The general idea of CBMC is to divide the insertion (or deletion) trial into two steps (Hensen et al., 2001). First, the central atom is inserted (oxygen for water). Then, the other atoms (hydrogen atoms for water) are inserted. The algorithm of the insertion trial we implemented was:

1. We generated k_O trial positions of the O atom and computed the

Lennard-Jones interaction u^i_{LJ} for each position i.

2. We selected one position with probability

$$p_i = \frac{\exp\left(-\beta u^i_{LJ}\right)}{W_O}, \tag{3.2}$$

where $W_O = \sum_{i=1}^{k_O} \exp\left(-\beta u^i_{LJ}\right)$ is the Rosenbluth factor.

3. We then generated k_H trial orientations and computed the short-range coulombic interaction u^i_{SR} for each orientation i.

4. We selected one orientation with probability

$$p_i = \frac{\exp\left(-\beta u^i_{SR}\right)}{W_H}, \tag{3.3}$$

where $W_H = \sum_{i=1}^{k_H} \exp\left(-\beta u^i_{SR}\right)$ is the Rosenbluth factor.

5. Finally, we accepted the insertion trial with probability

$$P_{acc} = \min\left[1, \frac{V}{\Lambda^3(N+1)} \frac{W_O}{k_O} \frac{W_H}{k_H} \exp\left(\beta(\mu - \Delta u_{LR})\right)\right], \tag{3.4}$$

where Δu_{LR} was the change in the long-range part of the Ewald correction.

For the deletion trial, we applied the same algorithm. However, we generated only $k_O - 1$ positions and $k_H - 1$ orientations, since the first trial configuration was the actual configuration of the molecule.

The deletion trial was accepted with probability

$$P_{acc} = \min\left[1, \frac{\Lambda^3 N}{V} \frac{k_O}{W_O} \frac{k_H}{W_H} \exp\left(-\beta(\mu - \Delta u_{LR})\right)\right]. \tag{3.5}$$

We chose the parameters k_O and k_H in order to maximize the efficiency of the computation. We performed a simulation of bulk water at 300 K and $\rho \approx 1$ g/cm^3. We measured the acceptance probability of the biased insertion trial over 1.10^6 Monte Carlo steps and the computation time for various k_O and k_H. Figure 3.5 shows the ratio $P_{acc}/(P^{ref}_{acc}\tau)$, where P_{acc} is the acceptance probability, P^{ref}_{acc} is the acceptance probability in the reference

case (i.e. $k_O = 1$ and $k_H = 1$) and τ is the computation time scaled by the reference computation time.

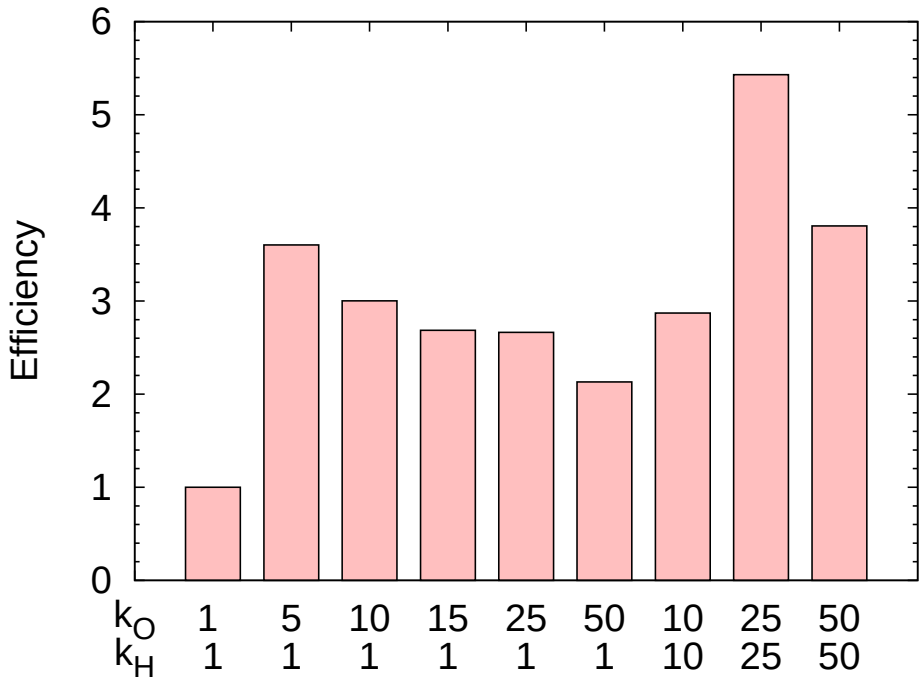

Figure 3.5: Efficiency of the biased insertion for various CBMC parameters k_O and k_H. The efficiency is the ratio $P_{acc}/(P_{acc}^{ref}\tau)$, where P_{acc} is the acceptance probability, P_{acc}^{ref} is the acceptance probability in the reference case (i.e. $k_O = 1$ and $k_H = 1$) and τ is the computation time scaled by the reference computation time.

Figure 3.5 shows that $k_O = 25$ and $k_H = 25$ yielded the maximum efficiency. In that case the acceptance probability was 0.21 (in contrast to 0.01 in the reference case) and $\tau = 3.9$. In the following Sections, all GCMC simulations were performed with this set of parameters.

Figures 3.6 shows the densities computed from CBMC at various chemical potentials at 300 K with the rigid SPC model together with a linear regression. In order to compute the chemical potential of bulk water, we performed several GCMC simulations for several chemical potentials. The retained value for the chemical potential was the one for which the computed density was the density of bulk water ($\rho = 0.997$ g.cm^{-3}). For the

SPC model, at the density of bulk water, the computed chemical potential was equal to -45.8 kJ/mol and the corresponding fugacity was equal to 3255 Pa.

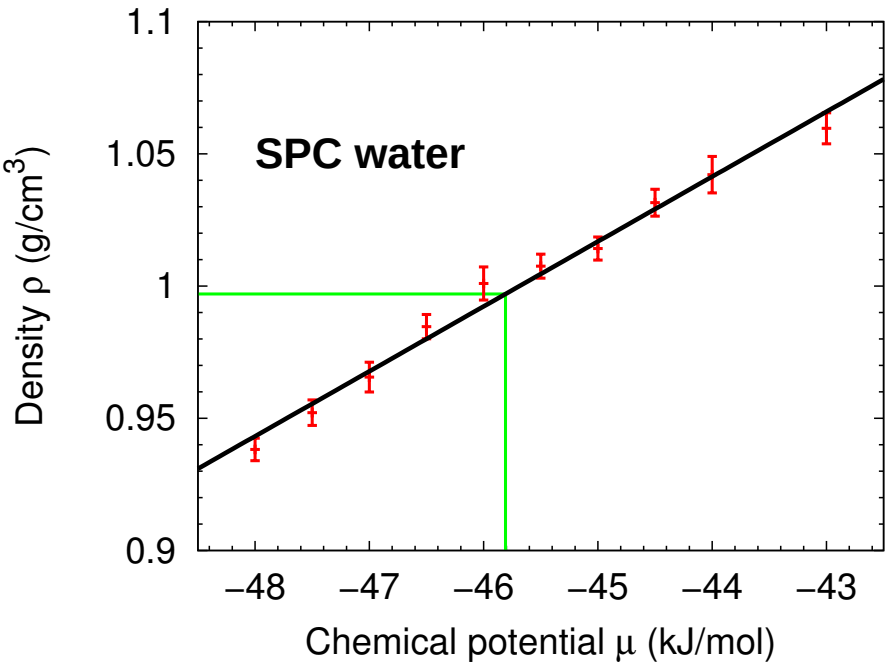

Figure 3.6: Density ρ versus chemical potential μ for rigid SPC water at 300 K. For a density of water $\rho = 0.997$ g.cm^{-3}, the chemical potential of SPC water is equal to -45.8 kJ/mol.

To fill the interlayer space with rigid SPC water molecules for each clay, each cation, and each pore size, we ran GCMC simulations. The interlayer water was in equilibrium with water at a fugacity of 3255 Pa, i.e. a reservoir of bulk water at ambient pressure and at a temperature of 300 K. The clay layers and water molecules were kept rigid. The simulation cell was equilibrated during 5 million steps and the number of molecules was sampled during the following 16 million steps.

Pressure computation

We ran molecular dynamics in the canonical ensemble (NVT ensemble) at 300 K. The interlayer space was filled with the number of water molecules

obtained from the GCMC simulations. The equations of motions were integrated using the Verlet algorithm with a timestep of 1 fs and the system was thermostated using Langevin Dynamics (Lelièvre et al., 2010). In all our work, we used Langevin dynamics to thermostat the system during molecular dynamics runs in the canonical ensemble. The advantage of Langevin dynamics is that its ergodicity is mathematically established (Cancès et al., 2005). All molecular dynamics simulations were performed with the LAMMPS package (Plimpton, 1995). The simulation cell was equilibrated for 200 ps and the pressure was sampled during the following 800 ps. The components of the pressure tensor were computed using the virial formula (Frenkel and Smit, 2002).

Dielectric constant

The dielectric constant of a fluid with periodic boundary conditions is given by (Wu et al., 2006)

$$\varepsilon_0 = 1 + \frac{4\pi}{3\langle V\rangle\varepsilon}\beta\left(\langle \mathbf{M}^2\rangle - \langle \mathbf{M}\rangle^2\right) \tag{3.6}$$

where $\langle V\rangle$ is the average volume of the simulation cell, ε is the dielectric permittivity of vacuum and $\mathbf{M}$ is the total moment dipole of the fluid.

We computed the dielectric constant of bulk water by running a NPT molecular dynamics simulation (Wu et al., 2006). The temperature (300 K) and the pressure (1 bar) were kept constant with a Langevin thermostat and barostat. The system was composed of 287 water molecules. Both simulations with flexible and rigid SPC water molecules were run. For the rigid SPC water model, the molecules were kept rigid with the SHAKE algorithm. The system was equilibrated during 1 ns and the properties of the system were sampled for 5 ns. With rigid water molecules the timestep was 2 fs, while it was 1 fs with flexible molecules.

Table 3.2 gives the computed values of the dielectric constants of bulk water for the rigid and for the flexible SPC models. We computed the dielectric constant of the rigid SPC water model to compare it to the value computed by Wu et al. (2006). The experimental value of the dielectric constant of

water is 78.5.

Model	ε_0	Wu et al. (2006)
rigid SPC	65.5 ± 1.9	66.3
flexible SPC	94.2 ± 6.3	-

Table 3.2: Dielectric constants of bulk water computed with rigid and flexible SPC models.

In the clay pores, the longitudinal component ε_{xy} and the transversal component ε_z of the dielectric constant were computed by:

$$\varepsilon_{xy} = 1 + \frac{4\pi}{3V_{\text{pore}}\varepsilon}\beta\left(\langle M_{xy}^2\rangle - \langle M_{xy}\rangle^2\right) \tag{3.7}$$

and

$$\varepsilon_z = 1 + \frac{4\pi}{3V_{\text{pore}}\varepsilon}\beta\left(\langle M_z^2\rangle - \langle M_z\rangle^2\right), \tag{3.8}$$

where V_{pore} is the volume accessible to water, and M_{xy} and M_z are the components of the total dipole of all water molecules in the plane of the clay layers and in the direction orthogonal to the clay layers, respectively. The volume accessible to water is the total volume of the pore minus the volume occupied by the cations and the volume occupied by the external atoms of the layers. To compute the components of the dielectric constants of confined water, we ran molecular dynamics in the canonical ensemble at 300 K. The system was equilibrated for 2 ns and the total dipole vector of water was sampled during 8 ns.

3.2.2 Explicit Solvent Primitive Model

The Explicit Solvent Primitive Model is an extension of the Primitive Model we developed to take into account the solvent explicitly. The clay layers were represented by infinite planes bearing a uniform surface charge. The cations and the water molecules were represented by point charges and point dipoles, respectively, embedded in soft spheres. z denotes the direction orthogonal to the infinite surfaces and xy denotes the plane parallel to the

infinite surfaces. The system was infinite in the x and y directions, in which periodic boundary conditions were enforced. The system had a slab geometry: it was finite in the z direction and no periodicity was enforced in that direction. L_x, L_y, and L_z denote the length of the system in the x, y, and z directions, respectively.

In the ESPM model, the atomic structure of the clay layers was not explicitly taken into account. The clay layers were considered as flat surfaces with which the ions and solvent molecules interacted via a 9-3 Lennard-Jones potential and a coulombic interaction:

$$U_{iW} = \frac{A}{z_i^9} - \frac{B}{z_i^3} - \frac{q_i|z_i|}{2\varepsilon_0} \tag{3.9}$$

where z_i is the distance of the particle to the wall, q_i the charge of the particle, and A and B the parameters of the potential. The parameters of the 9-3 Lennard-Jones potential were obtained by fitting the 9-3 Lennard-Jones function on the potential energy of the interaction between a single clay layer and a cation or a water molecule versus the clay-particle distance (see Figure 3.7) computed with the full-atomistic model and the CLAYFF force field. All fitted parameters are given in Table 3.3.

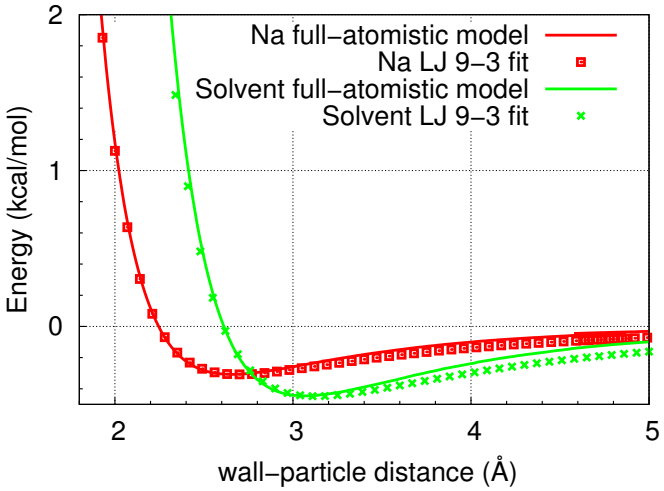

Figure 3.7: Fitting of the parameters of the 9-3 Lennard-Jones potential used in the ESPM simulations on the data computed with the full-atomistic model.

particle	A (kcal.mol^{-1}.Å^9)	B (kcal.mol^{-1}.Å^6)
solvent	6516	20.67
Na	1155	9.040
Ca	3005	12.91
Al	161.4	4.402

Table 3.3: Parameters of the 9-3 Lennard-Jones potential for the wall-particle interaction of the ESPM simulations.

The solvent particles and the ions interacted which each other via a Lennard-Jones interaction and a dipole-dipole, a charge-charge or a charge-dipole interaction. The Lennard-Jones parameters of the solvent and the cations were the same as the ones of the oxygen atoms of water and the cations in CLAYFF.

We chose the dipole moment of the solvent particles so that the dielectric constant of the bulk dipolar fluid was equal to that of bulk water, i.e. 78.5. We ran molecular dynamics simulations of 907 point dipoles at a density of 1 g.cm^{-3} and computed the dielectric constant of the fluid for various values of the dipole moment. Figure 3.8 displays the value of the dielectric constant in function of the dipole moment of the solvent particles and the fit of these data with an exponential function. A dielectric constant equal to 78.5 was obtained with a dipole moment equal to 1.7 D. This value was lower than the experimental dipole moment of water molecules in a liquid phase (i.e. about 2.6 D). Indeed, our simple model was not detailed enough to capture the dielectric response of water. In particular, we did not consider the hydrogen bonds.

The long-range charge-charge, dipole-dipole and charge-dipole interactions were handled with the Ewald summation technique with the EW3DC correction term of Yeh and Berkowitz (1999). To take into account the slab geometry, the Ewald sum was computed as if the system was periodic in the z-direction but a volume of vacuum of thickness $5L_z$ was inserted between the slabs and the following surface energy term E_{surface} was added to the standard 3D Ewald sum:

$$E_{\text{surface}} = \frac{2\pi}{L_x L_y L_z} D_z^2, \tag{3.10}$$

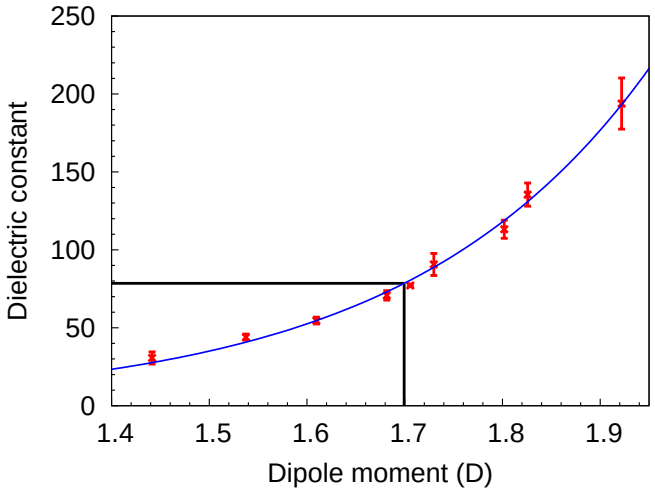

Figure 3.8: Dielectric constant of a bulk dipolar fluid made of point dipoles, in function of the dipole moment of the fluid particles. The solid line is an exponential fit.

where D_z is the z component of the total dipole moment of the simulation cell.

Though the whole system was charge neutral, the subsystem of point particles had a nonzero net charge because only counterions were present in the pore. Thus, a divergence of the long-range coulombic energy arose. To regularize this energy, Ballenegger and Arnold (2009) proposed to add the following correcting term $E_{\text{correction}}$ to the standard Ewald sum

$$E_{\text{correction}} = -\frac{2\pi}{L_x L_y L_z}\left(Q\sum_i q_i z_i - Q^2\frac{L_z^2}{12}\right) \tag{3.11}$$

where Q is the net charge of the system. A review of Ewald summation technique for systems consisting of charges and dipoles is given by Stenhammar et al. (2011).

In the isotropic case, the susceptibility χ_{iso} of water in presence of ions is defined by (Caillol et al., 1986; Chandra and Patey, 1994; Chandra, 2000):

$$\chi_{\text{iso}} = \frac{1}{3k_BTV}\left(\langle \mathbf{M}_W^2\rangle + \langle \mathbf{M}_W.\mathbf{M}_I\rangle\right), \tag{3.12}$$

where $\mathbf{M}_W$ is the total dipole of the water molecules and $\mathbf{M}_I$ is the total moment of the ion cloud. However, the systems under consideration in this work had a slab geometry and were transverse isotropic. Therefore, the dielectric response of water confined in slit pores was expected to be strongly anisotropic. In the case of a slab geometry, the relations between the components of the dielectric constant and the longitudinal component χ_{xy} and the transversal component χ_z of the susceptibility are (Froltsov and Klapp, 2007)

$$\epsilon_{xy} = 1 + 2\pi\chi_{xy} \tag{3.13}$$

and

$$\frac{1}{\epsilon_z} = 1 - 4\pi\chi_z, \tag{3.14}$$

where the longitudinal component χ_{xy} and the transversal component χ_z of the susceptibility are given by (Chandra, 2000)

$$\chi_{xy} = \frac{1}{2k_B T V_{pore}} \left(\langle \mathbf{M}_{W,xy}^2 \rangle + \langle \mathbf{M}_{W,xy} \mathbf{M}_{I,xy} \rangle \right) \tag{3.15}$$

and

$$\chi_z = \frac{1}{k_B T V_{pore}} \left(\langle M_{W,z}^2 \rangle + \langle M_{W,z} M_{I,z} \rangle \right), \tag{3.16}$$

where $\mathbf{M}_{W,xy}$ and $M_{W,z}$ are the longitudinal and the transversal components of the total dipole $\mathbf{M}_W$ of the water molecules, respectively, and $\mathbf{M}_{I,xy}$ and $M_{I,z}$ are the longitudinal and the transversal components of the total dipole $\mathbf{M}_I$ of the ion cloud.

The longitudinal cross-correlation term $\langle \mathbf{M}_{W,xy} \mathbf{M}_{I,xy} \rangle$ is equal to zero. Therefore, the components of the dielectric constant read

$$\epsilon_{xy} = 1 + \frac{2\pi}{V_{pore}} \langle \mathbf{M}_{W,xy}^2 \rangle \tag{3.17}$$

and

$$\frac{1}{\epsilon_z} = 1 - \frac{4\pi}{V_{pore} k_B T} \left(\langle M_{W,z}^2 \rangle + \langle M_{W,z} M_{I,z} \rangle \right). \tag{3.18}$$

We used Equation 3.17 to compute the longitudinal component of the dielectric constant. However, from a practical point of view, we could not use Equation 3.18 to compute the transversal component of the dielectric constant: first, even when no ion was present, the convergence of this computation was too slow to be used; second, when the surfaces carried a net surface charge, the fluctuations of the ionic cloud made it difficult to isolate the dielectric response of the confined water and made the computation converge even more slowly.

Traditionally, the properties of the Primitive Model were computed with Monte Carlo algorithms. Therefore, the first attempts to add an explicit solvent to the Primitive Model via point dipoles were performed in the Monte Carlo framework. However, the Monte-Carlo simulations of such systems with realistic values of the charge of the ions, of the charge of the surfaces, and of the dipole of the solvent molecules proved not to converge in a reasonable time (Boda et al., 1998). Figure 3.9 displays the potential energy of the system versus the number of pair distance computations for a case with realistic charges and dipoles, and for a case with significantly lower charges and dipoles. We compared the convergence of two sampling algorithms: Monte Carlo and molecular dynamics with a Langevin thermostat (Lelièvre et al., 2010). In the low-charge case (see Figure 3.9-a), both methods converged quickly to the same value of energy. However, with realistic values of the charge and of the dipole moment, Figure 3.9-b shows that when Langevin dynamics was used, the energy converged much quicker than with Monte Carlo. In the latter case, the potential energy of the simulation cell actually never converged. With Langevin dynamics, the forces on all particles are computed at each timestep and the particles are moved collectively. These collective moves proved to be crucial to the effectiveness of the simulation.

Starting from simulation cells with a number of water molecules given by the densities computed with the full-atomistic GCMC simulations, we used

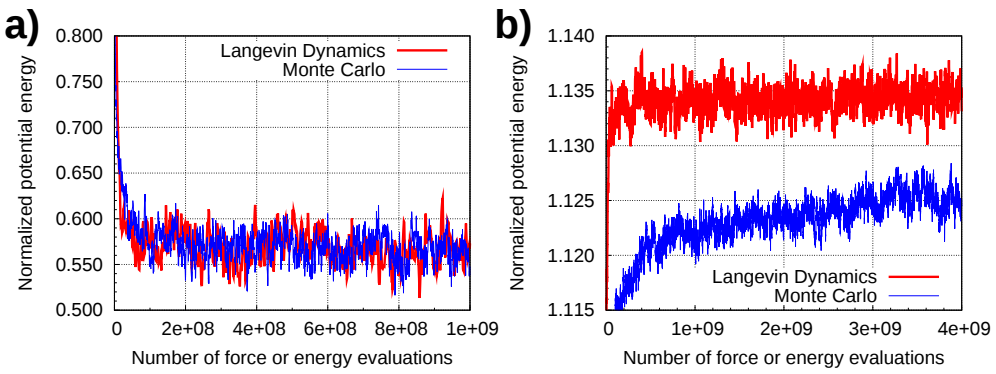

Figure 3.9: Computations with the Explicit Solvent Primitive Model. Potential energy of the simulation cell versus number of pair distance computations for (a) unrealistically low values of the charge q of the cations and of the dipole moment μ of the solvent particles: $q = 0.2$e and $\mu = 0.9$ D and (b) realistic values of the charge q of the cations and of the dipole moment μ of the solvent particles: q= 2e and $\mu = 1.8$ D, for two different sampling methods: Monte Carlo and Langevin Dynamics.

Verlet algorithm with a timestep of 1 fs to integrate the equations of motion and a Langevin dynamics thermostat with a Langevin parameter equal to 100. The system was equilibrated for 200 ps and the properties of the system were sampled in the following 1 ns. The lateral dimension of the simulation cell was $L_x = L_y = 43.98$ Å. The masses of the particles were those of the corresponding atomic elements. The moment of inertia of the solvent molecules was taken as the moment of inertia of a homogeneous sphere that had a mass of 18 g/mol and a diameter of 1.7 Å. Both the translational and rotational degrees of freedoms of the solvent particles were updated with the Verlet algorithm and thermostated with the Langevin thermostat.

The transversal component of the pressure was computed at one of the walls. All interactions of the point charges and point dipoles with the wall were summed and divided by the area of the wall so as to obtain the total pressure. The net pressure at a given pore size was then computed as the subtraction of the pressure of the bulk fluid (computed for a wall-wall distance equal to 30 Å) from the total pressure just calculated.

3.2.3 Error estimation

The statistical error was estimated with the block averaging method (Lelièvre et al., 2010). We divided the production phase in m blocks of n steps. For each block, we computed the block average A_n^b of observable A. If n was large enough, we expected that

$$A_n^b \sim \mathcal{N}(\langle A \rangle, \frac{\sigma^2}{n}). \tag{3.19}$$

We computed

$$\sigma_{n,m}^2 = \frac{1}{m} \sum_{b=1}^{m} \left(A_n^B - \langle A \rangle \right)^2 . \tag{3.20}$$

and plotted $n\sigma_{n,m}^2$ versus n. If n and m were large enough, one expects $n\sigma_{n,m}^2 \approx \sigma^2$.

Figure 3.10 displays $n\sigma_{n,m}^2$ versus n in the case of a GCMC simulation of rigid SPC water at $\mu = -47$ kJ/mol. This figure provides both the correlation length (in this case 1.10^6 steps) and an estimate of the variance σ. The 95 % confidence interval is then given by $\pm$ 1.96σ.

3.3 Results

3.3.1 Dielectric constant of confined water

First, we ran configurational-bias grand canonical Monte Carlo simulations with the full-atomistic model. The pores were equilibrated with a reservoir of bulk water at 300 K. Figure 3.11 displays the density of water in the pores versus pore width for various clays and cations. The pore width is defined as the distance between the external oxygen atoms planes of the layers. The density was computed from the number of water molecules in the simulation box obtained from GCMC and from the volume accessible to water. The volume accessible to water was defined as the difference between the total volume of the pore and the volume occupied by the cations and the external oxygen atoms of the clay layers.

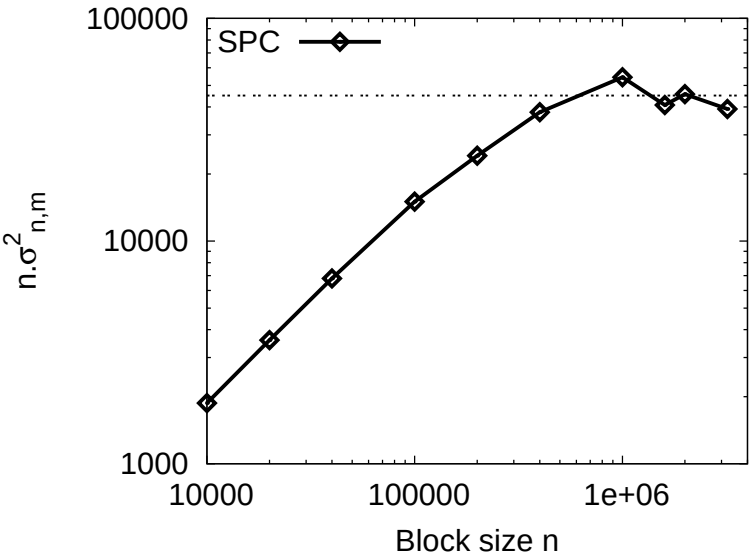

Figure 3.10: Error estimation with the block averaging method in the case of a GCMC simulation of rigid SPC water at $\mu = 47$ kJ/mol.

Figure 3.11 shows that for small pore sizes, the water density differed significantly from 1 g.cm^{-3}. For larger pore sizes, the water density tended to the bulk value of 1.0 g.cm^{-3} in the case of montmorillonite (Mmt). In the case of vermiculite (Vmt), the water density was higher and tended to 1.15 g.cm^{-3} at a pore size of 30 Å. Because of the higher surface charge, the cation density in the interlayer space of vermiculite was larger than in the interlayer space of montmorillonite. The hydrophilicity of clay layers stems from the interlayer cations: one of the main driving forces of the water adsorption is the hydration of these cations (Hensen and Smit, 2002; Salles et al., 2007). Thus, a higher cation density results in a higher water uptake. These water densities were then used to prepare the initial states of all following NVT simulations.

The first property of charged lamellar systems we investigated was the dielectric constant of the confined water. Many experimental and simulation works show that structure and dynamics of water in a confined geometry or close to interfaces differ significantly from the properties of bulk water (Froltsov and Klapp, 2007; Wander and Clark, 2008; Senapati and Chandra,

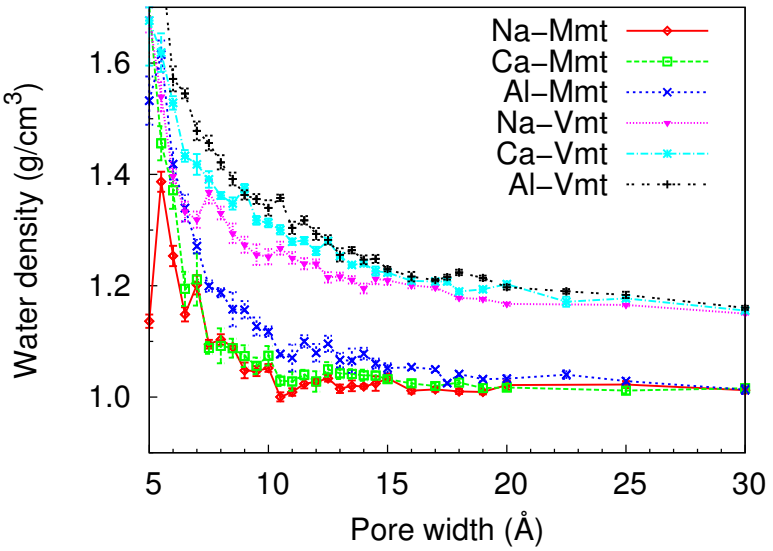

Figure 3.11: Water density in the interlayer space versus pore width for various interlayer cations computed by GCMC simulations on the full-atomistic models. The two systems considered are a typical montmorillonite (labeled Mmt) with a surface charge σ = -0.124 C.m^{-2} and a typical vermiculite (labeled Vmt) with a surface charge σ = -0.248 C.m^{-2}.

2001; Lin et al., 2009). Indeed, water molecules adsorbed on a surface interact strongly with this surface via short-range interactions which decrease their ability to rotate in an electric field. This reduced mobility leads to a dielectric constant in the adsorbed layers lower than in a bulk solution. The nature of the surfaces in contact with the confined water and of the counterions that balance the surface charge also play a crucial role (Hasted et al., 1948; Wander and Clark, 2008; Bonthuis et al., 2012). Laird (1996) showed that in charged clays the dielectric constant of the interlayer water is a function of basal spacing and that this dependency is necessary to explain crystalline swelling.

The dielectric constant of water confined in a spherical nanocavity decreases with the diameter of the cavity (Senapati and Chandra, 2001). For instance, for a diameter of 12.2 Å, the dielectric constant drops from 81 to 42. Furthermore, the dielectric tensor of polar fluids in slit or cylindrical pores is very anisotropic (Lin et al., 2009) and non-homogeneous (Froltsov and

Klapp, 2007). Near an interface, strong oscillations of the dielectric constant are observed (Ballenegger and Hansen, 2005).

The presence of ions has also a noticeable effect on the dielectric constant of water. Water molecules in the hydration shells of the ions are submitted to a strong electric field and lose part of their rotational mobility. As a consequence of this dielectric saturation phenomenon, a decrease of the dielectric constant with increasing salt concentration has been observed experimentally (Hasted et al., 1948). In contrast, Zhu et al. (2012) recently presented a computational study of the dielectric response of nanoconfined electrolytes, in which they showed an anomalous increase of the transversal component of the dielectric tensor with salt concentration until a critical concentration.

Figure 3.12 displays the longitudinal component of the dielectric constant of water confined between charged clay layers. Upon confinement, water exhibited a strong drop of its dielectric constant. The stronger the electrostatic coupling was (i.e. the higher surface charge or the higher cation valency was), the more significant the drop was. We could not compute the transversal component of the dielectric constant because the convergence of the computation of this component was too slow, as a consequence of the geometry and of the presence of a strong electrostatic coupling.

Thus, the assumption of the Primitive Model that the dielectric constant of confined water is equal to that of bulk water does not hold at low pore widths. Such assumption is problematic, since the dielectric response of the solvent impacts strongly on the cohesion of the system. To illustrate the key role of the dielectric response of the solvent on the behavior of the system, we plotted on Figure 3.13 the pressure computed with the Primitive Model for various values of the dielectric constant in the case of a weak electrostatic coupling (e.g. Na-montmorillonite). For low dielectric constants, the system exhibited a range of pore widths for which the pressure was attractive, while for high dielectric constants it did not.

It is therefore necessary to take the solvent into account explicitly. We introduced the Explicit Solvent Primitive Model to keep the simple description of the Primitive Model while modeling the solvent explicitly with point dipoles. Figure 3.14 shows the longitudinal component of the dielectric con-

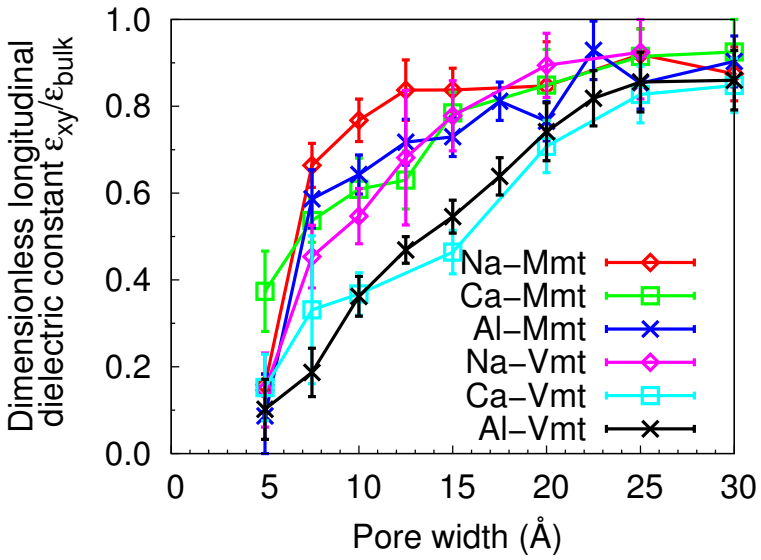

Figure 3.12: Ratio of the longitudinal component ϵ_{xy} of the dielectric constant of water confined in a charged pore to the dielectric constant ϵ_{bulk} of bulk water computed with the full-atomistic model. The two systems considered are a typical montmorillonite (Mmt) with a surface charge of σ = -0.124 C.m^{-2} and a typical vermiculite (Vmt) with a surface charge of σ = -0.248 C.m^{-2}.

stant in a charged slit pore computed with the Explicit Solvent Primitive Model. As with the full-atomistic, the longitudinal component of the dielectric constant computed with the ESPM model decreased with the pore width. Upon confinement, we observed a stronger drop of the dielectric constant with the ESPM model than with the full-atomistic model. A reason for such discrepancy is that water is modeled as a point dipole in the ESPM model: such a simple description is not able to take into account the hydrogen bonds, which play an important role in the behavior of water.

3.3.2 Interaction pressure

Figure 3.15 shows the interaction pressure between layers of montmorillonite versus pore width either with Na interlayer cations or with Ca interlayer cations. Figures 3.15-a and 3.15-c display the results of the full-atomistic model. With Na counterions, metastable states at 6 Å and 8.5

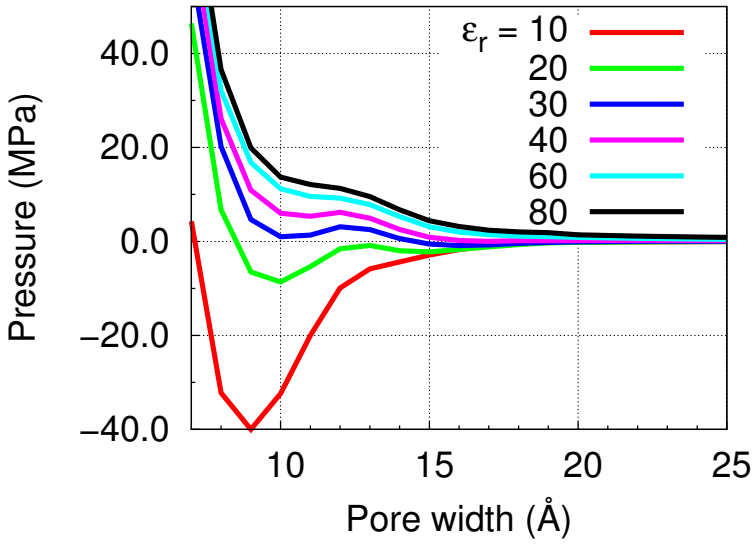

Figure 3.13: Pressure between charged surfaces versus the surface separation computed with the Primitive Model for various dielectric constants ϵ_r of the dielectric continuum. The surface charge is the surface charge of montmorillonite (i.e. $\sigma = 0.124$ C.m^{-2}) and the counterions are sodium cations.

Å can be observed. A pore width of 6 Å corresponds to a basal spacing of 12.5 Å and to the one-layer hydrate of montmorillonite (Hensen and Smit, 2002). A pore width of 8.5 Å corresponds to a basal spacing of 15 Å and to the two-layers hydrate. The interaction pressure computed with the ESPM model (Figures 3.15-b and 3.15-d) exhibited a pattern very similar to the one of the full-atomistic model: with Na counterions, we observed the same minima at 6 Å and 9 Å, the same maximum at 7 Å and the same oscillatory behavior between 10 and 15 Å. The very good agreement between the full-atomistic model and the ESPM model suggests that the ESPM model is able to capture the relevant physical mechanisms governing the cohesion of charged layers in a solvent, for a much lower computational cost than full-atomistic models (i.e. the same accuracy could be obtained about one order of magnitude more quickly).

We note that the value of the minimum pressure differs for the two models. For the full-atomistic model, the minimum pressure is -105 MPa for Na-montmorillonite and -128 MPa for Ca-montmorillonite and is reached

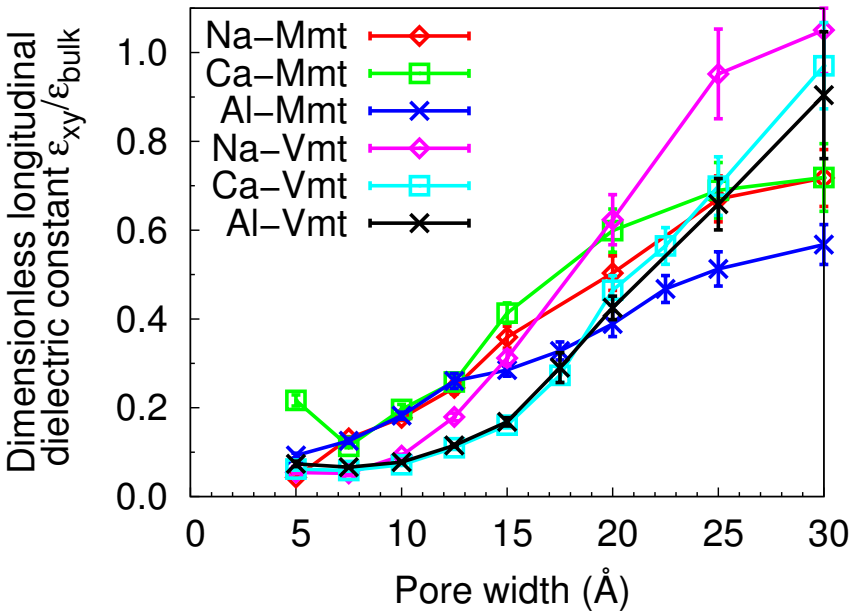

Figure 3.14: Ratio of the longitudinal component ϵ_{xy} of the dielectric constant of water confined in a charged pore to the dielectric constant ϵ_{bulk} of bulk water computed with the Explicit Solvent Primitive Model. The two systems considered are a typical montmorillonite (Mmt) with a surface charge of σ = -0.124 C.m^{-2} and a typical vermiculite (Vmt) with a surface charge of σ = -0.248 C.m^{-2}.

at a pore width of 10.5 Å in both cases. For the ESPM model, the minimum pressure is -250 MPa for Na-montmorillonite and -600 MPa for Ca-montmorillonite and is reached at a pore width of 11 Å for Na-montmorillonite and at a pore width of 8.5 Å for Ca-montmorillonite. The deeper pressure wells in the case of the ESPM model are explained by a dielectric constant lower than with the full-atomistic model (see Figures 3.12 and 3.14). Therefore, with the ESPM model the electrostatic interactions are stronger and the pressure more attractive than with the full-atomistic model.

Moreover, the ESPM model captures the experimental observation that Ca-montmorillonite exhibits a lower ability to being exfoliated compared to Na-montmorillonite (Segad et al., 2010). Indeed, the minimum pressure is stronger in the case of calcium than of sodium and therefore the energy necessary to overcome the pressure wells is higher in the case of calcium

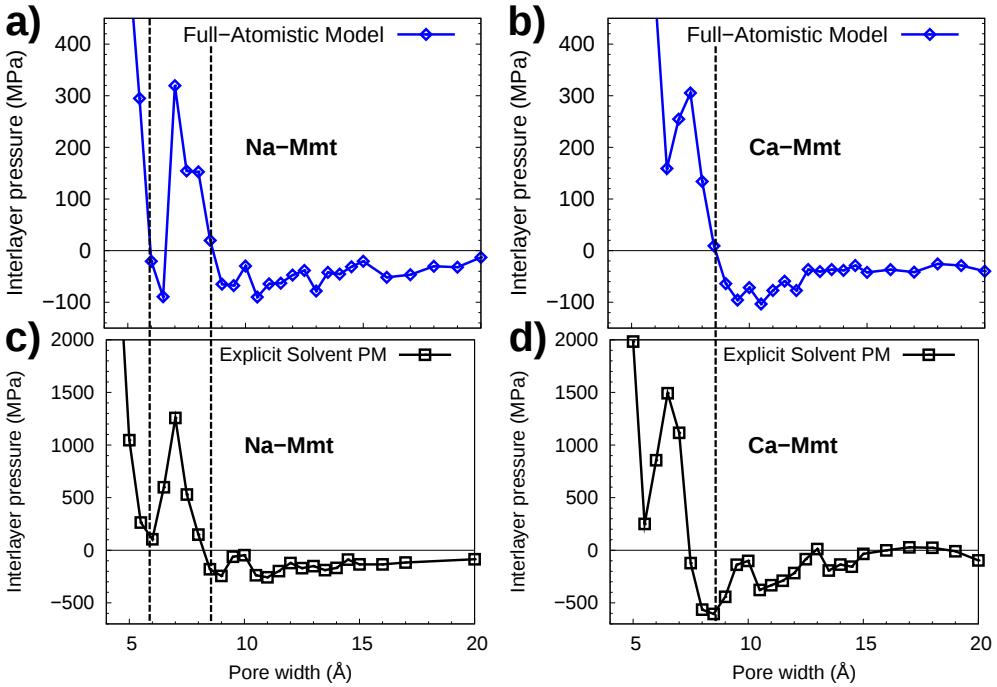

Figure 3.15: Interlayer pressure versus pore width for (a and b) Na-Montmorillonite and for (c and d) Ca-Montmorillonite computed with (a and c) the full-atomistic model or with (b and d) the Explicit Solvent Primitive Model.

than of sodium.

The results of the ESPM model contrast with the ones of the Primitive Model. Indeed the repulsive pressure predicted by the Primitive Model at any pore size in the case of Na-montmorillonite is invalidated by the ESPM model. Therefore, an explicit solvent proves to be critical to explain the cohesion of charged lamellae. The cohesion of Na-montmorillonite can be explained neither with the mean-field DLVO theory nor with the Primitive Model. According to the Primitive Model, the entropic repulsion is always greater than the electrostatic attraction due to ionic fluctuations. However, the assumption that the dielectric constant of the confined fluid is equal to the dielectric constant of bulk water leads to a significant underestimation of the energetic attractive contribution.

Figure 3.16 displays the interlayer pressure computed with the ESPM model and the Primitive Model in function of the pore size for the all six

systems under consideration. The results of the ESPM model show the significant effect of the surface charge on the interlayer pressure: for all cations, the pressure wells were much deeper for the vermiculite than for the montmorillonite. The nature of the cation also impacts strongly the interlayer pressure: for a given clay, the higher the valency of the cation was, the deeper the pressure wells were.

The results of the Primitive Model also highlight the effect of the electrostatic coupling: the higher the coupling was, the more attractive the interaction between layers was. However, the Primitive Model did not capture the cohesive behavior of Na-montmorillonite and Na-vermiculite. The ESPM model, as well as the full-atomistic model, showed that with sodium interlayer cations, stable states and attractive pressure wells exist no matter the surface charge, while the results of the Primitive Model showed that for the same systems the interaction pressure was always repulsive. Therefore, the solvent plays an important role in the cohesive behavior of the system. The effect of the solvent cannot be captured by a simple dielectric continuum as in the Primitive Model and the solvent has to be taken into account explicitly. Moreover, the results of the ESPM model suggest that ionic correlation forces play a significant role even at low electrostatic couplings. Such ionic correlation forces are the focus of the next section.

3.3.3 Ionic correlation forces

In order to better characterize the ionic correlation forces, in particular in the case of low electrostatic couplings, we analyzed the fluctuations of ionic density in more details. Figure 3.17-a displays the total dipole per surface unit of the ionic cloud in a slit pore over time computed with the ESPM model for a 10-Å-wide montmorillonite pore. Both the results for Na- and for Ca-montmorillonite are shown. The total dipole m_z per surface unit is computed as the sum over all the N cations in the simulation cell of the product of their charge q_i by their distance z_i to the mid-plane, divided by the product of the length L_x and L_z of the cell in the x and z directions,

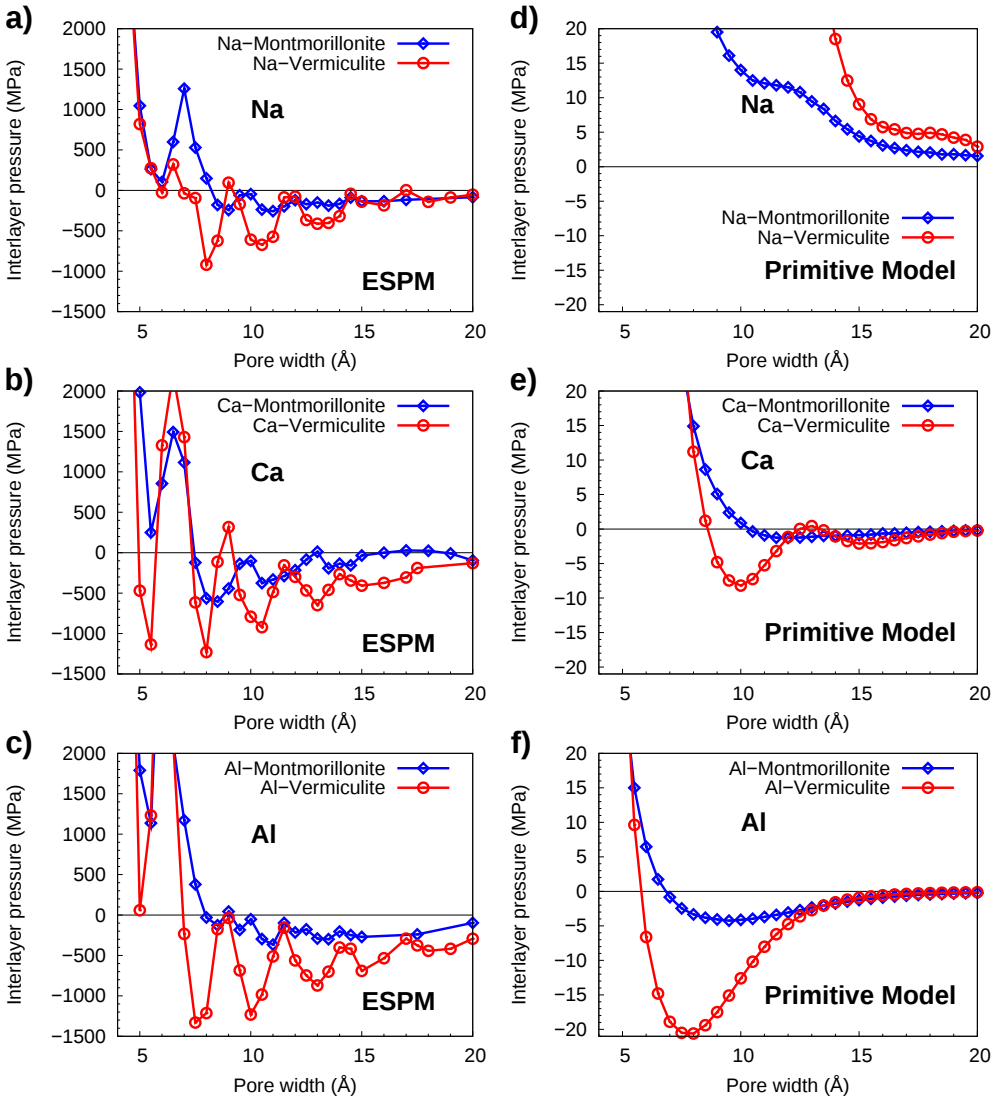

Figure 3.16: Interlayer pressure versus pore width for montmorillonite (blue lines and diamond symbols) and vermiculite (red lines and circle symbols) with (a and d) Na, (b and e) Ca, and (c and f) Al interlayer cations computed with (a, b, and c) the Explicit Solvent Primitive Model (ESPM) and (d, e, and f) the Primitive Model.

respectively:

$$m_z = \frac{1}{L_x L_y} \sum_{i=1}^{N} q_i z_i. \tag{3.21}$$

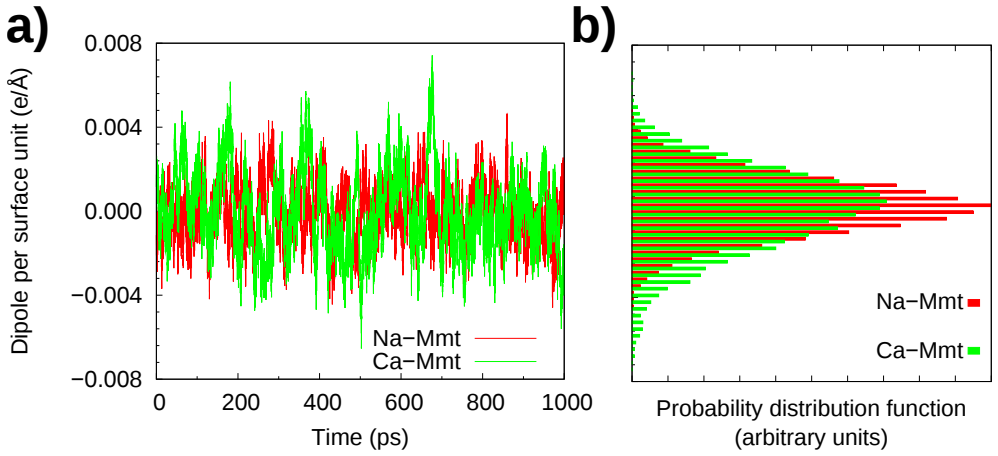

Figure 3.17: (a) Fluctuations over time of the total dipole m_z per surface unit of the ionic cloud in a 10-Å-wide pore for Na-montmorillonite and Ca-montmorillonite and (b) probability density function of the total dipole value.

Figure 3.17-b displays the probability distribution function of the total dipole m_z. The probability distribution function was symmetric for both cations and the average $\langle m_z \rangle$ was equal to zero. At this pore width, the variance of the distribution was slightly higher for Ca-montmorillonite than for Na-montmorillonite.

To analyze quantitatively the data displayed in Figure 3.17, we computed the autocorrelation function f of the fluctuation defined by:

$$f(\tau) = \frac{2}{\tau} \int_0^{\tau/2} m_z(t) m_z(t+\tau) dt. \tag{3.22}$$

Figure 3.18 displays the autocorrelation function f of the dipole fluctuation of a cloud of sodium cations and of a cloud of calcium cations in montmorillonite slit pores. The autocorrelation function could be fitted by an exponential function and the corresponding characteristic relaxation time τ_c was measured. This relaxation time τ_c was equal to 4.8 ps in the case of Na-montmorillonite and to 9.0 ps in the case of Ca-montmorillonite.

Figure 3.19-a displays the average over time of the square of the total dipole $\langle m_z^2 \rangle$ of the ionic cloud as a function of the width of the montmorillonite slit pore. Since the average $\langle m_z \rangle$ over time is statistically equal to

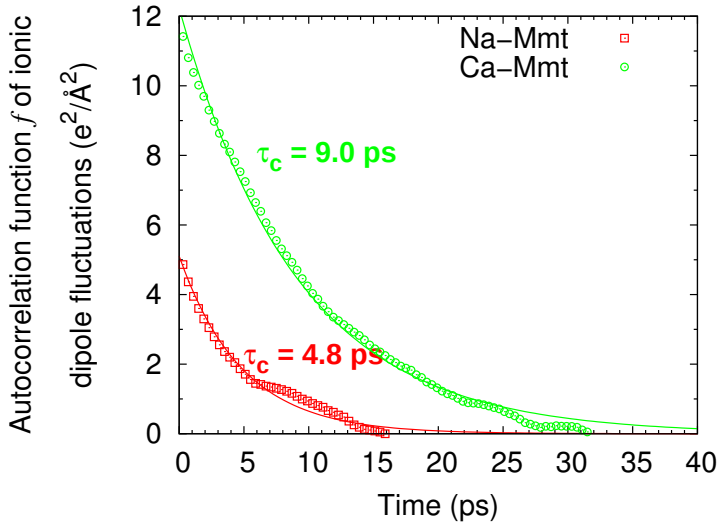

Figure 3.18: Autocorrelation function f of ionic dipole fluctuations and fit with an exponential function.

zero, $\langle m_z^2 \rangle$ is equal to the variance of the total dipole of the ionic cloud. Figure 3.19-a shows that this variance did not depend on the nature of the cation (sodium or calcium).

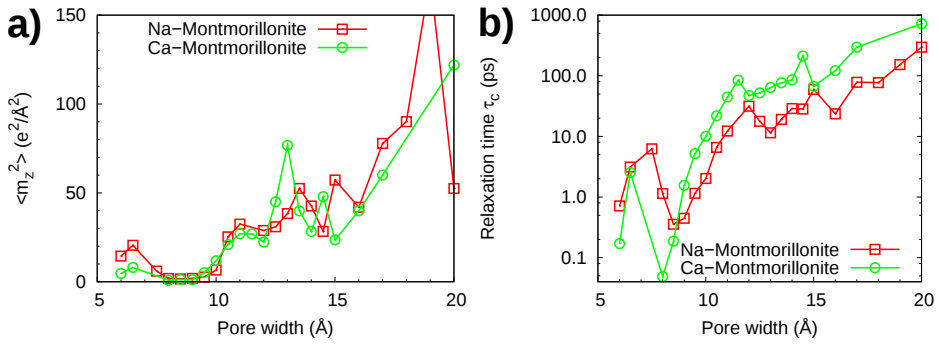

Figure 3.19: (a) Variance of the square of the total ionic dipole and (b) characteristic time τ_c of the decrease of the autocorrelation function f for Na-montmorillonite and Ca-montmorillonite.

Figure 3.19-b displays the characteristic relaxation time τ_c of the autocorrelation function f as a function of the pore width for sodium and calcium interlayer cations. For both cations, the relaxation time τ_c was roughly an increasing function of the pore width. Except at very low pore widths, the

characteristic relaxation time τ_c was always higher with calcium cations than with sodium cations. The two sets of data exhibited very similar features: we observed the same local maxima of relaxation time τ_c for pore widths of 7.5 Å, 12.5 Å and 15 Å and the strictly increasing of the relaxation time τ_c for pore sizes larger than 16 Å. However, these maxima could not be clearly correlated to stable states or to extrema of the interaction pressure.

In summary, we were able to observe numerically the fluctuations of the total dipole of the ionic cloud within a clay slit pore. The amplitude of these fluctuations was similar for sodium or calcium ions but depended on the pore width. However, the characteristic relaxation time τ_c of the autocorrelation function was much higher in presence of calcium counterions than in presence of sodium counterions, and therefore in presence of the counterions for which the cohesive interactions are stronger.

3.4 Conclusion

In this chapter, we showed that taking into account the solvent explicitly is necessary to describe the cohesion of charged lamellar systems. Indeed, the solvent exhibits a complex dielectric response which impacts strongly the electrostatic interactions in the system. In order to keep the simplicity of the Primitive Model while modeling water explicitly, we developed the Explicit Solvent Primitive Model, in which each water molecule is modeled by a point dipole. The ESPM model gives results which are in good agreement with the results of the full-atomistic model, but at a lower computational cost (i.e. approximately one order of magnitude more quickly). The ESPM model could be especially useful at the colloidal scale and to compute interactions between charged grains.

The ESPM model makes it possible to quantify the effect of the electrostatic coupling (i.e. the strength of the electrostatic interaction between a counterion and the charged surfaces) on the strength of the system. Both the cation valency and the surface charge impact the cohesion of the system. In addition, we were able to observe the ionic fluctuations in the pore and to quantify these fluctuations.

To improve the ability of the ESPM model to predict the cohesion of charged lamellar systems, we could refine the modeling of the solvent. Indeed, our simple model is not able to capture hydrogen bonds which are critical to the dielectric behavior of water. A solution could be to add to the point dipole a short-range angular potential which would depend on the relative orientation of neighbor molecules, as is the case of the Soft Sticky Dipole model (Liu and Ichiye, 1996).

Chapter 4

Computation of the elastic properties of clay layers upon hydration by molecular simulation

---

THIS CHAPTER *is devoted to the computation of the elastic properties of particles of montmorillonite by molecular dynamics simulations. Because of the softness of the material in the direction orthogonal to the clay layer at some water contents, the computation of the whole stiffness tensor was not trivial: we needed to implement the elastic bath method (Van Workum and de Pablo, 2003), which allows attenuating thermal strains and computing the stiffness via strain fluctuations in isothermal-isobaric simulations. We investigated the effect of water content, temperature, hydrostatic confining stress and interlayer cation on the elastic properties of swelling clays. In particular, we showed that the out-of-plane stiffness coefficients computed at 300 K differed significantly from the same coefficients computed at 0 K. The out-of-plane coefficients were very sensitive to both temperature and water content. In contrast, the dependence of the in-plane coefficients to temperature was slight. Moreover, the decrease of the in-plane coefficients with water content could entirely be explained by the change of geometry of*

the system due to the swelling of the interlayer space. The interlayer cation impacted the elastic properties of montmorillonite only in the driest states.

CE CHAPITRE *est consacré au calcul des propriétés élastiques des particules d'une argile gonflante (en l'occurrence la montmorillonite) par des simulations de dynamique moléculaire. En raison de la souplesse du matériau dans la direction orthogonale aux feuillets d'argiles à certaines teneurs en eau, le calcul de l'ensemble du tenseur de rigidité n'était pas immédiat : nous avons dû mettre en œuvre la méthode du bain élastique (Van Workum and de Pablo, 2003), ce qui permet d'atténuer les déformations thermiques et de calculer la rigidité via les fluctuations de déformation lors de simulations isothermes-isobares. Nous avons étudié l'effet de la teneur en eau, de la température, de la pression hydrostatique et du cation interfoliaire sur les propriétés élastiques des argiles gonflantes. En particulier, nous avons montré que les coefficients de rigidité hors plan calculés à 300 K différaient sensiblement des mêmes coefficients calculés à 0 K. Les coefficients hors plan étaient très sensibles à la température et à la teneur en eau. En revanche, la dépendance des coefficients dans le plan à la température était faible. Par ailleurs, la diminution des coefficients dans le plan avec la teneur en eau peut être entièrement expliquée par la variation de la géométrie du système en raison du gonflement de l'espace interfoliaire. Le cation interfoliaire a un effet sur les propriétés élastiques de la montmorillonite seulement dans les états les plus secs.*

Contents

4.1 Introduction

As highlighted in Section 1.2, the mechanical properties of clay-based materials highly depend on the water content (Bornert et al., 2010; Cariou et al., 2012; Pham et al., 2007). Moreover, the clay matrix plays a great role in the mechanical behavior of clayey rocks because of its softness with respect to the mineral inclusions and because if often plays the role of matrix. The sensitivity of the mechanical properties of clay materials to water originates from the scale of the clay layer. Therefore, building a macroscopic constitutive law which is able to predict the hydromechanical behavior of clay matrix in a bottom-up framework requires understanding and quantifying the hydromechanical behavior of the clay layers itself.

However, measuring the hydromechanical properties at the scale of the clay layers remains a challenge since, because of their layered structure, the behavior of the clay layers is expected to be very anisotropic. Bobko and Ulm (2008) measured the elastic properties of shales by nanoindentation and Ortega et al. (2007) used a multiscale homogenization model and a fitting procedure to back-calculate the transverse isotropic stiffness tensor

of clay particles from those nanoindentation results and their macroscopic tests. However, most of other experimental works report isotropic bulk and shear constants. Wang et al. (2001) immersed clay layers in a material of known elastic properties. They measured the elastic properties of the two-components composite and back-calculated the elastic constants of the clay layers. However, the water content of the clay layers was not controlled. Mondol et al. (2008) and Vanorio et al. (2003) measured the elastic constants of samples with various porosities by acoustic measurements and extrapolated the results to zero porosity to estimate the elastic constants of the clay minerals.

Molecular simulations made it possible to estimate the stiffness tensor of clays at the scale of the individual layer. Suter et al. (2007) and Mazo et al. (2008a,b) computed the stiffness tensor of a dry and a hydrated Na-montmorillonite by straining the simulation cell in all directions and by calculating the slopes of the simulated strain-stress relations. Zartman et al. (2010) used Density Functional Theory (DFT) and classical molecular dynamics to compute the stiffness tensor of layered silicates with various surface charges and submitted to various stresses. Ebrahimi et al. (2012) computed the stiffness tensor of Na-montmorillonite in function of the water content at 0 K. Teich-McGoldrick et al. (2012) computed the elastic constants of muscovite both at 0 K and at finite temperature and showed the effect of temperature and pressure on the stiffness of the layer.

This Chapter is dedicated to the computation of the elastic properties of a montmorillonite at the scale of the layer. We investigate the effect of the water content, of temperature, of hydrostatic confining stress, and of the nature of the interlayer cation on those elastic properties.

We use minimization techniques to compute the stiffness tensor of montmorillonite at 0 K. To compute the stiffness at finite temperature, we run molecular dynamics simulations in the isothermal-isobaric ensemble (Frenkel and Smit, 2002) and measure the fluctuations of the simulation cell parameters (Parrinello and Rahman, 1982). Because of the softness of the system in the direction orthogonal to the clay layers, we have to use the elastic bath method, initially proposed by Van Workum and de Pablo (2003), to obtain

converged and stable results.

The interest of this work lies in the fact that the stiffness tensor of a clay particle was computed over a wide range of thermo-hydric loadings. In particular, we investigated the impact of the nature of the interlayer cation on the elastic behavior at the nanoscale and we computed estimates of the elastic properties of a macroscopic clay matrix.

4.2 Computational methods

4.2.1 Computation of elastic tensor

The generalized Hooke's law in linear elasticity is given by:

$$\sigma_{ij} = \sum_{k=1}^{3}\sum_{l=1}^{3} C_{ijkl}\epsilon_{kl}, \tag{4.1}$$

where $\boldsymbol{\sigma}$ is the stress tensor, $\boldsymbol{\epsilon}$ the strain tensor and $\mathbf{C}$ the stiffness tensor.

We used the Voigt notation to represent the fourth-order stiffness tensor C_{ijkl} by a second-order symmetric tensor C_{ij}, where $i, j = 1, 2, ..., 6$. The indexes 1, 2 and 3 correspond to the directions x, y, and z, respectively, and the indexes 4, 5 and 6 correspond to shears in the planes yz, xz, and xy, respectively. The Hooke's law is then given by:

$$\begin{bmatrix} \sigma_{xx} \\ \sigma_{yy} \\ \sigma_{zz} \\ \sigma_{yz} \\ \sigma_{xz} \\ \sigma_{xy} \end{bmatrix} = \begin{bmatrix} C_{11} & C_{12} & C_{13} & C_{14} & C_{15} & C_{16} \\ & C_{22} & C_{23} & C_{24} & C_{25} & C_{26} \\ & & C_{33} & C_{34} & C_{35} & C_{36} \\ & & & C_{44} & C_{45} & C_{46} \\ & & & & C_{55} & C_{56} \\ & & & & & C_{66} \end{bmatrix} \cdot \begin{bmatrix} \epsilon_{xx} \\ \epsilon_{yy} \\ \epsilon_{zz} \\ 2\epsilon_{yz} \\ 2\epsilon_{xz} \\ 2\epsilon_{xy} \end{bmatrix}. \tag{4.2}$$

In this work, we used two methods to compute stiffness tensors: a static method and a finite temperature method. With the static method, the stiffness is obtained by minimizing the energy of the system and by allowing both the atomic coordinates and the cell parameters to relax. The stiffness tensor is then given by the second derivative of the energy of the system U

with respect to the strain $\boldsymbol{\epsilon}$ of the simulation cell (Gale and Rohl, 2003):

$$C_{ijkl} = \frac{1}{V} \frac{\partial^2 U}{\partial \epsilon_{ij} \partial \epsilon_{kl}}, \tag{4.3}$$

where V is the volume of the cell.

The components of the strain are given by:

$$\epsilon_{ij} = \frac{1}{2} \left(\left(h_{0,ik}^{-1} \right)^t h_{kl}^t h_{lm} h_{0,mj}^{-1} - \delta_{ij} \right), \tag{4.4}$$

where $\mathbf{h}_0$ and $\mathbf{h}$ are the cell matrix of the reference and deformed states, respectively, and $\mathbf{h}^t$ the transpose of $\mathbf{h}$.

To compute the stiffness at temperature T, we used simulations in the isothermal-isobaric ensemble and the Parinello-Rahman fluctuation formula (Parrinello and Rahman, 1982):

$$C_{ijkl} = \frac{k_B T}{\langle V \rangle} \left[\langle \epsilon_{ij} \epsilon_{kl} \rangle - \langle \epsilon_{ij} \rangle \langle \epsilon_{kl} \rangle \right]^{-1}. \tag{4.5}$$

To compute average elastic properties, we used the Voigt-Reuss-Hill (VRH) approximation (Hill, 1952). This approximation estimates the bulk modulus K and the shear modulus G of a random polycrystal as the arithmetic mean of the Voigt (Voigt, 1928) and Reuss (Reuss and Angew, 1929) bounds. This very common approach is not rigorous, but provides a good estimate of the macroscopic elastic properties.

4.2.2 Elastic bath method

The elastic bath method was proposed by Van Workum and de Pablo (2003) to improve the convergence of the computation of the elastic tensor by the fluctuation formula given by Equation (4.5). The main idea of the elastic bath method is to immerse the simulation cell in a so-called "elastic bath". This immersion consists in adding a fictitious strain energy to the Hamiltonian H of the system. The Hamiltonian H' of the system made of

the simulation cell and the elastic bath is now given by:

$$H' = H + \frac{1}{2} V_0 \mathbf{C}^B . \boldsymbol{\epsilon} : \boldsymbol{\epsilon}, \tag{4.6}$$

where $\mathbf{C}^B$ is the stiffness tensor of the elastic bath.

The elastic bath method is useful for both very stiff and very soft systems. For very stiff systems, the fluctuations of the cell parameters may be so small that they are not sampled adequately. In that case, the convergence of the fluctuation formula (4.5) is slow. By choosing a negative stiffness tensor of the elastic bath $\mathbf{C}^B$, the fluctuations of the cell parameters can be amplified and a better convergence of the elastic tensor of the system can be achieved. In contrast, for very soft systems, the fluctuations of the cell parameters may be too large and the assumption of small strains no longer holds. Moreover, significant drifts of the cell matrix can also be observed over time. By choosing a positive stiffness tensor of the elastic bath $\mathbf{C}^B$, the fluctuations of the cell parameters can be attenuated to stay within the small strains limit and to remove any drift of the simulation cell. There is no continuity of the covalent bonding between clay layers. Therefore, the system is expected to be soft in the direction orthogonal to the clay layer and we used the elastic bath method to attenuate the strain fluctuations in this direction.

An NPT simulation which conserves the extended Hamiltonian H' given by Equation (4.6) is run and Equation (4.5) is used to compute the stiffness tensor $\mathbf{C}^C$ of the composite material made of the clay layers immersed in the elastic bath. According to the theory of composite materials, the stiffness tensor $\mathbf{C}$ of the material is then given by (Van Workum and de Pablo, 2003):

$$\mathbf{C} = \mathbf{C}^C - \mathbf{C}^B. \tag{4.7}$$

Van Workum and de Pablo (2003) proposed the elastic bath method in the Monte Carlo framework and Cui et al. (2007b) extended it to molecular dynamics. Both works employed an isotropic elastic bath. In our work, we implemented the elastic bath method in a molecular dynamics barostat in order to make it possible to use any potentially anisotropic form of the

stiffness tensor of the elastic bath.

To run an isobaric simulation that conserved the extended Hamiltonian H' given by Equation (4.6), we had to modify the Nosé-Hoover barostat. The equations of the Nosé-Hoover barostat with anisotropic cell fluctuations and a hydrostatic pressure applied are given by (Parrinello and Rahman, 1981; Martyna et al., 1994; Shinoda et al., 2004):

$$\dot{\mathbf{r}}_i = \frac{\mathbf{p}_i}{m_i} + \frac{\mathbf{p}_g}{W_g}\mathbf{r}_i, \tag{4.8}$$

$$\dot{\mathbf{p}}_i = \mathbf{F}_i - \frac{\mathbf{p}_g}{W_g}\mathbf{p}_i - \frac{1}{3N}\frac{\mathrm{Tr}(\mathbf{p}_g)}{W_g}\mathbf{p}_i \tag{4.9}$$

$$\dot{\mathbf{h}} = \frac{\mathbf{p}_g}{W_g}\mathbf{h}, \tag{4.10}$$

and

$$\dot{\mathbf{p}}_g = V\left(\mathbf{P}_{int} - P_{ext}\mathbf{I}\right) + \left(\frac{1}{3N}\sum_{i=1}^{N}\frac{\mathbf{p}_i^2}{m_i}\right)\mathbf{I}, \tag{4.11}$$

where m_i, $\mathbf{r}_i$ and $\mathbf{p}_i$ are the mass, position and momentum, respectively, of atom i, $\mathbf{F}_i$ is the force on atom i, N is the number of atoms, W_g is the mass of the barostat, $\mathbf{p}_g$ is the cell momentum, P_{ext} is the applied hydrostatic pressure, $\mathbf{I}$ is the identity matrix and $V = \det(\mathbf{h})$ is the volume of the cell. Tr denotes the trace operator and $\dot{x}$ the time derivative of x. $\mathbf{P}_{int}$ is the internal pressure and is given by:

$$\mathbf{P}_{int,jk} = \frac{1}{V}\left(\sum_{i=1}^{N}\frac{(\mathbf{p}_i)_j(\mathbf{p}_i)_k}{m_i} + (\mathbf{F_i})_j.(\mathbf{r}_i)_k - \left(\frac{\partial U(\mathbf{r}_i,\mathbf{h})}{\partial \mathbf{h}}.\mathbf{h}^t\right)_{jk}\right) \tag{4.12}$$

where $U(\mathbf{r}_i, \mathbf{h})$ is the energy of the system. For most systems, the energy U does not depend on the cell matrix $\mathbf{h}$ and the last term of Equation (4.12) vanishes. However, in the case of the elastic bath method, the energy of the elastic bath depends on the cell matrix and therefore the last term of Equation (4.12), i.e. $\mathbf{P}_{bath} = U'_{bath}(\mathbf{h}).\mathbf{h}^t$, has to be computed. The component

Number n of water molecules per clay layer	Number of water layers	Water content (g/g of dry clay)
0	dry state	0.00
32	1 layer	0.09
64	2 layers	0.19
96	3 layers	0.28

Table 4.1: Equivalence between the number n of water molecules per clay layer in the simulation cell, the number of water layers in the interlayer space, and the water content.

$\mathbf{P}_{bath}$ of the internal pressure due to the elastic bath is given by:

$$\mathbf{P}_{bath} = \frac{V_0}{V}\mathbf{h}.\mathbf{h}_0^{-1}.\mathbf{C}^B.\boldsymbol{\epsilon}.\left(\mathbf{h}_0^{-1}\right)^t.\mathbf{h}^t. \tag{4.13}$$

4.2.3 Computational procedure

The atomic structure of montmorillonite was built as shown in Section 3.2. The negative charge of the layer was compensated by sodium or calcium interlayer cations. In addition, the interlayer space was filled by a given number n of water molecules. Table 4.1 provides the equivalence between the number n of water molecules per clay layer in the simulation cell, the number of water layers in the interlayer space, and the water content. The structural formula of the simulated layer of Na-montmorillonite was $Na_6[Si_{62}Al_2][Al_{28}Mg_4]$-$O_{160}(OH)_{32}.nH_20$ and that of the simulated layer of Ca-montmorillonite was $Ca_3[Si_{62}Al_2][Al_{28}Mg_4]O_{160}(OH)_{32}.nH_20$. Each simulation cell contained two montmorillonite layers, as shown in Figure 4.1. The energies and forces between atoms were computed with the CLAYFF force field (Cygan et al., 2004) and with periodic boundary conditions.

To determine a reference state, first we ran a molecular dynamics simulation in the NPT ensemble at a temperature $T = 300$ K and a pressure $P_{ext} = 1$ bar. The system was thermostated with Langevin dynamics with a parameter of 500 fs and the pressure was controlled with a Nosé-Hoover barostat with a parameter of 1000 fs. The system was equilibrated for 500 ps and the cell parameters were then sampled for 500 ps. The final configuration was deformed so that its cell parameters were equal to the average cell

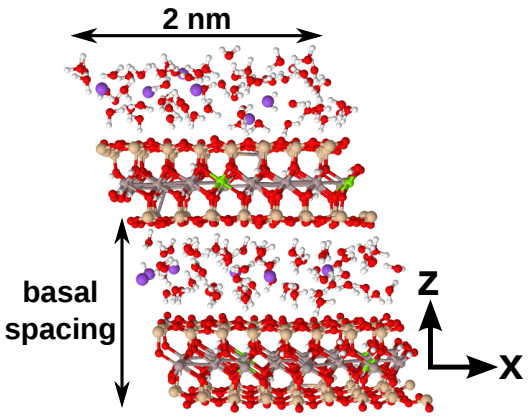

Figure 4.1: Simulation cell of a hydrated Na-montmorillonite.

parameters of the NPT run. Finally, a NVT simulation was run for 500 ps. This configuration was chosen as the reference state for strains, i.e. the box shape for which $\boldsymbol{\epsilon} = \mathbf{0}$: in the subsequent molecular dynamics simulations, strains were computed with respect to this reference. This average configuration was then used to compute the elastic constants either with the static method or with the finite temperature formula (4.5). All molecular dynamics simulations were performed with the LAMMPS package (Plimpton, 1995), in which we implemented our variation of the elastic bath method introduced in Section 4.2.2.

For the computations at 0 K, the minimization at constant pressure was performed using GULP (Gale, 1997; Gale and Rohl, 2003). All atomic coordinates and cell parameters were allowed to relax. We used the Newton-Raphson/BFGS minimization algorithm and switched to Rational Function Optimization when the norm of the gradient fell under 5×10^{-3} eV/Å in order to guarantee to find a stable minimum with a positive curvature. As the Hessian matrix is computed to minimize the energy with the Newton-Raphson method, all second derivatives of the energy with respect to strain are known, so that the elastic constants can be calculated with Equation (4.3).

For the computations at finite temperature, for each system a NPT molecular dynamics combined with our variant of the elastic bath method was run. The mechanical properties of clay minerals are very anisotropic. Clay layers

are expected to exhibit an orthotropic stiffness tensor but can be well approximated by a transversely isotropic tensor at high water contents (Ebrahimi et al., 2012). Therefore, although we computed all coefficients of the stiffness tensor, we present in this paper only results about the following relevant coefficients: C_{11}, C_{22}, C_{12}, C_{66}, C_{33}, C_{13}, C_{23}, C_{44}, and C_{55}. These 9 coefficients can be split into two groups: the in-plane coefficients C_{11}, C_{22}, C_{12}, and C_{66}, which correspond to deformation modes involving the crystalline structure of the clay layer, and the out-of-plane coefficients C_{33}, C_{13}, C_{23}, C_{44}, and C_{55}, which correspond to deformation modes involving the interlayer space. The crystalline structure of the clay layer itself is expected to be very stiff. Therefore, computing the in-plane components (i.e. C_{11}, C_{22}, C_{12}, and the shear component C_{66}) of the stiffness tensor with the fluctuation formula (4.5) did not require the use of the elastic bath method. Nevertheless, all deformation modes which stress the interlayer space are much softer, especially in presence of water, because of the discontinuity of chemical bonding between the layers. The corresponding out-of-plane coefficients of the stiffness tensor (i.e. C_{33}, C_{13}, C_{23}, C_{44}, and C_{55}) for various water contents could not be computed without the elastic bath method. Therefore, the tensor of the elastic bath was chosen so that the strain fluctuations were attenuated in the softest directions:

$$\mathbf{C}^B = \begin{bmatrix} 0 & 0 & \beta & 0 & 0 & 0 \\ & 0 & \beta & 0 & 0 & 0 \\ & & \beta & 0 & 0 & 0 \\ & & & \beta & 0 & 0 \\ & [\text{sym}] & & & \beta & 0 \\ & & & & & 0 \end{bmatrix} \tag{4.14}$$

where β is a constant taken equal to 50 GPa unless otherwise specified. The system was equilibrated for 1.5 ns and the cell parameters were then sampled for 8 ns. The strains were computed using Equation (4.4) and the stiffness tensor using Equations (4.5) and (4.7). The uncertainties were computed with the block averaging method (Frenkel and Smit, 2002), as presented in Section 3.2.

4.3 Results and discussion

4.3.1 Validation of use of the elastic bath method

Figure 4.2 displays the fluctuations of the shear strain ϵ_{yz} in function of time for Na-montmorillonite with 1 layer of water in the interlayer space (i.e. 32 water molecules by clay layer in the simulation cell) at 300 K. Without the elastic bath method, the fluctuations of the strain were too strong (up to 14 %) to apply the fluctuation formula (4.5) and compute the corresponding components of the stiffness tensor. When the water content was further increased up to 3 layers of water in the interlayer space, significant drifts of ϵ_{xz} and ϵ_{yz} were observed, making it impossible to measure the fluctuations. Figure 4.2 shows a significant attenuation of the shear strain fluctuations when the elastic bath was used with $\beta = 50$ GPa. The fluctuations remained in the small strain range and the stiffness could be computed with the fluctuation formula (4.5) and Equation (4.7). The elastic bath did not impact the fluctuations of temperature. For the simulations displayed in Figure 4.2, the average temperature was equal to 299.5 K and the standard deviation to 8.5 K without the elastic bath. With the elastic bath, the average temperature was equal to 298.9 K and the standard deviation to 8.4 K.

To ensure that the elastic bath method is reliable, we investigated the influence of the parameter β on the computed stiffness tensor. When using the elastic bath method, the stiffness of the bath had indeed to be chosen with care. The elastic bath had to be stiff enough to attenuate the fluctuations but not too stiff not to slow the convergence of the computation. Figure 4.3 displays the stiffness coefficient C_{33} (i.e. the stiffness in the direction orthogonal to the clay layers) in function of the water content for various values of β. In the dry state, we were able to compute the stiffness coefficient C_{33} without the elastic bath: the computed value was in very good agreement with the values computed with the elastic bath. In contrast, the values of C_{33} computed at 1 layer of water (i.e. about 0.09 g of water/g of dry clay) and 2 layers of water (i.e. about 0.19 g of water/g of dry clay) without the elastic bath differed significantly from the values computed with the elastic

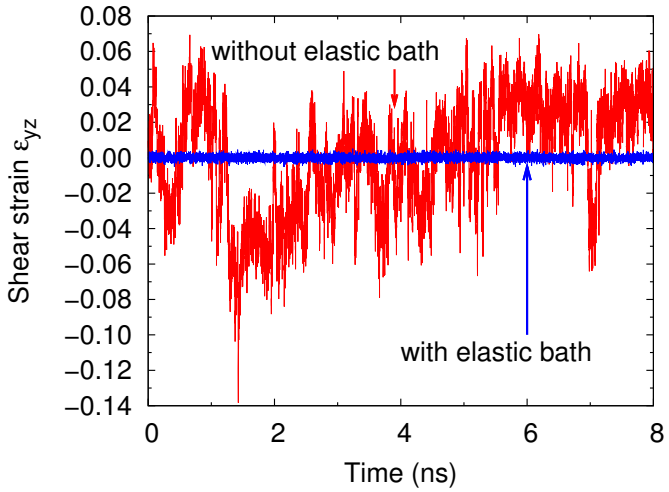

Figure 4.2: Fluctuations of the shear strain ϵ_{yz} in function of time with and without the elastic bath. The interlayer space contained 1 layer of water, the interlayer cation was sodium and the temperature was equal to 300 K.

bath. At higher water contents (i.e. more than 0.19 g of water/g of dry clay), the material was too soft in the direction orthogonal to the clay layers and the value computed for the coefficient C_{33} without the elastic bath was not measurable. This discrepancy demonstrates that the elastic bath method was really useful to compute the full stiffness tensor of a hydrated montmorillonite clay layer at finite temperature. The agreement between the results calculated for $\beta = 40$, 50 and 60 GPa was very good. In all following computations, we used $\beta = 50$ GPa.

4.3.2 Effect of water content

Table 4.2 compares our results on Na-montmorillonite to the stiffness tensors computed by Mazo et al. (2008a) for the 1-layer and the 2-layer hydrates. Our values for the in-plane coefficients C_{11}, C_{22}, C_{12}, and C_{66} were in good agreement with those of Mazo et al. (2008a). Indeed, although their methodology differed from ours, they used the CLAYFF force field to compute energies and forces within the clay layers. However, there was a significant discrepancy between our values of the coefficients C_{33}, C_{13}, C_{23},

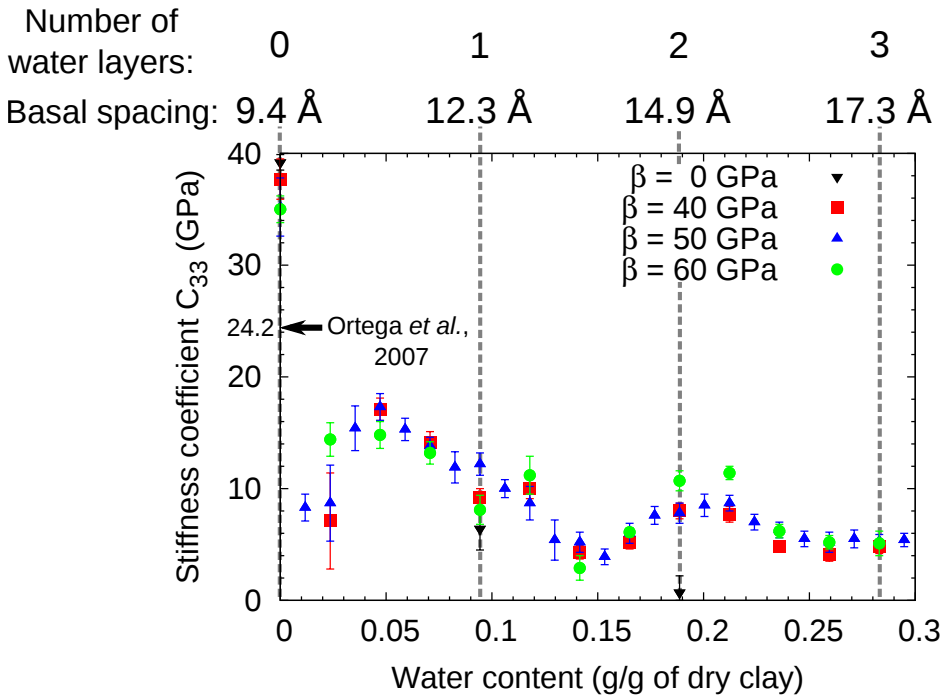

Figure 4.3: Coefficient C_{33} of the stiffness tensor at 300 K computed by molecular dynamics in function of the water content, for various values of the stiffness of the elastic bath (β = 0, 40, 50 or 60 GPa). On the top axis, we reported the typical values of the basal spacings of the 0, 1, 2, and 3-layer hydrates, computed by molecular dynamics. On the left axis, we reported the value back-calculated from ultrasonic pulse velocity data on shales by Ortega et al. (2007).

C_{44} and C_{55} of the stiffness tensor and the values computed by Mazo et al. (2008a). This difference can be explained by the use of two different water models: we used the flexible SPC model (Cygan et al., 2004) while Mazo et al. (2008a) used a flexible TIP3P model. Moreover, we used the Ewald summation to compute the long-range coulombic interactions, as required by CLAYFF (Cygan et al., 2004), while Mazo et al. (2008a) did not consider any interaction beyond a cut-off radius equal to 1.25 nm.

Figure 4.4 displays all stiffness coefficients, at 0 K and 300 K, for both Na-montmorillonite and Ca-montmorillonite, as a function of water content. Figure 4.4-a and Figure 4.4-d display the in-plane components of the stiffness tensor for Na-montmorillonite and for Ca-montmorillonite, respectively.

	This study				Mazo et al. (2008a)	
	0 layer	1 layer	2 layers	3 layers	1 layer	2 layers
C_{11}	292.3	217.0	186.8	160.1	231	189
C_{22}	274.2	208.7	177.2	151.7	229	191
C_{12}	132.4	101.1	86.5	75.6	105	84
C_{33}	35.2	12.2	7.8	5.3	80	62
C_{13}	17.0	3.9	3.4	4.1	17	6
C_{23}	17.3	3.9	3.6	3.5	15	5
C_{44}	10.6	1.7	1.6	0.2	21	2
C_{55}	18.5	1.9	0.3	0.9	22	4
C_{66}	82.3	61.5	52.5	44.7	68	56

Table 4.2: Components of the stiffness tensor of Na-montmorillonite at 300 K in GPa, when the clay contains 0, 1, 2, or 3 layers of water.

Those coefficients decreased slightly with temperature, which is typical for crystalline materials. Moreover, Figure 4.4-a and Figure 4.4-b showed no effect of the interlayer cation. Indeed, the interlayer cation did not affect the structure of the crystalline clay layers and therefore their stiffness. Our values were much greater than the in-plane coefficients measured on clay particles of shales by Ortega et al. (2007), who back-analyzed ultrasonic pulse velocity data with a micro-mechanical model. They reported the following values: $C_{11} = 44.9$ GPa and $C_{12} = 21.7$ GPa. Sliding of clay layers on each other within clay particles could be responsible for this discrepancy (Ebrahimi et al., 2012).

Figure 4.4-b and Figure 4.4-e display the coefficients C_{33}, C_{13} and C_{23} of the stiffness tensor for Na-montmorillonite and for Ca-montmorillonite, respectively. Figure 4.3 and Figure 4.4 show that the water content impacted strongly the out-of-plane elastic properties of clays. For Na-montmorillonite, the coefficient C_{33} (i.e. the stiffness normal to the plane of the clay layer) dropped from 35.2 GPa in the dry state to 8.3 GPa as soon as a few water molecules entered in the interlayer space. Then, with increasing water content, the coefficient C_{33} reached a maximum of 17.3 GPa before the first water layer was completely formed at 0.09 g of water/g of dry clay, and a minimum of 3.9 GPa before the second water layer was completely formed at 0.19 g of water/g of dry clay. Finally, the coefficient C_{33} stabilized to

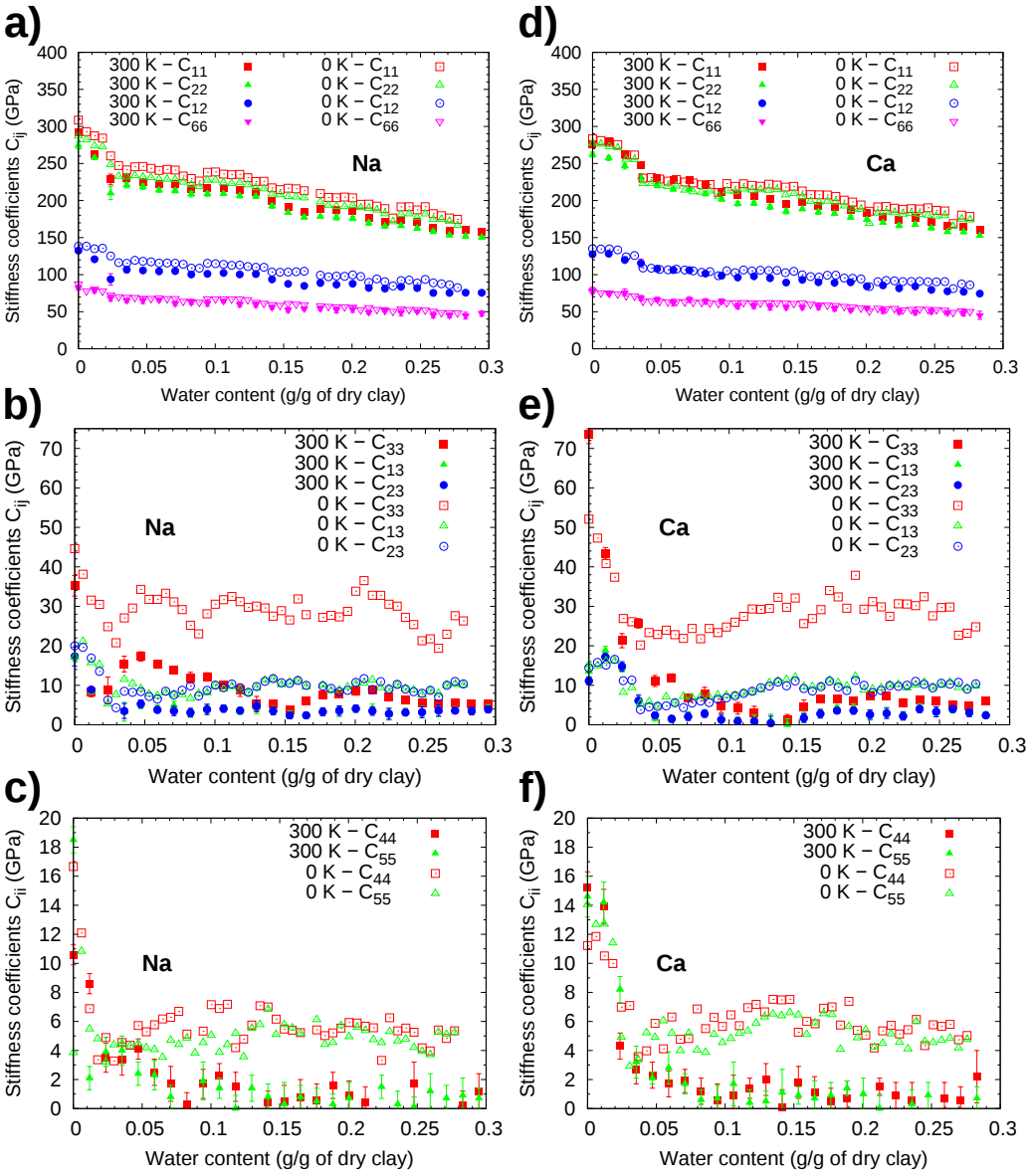

Figure 4.4: Coefficients of the stiffness tensor in function of the amount of water in the interlayer space at 0 and 300 K with Na (a, b and c) or Ca (d, e and f) interlayer cations: (a and d) in-plane coefficients C_{11}, C_{22}, C_{12} and C_{66}, (b and e) out-of-plane coefficients C_{33}, C_{13} and C_{23}, and (c and f) out-of-plane shear coefficients C_{44} and C_{55}.

5.4 GPa when the third water layer was formed, which happened at 0.28 g of water/g of dry clay. For the coefficient C_{33} Ortega et al. (2007) reported

a value of 24.2 GPa, which is close to the values we computed in the driest states. However, Ortega et al. (2007) computed the stiffness tensor of the clay matrix of shales, which is made of smectite, illite and kaolinite. In contrast with smectite, kaolinite does not adsorb water and illite adsorbs water poorly. Therefore, they are expected to be stiffer in the direction orthogonal to the layers than smectite. Therefore, the value reported by Ortega et al. (2007) may not be representative of values for pure monoionic montmorillonite. To our knowledge, no experimental anisotropic elastic data are available on monoionic smectites.

At 300 K, Na-montmorillonite and Ca-montmorillonite exhibited identical behaviors for water contents higher than 0.15 g/g of dry clay. In the dry state and for low water contents (i.e. up to 0.04 g/g of dry clay), Ca-montmorillonite was much stiffer in the z-direction than Na-montmorillonite: the coefficient C_{33} for dry Ca-montmorillonite was indeed equal to 73.5 ± 2.3 GPa while it was equal to 35.2 ± 2.6 GPa for Na-montmorillonite. In contrast, Ca-montmorillonite was softer in the z-direction than Na-montmorillonite for water contents between 0.05 and 0.15 g/g of dry clay.

Figure 4.4-c and Figure 4.4-f display the shear coefficients C_{44} and C_{55} of the stiffness tensor upon hydration. Na-montmorillonite and Ca-montmorillonite exhibited identical behaviors. Because water acts like a lubricant, the shear stiffness dropped from values between 10.6 and 18.5 GPa in the dry state to values between 0 and 2 GPa for water contents greater than 0.05 g/g of dry clay. The value reported by Ortega et al. (2007) for the coefficient C_{44} was equal to 3.7 GPa and was in good agreement with the value we computed at very low water contents.

Figure 4.5 displays the in-plane stiffness coefficients C_{11}, C_{22}, C_{12}, and C_{66} multiplied by the basal spacing for Na-montmorillonite at 300 K. This Figure shows that this product was independent of water content. Therefore, the decrease of the in-plane coefficients of the stiffness tensor with water content (which was observed in Figure 4.4) is a geometric effect due to the swelling of the interlayer space. In a low hydrated state and in a high hydrated state, forces needed to apply a given strain in a direction parallel to the clay layer are identical, because those forces are mostly supported by the crystalline

structure of the clay and not by the interlayer water. However, the area on which this force is applied is proportional to the basal spacing. Therefore, the stress needed to apply a given strain is inversely proportional to the basal spacing, and such is the corresponding coefficient of the stiffness tensor.

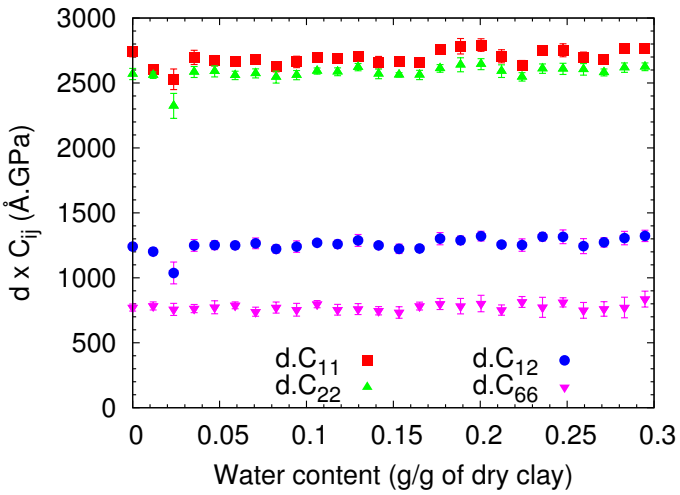

Figure 4.5: In-plane stiffness coefficients C_{ij} multiplied by the basal spacing d as a function of water content for Na-montmorillonite at 300 K.

This geometric effect did not explain the variations of the out-of-plane coefficients C_{33}, C_{13}, C_{23}, C_{44}, and C_{55} of the stiffness tensor with water content. Indeed, the surfaces on which forces are applied for these deformation modes are parallel to the clay layer and their area does not vary with basal spacing and thus with water content. The out-of-plane coefficients were very sensitive to water content because water impacts strongly the interactions between the clay layers.

In Table 4.3, we report the Young's and shear moduli of the montmorillonite layers in various hydration states computed from the stiffness tensor by assuming the material to be isotropic transverse. $\overline{E}$ and G_{xy} are the Young's and shear moduli, respectively, in the plane of the layers and are given by $\overline{E} = \frac{1}{2}\left(S_{11}^{-1} + S_{22}^{-1}\right)$ and $G_{xy} = S_{66}^{-1}$, where S_{ij} are the coefficients of the compliance tensor $\mathbf{S} = \mathbf{C}^{-1}$. E_z and $\overline{G}$ are the Young's and shear moduli in the direction orthogonal to the layer and are given by $E_z = S_{33}^{-1}$ and $\overline{G} = \frac{1}{2}\left(S_{44}^{-1} + S_{55}^{-1}\right)$.

Interlayer cation	Na			Ca		
Number of water layers	0	1	2	0	1	2
$\overline{E}$ (in GPa)	215	164	140	206	159	136
G_{xy} (in GPa)	80	61	52	78	60	51
E_z (in GPa)	33	12	7.5	71	5.2	5.9
$\overline{G}$ (in GPa)	14.2	1.3	0.9	14	1.0	0.6

Table 4.3: Isotropic transverse moduli of montmorillonite containing 0, 1, or 2 layers of water computed by molecular simulations.

Figure 4.6 shows estimations with the VRH approximation of the bulk modulus and the shear modulus of Na- and Ca-montmorillonite at 300 K upon hydration. Both montmorillonites exhibited the same shear behavior. For two sodium-rich montmorillonites (i.e. Swy-1 and Swy-2), Wang et al. (2001) measured shear moduli of 16.4 ± 2 GPa and of 20.3 ± 4 GPa, respectively. For two calcium-rich montmorillonites (i.e. STX-1 and SAz-1), they measured shear moduli of 24.4 ± 2 GPa and of 17.1 ± 1 GPa. The shear moduli we computed at low water content (between 15 and 30 GPa) are in good agreement with these experimental values. The samples used by Wang et al. (2001) were supposed to be dry. However, the water content was not controlled and water could have been adsorbed in the interlayer space when in contact with the ambient atmosphere. Moreover, the samples were not monoionized. For the bulk moduli, Wang et al. (2001) measured values equal to 29.7 ± 4 GPa and 34.7 ± 5 GPa for the two sodium-rich clays, and to 49.6 ± 3 GPa and 37.8 ± 3 GPa for the two calcium-rich clays. The bulk moduli we computed at low water content were higher because we overestimated the in-plane coefficients, as will be discussed in the next subsection. However, the order of magnitude we obtained is the same as the one measured by Wang et al. (2001). Like Wang et al. (2001), we observed that, in the driest states, Ca-montmorillonite was stiffer than Na-montmorillonite.

In Figure 4.6, we plotted the macroscopic elastic moduli in function of water content, because water content is the control variable of the hydro-mechanical behavior of swelling clays as shown in Section 2.3.1. However, most experiments are performed at a controlled relative humidity. To obtain the experimental elastic moduli as a function of water content, one has to

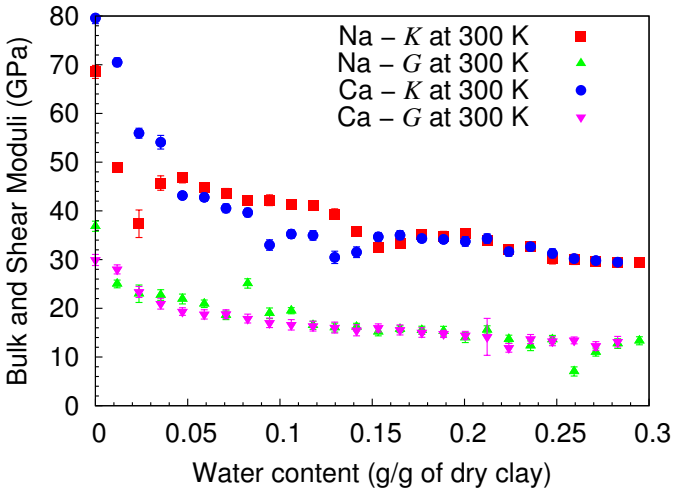

Figure 4.6: Bulk modulus K and shear modulus G of an isotropic montmorillonite polycrystal at 300 K with Na or Ca interlayer cations.

combine the mechanical data of our work with adsorption isotherms, such as those presented in Figure 2.8 for self-supporting clay films.

4.3.3 Effect of temperature

Figure 4.4 displays the coefficients of the stiffness tensor computed both at 300 K by molecular dynamics and at 0 K by minimization in function of water content. Two categories of coefficients of the stiffness tensor, i.e. the in-plane and the out-of-plane coefficients, exhibited very different features when temperature was increased from 0 K to 300 K. The in-plane coefficients (i.e. C_{11}, C_{22}, C_{12}, and C_{66}) were slightly lower at 300 K than at 0 K while the out-of-plane coefficients (i.e. C_{33}, C_{13}, C_{23}, C_{44}, and C_{55}) were very sensitive to temperature. For instance, at high water contents, the stiffness C_{33} computed at 0 K was approximately 4 times as large as when computed at 300 K. This significant discrepancy between the results at 0 K and 300 K highlights the need to compute the stiffness of such hydrated materials at finite temperature in order to get meaningful results.

In Table 4.4 we report our values of the in-plane Young's moduli E_x and E_y and of the in-plane shear modulus G_{xy} of a dry Na-montmorillonite

	Minimization - 0 K	DFT by Zartman et al. (2010)	MD - 300 K
E_x	235	160	221
E_y	218	160	210
G_{xy}	83	71	80

Table 4.4: Comparison of the values of the in-plane moduli of montmorillonite layers we computed by minimization at 0 K and by Molecular Dynamics (MD) at 300 K with the values computed with DFT by Zartman et al. (2010).

at 0 K and 300 K, and the values estimated by Zartman et al. (2010) by DFT calculations on pyrophyllite and mica, which should be representative of values at 0 K. citetZartman2010 reported a good agreement between their DFT results on mica and experimental measurements on macroscale single mica crystals. The accuracy of the estimates lay within ± 10 %. The in-plane elastic moduli were computed from the stiffness tensor with:

$$E_x = \frac{1}{S_{11}} \text{ and } E_y = \frac{1}{S_{22}}. \tag{4.15}$$

With respect to DFT calculations, our simulations overestimated the values of the in-plane elastic moduli. This systematic overestimation of 17 % for the in-plane shear modulus and of 36 to 47 % for the in-plane Young's moduli is due to the CLAYFF force field. Indeed, the interaction parameters of CLAYFF were fitted on structural parameters and not on second-order properties such as elastic properties (Cygan et al., 2004). To improve the quality of the numerical predictions, Shahsavari et al. (2011) re-parametrized CLAYFF including the full DFT elastic tensor in the fitting data set in order to compute the elastic properties of calcium silicate hydrates. However, re-parameterizing CLAYFF using second-order properties while keeping its universality for clay minerals remains a challenging work.

Figure 4.7-a displays the in-plane elastic coefficients C_{11} and C_{12} of Na--montmorillonite in function of temperature for various hydration states: those coefficients decreased linearly with temperature. A similar trend was reported by Teich-McGoldrick et al. (2012) for muscovite. More generally, the Young's moduli of crystalline materials such as metals have long been known to decrease linearly with temperature (Brillouin, 1940). Increasing

the temperature causes the average distance between atoms to increase and therefore the force between two atoms and the derivative of this force with respect to the distance between atoms to decrease.

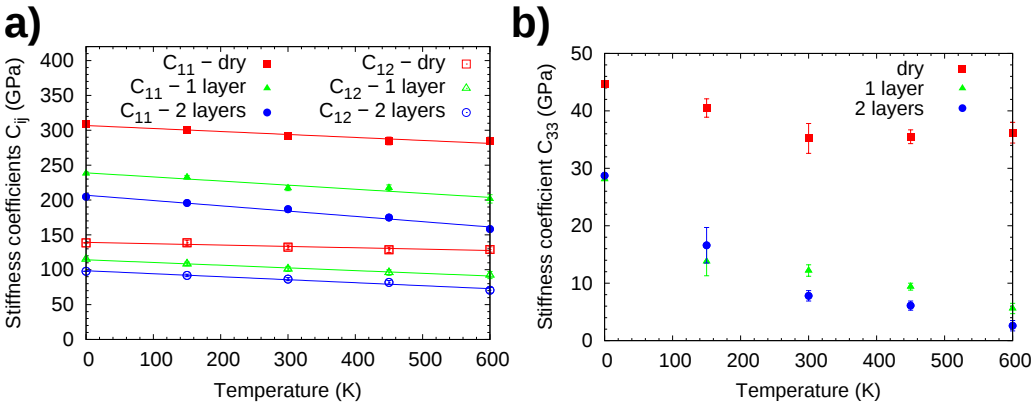

Figure 4.7: Coefficients C_{11} and C_{12} (a) and coefficient C_{33} (b) of the stiffness tensor of Na-montmorillonite in function of temperature for various water contents in the clay layer (i.e. 0, 1, and 2 layers of water). The solid lines on Figure a) are linear fits of the data.

Figure 4.7-b displays the elastic coefficient C_{33} (i.e. the stiffness normal to the plane of the clay layers) in function of temperature for various hydration states. A very significant drop of this coefficient was observed between 0 K and 300 K for all hydration states: the coefficient C_{33} decreased by 21 %, 57 %, and 73 % for the 0-layer, 1-layer, and 2-layer hydrates, respectively. Between 300 K and 600 K, the value of the coefficient C_{33} did not change for the dry clay and decreased less (by about 20 %) for the 1-layer and the 2-layer hydrates than between 0 K and 300 K. The effect of temperature on this coefficient was much greater than on the in-plane elastic coefficients. Moreover, this effect was all the stronger that the amount of water in the interlayer space was great.

Figure 4.7 confirms that the two categories of coefficients of the stiffness tensor, i.e. the in-plane and the out-of-plane coefficients, behaved very differently with temperature. The mechanisms of elasticity in the in-plane and in the transverse directions are indeed very different. The montmorillonite layer itself exhibits a slightly defective crystalline structure. The displacement of

each atom within the layer is very small and the variations of the elastic coefficients with temperature are small. Therefore, the elastic behavior of the montmorillonite layer is governed by enthalpic elasticity. In contrast, in the transverse direction, the displacements of the atoms can be very significant. The interlayer cations and the water molecules are free to move in the interlayer space. Moreover, the clay layers can move with respect to each other and the elastic coefficients are very sensitive to temperature, since there is no covalent bonding in this direction. The nature of the interactions responsible for the cohesion in this direction is not as simple as in the in-plane direction: hydrogen bonds between water molecules and between water molecules and the external oxygen atoms of the clay layers, long-range electrostatic interactions between cations, water and clay layers, short-range steric repulsion and entropic repulsion are all involved in the cohesion mechanisms. We showed in Chapter 3 that fluctuations of the ionic concentration in the interlayer space result in an instantaneous polarization which gives rise to an attractive ionic fluctuation interaction. These fluctuations of ionic density cannot be captured by simulations at 0 K. Thus, the behavior of the system is governed by a competition between repulsive entropic forces and attractive energetic forces (Jönsson and Wennerström, 2004; Pellenq et al., 1997). This complex origin of the cohesion between the clay layers makes it impossible to predict realistic elastic properties at 300 K, in particular the ones in the out-of-plane direction, by performing computations at 0 K.

Table 4.5 reports the linear thermal expansion coefficient in each direction. The in-plane expansion coefficients did not depend on the water content and were on average equal to $1.0 \pm 0.2 \times 1.10^{-5}$ K^{-1}. In the dry state, in the out-of-plane direction, the linear expansion coefficient was three times as high as in the in-plane direction and was not measurable in the hydrated states. Indeed, the basal spacing was not a linear function of temperature for the monolayer and the bilayer hydrates. Our values in the dry state are close to those computed for muscovite by Teich-McGoldrick et al. (2012) with molecular dynamics (i.e. 1.43, 1.30, and 3.02×1.10^{-5} K^{-1} in the x, y, and z directions, respectively) and measured experimentally by Pavese et al. (1999) (i.e. 0.83, 1.00, and 2.13×1.10^{-5} K^{-1} in the x, y, and z directions, respec-

	dry state	1 layer of water	2 layers of water
α_x	0.96	0.75	0.95
α_y	0.88	1.16	1.13
α_z	2.95	-	-

Table 4.5: Linear thermal expansion coefficients for various hydration states in the range of 150 K to 600 K ($\times 1.10^{-5}$ K^{-1}).

tively). Muscovite has an atomic structure which is slightly different from montmorillonite; in particular, the surface charge of muscovite is twice as high as the one of montmorillonite. However, to our knowledge, similar data for smectites are not available in the literature.

4.3.4 Effect of hydrostatic confining stress

All results presented in the previous subsections were obtained with molecular dynamics simulations performed at a hydrostatic confining stress equal to 1 bar. This subsection is dedicated to the investigation of the effect of the compressive confining stress on the elastic properties of Na-montmorillonite at 300 K. We will now refer to the hydrostatic compressive stress as to the confining stress. We chose values of the confining stress P_{ext} in the range 0.1 MPa to 10 GPa. In the range 0.1 MPa to 100 MPa, confining stress has very little effect on the cell parameters and the elastic coefficients of montmorillonite layers. Therefore, we had to increase the confining stress to unrealistic values up to 10 GPa.

Figure 4.8-a displays the a axis of Na-montmorillonite (i.e. a cell parameter in the plane of the layer) in function of the confining stress for various water contents. The change in the b axis is not plotted but exhibited very similar features. For all water contents, the cell parameter a decreased slightly (by about 1 % between 0.1 MPa and 10 GPa) with confining stress. Figure 4.8-b displays the basal spacing in function of the confining stress. For all water contents, the change in the basal spacing with the confining stress was quite linear up to 2 GPa. Between 0.1 MPa and 10 GPa, the relative variation in the basal spacing was much greater than the relative variation of the cell parameter in the in-plane directions and was all the more significant

than the water content was high: the basal spacing decreased by about 7 %, 16 %, and 23 % with 0, 1, and 2 layers of water, respectively.

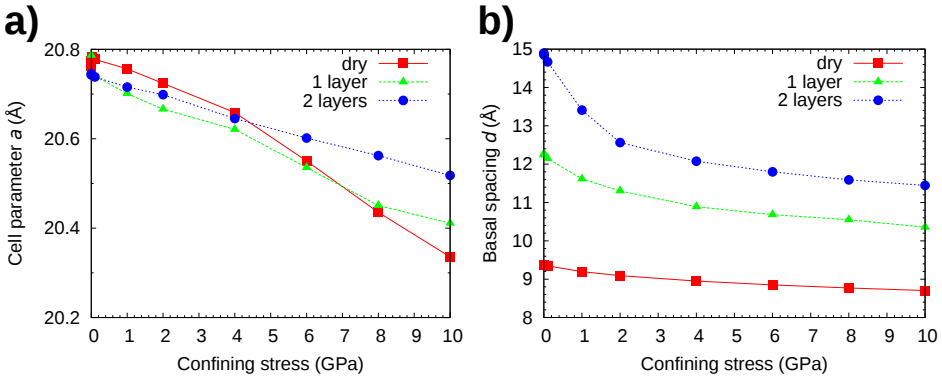

Figure 4.8: (a) Cell parameter a and (b) basal spacing d of Na-montmorillonite at 300 K in function of the confining stress for various water contents (i.e. 0, 1, and 2 layers of water).

Figure 4.9 displays the coefficients of the stiffness tensor of Na-montmorillonite at 300 K as a function of confining stress. Figure 4.9-a shows the evolution of the in-plane coefficients C_{11} and C_{12} with confining stress. The other in-plane coefficients exhibited similar features. Only the stiffness coefficients of the 2-layers hydrate were strictly increasing over the entire range of pressures. In the dry state, the coefficients increased for confining stresses between 0 GPa and 4 GPa and then decreased for confining stresses between 4 GPa and 10 GPa. With 1 layer of water, the coefficients increased with confining stress and reached a plateau at confining stresses higher than 4 GPa. Figure 4.9-b displays the out-of-plane coefficient C_{33} versus confining stress. The increase of C_{33} between 0 GPa and 10 GPa was very significant: for instance, in the dry state, C_{33} increased from 35 GPa to 226 GPa. Figure 4.9-c displays the out-of-plane shear coefficients C_{44} and C_{55} as a function of confining stress. The coefficients C_{55} of the 0, 1 and 2-layer states increased from 19 GPa to 59 GPa, from 1.9 GPa to 30 GPa, and from 0.3 GPa to 18 GPa, respectively. For the dry state, the discrepancy between the coefficients C_{44} and C_{55} became very significant when the confining stress was increased: at 10 GPa, the coefficient C_{44} was equal to 23 GPa while the coefficient C_{55} was equal to 59 GPa.

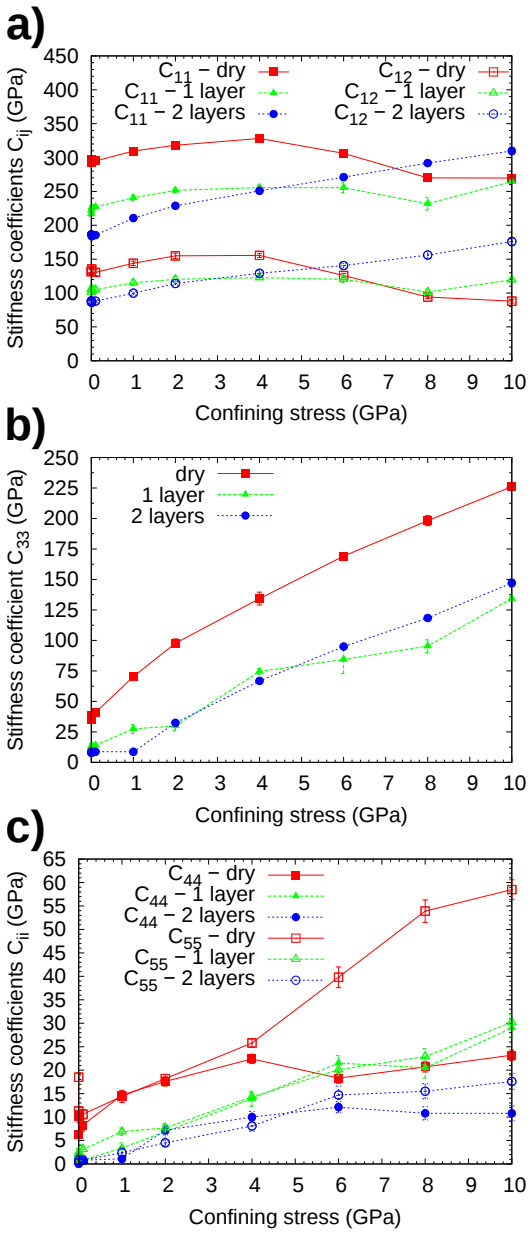

Figure 4.9: (a) In-plane coefficients C_{11} and C_{12}, (b) out-of-plane coefficient C_{33}, and (c) out-of-plane coefficients C_{44} and C_{55} of the stiffness tensor of Na-montmorillonite at 300 K in function of the confining stress for various water contents.

Figure 4.10 displays the bulk modulus and the shear modulus of the clay layer as a function of confining stress. We recall that those moduli were

estimated with the VRH estimate. All bulk moduli increased with confining stress, but at paces that depended on their water content. Compared to the dry clay and to the 1-layer hydrate, the bulk modulus of the 2-layer hydrate was the lowest at 0 GPa but was the largest at 10 GPa. All shear moduli increased in a roughly linear manner, at a pace that was roughly independent of the water content.

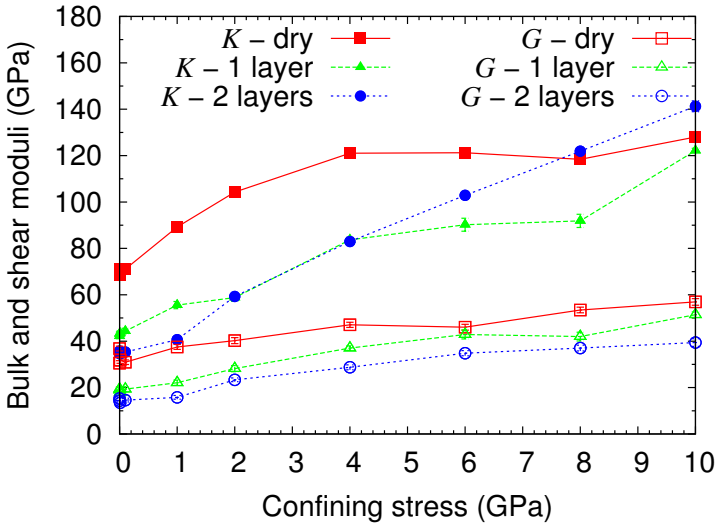

Figure 4.10: Bulk modulus K and shear modulus G of Na-montmorillonite at 300 K in function of confining stress at various water contents (i.e. 0, 1, and 2 layers of water).

4.4 Conclusion

In this Chapter, we reported values for all relevant components of the stiffness tensor of montmorillonite upon hydration. We succeeded in computing the stiffness of hydrated montmorillonite at finite temperature by implementing the elastic bath method. The out-of-plane stiffness coefficients computed by minimization at 0 K or by molecular dynamics at 300 K differed significantly from each other. This discrepancy demonstrates that the elastic properties of montmorillonite at finite temperature cannot be inferred from computations at 0 K.

The coefficients of the stiffness tensor of montmorillonite could be split into two groups: the in-plane coefficients (i.e. C_{11}, C_{22}, C_{12} and C_{66}) and the out-of-plane coefficients (i.e. C_{33}, C_{13}, C_{23}, C_{44} and C_{55}). Indeed, because of the layered structure of clay, the behaviors in the plane of the layer and in the direction orthogonal to the layer are governed by very different interactions. The in-plane coefficients were not very sensitive to temperature and to water content. Their slight decrease with water content could be entirely explained by the geometric effect of the swelling of the interlayer space. In contrast, the out-of-plane coefficients decreased significantly with temperature and water content. The interlayer cation, here Na^+ or Ca^{2+}, impacted the out-of-plane coefficients only in the low hydrated states. Moreover, the out-of-plane coefficients increased very significantly when the hydrostatic confining stress was increased up to 10 GPa, while the in-plane coefficients did not.

Building a relevant hydro-mechanical constitutive law at the scale of the engineer remains a challenge. The modeling of clay-based materials at the macroscopic scale requires the use of specific homogenization tools and a deep knowledge of their complex multiscale structure. Moreover, water is adsorbed not only in the interlayer space but also in the mesopores and the macropores. Therefore, deformation mechanisms at the scales of the particles or of the aggregates and the effect of water on these mechanisms need also to be studied. Although we showed that the interlayer cation did not impact significantly the mechanical behavior at the scale of the clay layer, the size and the arrangement of clay particles, and therefore the mechanical

properties at the mesoscale, are highly dependent on the nature of the cation (Shomer and Mingelgrin, 1978; Schramm and Kwak, 1982), as was shown in Chapter 3. In the next Chapter, we will investigate the elastic properties of clays at the mesoscale by performing tensile tests on well-ordered clay films. In particular, we will focus on the impact of water content and of the nature of the interlayer cation on those elastic properties.

Chapter 5

Effect of water content on the elastic properties of clay films

---

THIS CHAPTER *presents the measurement of the elastic properties of the clay films described in Chapter 2. We designed an original experimental device that makes it possible to perform tensile tests on clay films under controlled relative humidity. The samples were stressed in tension in the plane of the clay films in order to focus on the deformation mechanisms parallel to the clay layers. To measure the deformations of these very fragile samples, we needed to use a contact-free method: we used digital image correlation techniques to measure the overall deformation of the samples. We showed that this experimental setup makes it possible to measure the global deformation with a good accuracy. The samples exhibited an elastoplastic behavior. We investigated the effect of the interlayer cation and of the water content on the elastic properties of the films. In particular, we highlighted the decrease of Young's modulus with water content. Also, the Ca-exchanged montmorillonite films were stiffer than the Na-exchanged montmorillonite films and their Young's moduli were more sensitive to water content. Finally, we compared the experimental results at the scale of the films with the results obtained with molecular simulations at the scale of the clay layers and presented in Chapter 4.*

Ce Chapitre *présente la mesure des propriétés élastiques des films fins d'argile présentés au Chapitre 2. Nous avons conçu un dispositif expérimental original qui permet de solliciter en traction des films d'argile à humidité contrôlée. Les échantillons étaient sollicités en traction dans le plan des films d'argile afin d'isoler les mécanismes de déformation parallèles aux feuillets d'argile. Afin de pouvoir mesurer la déformation de ces échantillons très fragiles, nous avons du utiliser une méthode sans contact : nous avons employé les techniques de corrélation d'image afin de mesurer la déformation globale des échantillons. Nous avons montré que ce montage expérimental permettait de mesurer la déformation globale avec une bonne précision. Les échantillons avaient un comportement élastoplastique. Nous avons étudiés l'effet du cation interfoliaire et de la teneur en eau sur les propriétés élastiques des films. En particulier, nous avons mis en évidence la diminution du module d'Young avec la teneur en eau. De plus, les films de montmorillonite calcique étaient plus raides que les films de montmorillonite sodique et leur module d'Young était plus sensible à la teneur en eau. Enfin, nous avons comparé les résultats obtenus expérimentalement à l'échelle des films avec les résultats obtenus par simulations moléculaires à l'échelle du feuillet d'argile et présentés dans le Chapitre 4.*

Contents

5.1 Introduction

The macroscopic mechanical properties of clay-based materials are known to be sensitive to relative humidity. Figure 1.10 displays the stress-strain relations obtained by uniaxial compression tests on argillite at various relative humidities (Bornert et al., 2010): the clayey rocks exhibit a softening with increasing relative humidity. In Chapter 4, we investigated the elastic properties of clay layers in function of water content using molecular dynamics. We highlighted and quantified the decrease of some stiffness components with water content. However, upscaling the hydromechanical properties from the scale of the clay layer to the scale of the engineer in order to build predictive macroscopic constitutive laws is a challenging work. As displayed in Figure 1.8, clayey rocks exhibit a complex multiscale structure from the nanometer to the meter. Therefore, the gap between properties at the scale of the clay layer (that we computed in the previous Chapter) and properties at the macroscopic scale is huge. In order to overcome this gap, we proposed an intermediate step consisting in investigating the hydromechanical

properties of mesoscopic model materials, i.e. self-standing clay films. In Chapter 2, we presented the measurement of the humidity-induced swelling of these films. The present Chapter is devoted to the study of their short-term hydromechanical properties.

We performed tensile experiments on clay films. Zabat (1996) performed such tests at ambient relative humidities. In contrast, in our work, we controlled the relative humidity during the tests in order to investigate the impact of humidity on the elastic properties of the films. The clay films were stressed in tension in a direction parallel to the plane of the films, as shown in Figure 5.1. The rationale for doing so is to focus on deformation mechanisms in the plane parallel to the clay layers.

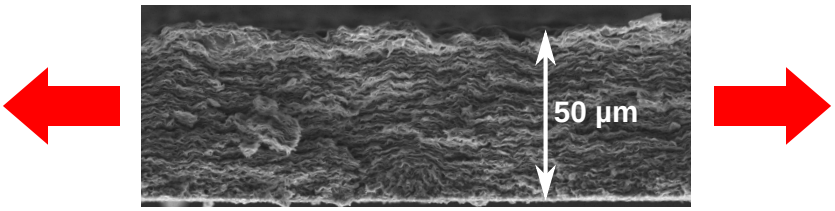

Figure 5.1: Tensile testing of clay films.

In the literature, one can find that montmorillonite-based films were also investigated to make films which mimic the mechanical properties of nacre (Wang et al., 2012; Walther et al., 2010; Bennadji-Gridi et al., 2006). Nacre is a layered composite material made of mineral platelets (called aragonite) separated by a biopolymer. Nacre can be found within the shell of some molluscs or as the coating of pearls. Its mechanical properties are remarkable because of its unique organic-inorganic and brick-and-mortar composite structure: nacre is stiff and very tough. Phyllosillicates, and montmorillonite in particular, are extensively used to prepare materials with mechanical properties similar to those of nacre (Wang et al., 2012). For instance Walther et al. (2010) intercalated polymers between clay platelets to make films on which they performed tensile tests: they measured elastic and strength properties close to those of real nacre. Bennadji-Gridi et al. (2006) also prepared Na,Ca-montmorillonite films on which they performed bending tests: they measured a bending strength equal to 120 MPa, which is comparable to the

one of other man-made nacre-like structured materials, but lower than the one of natural nacre (which is around 190 MPa). In our work, we prepared similar montmorillonite films, on which we performed tensile tests.

In the second Section of this Chapter, we present the experimental setup we used to perform tensile tests under controlled relative humidity and the methods we used to measure the elastic properties of the films. The results of these tests are presented in the third Section and discussed in the fourth Section with regards to the results of the molecular simulations obtained in Chapter 4.

5.2 Experimental methods

The materials we used for the tensile tests are those described in Chapter 2: a natural montmorillonite (coined Swy-2-raw) which contains both sodium and calcium interlayer cations, a Ca-saturated montmorillonite (coined Swy-2-Ca), and two Na-saturated montmorillonites (coined Swy-2-Na and Cloisite-Na). Films were prepared according to the procedure described in Section 2.2.

5.2.1 Tensile tests

First, in each prepared film, samples which were 93-mm-wide and 80-mm-long were cut with sharp blades. The ends of each sample were reinforced with sandpaper before being placed in the grips of the tensile test machine. The free length of the sample was equal to 50 mm. Figure 5.2 displays the setup of the sample in the tensile test apparatus.

The tensile tests were carried out under controlled relative humidities in an environmental chamber made of PMMA and built around the testing machine, as shown in Figure 5.2. The relative humidity was controlled with saturated salt solutions. However, the environmental chamber we used was not perfectly air-tight because the tensile test machine had to go through the upper panel. Therefore, compressed air was blown into a salt solution so that it reached the desired relative humidity. The humidified air was then in-

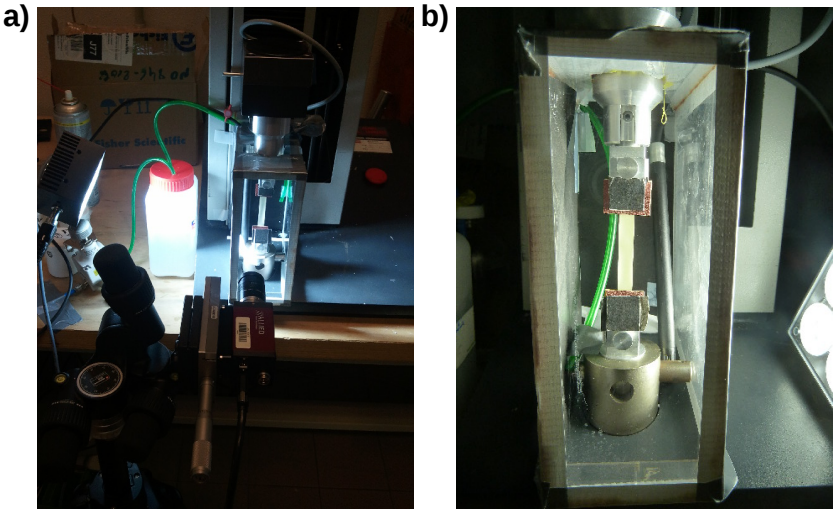

Figure 5.2: Pictures of the tensile test experimental setup: (a) overall view and (b) sample in the grips of the tensile test machine.

jected in the environmental chamber. Thus, the pressure in the chamber was slightly higher than in the room and the relative humidity in the chamber was less sensitive to leaks than if no overpressure had been applied. Moreover, by doing so the equilibration of the chamber required only about 30 minutes. The relative humidity and temperature were recorded continuously with a thermo-hygrometric sensor. Since our samples were only a-few-dozen-microns-thick, the equilibration of the films with the relative humidity in the environmental chamber required only one hour.

During the tensile tests, we controlled the displacement of the upper grip to perform one or two loading-unloading cycles. A force sensor recorded continuously the force with an accuracy of 1 mN. Our samples were very thin and very fragile and could not be instrumented with gauges. Therefore, we measured strains by using digital image correlation (DIC), which has the advantage to be a contact-free technique and was introduced in Section 2.2.3. Figure 5.2-a shows the digital imaging setup during a tensile test. Figure 5.3 displays a global schematic diagram of the experimental setup.

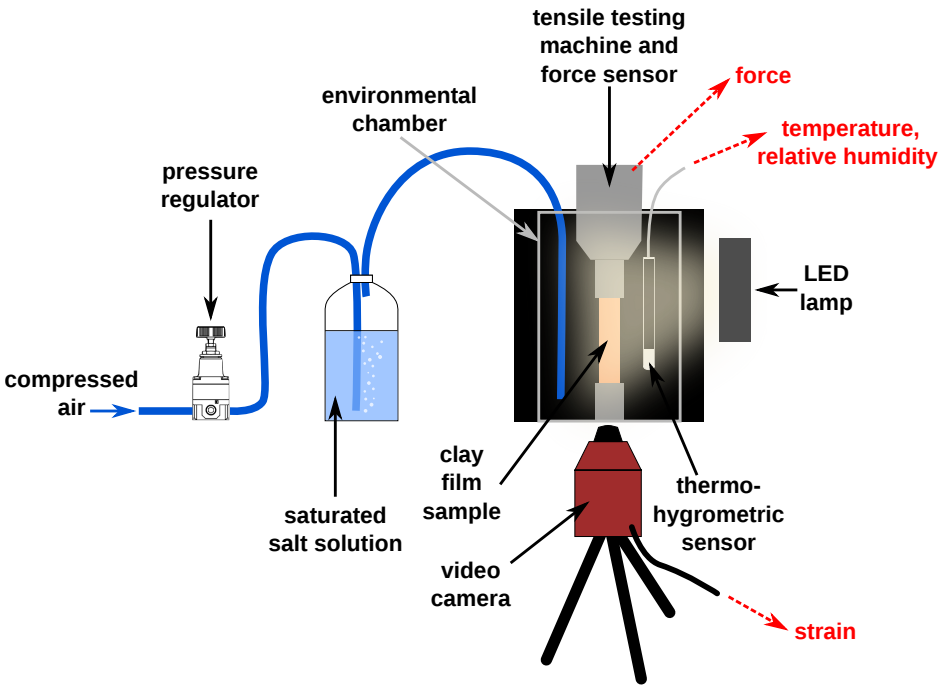

Figure 5.3: Experimental setup for the tensile testing of clay films under relative humidity control.

5.2.2 Measurement of elastic properties

To take images of the samples during the tests, a Pike ALLIED Technology camera was used. The CCD sensor was 2048×2048-pixels-wide and the gray levels were encoded on 8 bits. We used the software Coriander to control the camera and the software dcamaqx to acquire the images (this latter being developed by M. Bornert). Figure 5.4 displays an image of a film taken during a test and a zoom on the texture of the surface. To improve the contrast of the images, carbon powder was scattered all over the surface. During experiments at ambient relative humidity, we used a Pike ALLIED Technology camera with a lower resolution: the CCD sensor was 1388×1038-pixels-wide.

The images were acquired continuously during the tests at a minimum interval of 25 ms. All images were then analyzed by DIC, as described in Section 2.3 of Chapter 2. We used 30-pixels-wide correlation windows and subpixel optimization. The physical size of a correlation window was 730 μm

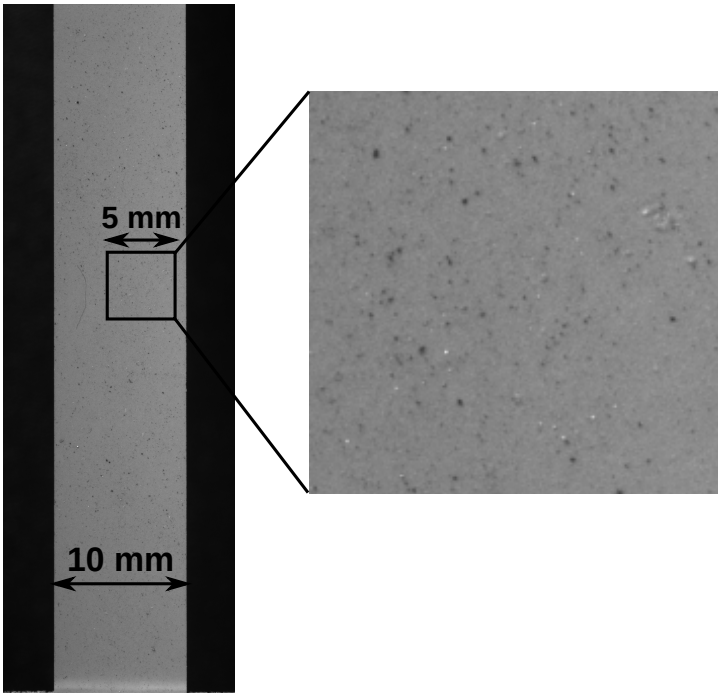

Figure 5.4: Image of a sample during a tensile test and zoom on the texture of the surface. The image of the unzoomed sample is 2048-pixels high.

with the higher resolution camera. With the lower resolution camera, the physical size of the correlation window was 1 mm.

Figure 5.5-a displays the strain computed by DIC over two loading-unloading cycles. The measurement of the force (Figure 5.5-b) was synchronized with the measurement of the strain by matching the maxima of the two sets of data. Figures 5.5-c and -d show the force-strain curves for the two loading-unloading cycles. The slopes of the two unloading curves are in very good agreement with each other: 638 $\pm$ 17 N for the first one and 622 $\pm$ 15 N for the second one.

To compute the Young's modulus of the clay films, we used the slope of the unloading portion of the force-strain curve, together with the section of the sample at any relative humidity. To estimate this section, first, we measured the thickness of the samples at a reference relative humidity of 35 % with an Environmental Scanning Electron Microscope. We then used the swelling measurements presented in Figure 2.7 to estimate the thickness

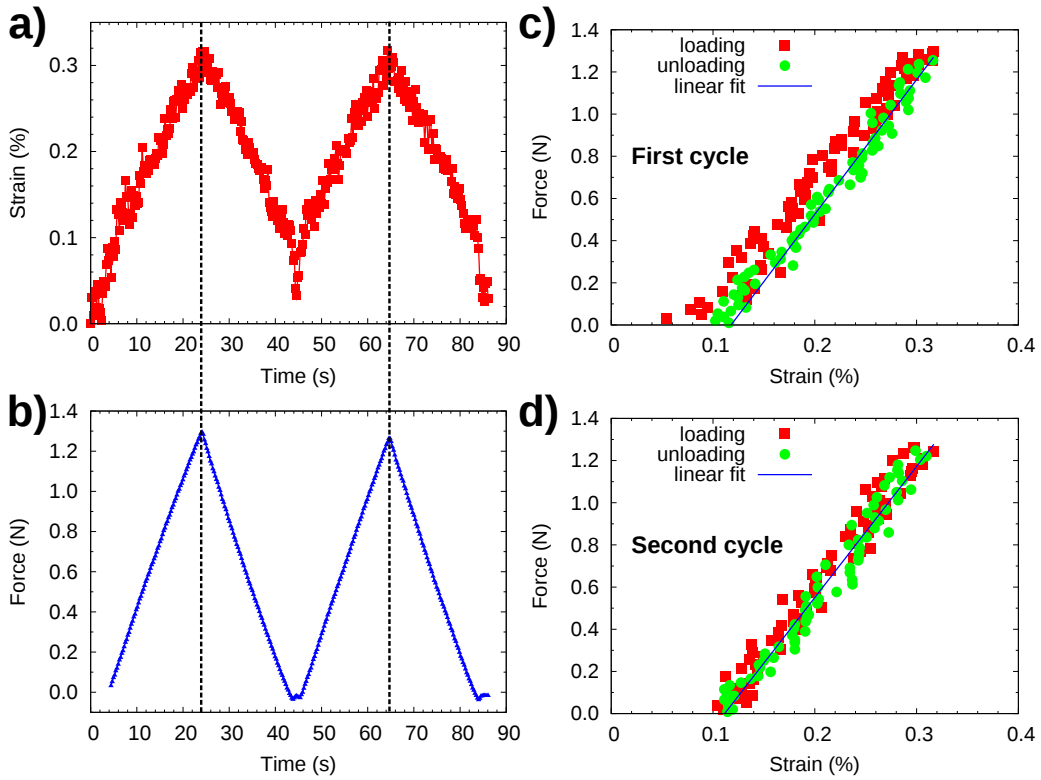

Figure 5.5: Measurement of the Young's modulus of a Swy-2-Na clay film. (a) Strain in function of time, measured by digital image correlation. (b) Force in function of time synchronized with the strain. Force-strain curve for (c) the first and (d) the second loading-unloading cycles. The linear fit was performed on the unloading portion of each cycle. The slope of the fit was 638 ± 17 N and 622 ± 15 N for the first and second unloadings, respectively.

of the films at any water content and the adsorption isotherms presented in Figure 2.8 to estimate the water content at each relative humidity. We considered that the thickness was a linear function of water content: this hypothesis is supported by the data displayed in Figure 2.7 in the range of relative humidities from 14 % to 95 %. However, since we did not perform any swelling measurement for relative humidities below 14 %, we had to assume that this linear behavior held for those relative humidities. The adsorption isotherms displayed in Figure 2.8 made it possible to obtain the Young's moduli as a function of relative humidity.

5.2.3 Estimation of uncertainties

The strains measured in this work were on the order of a few 10^{-3} only (see Figure 5.5). Therefore, quantifying the uncertainty on the deformation measurement was of fundamental importance. The uncertainty stems from both the experimental setup which is used to acquire the images (which leads to what is called the "extrinsic" error) and from the DIC procedure introduced in Section 2.2.3 (which leads to what is called the "intrinsic" error) (Sutton et al., 2009; Bornert et al., 2008). Examples of sources of "extrinsic" errors are out-of-plane displacements and image noise. The image noise can be decreased by enhancing the contrast by controlling the illumination and the patterns of the image, and by digitalizing the images such that the gray histogram is as wide as possible. The sources of the "intrinsic" errors lie in the correlation algorithm: choice of the shape functions, of the correlation window size, of the correlation function, and of the subpixel interpolation functions. Due to the small magnitude of the deformations, the effects of the shape and correlation functions on the uncertainty are negligible. In contrast, the subpixel interpolation plays a more critical role on the error. Indeed, to measure deformations with subpixel accuracy using DIC, the correlation coefficient introduced in Equation 2.3 has to be computed between the center of the pixels, so that gray levels on pixels have to be interpolated. This approximation is the source of the so-called "systematic error". The error coming from other sources of uncertainty is called the "random error".

The systematic and random errors can be estimated by comparing the displacement field computed by DIC to a known homogeneous displacement field (Dautriat et al., 2011). Here, we moved the camera away from the sample by 200 μm to apply an apparent homogeneous shrinkage to the sample and we correlated the image after the move with the image before the move. Figure 5.6-a displays the strain field ϵ_{yy} in the vertical direction. Because of the systematic error, the strain field was not homogeneous and "Moiré-like" fringes could be observed. Each band corresponds to an additional apparent displacement of one pixel. This pattern shows that the error on the local deformation can be correlated to the fractional part of the displacement

expressed in pixels.

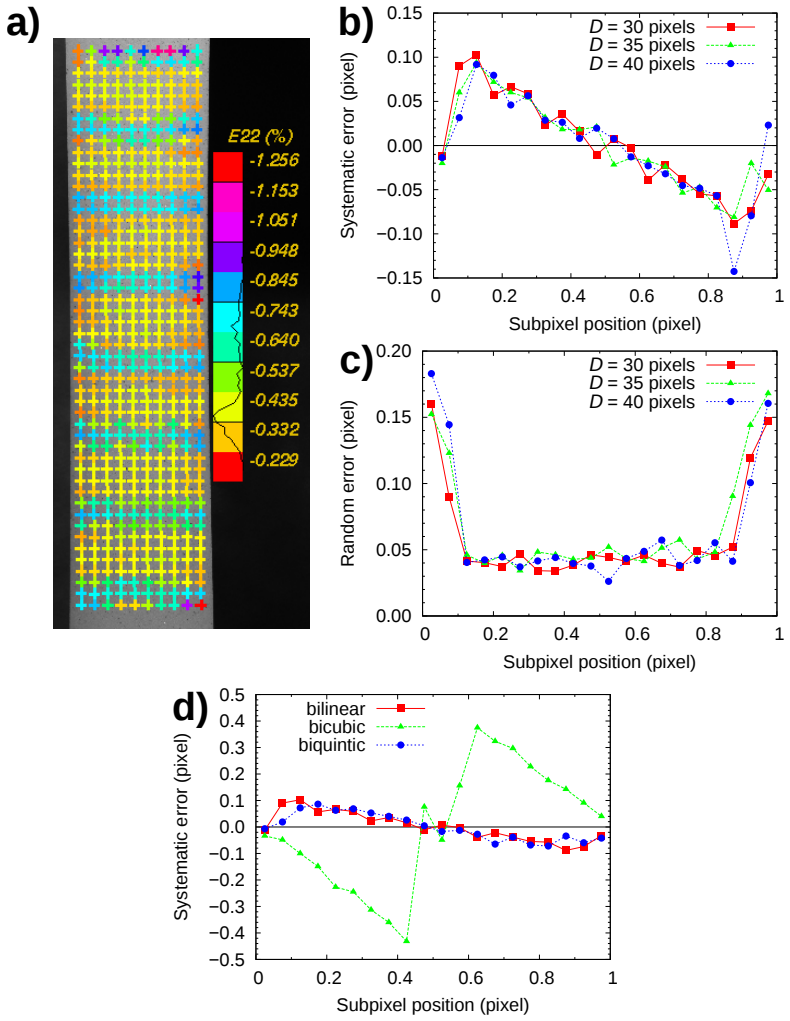

Figure 5.6: (a) Map of the vertical strain ϵ_{yy} estimated by DIC for a homogeneous apparent shrinkage of the sample. (b) Systematic error on the vertical displacement in function of the fractional part of the displacement expressed in pixels, for various sizes D of the correlation windows and for a bilinear interpolation. (c) Random error on the vertical displacement in function of the fractional part of the displacement in pixels for various subset sizes D and for a bilinear interpolation. (d) Systematic error on the vertical displacement in function of the fractional part of the displacement in pixels for various interpolation functions for a size D of the correlation windows equal to 30 pixels.

The bias u_e, which is the difference between the estimated displacement

and the true displacement, can be computed on each point of the grid of points used to measure the strain. The expectation of u_e and the variance of u_e give information about the systematic error and the random error, respectively. Wang et al. (2009) showed that both the bias u_e and the variance of the bias u_e depend on the size of the correlation windows, the function used to interpolate the gray levels, the fractional part of the displacement in pixels, the image noise, and the contrast. Figure 5.6-b displays the systematic error on the vertical displacement, inferred from the expectation of the bias u_e, in function of the fractional part of the displacement for various sizes D of the correlation windows ranging from 30 to 40 pixels and for a bilinear interpolation function. The curves had a characteristic S-shape and show that the systematic error did not depend on the size of the correlation windows in the range of sizes considered. The maximal systematic error was approximately equal to 0.1 pixel. Figure 5.6-c displays the random error on the vertical displacement, inferred from the standard deviation of the bias u_e, in function of the fractional part of the displacement for various sizes D of the correlation windows. The maximal random error was approximately equal to 0.15 pixel. Figure 5.6-d displays the systematic error for various interpolation functions (i.e. bilinear, bicubic and biquintic) for a size D of the correlation windows equal to 30 pixels. These curves also had a characteristic S-shape. The curves for the bilinear and biquintic interpolations yielded identical systematic errors which were smaller than those yielded by the bicubic interpolation. Therefore, we used the bilinear interpolation in all following DIC computations.

According to Allais et al. (1994), the error $\sigma(E_{ij})$ on the global deformation E_{ij} (i.e. computed on the whole grid) is given by:

$$\sigma(E_{ij}) = \alpha\sqrt{\frac{2}{N}}\frac{\sigma(u_i)}{L_j}, \tag{5.1}$$

where α is a coefficient close to 1, $\sigma(u_i)$ is the error on the displacement in direction i, N is the number of independent measured displacements and L_j is the gauge length along direction j. Assuming the systematic errors and the random errors were independent, the error on the global vertical deformation

for the grid presented in Figure 5.6-a (for which $N = 10$ and $L = 1500$ pixels) was equal to 6×10^{-5}.

We now aim at estimating the error $\sigma(\varepsilon_{ij})$ on the local deformation ε_{ij} at a given point on the grid. Considering that such local deformation is computed by performing integration along a contour made of the 8 closest neighbors to the point, the error $\sigma(\varepsilon_{ij})$ is given by (Allais et al., 1994):

$$\sigma(\varepsilon_{ij}) = \frac{\sqrt{3}\sigma(u_i)}{4A}, \tag{5.2}$$

where A is the grid spacing. With $A = 30$ pixels, the error $\sigma(\varepsilon_{ij})$ on the local deformation ε_{ij} was equal to 3×10^{-3}.

Therefore, we estimated errors on the order of 6×10^{-5} on the global strains, and on the order of 3×10^{-3} on the local strains. These errors must be compared with the strains to which the samples were subjected, which were on the order of a few 10^{-3}. We conclude from this uncertainty estimation that the accuracy was sufficient to carry out a quantitative analysis of the global strain, but was not sufficient to carry out a quantitative analysis of the local strain. Therefore, we were unable to observe potential heterogeneities of the local strain field.

5.3 Results

5.3.1 Mechanical behavior at ambient conditions

This Section is dedicated to providing results obtained in ambient conditions (i.e. temperature of about 25 ^{o}C and relative humidity of about 25 %): we describe qualitatively the stress-strain curves obtained, characterize the potential effects of cycling-induced damage and finally compare our results with those obtained by Zabat (1996) on similar systems.

Figure 5.7 displays a typical stress-strain curve of a tensile test on a Cloisite-Na clay film in ambient conditions. The sample was first loaded up to 18 MPa, then unloaded to 4 MPa and finally loaded to failure. The unloading portion showed the existence of a residual strain of about 0.11 %

and therefore of a plastic deformation. All samples (i.e. Swy-2-raw, Swy-2-Ca, Swy-2-Na, and Cloisite-Na) exhibited an elastoplastic behavior. In Figure 5.7, on the unloading portion, we measured a Young's modulus equal to 4.0 ± 0.1 GPa (see fitted green line). The elastic limit was equal to a strain of about 0.3 %. Therefore, in all following tensile tests, we remained in a range of strains smaller than 0.3 %. The failure of the film occurred at a strain equal to 0.68 % and a stress equal to 20.3 MPa.

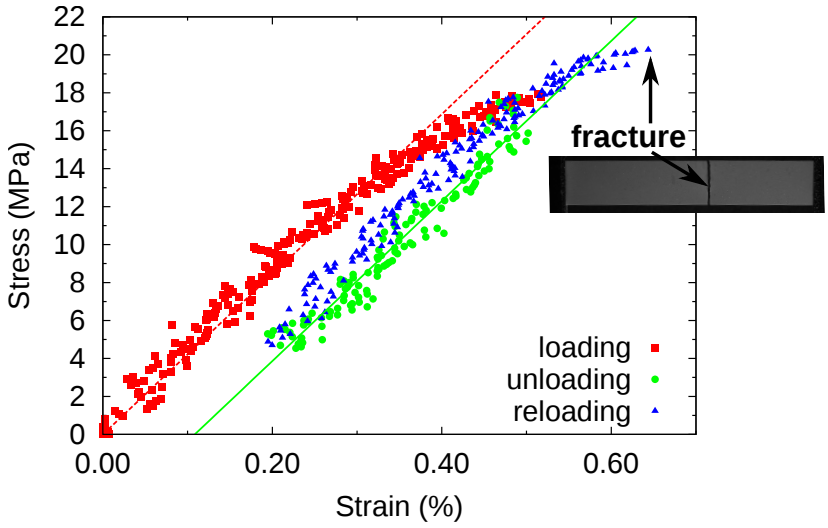

Figure 5.7: Stress-strain curve of a tensile test on a Cloisite-Na film. The sample was loaded, unloaded, and then reloaded to failure. The Young's modulus was measured during the unloading portion (green solid line). The dashed red line was obtained by shifting the linear function fitted on the unloading portion in order to pass through the origin. The inset is a picture of the sample just after failure.

In order to evaluate the potential influence of cycling and of loading rate on the measurements, we applied cycles of tensile stresses to a sample at various strain rates. Figure 5.8 displays the Young's modulus of a Swy-2-Ca film as a function of the number of loading cycles at ambient relative humidity. The sample was loaded and unloaded 20 times at various displacement rates, ranging from 0.3 μm/s to 32 μm/s. The maximum strain was equal to 0.2 %. From Figure 5.8, no damage was observed during the successive loading-unloading cycles. Moreover, the Young's modulus did not depend

on the displacement rate. The Young's modulus of Swy-2-Ca was equal to 4.65 ± 0.24 GPa. The relative uncertainty on the Young's modulus was therefore equal to about 5 %.

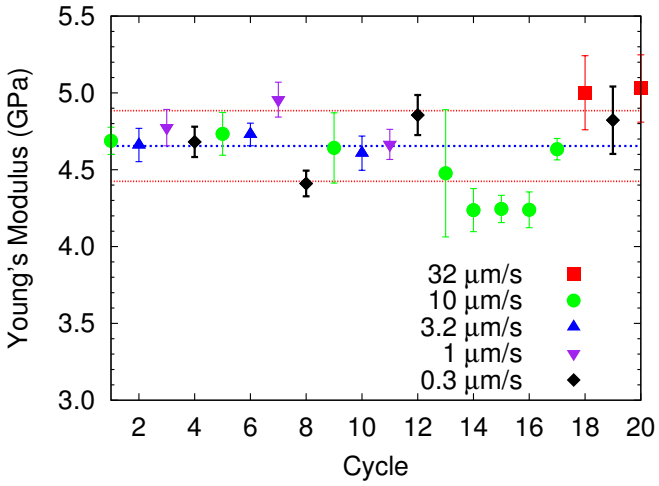

Figure 5.8: Young's modulus of a Swy-2-Ca film as a function of the number of loading-unloading cycles. The experiments were performed at ambient relative humidity (∼35 %) and at various displacement rates. The blue dashed-line is the average Young's modulus and the red dotted-lines are the average plus or minus the standard deviation. The error bars were obtained by computing the uncertainties associated to the linear fit of the stress-strain data.

Table 5.1 displays the Young's moduli and tensile strengths of various films made with all materials under ambient conditions (i.e. temperature of about 25 °C and relative humidity of about 35 %). In Figure 5.8, the Young's modulus was averaged over several cycles on only one sample. The data presented in Table 5.1 were averaged over several samples (i.e. from 3 to 9 samples) for each material. We can observe that relative uncertainties on both Young's moduli and tensile strengths were all smaller than 19 %, thus proving that both manufacturing and measurement were repeatable. Under room temperature and ambient relative humidity, Swy-2-Ca was the stiffest material with a Young's modulus equal to 4.4 ± 0.3 GPa. Swy-2-raw was slightly softer than Swy-2-Ca with a Young's modulus equal to 4.1 ± 0.2 GPa. Swy-2-Na and Cloisite-Na were the softest materials with

material	Young's modulus (GPa)	Tensile strength (MPa)
Swy-2-raw	4.1 ± 0.2	18.5 ± 1.2
Swy-2-Ca	4.4 ± 0.3	8.1 ± 0.3
Swy-2-Na	3.3 ± 0.6	not measured
Cloisite-Na	3.7 ± 0.3	18.2 ± 2.9

Table 5.1: Young's modulus and tensile strength of the clay films at ambient temperature (∼25 ^{o}C) and ambient relative humidity (∼35 %). We performed no failure experiment on Swy-2-Na.

Young's moduli equal to 3.3 ± 0.6 GPa and 3.7 ± 0.3 GPa, respectively. However, the latter exhibited a much higher tensile strength (about 18 MPa) than Swy-2-Ca (about 8 MPa).

Although Zabat (1996) also observed an elastoplastic behavior on similar clay films, the strengths and Young's moduli he measured were higher than the ones we measured, although the order of magnitude was the same. For instance, for a Na-exchanged montmorillonite clay film, Zabat measured a strength of 40 MPa, a strain at failure equal to 1.2 % and a Young's modulus equal to 6 GPa. However, Zabat did not control nor measure the relative humidity, which could partly explain the discrepancy.

5.3.2 Effect of water content

We measured the elastic properties of Swy-2-raw, Swy-2-Ca, and Swy-2-Na at various relative humidities. A sample was put in the tensile test apparatus in an environmental chamber, as presented in Figure 5.3. The sample was then equilibrated at various successive relative humidities. After each equilibration, the sample was loaded and unloaded to measure the elastic modulus. How the applied force was translated into an applied stress, which required knowing an estimate of the thickness, was explained in Section 5.2.2.

Figure 5.9 displays the Young's modulus of samples Swy-2-raw, Swy-2-Ca and Swy-2-Na versus relative humidity and water content. Several samples of each material were tested: we observed a good reproducibility of the tests. Swy-2-Ca was the stiffest clay film, with Young's moduli ranging from 2.4 GPa at high water content to 6.2 GPa at low water content, while the Young's

moduli of Swy-2-Na ranged from 1.0 GPa to 5.6 GPa. Swy-2-raw exhibited an intermediate behavior: at low water content, Swy-2-raw was softer than Swy-2-Ca (5.6 GPa versus 6.2 GPa, respectively); however, at a water content of 0.2 g/g of dry clay, the Young's modulus of Swy-2-raw was higher than the one of Swy-2-Ca (3.3 GPa versus 2.8 GPa).

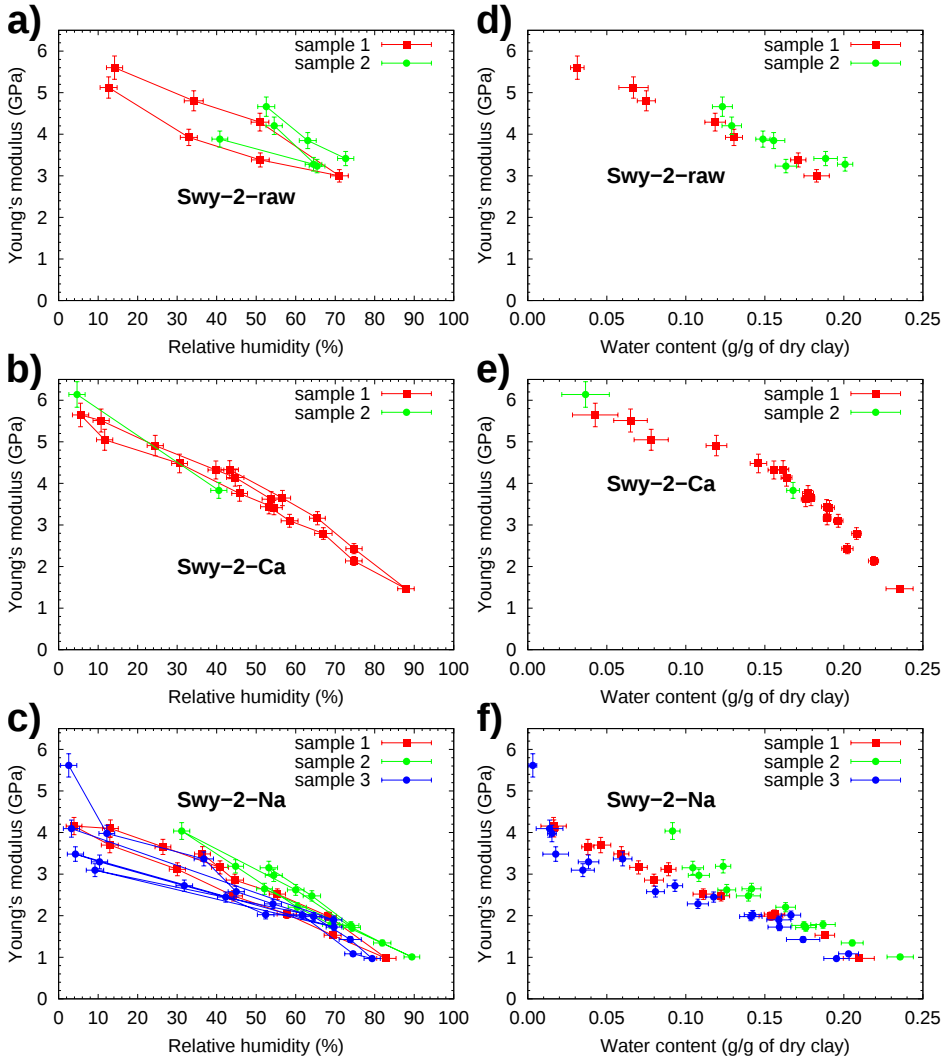

Figure 5.9: Young's modulus of clay films as a function of relative humidity and water content: (a) and (d) Swy-2-raw, (b) and (e) Swy-2-Ca, (c) and (f) Swy-2-Na. For each material, several samples were tested at various relative humidities.

The nature of the cation had a clear impact on the elastic properties of

clay films at given water content. The Ca-exchanged montmorillonite was always stiffer than the Na-exchanged montmorillonite. But we also observed an effect of the nature of the cation on the softening of the films with the increase of water content. Between the smallest and the largest water contents (i.e. about 0.02 g/g and 0.24 g/g, respectively), the ratio of the Young's moduli was equal to approximately 6 for the Ca-exchanged samples while it was equal to approximately 3 in the case of the Na-exchanged films. The Young's modulus of Ca-montmorillonite was therefore much more sensitive to water than that of Na-montmorillonite. Again, the natural clay Swy-2-raw exhibited an intermediate behavior.

We saw in Section 4.3.2 that the decrease of the in-plane stiffness upon an increase of water content was a geometrical effect consecutive to an increase of basal spacing. In order to obtain results insensitive to this geometrical effect, we now choose to focus no more on the Young's modulus of the clay films, but on an elastic modulus per clay layer. Figure 5.10 displays this elastic modulus per clay layer upon a full adsorption/desorption cycle for Swy-2-Ca, Swy-2-Na, and Swy-2-raw. The elastic modulus per clay layer was computed as the slope of the force-strain curve divided by an estimate of the number of clay layers in the film, the basal spacing of a dry clay layer (9.55 Å in both cases), and the width of the sample. The number of clay layers in the thickness of a film was estimated by dividing the surface density of the dry film by the surface density of a clay layer and was equal to 25000, 16000, and 40000 for Swy-2-Ca, Swy-2-Na, and Swy-2-raw, respectively. As expected, all samples exhibited a softening upon hydration and a stiffening upon dehydration with an hysteresis between the two branches. Moreover, Swy-2-Ca and Swy-2-raw were stiffer than Swy-2-Na, all the more so as the relative humidity was low. The fact that the elastic modulus per clay layer was larger for Ca-montmorillonite than for Na-montmorillonite at a given humidity is surprising. Indeed, at low relative humidities, the adsorption isotherms displayed in Figure 2.8 and the X-ray diffraction results presented in Figure 2.9 show that the water content and the basal spacing are larger for Ca-montmorillonite than for Na-montmorillonite. Therefore, we could have expected Swy-2-Ca to exhibit an elastic modulus lower than the one of

Swy-2-Na. Moreover, Swy-2-raw, although containing more sodium cations than calcium cations, exhibited elastic moduli per clay layer close to the ones of Swy-2-Ca.

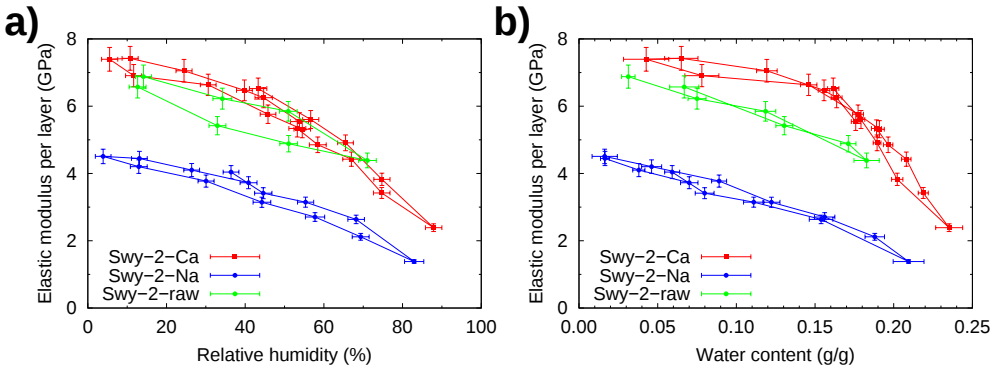

Figure 5.10: Elastic modulus per clay layer of Swy-2-Ca, Swy-2-Na, and Swy-2-raw, as a function of (a) relative humidity and (b) water content.

5.4 Discussion

5.4.1 Effect of the interlayer cation

The experimental results presented in Section 5.3 showed that the mechanical properties of the clay films depended on the nature of the interlayer cation: at given water content, the Ca-saturated samples were always stiffer than the Na-saturated samples, while the natural montmorillonite (which contained both Na^+ and Ca^{2+} cations) exhibited an intermediate behavior. This result is not supported by the results of molecular simulations presented in Chapter 4. Indeed, the molecular dynamics computations showed a limited impact of the nature of the interlayer cation on the elastic properties of the layer, except in the driest states. As soon as the first water layer was formed, no dependence of the coefficients of the stiffness tensors or of the estimated bulk and shear moduli on the interlayer cation could be observed.

However, the dependence of the elastic properties of clay-based materials on the interlayer cation was also observed by Wang et al. (2001). Their

experimental results show that Ca-rich montmorillonites are stiffer than Na-rich montmorillonites. Note however that the water content of their samples was not controlled and therefore was very uncertain. To our knowledge, there is no other work available in the literature in which the mechanical properties of a same clay saturated with various cations are compared.

If the reason for the dependence of the elastic properties of clay-based materials cannot be found at the scale of the clay layer, it must be found at a scale above. Indeed, the nature of the cation has also an effect on the size and the arrangement of the clay particles and on the mesostructure of the material (Shomer and Mingelgrin, 1978; Schramm and Kwak, 1982). In Chapter 3, we investigated the interactions between two charged surfaces with water and cations in-between. We showed that the interactions between clay layers were stronger when the counterions were calcium ions than sodium ions. Moreover, experiments show that exfoliating smectite layers saturated with calcium is very difficult (Segad et al., 2010, 2012a,b) and that Ca-exchanged smectite layers form thicker tactoids in solution than Na-exchanged smectite layers (Schramm and Kwak, 1982). Therefore, in our self-standing films, the lengths of contact between clay layers can be assumed to be larger when the montmorillonite is saturated with calcium counterions than with sodium counterions. Therefore, comparing again Ca-exchanged montmorillonite with Na-exchanged montmorillonite, each interlayer space of the former is expected to be stressed on a larger area and as a result, at a given applied force, the shear stresses are expected to be smaller, and so are the strains. Such mesostructural difference could explain our experimental observation that Ca-exchanged films were stiffer than Na-exchanged films.

In conclusion, the macroscopic hydromechanical behavior of clays depends strongly on the structure at scales larger than the scale of the layer. The mechanical behavior of our films cannot be predicted from that of the layers, which shows that the upscaling is difficult, in spite of working with well-ordered model samples. The mesostructure should be taken into account in a realistic model to obtain a good estimate of the Young's modulus of an ensemble of particles, ordered or not. In the next Section, a quantitative comparison between the experimental results on our films and the results

of molecular simulation will aim at providing further insight in the main deformation mechanisms.

5.4.2 Comparison with molecular simulations

In Chapter 4, we computed all coefficients of the stiffness tensor for Na-montmorillonite and Ca-montmorillonite. The comparison between the Young's moduli obtained experimentally on clay films in the previous Section and the elastic moduli computed by molecular dynamics in Chapter 4 and presented in Table 4.3 confirms that the shear interlayer space plays an important role in the deformations of the films. Indeed, the Young's moduli of the clay films have the same order of magnitude as the out-of-plane shear modulus $\overline{G}$ (i.e. a few GPa). In contrast, the tensile in-plane moduli of the clay layers were two orders of magnitude larger (between 130 and 220 GPa) than the Young's moduli of the clay films. Moreover, the experimental Young's moduli were very sensitive to water content, as were the out-of-plane shear coefficients of the clay layers.

Several deformation mechanisms could take place in the clay film (Zabat, 1996):

- Elongation of the clay layers or the clay particles. When stressed in tension, the spatial oscillation of the clay particles could be flattened.
- Alignment of the clay layers that form an angle with the direction of tension.
- Shear of the clay layers and clay particles.
- Sliding of the clay layers with respect to each others.

The first mechanism depends mainly on the in-plane coefficient of the stiffness tensor of the layers and is therefore not very sensitive to water content. The second mechanism is also independent from water content. This insensitivity to water content discards these first two mechanisms as the main mechanisms governing the behavior of the clay films. The third and fourth mechanisms are very sensitive to water content and could explain the softening of the films observed experimentally. However, the fourth mechanism does not correspond to a recoverable deformation and therefore cannot

explain an elastic behavior.

Assuming that shear was the main deformation mechanism, we wondered whether we could predict quantitatively the elasticity of the clay films from that of the clay layers. To do so, we considered the heterogeneity of the hydration states of the clay layers within a clay particle. Indeed, X-ray diffraction experiments showed that, at a given relative humidity, several discrete hydration states coexist within a clay particle (Bérend et al., 1995; Cases et al., 1997; Ferrage et al., 2005). Figures 5.11-a and 5.11-b display the relative abundance of clay layers containing 0, 1, or 2 layers of water measured by Ferrage et al. (2005) on the clay Swy-1 (very similar to the clay Swy-2) exchanged either with sodium or with calcium. We then considered a clay film as an ensemble of springs in parallel. Three types of spring coexisted in the film, corresponding to three hydration states, and were distributed according to the relative abundances displayed in Figures 5.11-a and 5.11-b. The spring constant of each type of spring was computed from the shear moduli $\overline{G}$ (Table 4.3) and the basal spacings (Figure 4.3) obtained by molecular dynamics. Figure 5.11-c displays the Young's moduli of a Na-exchanged and a Ca-exchanged heterogeneous stack of clay layers. The order of magnitude of the Young's moduli obtained with this simple model was in good agreement with the experimental Young's moduli measured on clay films. However, this model predicted that a Na-exchanged film is stiffer than a Ca-exchanged film, while the opposite was observed experimentally. Indeed, at a given relative humidity, the water uptake in the interlayer space is always experimentally smaller for Na-montmorillonite than for Ca-montmorillonite. Na-montmorillonite is made of less hydrated and therefore stiffer springs, thus resulting in a predicted Young's modulus that was always larger. Moreover, we did not observe experimentally the significant increase of the Young's modulus of Na-montmorillonite predicted by this simple model at low relative humidities.

In conclusion, the comparison between the experimental results on clay films and the stiffness data obtained by molecular simulations did not make it possible to establish clearly the main deformation mechanisms of the clay films. The shear of the clay layers was the only deformation mechanism which

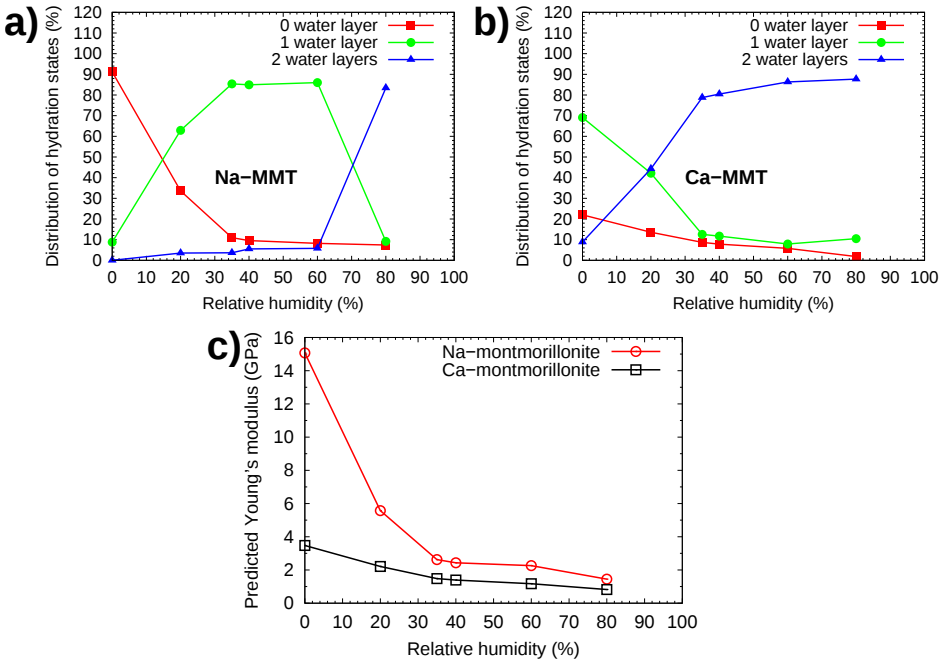

Figure 5.11: Relative abundance of various hydration states in clay particles as a function of relative humidity for (a) Na-montmorillonite and (b) Ca-montmorillonite (Ferrage et al., 2005). (c) Predicted Young's modulus of a heterogeneous stack of hydrated layers of montmorillonite.

could explain qualitatively the hydromechanical behavior (i.e. elasticity and dependence on water content) of the clay films. A simple upscaling sheme also showed that this mechanism can predict a stiffness with the right order of magnitude. However, the agreement between prediction and measurement was far from perfect. Such study shows that the upscaling of the mechanical properties from the scale of the layer to the upper scales remains very challenging, even when working on a well-ordered system.

5.5 Conclusion

In this Chapter, we measured the mechanical properties of self-standing clay films. The samples were placed in a tensile test apparatus in order to measure their stress-strain response. The mechanical test was simple enough to extract meaningful data with a minimum of assumptions. The experiments

were performed in an environmental chamber in order to control the relative humidity and therefore the water content of the samples. We used digital image correlation to measure the deformations of the samples during the tests in a contact-free manner. This experimental setup made it possible to obtain the Young's moduli of the clay films as a function of their water content or relative humidity.

All samples (i.e. Ca-montmorillonite, Na-montmorillonite, and raw montmorillonite that contained both sodium and calcium) exhibited a softening upon hydration. Ca-montmorillonite was stiffer than Na-montmorillonite at any water content. However, the softening of the former with increasing water content was more pronounced than the softening of the latter. The Young's modulus measured experimentally on the clay films had the same order of magnitude as the out-of-plane shear moduli computed by molecular dynamics in Chapter 4 and were 2 orders of magnitude smaller than the computed in-plane tensile coefficients of those same clay layers. However, in contrast with the experiments on films, the results of molecular simulations showed no dependence of the elastic properties on the nature of the interlayer cation. This discrepancy between the numerical results at the scale of the clay layer and the experimental results at the scale of the clay film demonstrate the importance of the mesoscale structure in the mechanical behavior of clay-based materials at larger scales and the relevance of performing such tests on mesoscale model materials.

The effect of the arrangement of the layers and of the particles must be further investigated. For instance, films with various thicknesses could be prepared. The thicker the film, the less parallel the layers and the rougher its surface would be. The evaporation rate during the drying of the film could also be controlled: various evaporation rates could potentially produce films with various mesostructures and thus various Young's moduli and strengths. The tensile experiments could be combined to microstructural characterization tools, such as small-angle X-ray or neutron scattering in order to get more information about the mesostructure of the films and its impact on their hydromechanical response.

In the next Chapter, we will extend this experimental work on clay films

to the long-term hydromechanical properties by performing creep tests at various relative humidities. In parallel, we will investigate these creep properties at the scale of the clay layers by using molecular simulations.

Chapter 6

Creep behavior of clays

In this chapter, *we investigated the creep properties of clays, and in particular the effect of water on these properties. We performed creep tests under controlled relative humidity on the self-supporting clay films presented in Chapters 2 and 5. The main result of these experiments was that, after a transient period that lasted for a few hundreds of seconds, the deformation was a linear function of the logarithm of time. The slope of this linear function was an increasing function of water content and load. Moreover, the amplitude of the creep strain was much higher for Na-exchanged samples than for Ca-exchanged samples. We also present molecular simulations of the time-dependent mechanical behavior of hydrated clay layers. When the interlayer space contained only one layer of water, the relation between the applied shear stress and the shear rate was given by the Bingham law: the shear rate was equal to zero up to a yield stress above which the shear rate was an affine function of the shear stress. When the interlayer contained two or more layers of water, the shear rate was a linear function of the applied shear stress. We discuss and compare the experimental and numerical results, aiming at finding the origin of the logarithmic creep of our clay samples and of clay-based materials in general.*

DANS CE CHAPITRE, *nous étudions les propriétés de fluage des argiles, et en particulier l'effet de l'eau sur ces propriétés. Nous avons réalisé des tests de fluages à humidité relative contrôlée sur les films autoporteurs présentés aux Chapitres 2 et 5. Le résultat principal de ces expériences fut que, après une période transitoire de quelques centaines de secondes, la déformation est une fonction linéaire du logarithme du temps. La pente de cette fonction linéaire était une fonction croissante de la teneur en eau et de la charge. De plus, l'amplitude du fluage était beaucoup plus importante pour les échantillons de montmorillonite sodique que pour les échantillons de montmorillonite calcique. Nous présentons également des simulations moléculaires du comportement mécanique des feuillets d'argile au cours du temps. Lorsque l'espace interfoliaire contenait une couche d'eau, la relation entre la contrainte de cisaillement appliquée et le taux de cisaillement était donné par la loi de Bingham : le taux de cisaillement était égal à zéro jusqu'à une contrainte d'écoulement au-delà de laquelle le taux de cisaillement était une fonction affine de la contrainte de cisaillement. Lorsque l'espace interfoliaire contenait deux couches d'eau et plus, le taux de cisaillement était une fonction linéaire de la contrainte appliquée. Nous discutons et comparons ensuite les résultats expérimentaux et numériques afin d'expliquer l'origine du fluage logarithmique de nos échantillons d'argile et des matériaux argileux en général.*

Contents

6.1 Introduction

The estimation of the creep of geomaterials is of crucial importance in civil engineering. The creep of soils, called secondary consolidation or secondary compression in geotechnical engineering, can cause settlements equal to "tens of percent of the total settlement" (Feda, 1992) and can have huge safety and economical consequences, especially for structures expected to last for several dozens of years. Therefore, the creep of soils has to be predicted accurately on timescales that can hardly be reached by experiments. Sone and Zoback (2010) performed mechanical tests on shales, observed a linear evolution of the creep strain with the logarithm of time after a transient period and showed that the amplitude of the creep increased with the clay volume fraction. This observation highlights the important role of the clay matrix in the creep phenomenon and the need to investigate its delayed behavior further. Figure 1.9 displays the results of an oedometric test on

bentonite and shows that after the primary consolidation, which corresponds to the dissipation of the excess pore pressure, the displacement became a linear function of the logarithm of time (Ichikawa et al., 2004).

For soils in general, settlements during the secondary consolidation phase have long been known to be a linear function of the logarithm of time (Feda, 1992) and are usually characterized by the coefficient of secondary consolidation $C_\alpha = d\varepsilon/d\log t$. The amplitude of the creep of clay-based materials like argillite is known to depend on water content and load (Yang et al., 2011). However, the precise dependence of C_α on water content, temperature, or load is still poorly characterized and understood.

In this Chapter, we focus on the role of water on the amplitude of creep. We perform creep tests on the self-standing films of which we already measured the swelling properties in Chapter 2 and the elastic properties in Chapter 5. These creep tests make it possible to quantify the creep of well-ordered mesoscopic model samples and its dependence on the nature of the interlayer cation, the relative humidity, and the applied load. We also investigate the creep at the scale of the interlayer by using molecular dynamics. We aim at explaining the origin of the logarithmic dependence of creep to time of clay-based materials. Our final goal is to explain the origin of the logarithmic dependence of creep on time for clay-based materials.

In the second Section of this Chapter, we present the experimental results of the creep tests performed on the clay films. The third Section is devoted to the computation of time-dependent properties at the scale of the clay layer by molecular simulations. In the fourth Section, we extend an analytical model of a bonded joint to the viscoelastic response of a clay layer in order to test whether the corresponding mechanism of deformation can explain a creep that is logarithmic with respect to time.

6.2 Effect of water content on the creep properties of clay films

6.2.1 Experimental methods

The materials we used for the creep tests were the clays already used in Chapter 2 and Chapter 5: Swy-2-Ca and Swy-2-Na. Like for the tensile tests presented in Chapter 5, the samples were 93-mm-wide and 80-mm-long. The ends of the samples were reinforced with sandpaper before being placed in the grips of the creep test device. The free length of the samples was equal to 50 mm. Figure 6.1-a displays the experimental setup we used to perform creep tests. One end of the sample was placed in a fixed grip and the other end was fixed to a mobile ball slide which could move linearly on a rail. The sample was loaded by a weight attached to a string, itself attached to the mobile ball slide. A pulley formed the vertical gravitational force into a horizontal force on the ball slide. In order to minimize friction, the mobile part had a linear-motion bearing at the contact with the rail and the rail was lubricated. Before performing any experiment, we calibrated the device: to measure the friction, we loaded the device with various weights. For each weight, we measured the force transmitted by the ball slide with a force sensor having an accuracy of 1 mN. Figure 6.1-b displays the force measured by the sensor in function of the force applied to the device. We fitted the data with a linear function. The slope of this function was equal to 1 and the extrapolation to a measured force equal to zero gave a friction of 0.11 ± 0.1 N. Every applied force was corrected by taking into account this friction in all results presented in this Chapter. To be consistent from one sample to another, the load will be expressed in force per clay layer, i.e. the force transmitted to the sample divided by the number of clay layers in the sample.

To perform creep tests at various relative humidities, the creep tests device was placed in an environmental chamber. The relative humidity was controlled with saturated salt solutions and measured with a hygrometric sensor. Figure 6.2 shows the experimental setup. The deformations of the

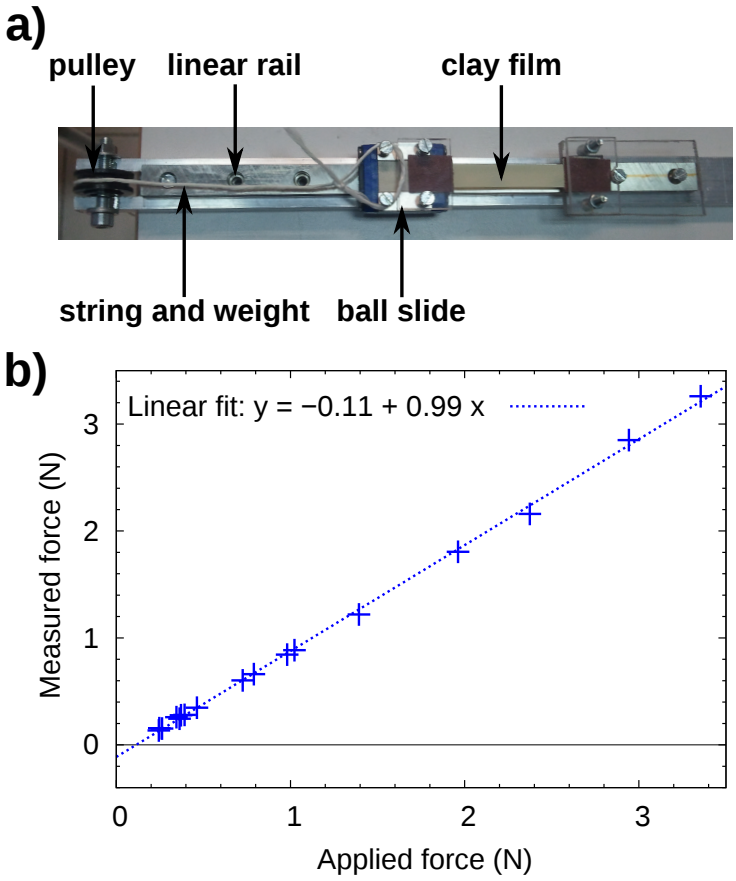

Figure 6.1: (a) Experimental setup used to perform creep test. The right end of the sample was fixed and the left end of the sample was attached to a mobile ball slide. A load was applied to the ball slide via a weight attached to a string and a pulley. (b) Force transmitted by the device and measured by a force sensor as a function of the force applied by a weight. We measured a friction of 0.11 ± 0.1 N.

samples were measured by taking images of the samples and by analyzing them with digital image correlation (DIC). This technique was described in details in Section 2.2.3 and in Section 5.2.3. The camera and the correlation procedure were the same as those used in Chapter 5. We measured only the global deformation of the samples, because the accuracy of our measurement was not sufficient to obtain quantitative information on the local strain field. Before each creep test, the sample was placed in a chamber in equilibrium with pure water to equilibrate it at a relative humidity close to 100 %. The

water was then replaced with a saturated salt solution to bring the chamber to the desired relative humidity. The hydric starting points of all tests were therefore located on the desorption branch of the adsorption isotherms.

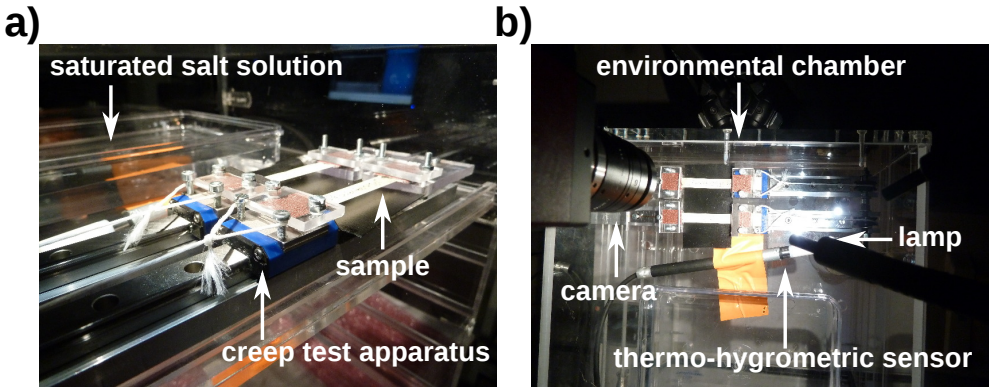

Figure 6.2: Pictures of the creep test experimental setup under controlled relative humidity: a) Creep test device in the environmental chamber and b) overall view of the setup.

As will be seen in the next Section, after a transient period, for all films the creep strain evolved linearly with the logarithm of time. By analogy with soils, we introduce a creep coefficient α defined as the slope of the creep strain versus logarithm of time curve:

$$\alpha = \frac{d\epsilon}{d(\log t)}. \tag{6.1}$$

The conditions and results of all tests are reported in Appendix A.

6.2.2 Results

Figure 6.3 displays the typical deformations of a clay film with time. At t = 0 s, a load equal to 26.1 μN per clay layer was applied and was kept constant during the test. The samples exhibited an instantaneous elastic deformation. The creep strain was then calculated as the difference between the total strain and this instantaneous elastic deformation: thus, the creep strain was the delayed part of the deformation. In Figure 6.3 we plotted the creep strain in function of time, on a logarithmic scale. After 500 to

600 s, the deformation was a logarithmic function of time. On this Figure, two tests performed on two Swy-2-Ca films are displayed: the first one was performed at a relative humidity of 92.0 ± 2.9 % and the second one at a relative humidity of 77.7 ± 2.0 %. The test at 92 % was stopped when the sample failed while we stopped the test at 78 % before failure. Relative humidity had a very clear impact on the creep rate. The creep strain was a linear function of the logarithm of time for both tests and the slope α of this function (which we named creep coefficient) was larger at a higher relative humidity: the creep coefficient α was equal to 0.22 % at a relative humidity of 92 % but to 0.05 % at 78 %.

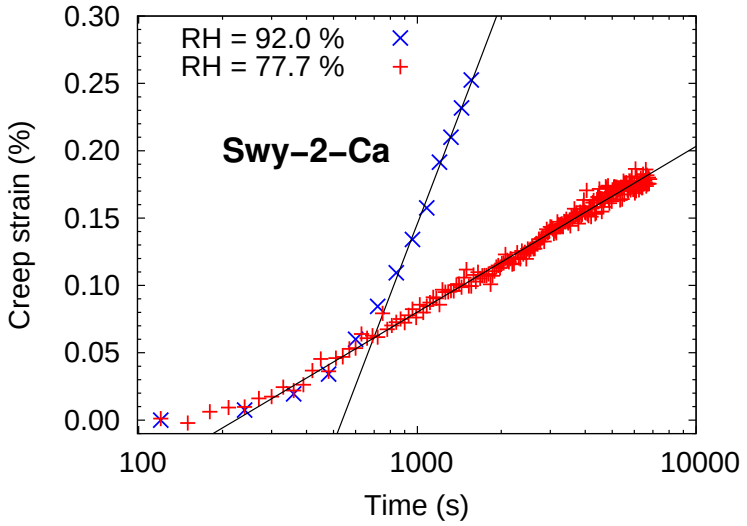

Figure 6.3: Creep strain of films of Swy-2-Ca as a function of time (logarithmic scale) at various relative humidities. The force transmitted to the samples was identical for both tests (i.e. 26.1 μN per clay layer).

Figure 6.4 displays the creep strain of two Swy-2-Na films in function of time, on a logarithmic scale. The two tests were performed at the same relative humidity, but at various loads (8.1 and 20.2 μN per clay layer, respectively). The test with a load equal to 20.2 μN per layer was stopped when the sample failed while we stopped the test with a load of 8.1 μN per layer before failure. For both films, after a transient period, the creep strain was a logarithmic function of time. However, the amplitude of the creep

increased with load. For a load equal to 8.1 μN per clay layer, the creep coefficient α was equal to 0.21 %, while this creep coefficient was equal to 0.91 % for a load equal to 20.2 μN per layer. Therefore, the amplitude of creep increased faster than the load: when the load was multiplied by 2.5, the creep coefficient α increased by a factor 4.3. A more thorough study of the effect of the load on the creep coefficient is presented next.

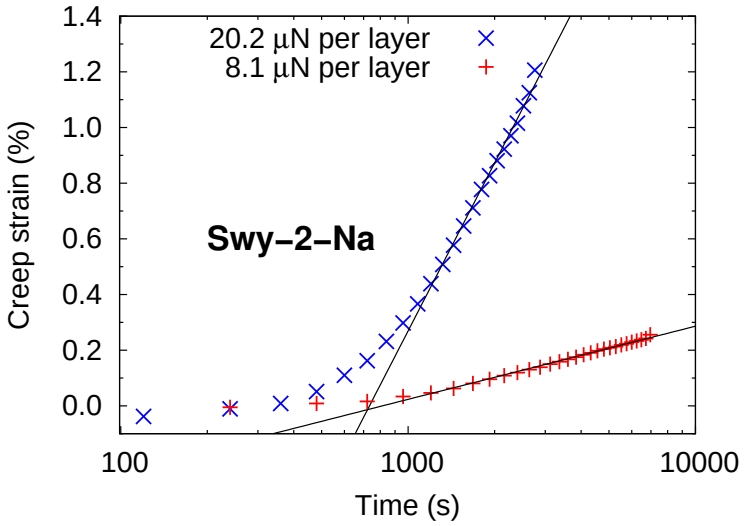

Figure 6.4: Creep strain of Swy-2-Na films as a function of time at various applied forces. The relative humidity was identical for both tests ($\sim$ 92 %).

Figure 6.5 displays the creep coefficient α in function of load for Swy-2-Ca and Swy-2-Na at a given relative humidity. Four sets of data are displayed: an experiment on two identical films of Swy-2-Ca, an experiment on another film of Swy-2-Ca, an experiment on two identical films of Swy-2-Na, and an experiment on another film of Swy-2-Na. Each experiment was performed independently from each other, and two films tested during the same experiment were loaded at the same time in the same environmental chamber. When the films were loaded during the same experiment, for both materials, the creep coefficient was an increasing function of load in a roughly linear manner. However, experiments performed at different times were not consistent with each other. Although the measured relative humidities were close between two experiments (e.g. 77.5 $\pm$ 2.8 % and 77.7 $\pm$ 2.5 % for the two

sets of data on films of Swy-2-Ca), the actual relative humidities with which the films were in equilibrium could have differed significantly. The uncertainties on the measurement of the relative humidities can result in difference of relative humidities larger than 5 %. Indeed, the respective location of the saturated solution and of the hygrometric sensor, and the local temperature can impact significantly the measurement of the relative humidity. Moreover, at relative humidities around 80 %, the creep coefficient α was very sensitive to relative humidity, as is shown next. Such uncertainty could explain the discrepancy between the sets of experiments 1 and 2. In any case, experiments under the very same environmental conditions suggested that the creep coefficient depends on the load and that this dependence is linear. Therefore, we introduce the creep compliance κ (expressed in $\mathrm{Pa}^{-1}.\mathrm{m}^{-1}$), defined by

$$\kappa = \alpha \frac{b}{F}, \tag{6.2}$$

where F is the force applied by clay layer and b is the width of the sample ($b = 9.3$ mm for all creep tests).

Figure 6.6 displays the creep compliance κ in function of relative humidity for both the Ca-exchanged montmorillonite and the Na-exchanged montmorillonite. At a given relative humidity, the creep compliance was much higher for Na-exchanged montmorillonite than for the Ca-exchanged montmorillonite, by about one order of magnitude. Also, for both types of films, we observed a tremendous effect of relative humidity on the creep compliance: for both types of films, when increasing the humidity from about 60 % to about 95 %, the creep compliance increased by about two orders of magnitude.

We performed creep tests for relative humidities below 50 %, but we could observe no creep: the very low creep compliance at low relative humidities indeed required very long tests. Controlling the relative humidity with a high accuracy during such periods of several days was impossible: the relative humidity and water content fluctuated slightly over time. The creep was therefore indistinguishable from the slight swelling and shrinkage of the film

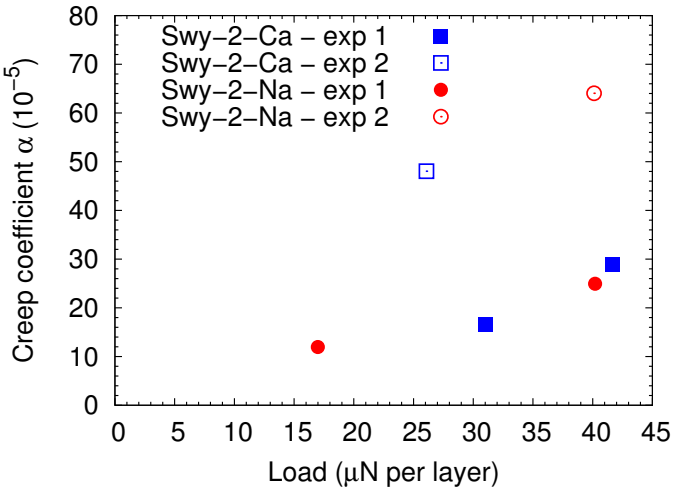

Figure 6.5: Creep coefficient α as a function of load at a given relative humidity. For each film, exp 1 and exp 2 correspond to two different experiments. During experiment 1, two identical films were loaded at the same time in the same environmental chamber. The relative humidity was equal to 77.5 $\pm$ 2.8 % and 81.3 $\pm$ 1.5 % for Swy-2-Ca and Swy-2-Na, respectively. Experiment 2 was performed on different films, at a different time. The relative humidity was equal to 77.7 $\pm$ 2.5 % and 80.3 $\pm$ 2.3 % for Swy-2-Ca and Swy-2-Na, respectively.

or the small variations of the elastic properties shown in Figure 5.9.

Figure 6.7 displays the creep compliance as a function of water content for Swy-2-Ca and Swy-2-Na. We performed a linear regression of the logarithm of the compliance versus water content (dashed lines in Figure 6.7) and obtained a correlation coefficient equal to 0.83 for Swy-2-Ca and to 0.78 for Swy-2-Na. The compliance can therefore be well approximated by an exponential function of water content.

The viscoelastic properties of the films could be further analyzed by applying a dynamic loading. Performing dynamic tests would make it possible to measure the storage and the loss moduli of the films and therefore to quantify the elastic energy and the dissipated energy.

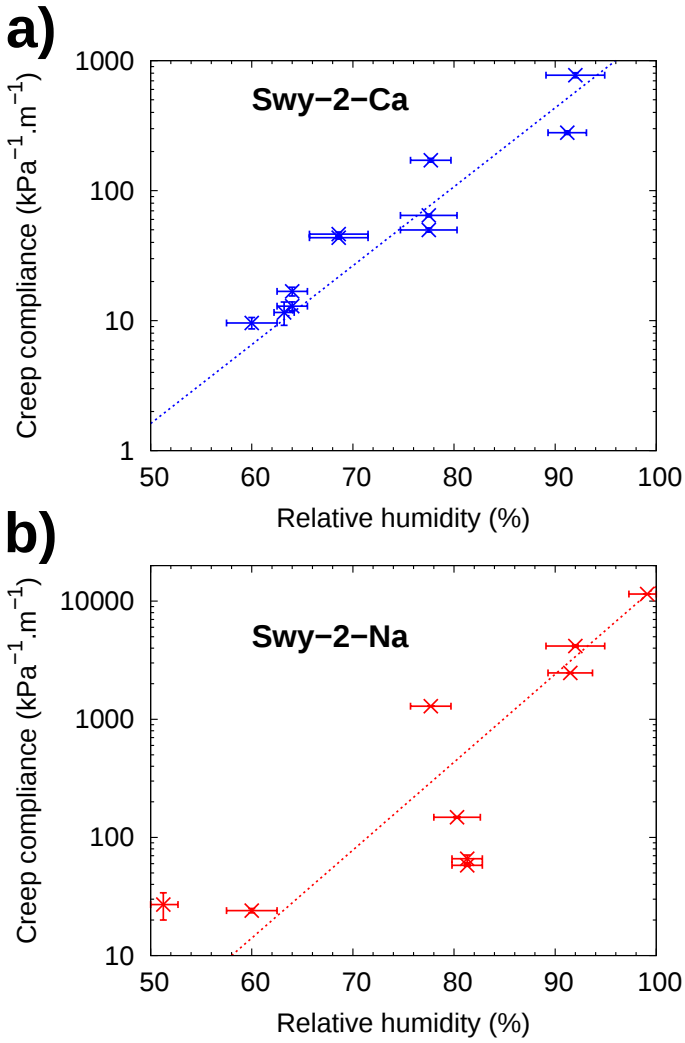

Figure 6.6: Creep compliance κ in function of relative humidity for (a) sample Swy-2-Ca and (b) Swy-2-Na. Dotted lines are visual guides.

6.3 Effect of water content on the creep properties of clay layers

In this Section, we present results of molecular dynamics computations on montmorillonite layers with various water contents. We focus on the time-dependent response of clay layers subjected to a shear stress.

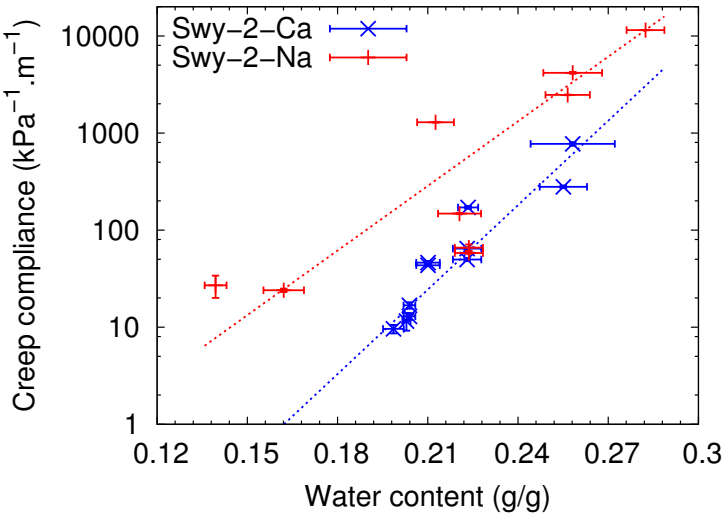

Figure 6.7: Creep compliance κ in function of water content for samples Swy-2-Ca and Swy-2-Na.

6.3.1 Computational methods

To model a Na-exchanged montmorillonite, we used the same molecular structure as described in Section 4.2. All forces and interactions were computed with the CLAYFF force-field (Cygan et al., 2004). First, we performed an isobaric-isothermal (NPT) molecular dynamics simulation at a hydrostatic pressure of 1 bar and a temperature of 300 K to equilibrate the system. The barostat and thermostat are described in Chapter 4. Then, we added to the barostat a shear stress τ parallel to the clay layers and ran a simulation for a maximum of 10 ns. All cell parameters could fluctuate according to the applied barostat and thermostat. We sampled the shear strain γ in the direction of the applied shear stress. The shear strain γ is defined by

$$\gamma = \frac{\delta - \delta_0 + \Delta}{\langle l_z \rangle} \tag{6.3}$$

where δ and δ_0 are the current and initial relative displacements of the two faces of the simulation cell orthogonal to the z-axis, respectively, Δ is the accumulated displacement, and $\langle l_z \rangle$ is the average of the distance l_z between these two faces. Since the applied shear stress induced large shear strains,

the simulation cell deformed significantly during the simulation. Therefore, when δ exceeded $l_z/2$, the simulation cell was flipped and the atom positions were remapped, so that δ was equal to $-l_z/2$. The two configurations (i.e. before and after the box was flipped) were strictly equivalent. The accumulated displacement Δ was then incremented by the amount l_z. The atom trajectories and momenta and the barostat were unaffected by this process. We then measured the shear rate $\dot{\gamma}$ by fitting a linear relation to the shear strain versus time curve. All simulations were run with the software LAMMPS (Plimpton, 1995).

We did not have to use Non-Equilibrium Molecular Dynamics (NEMD) methods (Evans and Morriss, 1990; Tuckerman, 2010; Joubaud and Stoltz, 2012), such as the SLLOD equations of motion, to model the time-dependent response of the clay layers. Indeed, such methods are necessary when modeling homogeneous flows in bulk fluids. In our case, solid walls (i.e. the clay layers) were present and were able to apply a flow to the fluid part.

6.3.2 Results

Figure 6.8 displays the typical shear strain in function of time obtained from the molecular dynamics simulations of a Na-montmorillonite with 2 water layers. In that case, the shear strain was a linear function of time. At each applied shear stress, we fitted the data with a linear function, the slope of which yielded the shear rate $\dot{\gamma}$. As expected, the shear rate $\dot{\gamma}$ was an increasing function of the applied shear stress.

We performed the molecular simulations on Na-montmorillonite at various water contents: 0.09 g/g, 0.19 g/g, and 0.28 g/g, corresponding to an an interlayer space containing 1, 2, or 3 layers of water, respectively (see Table 4.1).

Figure 6.9 displays the shear rate as a function of the applied shear stress for Na-montmorillonite and Ca-montmorillonite in various hydration states. We did not plot data for the dry state because for such state we could observe no viscosity: the clay layers behaved like a solid. However, as soon as the first layer of water was formed, a viscous response could be measured. For

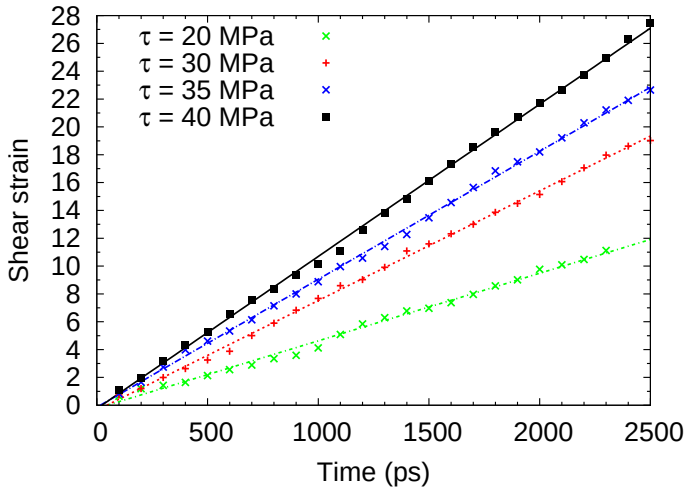

Figure 6.8: Shear strain of the simulation cell which contains the clay layers as a function of time at various applied strains. For the sake of clarity, only 1 every 1000 points was plotted. The interlayer space contained sodium cations and two layers of water.

montmorillonite with one water layer, the viscous behavior was governed by a Bingham plastic flow (Bingham, 1922): below a yield stress τ_c, the clay layers exhibited no delayed deformation while for shear stresses larger than τ_c the shear rate was proportional to the difference between the stress and the yield stress. In such case, the shear rate $\dot{\gamma}$ is thus governed by:

$$\dot{\gamma} = \begin{cases} 0 & \text{if} \quad \tau \leq \tau_c \\ \eta^{-1}\left(\tau - \tau_c\right) & \text{if} \quad \tau > \tau_c \end{cases}, \tag{6.4}$$

where η is the viscosity. When the number of water layers was increased to 2 or 3, the yield stress τ_c dropped.

In Table 6.1, we report the yield stress and the viscosity for each hydration state with sodium or with calcium interlayer cations. We observe that, as expected, the viscosity η was a decreasing function of the water content. The interlayer cation had an effect on the parameters of the Bingham plastic law. The yield stresses and the viscosities were higher for Ca-montmorillonite than for Na-montmorillonite.

By considering that only water contributed to the viscous flow, we com-

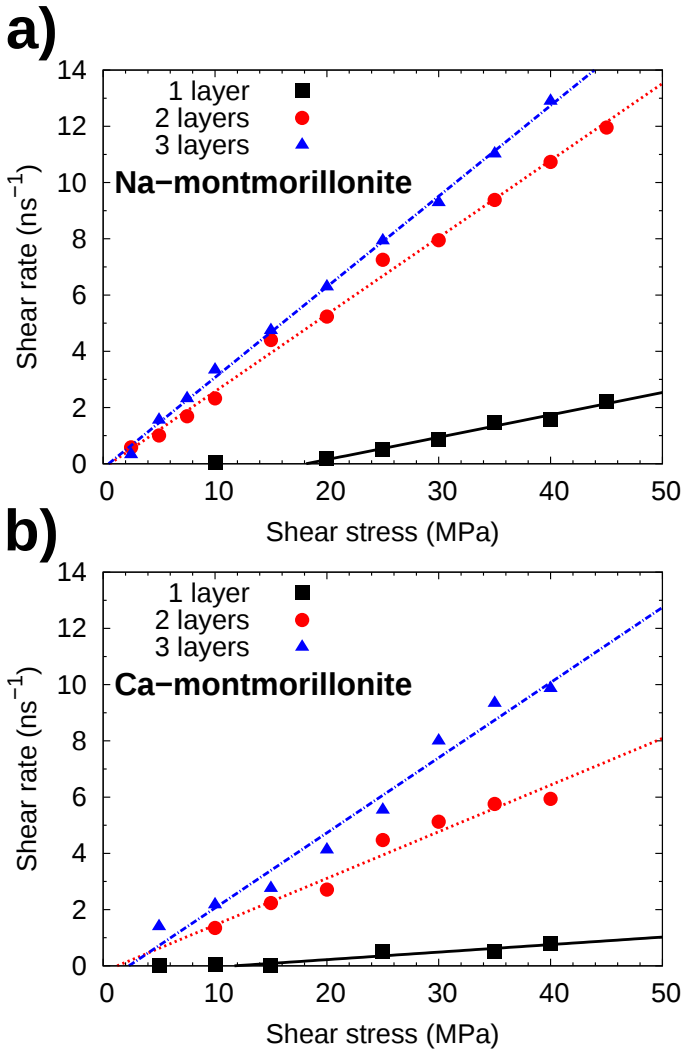

Figure 6.9: Shear rate in function of the applied shear stress computed by molecular dynamics for (a) Na-exchanged montmorillonite layers and (b) Ca-exchanged montmorillonite layers with 1, 2, and 3 water layers in the interlayer space. The error bars are smaller than the symbols.

puted the effective viscosity of the interlayer water. We measured the thickness of the film of interlayer water on the density profile of the oxygen atoms of water in the interlayer space. The water film was 3.2-Å-, 5.8-Å-, and 8.2-Å-thick and the basal spacing was equal to 12.3 Å, 14.9 Å, and 17.3 Å, when the interlayer space contained 1, 2, and 3 layers of water, respectively. In the interlayer space of Na-montmorillonite, the viscosity of 1 layer of water

Ion	number of water layers	Yield stress τ_c (MPa)	Viscosity η (10^{-3} Pa.s)	Viscosity of the water layers (10^{-3} Pa.s)
Na	1	18.5 ± 1.2	12.3 ± 0.9	3.2 ± 0.2
	2	1.0 ± 1.1	3.6 ± 0.1	1.4 ± 0.05
	3	0.5 ± 0.3	3.1 ± 0.05	1.5 ± 0.02
Ca	1	14.1 ± 4.9	32 ± 9	8.3 ± 2.3
	2	2.2 ± 2.3	5.8 ± 0.5	2.3 ± 0.1
	3	2.9 ± 1.6	3.6 ± 0.3	1.7 ± 0.2

Table 6.1: Yield stress and viscosity of the Bingham plastic flow for various hydration states of Na-montmorillonite and Ca-montmorillonite. The viscosity of the water layers was computed assuming that the clay layers were rigid and that only water contributed to the viscous flow.

was equal to 3.2 10^{-3} Pa.s. The viscosities of 2 and 3 layers of water were identical and were equal to about 1.5 10^{-3} Pa.s. This value was larger than the viscosity of water determined experimentally at 1 bar and 300 K (i.e. 0.89 10^{-3} Pa.s (Harris and Woolf, 2004)). This value was also larger than the viscosity of bulk water determined by molecular dynamics with the SPC model at 1 bar and 300 K (i.e. between 0.29 10^{-3} Pa.s and 0.45 10^{-3} Pa.s (Hess, 2002)). Therefore, we observed a clear effect of confinement, which increased the apparent viscosity of water.

6.3.3 Discussion

Measurements of the settlements over time on large-scale facilities (Feda, 1992), macroscopic oedometric testing on bentonite (Ichikawa et al., 2004), and the mesoscopic creep tests on thin clay films described in Section 6.2 all exhibit creep strains of clay-based materials that evolve as a linear function of the logarithm of time. In contrast, in the previous Section, we observed numerically that clay layers exhibited creep strains that evolved linearly with time. Therefore, there is a discrepancy that leads us to wonder: what is the origin of the logarithmic creep of clays? In particular, one can wonder whether this origin can be found at the scale of the clay layers (which would imply that our molecular simulations missed some physics of the problem) or at a scale above.

An explanation that could hold both at the scale of the clay layer or at a scale above is an energetic explanation by Nabarro (2001), who proposed two models of logarithmic creep: the work-hardening model and the exhaustion model. Both models assume the application of the transition state theory and the existence of a spectrum of activation energies. In the work-hardening model, initially the activation energy of all thermally activated processes is identical. Nevertheless, this activation energy evolves with time. In the exhaustion model, a distribution of activation energies is considered: the smallest barriers are exhausted firsts and the characteristic time to overcome a barrier increases with the activation energy. As a result, the creep rate decreases with time and creep is logarithmic. Could one of those two models explain a logarithmic creep at the scale to the clay layer? Apparently not. Indeed, the thermally activated events which have an activation energy which would vary with time are yet to be found. And, still at the scale of the layer, except in the dry state, the behavior is viscous, due to the lubrication by one or several layers of water between two clay layers. Why, at finite temperature, this lubrication would lead to a distribution of activation energies is also unclear. Note however that the models proposed by Nabarro (2001) could be valid at scales above that of the clay layer.

One physical issue with our molecular simulations could be that periodic boundary conditions make it necessary to simulate infinite clay layers. One could wonder whether the reason for a logarithmic creep could not be found at the scale of the clay layer, in the fact that the size of the clay layers is finite. In the next Section, we consider a type of mechanism specific to layers with a finite size and check whether this mechanism can explain a logarithmic creep.

6.4 Shear-lag model

In this Section, we present the so-called shear-lag model and extend it to viscoelasticity in order to test if it could explain a logarithmic creep at the scale of the clay layer.

6.4.1 Elastic response

The structure of a clay layer can be compared to an adhesive-bonded joint (see Figure 6.10). An adhesive-bonded joint is a joining process in which two surfaces are hold together by an adhesive. Applications of such a technique include the assembly of composite materials for aircrafts or the reinforcement of civil engineering structures with composite materials. In the case of montmorillonite, the crystalline clay layers can be considered as the adherends and the electrolyte in the interlayer space as the adhesive.

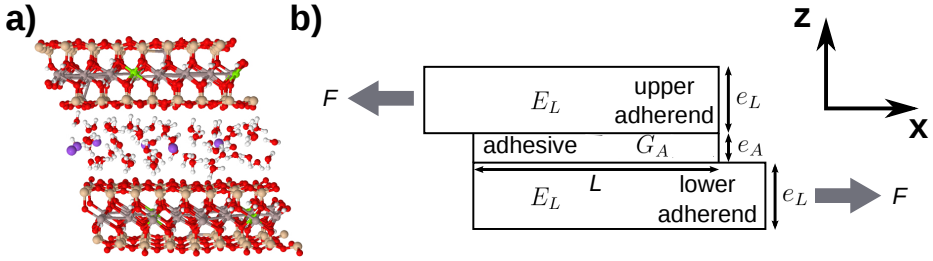

Figure 6.10: Analogy between (a) a sheared clay layer and (b) a sheared single bonded joint.

In the elastic case, Volkersen (1938) showed that the shear in the adhesive is not uniform. The main assumptions of the theory of Volkersen are that the adherends deform only in tension and the adhesive deforms only in shear. In the case of a symmetric joint, using the mechanical equilibrium of the system and the Hooke's law of linear elasticity, the shear stress $\tau(\overline{x})$ in the adhesive is governed by the following differential equation:

$$\frac{d^2}{d\overline{x}^2}\tau(\overline{x}) - \lambda^2\tau(\overline{x}) = 0, \tag{6.5}$$

with

$$\lambda^2 = \frac{2G_A L^2}{e_A e_L E_L}, \tag{6.6}$$

where G_A is the shear modulus of the adhesive, E_L the Young's modulus of the adherends, e_A the thickness of the adhesive, e_L the thickness of the adherends, L the length of the joint and $\overline{x} = x/L$ the dimensionless coor-

dinate along the joint. Solving this differential equation with the boundary conditions

$$\tau(0) = \tau(1) \text{ and } \int_0^1 \tau(\overline{x})d\overline{x} = \tau_0 = 2\frac{F}{be_L}, \tag{6.7}$$

where F is the loading, b the width of the joint, and τ_0 the average shear stress in the adhesive, yields

$$\tau(\overline{x}) = \frac{\tau_0\lambda}{2}\left(\frac{1+\cosh(\lambda)}{\sinh(\lambda)}\cosh(\lambda\overline{x}) - \sinh(\lambda\overline{x})\right). \tag{6.8}$$

Figure 6.11 displays the shear stress distribution along the joint for various parameters. This distribution is not uniform: the shear stress is at a maximum at the ends of the joint and at a minimum at the middle of the joint. This non-uniform distribution is called the "shear lag" effect and is a direct consequence of the finite size of the joint. λ^{-1} is the characteristic dimensionless length over which the shear stress decreases.

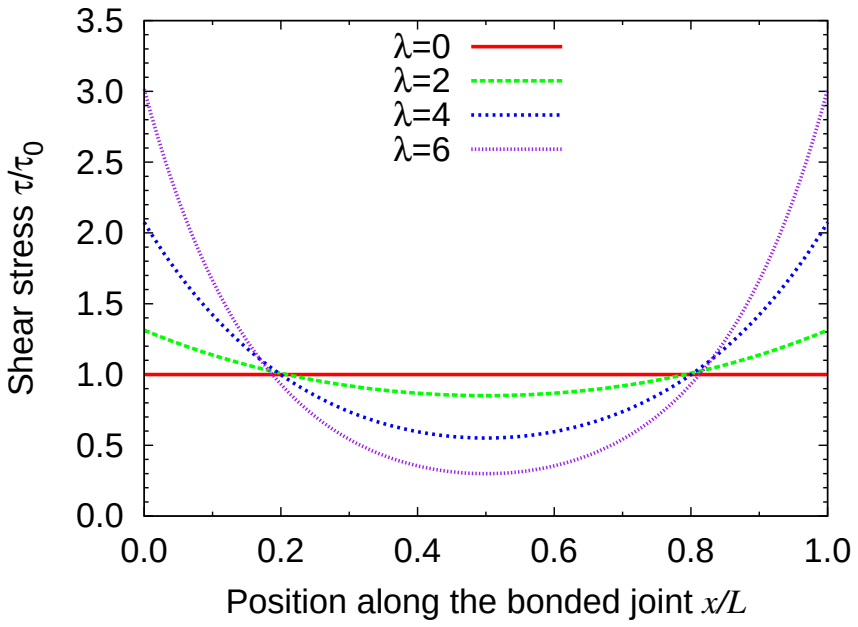

Figure 6.11: Dimensionless shear stress along a bonded joint for various values of the characteristic dimensionless length λ^{-1}.

This shear-lag theory was initially proposed to model the response of

bonded joints. However, more recently, it was also successfully used to model the tensile behavior of nacre (Khota et al., 2001): the aragonite platelets and the biopolymer matrix played the role of the adherend and the adhesive, respectively. The elastic moduli obtained with the model were in very good agreement with the experimental values. Naturally, we wondered what this shear-lag effect would yield for a viscoelastic adhesive. The extension of the shear-lag theory to viscous effects is the topic of the next section.

6.4.2 Viscoelastic response

We extend the shear-lag theory to the case of a viscoelastic adhesive. All variables depend now on both dimensionless position $\overline{x} = x/L$ and time t, e.g. $\gamma = \gamma(\overline{x}, t)$ and $\tau = \tau(\overline{x}, t)$. We assume that the behavior of the adhesive is governed by a Maxwell rheological model:

$$\frac{\partial \gamma}{\partial t} = \frac{1}{G_A}\frac{\partial \tau}{\partial t} + \frac{\tau}{\eta_A} \tag{6.9}$$

where γ is the shear strain in the adhesive and η_A the viscosity of the adhesive.

The equilibrium between the axial stresses σ_U and σ_L in the upper and lower adherends, respectively, and the shear stress τ is

$$e_A\tau = -\frac{\partial \sigma_U}{\partial x} \text{ and } e_A\tau = \frac{\partial \sigma_L}{\partial x}. \tag{6.10}$$

The shear strain in the adhesive is given by

$$\gamma = \frac{u_L - u_U}{e_A} \tag{6.11}$$

where u_U and u_L are the displacements of the upper and lower adherends, respectively, in the x direction. The derivation of Equation (6.11) twice with respect to x and using Hooke's law in the adherends and the equilibrium Equation (6.10) yields

$$\frac{\partial^2 \gamma}{\partial x^2} = \frac{2}{E_L e_A e_L}\tau. \tag{6.12}$$

Combining Equations (6.9) and (6.12) yields the following differential

equation:

$$\frac{\partial^2}{\partial x^2}\frac{\partial}{\partial t}\tau + \frac{1}{\alpha}\frac{\partial^2}{\partial x^2}\tau = \frac{\lambda^2}{L^2}\frac{\partial}{\partial t}\tau \tag{6.13}$$

where $\alpha = \eta_A/G_A$ is a characteristic time. We introduce the dimensionless time $\bar{t} = t/\alpha$ and obtain the following dimensionless equation:

$$\frac{\partial^2}{\partial \overline{x}^2}\frac{\partial}{\partial \bar{t}}\tau + \frac{\partial^2}{\partial \overline{x}^2}\tau = \lambda^2\frac{\partial}{\partial \bar{t}}\tau. \tag{6.14}$$

By integrating Equation (6.14) in space and using the condition (6.7), we obtain the following boundary condition:

$$\frac{\partial \tau}{\partial \overline{x}}(0,\bar{t}) = -\frac{\partial \tau}{\partial \overline{x}}(1,\bar{t}) = -\frac{\tau_0\lambda^2}{2}\exp(-\bar{t}). \tag{6.15}$$

The initial condition is given by the elastic solution (6.8).

To solve numerically the differential equation (6.14), we implemented a finite difference scheme. We used a scheme implicit in space to improve the numerical stability and the convergence. The space step was equal to 0.01 and the time step to 0.1. Figure 6.12 displays the numerical solution of Equation (6.14) for $\lambda = 50$: the displayed parameter is the dimensionless shear rate $\dot{\gamma}$ at the extremities of the adhesive of a bonded joint given by:

$$\dot{\gamma} = \frac{\partial \gamma}{\partial \bar{t}}(\overline{x} = 0, \bar{t}). \tag{6.16}$$

Three creep regimes can be observed. After a transient period, the logarithm of the shear rate was an affine function of time. The slope of this function was equal to -1/2. Therefore, the creep strain during this secondary regime was a linear function of $\sqrt{\bar{t}}$. Finally, the shear rate converged to a finite value and the shear deformation was therefore a linear function of time. The same three creep regimes were observed for other values of the characteristic length λ^{-1}.

Interestingly, this short extension of the shear-lag model to viscoelasticity shows that clay layers with a finite size could behave differently from clay layers simulated by molecular dynamics, since those latter are infinite in space by construction. The creep obtained by molecular simulations, which

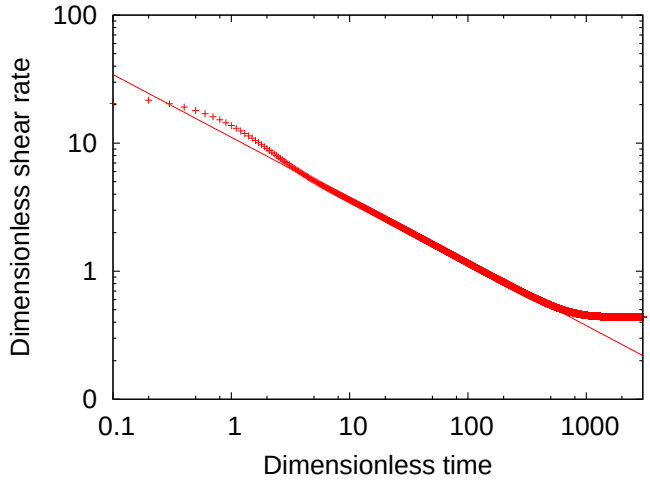

Figure 6.12: Dimensionless shear rate $\dot{\gamma}$ as a function of dimensionless time at the extremities of the adhesive of a bonded joint computed by a finite difference scheme for $\lambda = 50$. The solid line is a fit of the data between $\bar{t} = 10$ and $\bar{t} = 500$.

was a linear function of time, is observed on layers with a finite size only after a transient period. We were hoping that creep during this transient period would have been a linear function of the logarithm of time, but this was unfortunately not the case: this creep was a linear function of the square root of time. In conclusion, this study allowed us to discard the shear-lag effect as a potential candidate for the origin of logarithmic creep at the scale of the clay layer.

6.5 Conclusion

In this chapter, we presented both experimental and numerical results of the creep behavior of swelling clays. We used molecular dynamics to investigate the effect of water on the creep at the scale of the layer. Interlayer water lubricated the contact between the layers and the creep was a linear function of time. The viscous behavior of the hydrated clay layers was well captured by a Bingham model. The yield stress was significantly lower for the clay layers that contained 2 or 3 layers of water than for the clay layer that contained

only 1 layer of water. In contrast, at all humidities and stress considered, we observed experimentally that clay films creeped logarithmically with time.

This logarithmic creep cannot be explained by the linear creep simulated numerically at the scale of the layer. Wondering whether the finite size of the clay layers could play a role in the explanation, we investigated a simple analytical model of a bonded joint and applied it at the scale of the clay layer. This shear lag model shows that the distribution of shear stress can be nonuniform in an adhesive between two adherends. In a viscoelastic adhesive, this distribution becomes more uniform over time. Even for an adhesive with a Maxwell-type rheological behavior, taking into account the finite size of the clay layer can thus lead to a transient creep that is not linear with respect to time. However, this model did not lead to a transient creep that depended linearly on the logarithm of time, but on the square root of time.

At the scale of the clay layers, molecular simulations showed that Na-montmorillonite and Ca-montmorillonite responded slightly differently to shear. The viscosity and the yield stress were higher for Ca-montmorillonite than for Na-montmorillonite. The amplitude of the yield stress could impact the time-dependent behavior of the clay layers. Moreover, the nature of the cation impacts strongly the size of the particles and their arrangement (Shomer and Mingelgrin, 1978; Schramm and Kwak, 1982), which in turn could impact the creep behavior of mesoscopic samples.

Therefore, we have no rationale explanation following which creep at the scale of the clay layer should be logarithmic with respect to time. As a consequence, our results strongly suggest that the origin of the logarithmic creep of clay materials originates from the mesoscopic scale (i.e. an assembly of clay layers and particles) and not from the scale of the clay layers.

Chapter 7

Conclusions and perspectives

In this chapter, *we summarize the main results of this thesis. We present the conclusions of the experimental and numerical works and show the relevance and complementarity of the two approaches. We also highlight how this work could be extended and suggest research perspectives.*

Dans ce Chapitre, *nous résumons les principaux résultats de cette thèse. Nous présentons les conclusions du travail expérimental et du travail numérique et nous montrons la pertinence et la complémentarité des deux approches. Nous soulignons également comment ce travail pourrait être poursuivi et proposons des perspectives de recherche.*

Contents

This Chapter presents a summary of the main findings of this thesis. Based on these contributions to the clay materials science, suggestions for future research and perspectives are proposed.

7.1 Summary and conclusions

This thesis aimed at better understanding the fundamental mechanisms of the hydration and deformation of swelling clays. In particular, we focused on the multiscale aspects, both in space and time. The objective was to supply models at a larger scale with a solid physical basis in order to make it possible to build predictive macroscopic constitutive laws for clay-based materials in a bottom-up approach.

Our strategy consisted in using molecular simulations to quantify the mechanical properties of clays at the scale of the layer and experiments on self-standing clay films to understand how the behavior at the scale of the clay layer impacted properties at the mesoscale. Molecular simulations made it possible to compute the swelling, cohesion, elastic and viscous properties at the scale of the clay layers. Since the multiscale structure of clays remains complex and challenging, experiments on clay films aimed at filling the gap between the scale of the layer and the macroscopic scale.

This study revealed the following results about the hydromechanical behavior of clay-based materials:

– The interlayer crystalline swelling governs the swelling at the mesoscale when free swelling is possible. The combination of environmental scanning electron microscopy with digital image correlation made it possible to observe and quantify the swelling of well-ordered clay films that were a-few-dozen-μm-thick (see Chapter 2). The comparison between

the results of this experiment and data at the scale of the layer, such as X-ray diffraction and molecular simulations, showed that the swelling and the amount of adsorbed water were comparable for the films and for the interlayer space.

- We proposed a numerical model, the Explicit Solvent Primitive Model, to understand the interactions in mesopores between clay layers (see Chapter 3). We showed that taking into account the solvent explicitly had a significant impact on the cohesion of the model. Ionic correlation forces were always present between the clay layers and always played an important role, even in the case of layers carrying a low surface charge balanced by monovalent counterions.
- We were able to compute all coefficients of the stiffness tensor of clay layers at finite temperature using molecular dynamics (see Chapter 4). These coefficients can be split in two groups: the in-plane and the out-of-plane coefficients. The elastic behavior within the clay layers is governed by enthalpic elasticity. Therefore, the in-plane coefficients were not very sensitive to temperature and water content. In contrast, the interactions between the layers have a significant entropic origin. Thus, the out-of-plane coefficients decreased notably with temperature and water content. However, the nature of the cation had no impact on the elastic properties of the clay layers, except in the dry state.
- Tensile tests on clay films under controlled relative humidity highlighted the softening of clays upon hydration (see Chapter 5). The Young's moduli of the films had the same order of magnitude (i.e. a few GPa) as the out-of-plane shear moduli of the layers. The nature of the interlayer cation impacted the Young's moduli of the films: at given water content films made with Ca-montmorillonite were stiffer than films made with Na-montmorillonite, though the former softened more than the latter upon hydration. This contradiction with the results of molecular simulations suggests that the elastic deformation is not controlled by mechanisms occurring at the scale of the clay layer only, but also at a larger mesoscopic scale.
- When creeping, infinite hydrated clay layers creep linearly with respect

to time. This conclusion was obtained by molecular dynamics, in which we applied shear stresses on clay layers in various hydration states. The viscous behavior of the clay layers could be well modeled by a Bingham law: above a yield stress, the computed shear rate was a linear function of the difference between the stress and the yield stress. The obtained viscosity had the same order of magnitude but was larger than that of bulk water as a consequence of confinement. The obtained yield stress was much greater when the interlayer contained 1 layer of water than when it contained 2 or 3 layers of water.

– After a few hundreds of seconds, the creep of the clay films was a logarithmic function of time (see Chapter 6). The creep compliance was an exponential function of the water content and relative humidity. Moreover, the amplitude of creep was about ten times as large for Na-montmorillonite as for Ca-montmorillonite. Results by molecular dynamics were unable to explain the observed logarithmic creep, which strongly that the mechanisms responsible for the logarithmic creep of clays have to be looked for at a mesoscopic scale.

7.2 Future research

In this thesis, we studied and quantified the hydromechanical behavior of swelling clays at the scale of the layer. We also performed mechanical tests on an original mesoscopic model material in order to investigate if the properties computed at the scale of the layer could explain those observed at the upper scale. We noted discrepancies between the two scales, suggesting that the arrangement of the clay particles plays a significant role on the mechanical properties of the material. Further investigations should therefore focus on the scale of the particle and of the assembly of particles.

At the scale of the clay layer, the nature of the cation had little effect on the mechanical properties. In contrast, it impacted very significantly both the elastic and the creep properties of the clay films. Macroscopic mechanical tests on one clay exchanged with various cations would provide valuable information: surprisingly, we could find no such experiment in the

literature. The structure and properties of clays that contain several types of cations in the interlayer space, which is the natural situation in most cases, need also to be explained.

The distribution of basal spacing within clay particles is known to be heterogeneous. The origin of this heterogeneity and its effect on the mechanical properties were not studied in this work and remain unclear.

Our work provided an insight on the mechanical behavior of clays at the scales of the clay layer and of a clay film. However, our work needs to be extended to upper scales in order to obtain reliable and predictive hydromechanical constitutive laws for clay matrix.

Our experiments on clay films revealed that their creep is a logarithmic function of time. Molecular simulations showed that this logarithmic creep cannot be explained at the scale of the layer. Therefore, the origin of the logarithmic creep still remains unexplained. We suggest investigating this challenging question at the scale of the clay particles and of the assembly of clay particles.

7.3 Perspectives

Concrete is another example of material which, after a transient period, creeps logarithmically with time, and the properties of which have huge repercussions on the safety and design of civil infrastructures. The microstructure of cement, which is also multiscale, heterogeneous, and complex, is very similar to the one of clay-based materials (Pellenq and Van Damme, 2004). The calcium silicate hydrates (C-S-H), like smectite clays, exhibit a plate-like structure with counterions and water molecules between charged silica chains (Pellenq et al., 2009). Like clay, C-S-H creeps logarithmic with respect to time after a transient period. But, unlike clay, C-S-H does not lose its cohesion when immersed in water. Nanoindentation tests on cement pastes (Vandamme and Ulm, 2009) revealed the nanogranular nature of C-S-H and showed that the logarithmic creep of C-S-H was caused by rearrangements of nanoscale particles. However, the origin of the logarithmic creep of cement-based materials also remains unexplained. The results of experiments on

cement-based materials and the similarities of microstructure provide an interesting lead to understand the mechanical behavior of clays. Conversely, our work could also be beneficial to the understanding and the control of the hydromechanical behavior of cement and concrete.

Appendix A

Results of the creep tests on clay films

The two following Tables report the data of all the creep tests performed on films of Swy-2-Ca and Swy-2-Na, respectively.

Film	Dry density (mg/cm^2)	Number of clay layers	Relative humidity (%)	Water content (g/g of dry clay)	Force applied (mN)	Force per layer (μN)	Creep coefficent α ($\times 10^{-5}$)	Creep compliance κ ($kPa^{-1}.m^{-1}$)
Swy-2-Ca	3.8	14800	92.0 ± 2.9	258 ± 14	387	26.1	217 ± 9	773 ± 34
Swy-2-Ca	3.8	14800	91.2 ± 1.9	255 ± 8	187	12.6	38.0 ± 1.2	279 ± 9
Swy-2-Ca	3.8	14800	77.7 ± 2.9	223 ± 3	387	26.1	52.6 ± 0.3	171 ± 6
Swy-2-Ca	5.6	22000	77.5 ± 2.8	223 ± 5	682	31.0	16.6 ± 0.6	50 ± 2
Swy-2-Ca	5.6	22000	77.5 ± 2.8	223 ± 5	916	41.7	28.9 ± 0.7	64 ± 2
Swy-2-Ca	3.8	14800	68.6 ± 2.9	210 ± 4	622	42.0	19.6 ± 0.4	43 ± 1
Swy-2-Ca	3.8	14800	68.6 ± 2.9	210 ± 4	771	52.0	25.9 ± 1.0	46 ± 2
Swy-2-Ca	5.6	22000	64.0 ± 1.5	204 ± 2	1168	53.1	9.6 ± 0.7	17 ± 1
Swy-2-Ca	5.6	22000	64.0 ± 1.5	204 ± 2	1047	47.6	3.1 ± 0.6	13 ± 1
Swy-2-Ca	5.6	22000	63.2 ± 1.0	203 ± 2	779	35.3	4.4 ± 0.9	12 ± 2

Film	Dry density (mg/cm^2)	Number of clay layers	Relative humidity (%)	Water content (g/g of dry clay)	Force applied (mN)	Force per layer (μN)	Creep coefficent α ($\times 10^{-5}$)	Creep compliance κ ($kPa^{-1}.m^{-1}$)
Swy-2-Na	5.9	22800	99.1 ± 1.8	282 ± 6	240	10.5	1300 ± 2.4	11476 ± 21
Swy-2-Na	4.9	19100	92 ± 2.9	258 ± 10	387	20.2	905 ± 21	4176 ± 98
Swy-2-Na	6.0	23100	91.5 ± 2.2	257 ± 7	187	8.1	215 ± 1.9	2468 ± 21
Swy-2-Na	5.9	22800	81.3 ± 1.5	224 ± 5	917	40.2	24.9 ± 0.4	58 ± 1
Swy-2-Na	5.9	22800	81.3 ± 1.5	224 ± 5	387	17.0	12.0 ± 1.0	66 ± 5
Swy-2-Na	5.9	22800	80.3 ± 2.3	221 ± 7	915	40.1	64.0 ± 1.1	148 ± 2
Swy-2-Na	6.0	23100	77.7 ± 2.0	213 ± 6	387	16.7	231 ± 0.4	1289 ± 2
Swy-2-Na	6.0	23100	60 ± 2.5	162 ± 7	771	33.3	8.8 ± 0.3	24 ± 1
Swy-2-Na	5.9	22800	51.3 ± 1.5	139 ± 4	683	29.9	8.7 ± 2.2	27 ± 7

Bibliography

Aadnoy, B. S. and Ong, S. (2003). Introduction to special issue on borehole stability. *Journal of Petroleum Science and Engineering*, 38(3-4):79–82. *Cited page 36*

Allahyarov, E., Gompper, G., and Löwen, H. (2005). DNA condensation and redissolution: interaction between overcharged DNA molecules. *Journal of Physics: Condensed Matter*, 17(20):S1827–S1840. *Cited page 85*

Allais, L., Bornert, M., Bretheau, T., and Caldemaison, D. (1994). Experimental characterization of the local strain field in a heterogeneous elastoplastic material. *Acta Metallurgica et Materialia*, 42(11):3865–3880. *Cited pages 65, 66, 162, and 163*

Alonso, E. E., Gens, A., and Josa, A. (1990). A constitutive model for partially saturated soils. *Géotechnique*, 40(3):405–430. *Cited page 44*

Anderson, R., Ratcliffe, I., Greenwell, H., Williams, P., Cliffe, S., and Coveney, P. (2010). Clay swelling — A challenge in the oilfield. *Earth-Science Reviews*, 98(3-4):201–216. *Cited pages 35, 36, 43, and 85*

ANDRA (2005a). Dossier 2005 Argile. Technical report. *Cited page 33*

ANDRA (2005b). Evaluation of the feasability of a geological repository in an argillaceous formation. Technical report. *Cited pages 31 and 33*

ANDRA (2012). Inventaire national des matières et déchets radioactifs - Résumé. Technical report. *Cited pages 30 and 31*

Arroyo, J. L., Li, H., Teppen, B. J., and Boyd, S. A. (2005). A simple method for partial purification of reference clays. *Clays and Clay Minerals*, 53(5):512–520. *Cited page 58*

Auvray, C., Giot, R., and Grgic, D. (2013). Nano-indentation tests on partially satured argillite: Experimental device and measurements. In *Eurock 2013: The 2013 ISRM International Symposium, "Rock Mechanics for Resources, Energy, and Environment"*. *Cited page 46*

Bailey, S. W. (1980). Summary of recommendations of AIPEA nomenclature committee. *Clay Minerals*, 15(85):85–93. *Cited page 39*

Ballenegger, V. and Arnold, A. (2009). Simulations of non-neutral slab systems with long-range electrostatic interactions in two-dimensional periodic boundary conditions. *The Journal of Chemical Physics*, (131):094107. *Cited page 102*

Ballenegger, V. and Hansen, J.-P. (2005). Dielectric permittivity profiles of confined polar fluids. *The Journal of chemical physics*, 122(11):114711. *Cited page 109*

Bennadji-Gridi, F., Smith, A., and Bonnet, J.-P. (2006). Montmorillonite based artificial nacre prepared via a drying process. *Materials Science and Engineering: B*, 130(1-3):132–136. *Cited page 154*

Bérend, I., Cases, J.-M., François, M., Uriot, J.-P., Michot, L. J., Masion, A., and Thomas, F. (1995). Mechanism of adsorption and desorption of water vapor by homoionic montmorillonites: 2. The Li+, Na+, K+, Rb+ and Cs+ -exchanged forms. *Clays and Clay Minerals*, 43(3):324–336. *Cited pages 41, 42, 48, 74, 75, 76, 77, 78, and 172*

Berendsen, H. J. C., Postma, J. P. M., Van Gunsteren, W. F., and Hermans, J. (1981). Interaction models for water in relation to protein hydration. *Intermolecular Forces*, 11((Suppl. 1)):331–338. *Cited page 94*

Bingham, E. C. (1922). *Fluidity and plasticity*, volume 1. McGraw-Hill New York. *Cited page 191*

Bloys, B., Davis, N., Smolen, B., Bailey, L., Houwen, O., Reid, P., Sherwood, J., Fraser, L., and Hodder, M. (1994). Designing and managing drilling fluid. *Schlumberger Oilfield Review*, 2(2):33–43. *Cited page 36*

Bobko, C. and Ulm, F.-J. (2008). The nano-mechanical morphology of shale. *Mechanics of Materials*, 40(4-5):318–337. *Cited pages 45 and 123*

Boda, D., Chan, K.-Y., and Henderson, D. (1998). Monte Carlo simulation of an ion-dipole mixture as a model of an electrical double layer. *Journal of Chemical Physics*, 109(17):7362 – 7371. *Cited page 104*

Bonthuis, D. J., Gekle, S., and Netz, R. R. (2012). Profile of the static permittivity tensor of water at interfaces: consequences for capacitance, hydration interaction and ion adsorption. *Langmuir*, 28(20):7679–94. *Cited page 108*

Bornert, M., Brémand, F., Doumalin, P., Dupré, J.-C., Fazzini, M., Grédiac, M., Hild, F., Mistou, S., Molimard, J., Orteu, J.-J., Robert, L., Surrel, Y., Vacher, P., and Wattrisse, B. (2008). Assessment of digital image correlation measurement errors: Methodology and results. *Experimental Mechanics*, 49(3):353–370. *Cited pages 63, 66, and 160*

Bornert, M., Valès, F., Gharbi, H., and Nguyen Minh, D. (2010). Multiscale full-field strain measurements for micromechanical investigations of the hydromechanical behaviour of clayey rocks. *Strain*, 46:33–46. *Cited pages 46, 47, 66, 123, and 153*

Brillouin, L. (1940). *Influence de la température sur l'élasticité d'un solide*, volume 99. Gauthier-Villars. *Cited page 141*

Caillol, J.-M., Levesque, D., and Weis, J. J. (1986). Theoretical calculation of ionic solution properties. *The Journal of Chemical Physics*, 85(11):6645. *Cited page 102*

Cancès, E., Legoll, F., and Stoltz, G. (2005). Theoritical and numerical comparison of some sampling methods for molecular dynamics. *ESAIM: Mathematical Modelling and Numerical Analysis*, 41:351–389. *Cited page 98*

Cariou, S., Duan, Z., Davy, C., Skoczylas, F., and Dormieux, L. (2012). Poromechanics of partially saturated COx argillite. *Applied Clay Science*, 56:36–47. *Cited pages 46, 47, and 123*

Carrier, B., Wang, L., Vandamme, M., Pellenq, R. J.-M., Bornert, M., Tanguy, A., and Van Damme, H. (2013). ESEM study of the humidity-induced swelling of clay films. *Langmuir*, 29(41):12823—-12833. *Cited page 56*

Cases, J.-M., Bérend, I., François, M., Uriot, J., Michot, L. J., and Thomas, F. (1997). Mechanism of adsorption and desorption of water vapor by homoinic montmorillonite: 3. The Mg2+, Ca2+, Sr2+ and Ba2+ exchanged forms. *Clays and Clay Minerals*, 45(1):8–22. *Cited pages 41, 42, 48, 74, 75, 76, 77, 78, and 172*

CGDD (2010). Le régime d'assurance des catastrophes naturelles en France métropolitaine entre 1995 et 2006. Technical report, Commissariat Général au Développement Durable. *Cited pages 34 and 35*

Chandra, A. (2000). Static dielectric constant of aqueous electrolyte solutions: Is there any dynamic contribution? *The Journal of Chemical Physics*, 113(3):903. *Cited pages 102 and 103*

Chandra, A. and Patey, G. N. (1994). Dielectric relaxation of electrolyte solutions: Molecular dynamics and theoretical results for ions in simple dipolar solvents. *The Journal of Chemical Physics*, 100(11):8385. *Cited page 102*

Chavez-Paez, M., Van Workum, K. L., de Pablo, L., and de Pablo, J. J. (2001). Monte Carlo simulations of Wyoming sodium montmorillonite hydrates. *The Journal of Chemical Physics*, 114(3):1405. *Cited page 91*

Costanzo, P. and Guggenheim, S. (2001). Baseline studies of the Clay Minerals Society source clays: Preface. *Clays and Clay Minerals*, 49(5):371–371. *Cited page 58*

Cour des Comptes (2012). The costs of the nuclear power sector. Technical report, Cours des comptes. *Cited page 31*

Coussy, O. (2011). *Mechanics and Physics of Porous Solids*. Wiley. *Cited page 43*

Cui, Y. J., Tang, A. M., Loiseau, C., and Delage, P. (2007a). Determining water permeability of a compacted-bentonite sand mixture under confined and free-swell conditions. In *Clays in natural and engineered barriers for radioactive waste confinement*. *Cited page 32*

Cui, Z., Sun, Y., Li, J., and Qu, J. (2007b). Combination method for the calculation of elastic constants. *Physical Review B*, 75:214101. *Cited page 127*

Cuisiat, F., Grande, L., and Hø eg, K. (2002). Laboratory testing of long term fracture permeability in shales. *Proceedings of SPE/ISRM Rock Mechanics Conference*. *Cited page 36*

Cygan, R. T., Liang, J.-J., and Kalinichev, A. G. (2004). Molecular models of hydroxide, oxyhydroxide, and clay phases and the development of a general force field. *The Journal of Physical Chemistry B*, 108(4):1255–1266. *Cited pages 76, 92, 94, 129, 134, 141, and 189*

D'Arcy, R. L. and Watt, I. C. (1970). Analysis of sorption isotherms of non-homogeneous sorbents. *Transactions of the Faraday Society*, 66(0):1236–1245. *Cited page 71*

Dautriat, J., Bornert, M., Gland, N., Dimanov, A., and Raphanel, J. (2011). Localized deformation induced by heterogeneities in porous carbonate analysed by multi-scale digital image correlation. *Tectonophysics*, 503(1-2):100–116. *Cited page 160*

Delage, P., Cui, Y. J., and Tang, A. M. (2010). Clays in radioactive waste disposal. *Journal of Rock Mechanics and Geotechnical Engineering*, 2(2):111–123. *Cited pages 32 and 41*

Delage, P., Howat, M., and Cui, Y. (1998). The relationship between suction and swelling properties in a heavily compacted unsaturated clay. *Engineering Geology*, 50(1-2):31–48. *Cited page 41*

Delville, A. (2012). Toward a detailed molecular analysis of the long-range swelling gap of charged rigid lamellae sispersed in water. *The Journal of Physical Chemistry C*, 116(1):818–825. *Cited pages 43 and 85*

Delville, A. and Pellenq, R. J.-M. (2000). Electrostatic attraction and/or repulsion between charged colloids: A (NVT) Monte-Carlo study. *Molecular Simulation*, 24(1-3):1–24. *Cited pages 87 and 89*

Derjaguin, B. V. (1941). Theory of the stability of strongly charged lyophobic sols and the adhesion of strongly charged particles in solutions of electrolytes. *Acta Physicochim. USSR*, 14:633–662. *Cited page 86*

Doumalin, P. (2000). *Microextensométrie locale par corrélation d'images numériques*. PhD thesis, École Polytechnique. *Cited page 64*

Ebrahimi, D., Pellenq, R. J.-M., and Whittle, A. J. (2012). Nanoscale elastic properties of montmorillonite upon water adsorption. *Langmuir*, 28(49):16855–16863. *Cited pages 124, 131, and 135*

Economides, M. and Nolte, K. (2000). *Reservoir Stimulation*. Wiley. *Cited page 36*

Evans, D. J. and Morriss, G. P. (1990). *Statistical Mechanics of Non equilibrium Liquids*. Academic Press. *Cited page 190*

Faro, T. M. C., Thim, G. P., and Skaf, M. S. (2010). A Lennard-Jones plus Coulomb potential for Al3+ ions in aqueous solutions. *The Journal of chemical physics*, 132(11):114509. *Cited page 92*

Feda, J. (1992). *Creep of Soils: and Related Phenomena*. Access Online via Elsevier. *Cited pages 45, 179, 180, and 193*

Ferrage, E., Lanson, B., Sakharov, B. A., and Drits, V. A. (2005). Investigation of smectite hydration properties by modeling experimental X-ray diffraction patterns: Part I. Montmorillonite hydration properties. *American Mineralogist*, 90:1358–1374. *Cited pages 41, 43, 48, 74, 172, and 173*

Frenkel, D. and Smit, B. (2002). *Understanding Molecular Simulation*. Academic Press. *Cited pages 94, 98, 124, and 131*

Froltsov, V. A. and Klapp, S. H. L. (2007). Dielectric response of polar liquids in narrow slit pores. *The Journal of Chemical Physics*, 126(11):114703. *Cited pages 103, 107, and 108*

Gale, J. D. (1997). GULP: A computer program for the symmetry-adapted simulation of solids. *Journal of the Chemical Societety, Faraday Transactions*, 93(4):629–637. *Cited page 130*

Gale, J. D. and Rohl, A. L. (2003). The General Utility Lattice Program (GULP). *Molecular Simulation*, 29(5):291–341. *Cited pages 126 and 130*

Gaucher, E., Robelin, C., Matray, J., Négrel, G., Gros, Y., Heitz, J., Vinsot, A., Rebours, H., Cassagnabère, A., and Bouchet, A. (2004). ANDRA underground research laboratory: Interpretation of the mineralogical and geochemical data acquired in the Callovian-Oxfordian formation by investigative drilling. *Physics and Chemistry of The Earth*, 29(1):55–77. *Cited page 33*

Guggenheim, S. and Martin, R. T. (1995). Definition of clay and clay mineral: Joint report of the AIPEA nomenclature and CMS nomenclature committees. *Clays*, 43(2):255–256. *Cited page 37*

Guldbrand, L., Jönsson, B., Wennerström, H. k., and Linse, P. (1984). Electrical double layer forces. A Monte Carlo study. *The Journal of Chemical Physics*, 80(5):2221. *Cited page 87*

Harris, K. R. and Woolf, L. A. (2004). Temperature and Volume Dependence of the Viscosity of Water and Heavy Water at Low Temperatures. *Journal of Chemical & Engineering Data*, 49(4):1064–1069. *Cited page 193*

Hasted, J. B., Ritson, D. M., and Collie, C. H. (1948). Dielectric Properties of Aqueous Ionic Solutions. Parts I and II. *The Journal of Chemical Physics*, 16(1):1. *Cited pages 108 and 109*

Hensen, E. J. M. and Smit, B. (2002). Why clays swell. *The Journal of Physical Chemistry B*, 106(49):12664–12667. *Cited pages 42, 48, 89, 107, and 111*

Hensen, E. J. M., Tambach, T. J., Bliek, A., and Smit, B. (2001). Adsorption isohterms of water in Li-, Na-, and K-montmorillonite by molecular simulation. *The Journal of Chemical Physics*, 115(7):3346. *Cited page 94*

Hess, B. (2002). Determining the shear viscosity of model liquids from molecular dynamics simulations. *The Journal of Chemical Physics*, 116(1):209. *Cited page 193*

Hill, R. (1952). The elastic behaviour of a crystalline aggregate. *Proceedings of the Physical Society. Section A*, 65(5):349. *Cited page 126*

Ichikawa, Y., Kawamura, K., Theramast, N., and Kitayama, K. (2004). Secondary and tertial consolidation of bentonite clay: Consolidation test, molecular dynamics simulation and multiscale homogenization analysis. *Mechanics of Materials*, 36(5-6):487–513. *Cited pages 45, 180, and 193*

Israelachvili, J. N. (1991). *Intermolecular and Surface Forces*. Academic Press Inc. *Cited page 86*

Jones, D. E. J. and Holtz, W. G. (1973). Expansive soils - The hidden disaster. *Civil Engineering*, 43(8):49–51. *Cited page 34*

Jönsson, B., Wennerstroem, H., and Halle, B. (1980). Ion distributions in lamellar liquid crystals. A comparison between results from Monte Carlo simulations and solutions of the Poisson-Boltzmann equation. *The Journal of Physical Chemistry*, 84(17):2179–2185. *Cited page 86*

Jönsson, B. and Wennerström, H. (2004). Ion-ion correlations in liquid dispersions. *The Journal of Adhesion*, 80:339–364. *Cited pages 87 and 143*

Joubaud, R. and Stoltz, G. (2012). Nonequilibrium shear viscosity computations with langevin dynamics. *Multiscale Modeling \& Simulation*, 10(1):191–216. *Cited page 190*

Karaborni, S., Smit, B., Heidug, W., Urai, J., and van Oort, E. (1996). The swelling of clays: Molecular simulations of the hydration of montmorillonite. *Science*, 271:1102 – 1104. *Cited pages 42 and 48*

Khota, S. P., Li, Y., and Guzelsu, N. (2001). Micromechanical model of nacre tested in tension. *Journal of Materials Science*, (36):2001–2007. *Cited page 197*

Kjellander, R., Marcelja, S., and Quirk, J. P. (1988a). Attractive double-sayer interactions between calcium clay particles. *Journal of Colloid and Interface Science*, 126(1):194–211. *Cited page 82*

Kjellander, R., Mareelja, S., Pashley, R. M., and Quirk, J. P. (1988b). Double-layer ion correlation forces restrict calcium-clay swelling. *Journal of Petroleum Science and Engineering*, 92(23):6489–6492. *Cited page 82*

Laird, D. A. (1996). Model for crystalline swelling of 2:1 phyllosilicates. *Clays and Clay Minerals*, 44(4):553–559. *Cited page 108*

Laird, D. A. (2006). Influence of layer charge on swelling of smectites. *Applied Clay Science*, 34(1-4):74–87. *Cited pages 41, 42, 43, and 85*

Lee, J. H. and Guggenheim, S. (1981). Single crystal X-ray refinement of pyrophyllite-1T. *American Mineralogist*, 66:350–357. *Cited page 91*

Lelièvre, T., Stoltz, G., and Rousset, M. (2010). *Free energy computations: A mathematical perspective*. Imperial College Pr. *Cited pages 98, 104, and 106*

Lin, Y., Shiomi, J., Maruyama, S., and Amberg, G. (2009). Dielectric relaxation of water inside a single-walled carbon nanotube. *Physical Review B*, 80(4):1–7. *Cited page 108*

Liu, Y. and Ichiye, T. (1996). The static dielectric constant of the soft sticky dipole model of liquid water: Monte Carlo simulation. *Chemical Physics Letters*, 256(June):334–340. *Cited page 119*

Loewenstein, W. (1954). The distribution of aluminum in the tetrahedra of silicates and aluminates. *American Mineralogist*, 39(1-2):92–96. *Cited page 92*

Magnenet, V., Giraud, A., and Auvray, C. (2011). About the effect of relative humidity on the indentation response of Meuse/Haute–Marne argillite. *Acta Geotechnica*, 6(3):155–166. *Cited page 46*

Maison, T. (2011). *Analyse à l'échelle microscopique des phénomènes d'humectation et de dessication des argiles*. PhD thesis, École centrale Paris. *Cited page 57*

Martyna, G. J., Tobias, D. J., and Klein, M. L. (1994). Constant pressure molecular dynamics algorithms. *The Journal of Chemical Physics*, 101(5):4177–4189. *Cited page 128*

Mazo, M. A., Manevitch, L. I., Gusarova, E. B., Berlin, A. A., Balabaev, N. K., and Rutledge, G. C. (2008a). Molecular dynamics simulation of thermomechanical properties of montmorillonite crystal. II. Hydrated montmorillonite crystal. *The Journal of Physical Chemistry C*, 112(44):17056–17062. *Cited pages 124, 133, 134, and 135*

Mazo, M. A., Manevitch, L. I., Gusarova, E. B., Shamaev, M. Y., Berlin, A. A., Balabaev, N. K., and Rutledge, G. C. (2008b). Molecular dynamics simulation of thermomechanical properties of montmorillonite crystal. 1. Isolated clay nanoplate. *The Journal of Physical Chemistry B*, 112(10):2964–9. *Cited page 124*

Mermut, A. R. and Faz Cano, A. (2001). Baseline studies of the clay minerals society source clays: Chemical analyses of major elements. *Clays and Clay Minerals*, 49(5):381–386. *Cited page 58*

Mesri, G. (1973). Coefficient of secondary compression. *Journal of the Soil Mechanics and Foundations Division*, 99(1):123–137. *Cited page 47*

Meunier, A. (2005). *Clays*. Springer. *Cited page 38*

Mondol, N. H., Jahren, J., and Bjorlykke, K. (2008). Elastic properties of clay minerals. *The Leading Edge*, pages 758–770. *Cited page 124*

Montes-H, G. (2005). Swelling-shrinkage measurements of bentonite using coupled environmental scanning electron microscopy and digital image analysis. *Journal of Colloid and Interface Science*, 284(1):271–7. *Cited page 56*

Montes-H, G., Duplay, J., Martinez, L., Geraud, Y., and Rousset-Tournier, B. (2003). Influence of interlayer cations on the water sorption and swelling-shrinkage of MX80 bentonite. *Applied Clay Science*, 23(5-6):309–321. *Cited pages 57 and 80*

Montes-H, G., Geraud, Y., Duplay, J., and Reuschle, T. (2005). ESEM observations of compacted bentonite submitted to hydration/dehydration conditions. *Colloids and Surfaces A: Physicochemical and Engineering Aspects*, 262(1-3):14–22. *Cited page 57*

Mooney, R. W., Keenan, A. G., and Wood, L. A. (1952). Adsorption of water vapor by montmorillonite. II. Effect of exchangeable cations and lattice swelling as measured by X-ray diffraction. *Journal of the American Chemical Society*, 74(6):1371–1374. *Cited pages 41 and 48*

Nabarro, F. R. N. (2001). The time constant of logarithmic creep and relaxation. *Materials Science and Engineering*, A309-310:227–228. *Cited page 194*

OECD (2012). Nuclear energy data 2012. Technical report, OECD. *Cited page 30*

Ortega, J. A., Ulm, F.-J., and Abousleiman, Y. (2007). The effect of the nanogranular nature of shale on their poroelastic behavior. *Acta Geotechnica*, 2(3):155–182. *Cited pages 45, 47, 123, 134, 135, 136, and 137*

Parrinello, M. and Rahman, A. (1981). Polymorphic transitions in single crystals: A new molecular dynamics method. *Journal of Applied Physics*, 52(December):7182–7190. *Cited page 128*

Parrinello, M. and Rahman, A. (1982). Strain fluctuations and elastic constants. *Strain*, 76(1):2662–2666. *Cited pages 124 and 126*

Pavese, A., Ferraris, G., Pischedda, V., and Ibberson, R. (1999). Tetrahedral order in phengite 2M(1) upon heating, from powder neutron diffraction, and thermodynamic consequences. *European Journal of Mineralogy*, 11(2):309–320. *Cited page 143*

Pellenq, R. J.-M., Caillol, J.-M., and Delville, A. (1997). Electrostatic attraction between two charged surfaces: A (N,V,T) Monte Carlo simulation. *The Journal of Physical Chemistry B*, 101(42):8584–8594. *Cited pages 87, 88, and 143*

Pellenq, R. J.-M., Kushima, A., Shahsavari, R., Van Vliet, K. J., Buehler, M. J., Yip, S., and Ulm, F.-J. (2009). A realistic molecular model of cement hydrates. *Proceedings of the National Academy of Sciences of the United States of America*, 106(38):16102–7. *Cited pages 86, 89, and 205*

Pellenq, R. J.-M., Lequeux, N., and Van Damme, H. (2008). Engineering the bonding scheme in C–S–H: The iono-covalent framework. *Cement and Concrete Research*, 38(2):159–174. *Cited pages 86 and 88*

Pellenq, R. J.-M. and Van Damme, H. (2004). Why does concrete set?: The nature of cohesion forces in hardened cement-based materials. *MRS Bulletin*, 29(5):319–323. *Cited pages 86, 88, and 205*

Pham, Q. T., Vales, F., Malinsky, L., Minh, D. N., and Gharbi, H. (2007). Effects of desaturation–resaturation on mudstone. *Physics and Chemistry of the Earth, Parts A/B/C*, 32(8–14):646–655. *Cited pages 46 and 123*

Plimpton, S. (1995). Fast parallel algorithms for short–range molecular dynamics. *Journal of Computational Physics*, 117:1–19. *Cited pages 98, 130, and 190*

Pospísil, M., Kalendová, A., Capková, P., Simoník, J., and Valásková, M. (2004). Structure analysis of intercalated layer silicates: Combination of

molecular simulations and experiment. *Journal of Colloid and Interface Science*, 277(1):154–61. *Cited page 59*

Push, R. and Yong, R. N. (2006). *Microstructure of smectite clays and engineering performance*. Taylor & Francis. *Cited pages 41 and 42*

Rappé, A. K. and Goddard, W. A. (1991). Charge equilibration for molecular dynamics simulations. *The Journal of Physical Chemistry*, 95:3358–3363. *Cited page 92*

République française, . (1991). Loi n° 91-1381 du 30 décembre 1991 relative aux recherches sur la gestion des déchets radioactifs. *Cited page 31*

République française, . (2006). Loi n° 2006-739 du 28 juin 2006 de programme relative à la gestion durable des matières et déchets radioactifs. *Cited page 31*

Reuss, A. and Angew, Z. (1929). Berechnung der Fließgrenze von Mischkristallen auf Grund der Plastizitätsbedingung für Einkristalle. *Applied Mathematical and Mechanics*, 9(1):49–58. *Cited page 126*

Romero, E. and Simms, P. H. (2008). Microstructure investigation in unsaturated soils: A review with special attention to contribution of mercury intrusion porosimetry and environmental scanning electron microscopy. *Geotechnical and Geological Engineering*, 26(6):705–727. *Cited page 56*

Roscoe, K. H. and Burland, J. (1968). On the generalised stress-strain behaviour of wet clay. *Engineering Plasticity*, pages 535–609. *Cited page 44*

Salles, F., Beurroies, I., Bildstein, O., Jullien, M., Raynal, J., Denoyel, R., and Damme, H. V. (2008). A calorimetric study of mesoscopic swelling and hydration sequence in solid Na-montmorillonite. *Applied Clay Science*, 39(3-4):186–201. *Cited page 44*

Salles, F., Bildstein, O., Douillard, J. M., Jullien, M., Raynal, J., and Van Damme, H. (2010). On the cation dependence of interlamellar and interparticular water and swelling in smectite clays. *Langmuir*, 26(7):5028–37. *Cited pages 41, 43, 44, 48, 56, 79, and 80*

Salles, F., Bildstein, O., Douillard, J.-m., Jullien, M., and Van Damme, H. (2007). Determination of the driving force for the hydration of the swelling clays from computation of the hydration energy of the interlayer cations and the clay layer. *The Journal of Physical Chemistry C*, 111(35):13170–13176. *Cited page 107*

Sammartino, S., Bouchet, a., Prêt, D., Parneix, J.-C., and Tevissen, E. (2003). Spatial distribution of porosity and minerals in clay rocks from the Callovo-Oxfordian formation (Meuse/Haute-Marne, Eastern France)—implications on ionic species diffusion and rock sorption capability. *Applied Clay Science*, 23(1-4):157–166. *Cited page 80*

Sato, T., Watanabe, T., and Otsuka, R. (1992). Effects of layer charge, charge location, and energy change on expansion properties of dioctahedral smectites. *Clays and Clay Minerals*, 40(1):103–113. *Cited pages 74, 75, and 85*

Schramm, L. L. and Kwak, J. C. T. (1982). Influence of exchangeable cation composition on the size and shape of montmorillonite particles in dilute suspension. *Clays and Clay Minerals*, 30(1):40–48. *Cited pages 41, 149, 170, and 200*

Segad, M., Hanski, S., Olsson, U., Ruokolainen, J., Å kesson, T., and Jönsson, B. (2012a). Microstructural and swelling properties of Ca and Na montmorillonite: (In situ) observations with Cryo-TEM and SAXS. *The Journal of Physical Chemistry C*, 116(13):7596–7601. *Cited page 170*

Segad, M., Jönsson, B., Akesson, T., and Cabane, B. (2010). Ca/Na montmorillonite: Structure, forces and swelling properties. *Langmuir*, 26(8):5782–90. *Cited pages 43, 85, 112, and 170*

Segad, M., Jönsson, B., and Cabane, B. (2012b). Tactoid formation in montmorillonite. *The Journal of Physical Chemistry C*, 116(48):25425–25433. *Cited page 170*

Senapati, S. and Chandra, A. (2001). Dielectric Constant of Water Confined in a Nanocavity. *The Journal of Physical Chemistry B*, 105(22):5106–5109. *Cited pages 107 and 108*

Shahsavari, R., Buehler, M. J., Pellenq, R. J.-M., and Ulm, F.-J. (2009). First-principles study of elastic constants and interlayer interactions of complex hydrated oxides: Case study of tobermorite and jennite. *Journal of the American Ceramic Society*, 92(10):2323–2330. *Cited page 89*

Shahsavari, R., Pellenq, R. J.-M., and Ulm, F.-J. (2011). Empirical force fields for complex hydrated calcio-silicate layered materials. *Physical Chemistry Chemical Physics : PCCP*, 13(3):1002–11. *Cited pages 89 and 141*

Shinoda, W., Shiga, M., and Mikami, M. (2004). Rapid estimation of elastic constants by molecular dynamics simulation under constant stress. *Physical Review B*, 69(13):16 –18. *Cited page 128*

Shomer, I. and Mingelgrin, U. (1978). A direct procedure for determining the number of plates in tactoids of smectites: The Na/Ca-montmorillonite case. *Clays and Clay Minerals*, 26(2):135–138. *Cited pages 41, 149, 170, and 200*

Sone, H. and Zoback, M. (2010). Strength, creep and frictional properties of gas shale reservoir rocks. In *44th U.S. Rock Mechanics Symposium and 5th U.S.-Canada Rock Mechanics Symposium.* *Cited pages 46 and 179*

Stenhammar, J., Trulsson, M., and Linse, P. (2011). Some comments and corrections regarding the calculation of electrostatic potential derivatives using the Ewald summation technique. *The Journal of chemical physics*, 134(22):224104. *Cited page 102*

Striolo, A., Klaessig, F., Cole, D. R., Wilcox, J., Chase, G. G., Sondergeld, C. H., and Pasquali, M. (2012). Identification of fundamental interfacial and transport phenomena for the sustainable deployment of hydraulic shale fracturing - Role of chemicals used. Technical report, National Science Foundation. *Cited page 36*

Suter, J., Coveney, P., Greenwell, H., and Thyveetil, M.-A. (2007). Large-scale molecular dynamics study of montmorillonite clay: Emergence of

undulatory fluctuations and determination of material properties. *The Journal of Physical Chemistry C*, 111(23):8248–8259. *Cited page 124*

Sutton, M. A., Schreier, H., and Orteu, J.-J. (2009). *Image correlation for shape, motion and deformation measurements*. Springer US, Boston, MA. *Cited pages 57, 63, and 160*

Tambach, T. J., Bolhuis, P. G., and Smit, B. (2004a). A molecular mechanism of hysteresis in clay swelling. *Angewandte Chemie International Edition*, 43(20):2650–2652. *Cited page 89*

Tambach, T. J., Hensen, E. J. M., and Smit, B. (2004b). Molecular simulations of swelling clay minerals. *The Journal of Physical Chemistry B*, 108(23):7586–7596. *Cited pages 42, 48, and 89*

Teich-McGoldrick, S. L., Greathouse, J. A., and Cygan, R. T. (2012). Molecular dynamics simulations of structural and mechanical properties of muscovite: Pressure and temperature effects. *The Journal of Physical Chemistry C*, 116(28):15099–15107. *Cited pages 124, 141, and 143*

Teif, V. B. and Bohinc, K. (2011). Condensed DNA: Condensing the concepts. *Progress in biophysics and molecular biology*, 105(3):208–22. *Cited page 85*

Tuckerman, M. E. (2010). *Statistical Mechanics: Theory and Molecular Simulation*. Oxford University Press. *Cited page 190*

USGS (2004). Landslide types and processes. Technical report, United States Geological Survey. *Cited page 35*

Valleau, J. P., Ivkov, R., and Torrie, G. M. (1991). Colloid stability: The forces between charged surfaces in an electrolyte. *The Journal of Chemical Physics*, 95(1):520–532. *Cited page 87*

Van Olphen, H. and Fripiat, J. J. (1979). *Data Handbook for Clay Materials and Other Non-metallic Minerals*. Pergamon Press. *Cited page 74*

van Oort, E. (2003). On the physical and chemical stability of shales. *Journal of Petroleum Science and Engineering*, 38(3-4):213–235. *Cited page 35*

Van Workum, K. L. and de Pablo, J. J. (2003). Improved simulation method for the calculation of the elastic constants of crystalline and amorphous systems using strain fluctuations. *Physical Review E*, 67:011505. *Cited pages 121, 122, 124, 126, and 127*

Vandamme, M. and Ulm, F.-J. (2009). Nanogranular origin of concrete creep. *Proceedings of the National Academy of Sciences of the United States of America*, 106(26):10552–7. *Cited page 205*

Vanorio, T., Prasad, M., and Nur, A. (2003). Elastic properties of dry clay mineral aggregates, suspensions and sandstones. *Geophysical Journal International*, 155:319–326. *Cited page 124*

Verwey, E. J. E. J. W., Overbeek, J. T. G., and Overbeek, J. T. J. T. G. (1999). *Theory of the stability of lyophobic colloids*. Dover Publications. *Cited page 86*

Voigt, W. (1928). *Lehrbuch der Kristallphysik*. Taubner, Leipzig. *Cited page 126*

Volkersen, O. (1938). Die Nietkraftverteilung in zugbeanspruchten Nietverbindungen mit konstanten Laschenquerschnitten. *Luftfahrtforschung*, 15(1/2):41–47. *Cited page 195*

Walther, A., Bjurhager, I., Malho, J.-M., Ruokolainen, J., Berglund, L., and Ikkala, O. (2010). Supramolecular control of stiffness and strength in lightweight high-performance nacre-mimetic paper with fire-shielding properties. *Angewandte Chemie (International ed. in English)*, 49(36):6448–53. *Cited page 154*

Wander, M. C. F. and Clark, A. E. (2008). Structural and dielectric properties of quartz−water interfaces. *The Journal of Physical Chemistry C*, 112(50):19986–19994. *Cited pages 107 and 108*

Wang, J., Cheng, Q., and Tang, Z. (2012). Layered nanocomposites inspired by the structure and mechanical properties of nacre. *Chemical Society reviews*, 41(3):1111–29. *Cited page 154*

Wang, L. (2012). *Micromechanical experimental investigation and modelling of strain and damage of argillaceous rocks under combined hydric and mechanical loads.* PhD thesis, École Polytechnique. *Cited pages 42, 57, 80, and 81*

Wang, L., Bornert, M., Chanchole, S., and Heripre, E. (2013a). Experimental investigation of the free swelling of crushed argillite. *Geotechnique letters*. *Cited page 57*

Wang, L., Bornert, M., Chanchole, S., Yang, D., Heripre, E., Tanguy, A., and Caldemaison, D. (2013b). Micro-scale experimental investigation of the swelling anisotropy of the Callovo-Oxfordian argillaceous rock. *Clay Minerals*, 48:391–402. *Cited page 57*

Wang, Y. Q., Sutton, M. A., Bruck, H. A., and Schreier, H. W. (2009). Quantitative error assessment in pattern matching: Effects of intensity pattern noise, interpolation, strain and image contrast on motion measurements. *Strain*, 45(2):160–178. *Cited page 162*

Wang, Z., Wang, H., and Cates, M. E. (2001). Effective elastic properties of solid clays. *Geophysics*, 66(2):428–440. *Cited pages 124, 139, and 169*

Wu, Y., Tepper, H. L., and Voth, G. A. (2006). Flexible simple point-charge water model with improved liquid-state properties. *The Journal of Chemical Physics*, 124(2):024503. *Cited pages 98 and 99*

Yang, D., Bornert, M., Chanchole, S., Wang, L., Valli, P., and Gatmiri, B. (2011). Experimental investigation of the delayed behavior of unsaturated argillaceous rocks by means of Digital Image Correlation techniques. *Applied Clay Science*, 54(1):53–62. *Cited pages 47 and 180*

Yeh, I.-C. and Berkowitz, M. L. (1999). Ewald summation for systems with slab geometry. *Chemical Physics*, 111(7):3155–3162. *Cited page 101*

Zabat, M. (1996). *Microtexture et propriétés mécaniques de films solides de particules colloïdales.* PhD thesis, Université d'Orléans. *Cited pages 57, 154, 163, 166, and 171*

Zartman, G. D., Liu, H., Akdim, B., Pachter, R., and Heinz, H. (2010). Nanoscale tensile, shear, and failure properties of layered silicates as a function of cation density and stress. *The Journal of Physical Chemistry C*, 114(4):1763–1772. *Cited pages 124 and 141*

Zheng, Y., Zaoui, A., and Shahrour, I. (2011). A theoretical study of swelling and shrinking of hydrated Wyoming montmorillonite. *Applied Clay Science*, 51(1-2):177–181. *Cited page 89*

Zhu, H., Ghoufi, A., Szymczyk, A., Balannec, B., and Morineau, D. (2012). Anomalous dielectric behavior of nanoconfined electrolytic solutions. *Physical Review Letters*, 109(10):1–5. *Cited page 109*